Advanced Biophotonic Materials: Developing a Toolkit for Light-Harvesting Nanocomposites Using Quantum Dots and Lipids

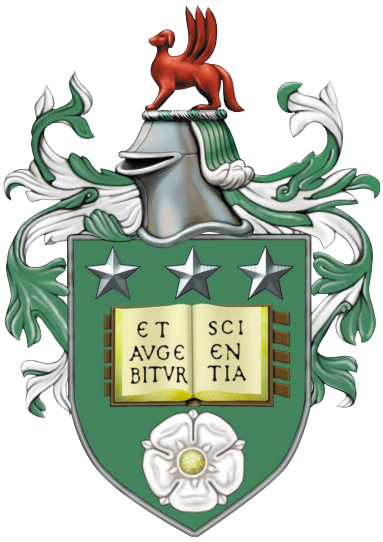

Joel Thomas Whipp

School of Physics and Astronomy
The University of Leeds

Submitted in accordance with the requirements for the degree of Doctor of Philosophy

November 2023

Declaration

The candidate confirms that the work submitted is his own and that appropriate credit has been given where reference has been made to the work of others.

In Chapter 4, the isolation, purification and characterisation of the light-harvesting protein (LHCII) was completed by Dr Ashley Hancock. All sample preparation and characterisation was completed by JTW.

In Chapter 5, all transmission electron microscopy data was collected by Dr Zabeada Aslam from the Leeds Electron Microscopy and Spectroscopy Centre (LEMAS) and analysed by JTW. Fluorescence lifetime imaging microscopy data was collected and analysed by Dr Ashley Hancock with sample preparation completed by JTW.

Acknowledgements

Firstly, I'd like to thank my supervisor, Peter Adams, for the time, effort, guidance, support, and kindness you have shown me throughout my PhD. You have been an amazing supervisor and are an amazing person with an infectious love for science, it's hard to put into words how grateful I am for everything. Next, I'd like to thank my co-supervisor Kevin Critchley for dedicating many more hours than a co-supervisor should. My project revolved so heavily around quantum dots in the end, and I'm so thankful for the knowledge and advice you provided in every single one of our many weekly meetings. I couldn't ask for a better supervision team, so thank you both so much and I wish you the very best in your future research. I'd also like to thank my unofficial third supervisor, Ashley Hancock, for not just dedicating many hours to taking and analysing FLIM data for me, but for also providing support and advice to myself and many others in MNP. I still owe you many pints. A big thank you to Abiral Tamang for all the help with the QD side of my project when I first started my PhD. Finally, I'd like to thank Zabeada Aslam for capturing some very nice EM images.

I'd like to thank the MNP group for making my PhD so enjoyable. I have been surrounded by many inspirational people and have made some truly amazing friends. Special thanks to Joe F (possibly your first proper thesis mention) for some very good banter and to Christa for some horrendous banter, you two have probably had the biggest impact on my time here and I can't thank you enough. I'd also like to thank (in no particular order) my fellow Leeds fan Amir, Foals fan Damien (mediocre band), gym-bro and pro

chef Min, Dela for the biscuits and motivational messages when I was writing up, Holly the MNP nerd (hope you managed to rob that bank), Aileen (I've been to Ireland more times than you), Matt H the MNP pirate, Alisha, Izzy (behind the phone) who can read menus in an Italian accent, TikTok star Anjali for the dry banter, Dylan the pub quiz king, Xinyu (better at golf than Tiger Woods), Maya the Simon and Garfunkel fan, Ahmad for all the football chat (I was actually expecting you to be good at football), Benard for the Spanish lessons, Thomas and Kalila (aka Bradley Wiggins and Laura Kenny) and the old guard Lucien, Fern, Sam and George (I haven't forgotten). I wish everyone in MNP the best for the future, in science and in life.

To my mum and dad (and Eden), thank you for providing me with a platform to pursue something I thoroughly enjoy doing, I wouldn't be able to do this without you. You make me proud every day and I hope I make you proud too.

Finally, Emma, where do I even begin? Thank you for 11 years of support, laughter, and happiness, all the way from school up until my many, many years at uni. We've both been working hard towards our future, and I can't wait to see what it holds.

Abstract

Quantum dots (QDs) have the potential to transfer their excited-state energy to biomolecules and other nanoparticles via Förster resonance energy transfer (FRET). When hydrophobic quantum dots are placed into aqueous suspensions, they often associate together to form a cluster of many QDs, to minimise the surface area exposed to water. Aggregated QDs are bright assemblies of potential interest in solar harvesting and bio-sensing, however, their structural and photophysical properties have not previously been characterised in detail. Research in this thesis shows that distinct lipid-stabilised 'nanocluster' structures can be controllably assembled using $CuInS_2$/ZnS QDs and a fully optical and structural analysis is performed.

Chapter 1 contains the motivation for the research, plus an introduction to the theory of FRET, the background of QDs and controlling QD clustering, and the development of bio-hybrid light-harvesting systems. Chapter 2 summarises the methodology used within this thesis. Chapter 3 details the results of my research in the utilisation of thin-film re-hydration methods to controllably assemble lipids and quantum dots into distinct nanocluster structures, covering QD synthesis optimisation and development of the self-assembly procedure. Characterisation of QD nanoclusters provided evidence of controlled nanocluster formation and a consistent, red-shifted fluorescence emission peak when compared to isolated QDs in organic solvents. Chapter 4 details attempts to associate QDs and light-harvesting complex II (LHCII), with evidence of successfully crosslinked bioconjugates that appear to exhibit FRET from the QDs to the LHCII. In Chapter 5, the structure and photophysics of hydrophobic QD nanoclusters were determined via electron microscopy, fluorescence microscopy, and spectroscopy techniques. Co-localisation of the lipid and QDs was observed, with evidence of downhill energy transfer from larger band gap to smaller band gap QDs. QD nanoclusters may have potential applications as a photo-active bio-hybrid material due to the retainment of energy transfer efficiency on a glass substrate and are a promising advancement of existing light-harvesting nanomaterials.

Contents

1 Introduction **19**

1.1 Motivation 19

1.1.1 Quantum Dot Nanoclusters for Use as a Light-Harvesting Material 19

1.1.2 Light-Harvesting Nanocomposite Materials 20

1.2 Absorption, Fluorescence and Förster Resonance Energy Transfer 21

1.2.1 Light Absorption and Fluorescence 21

1.2.2 Förster Theory 23

1.3 Quantum Dots 28

1.3.1 Semiconductors and Band Gaps 30

1.3.2 Quantum Confinement in 0-D Semiconductors 34

1.3.3 Photon Absorption Capabilities of Quantum Dots 38

1.3.4 Excited State Dynamics of Quantum Dots 41

1.3.5 Thermodynamics of Colloidal Quantum Dot Syntheses 42

1.3.6 Current Knowledge of QD Clustering and Aggregation 48

1.3.7 Quantum Dot Choice 54

1.4 Lipids 55

1.4.1 Common Structures and Compositions of Lipids and Detergents . 55

1.4.2 Model Environments for Membrane Proteins 58

1.4.3 Lipids and the Potential for Association with Quantum Dots . . . 59

1.5 Light-Harvesting Proteins 59

1.5.1 Light Harvesting in Photosynthetic Systems 60

1.5.2 Light-Harvesting Complex II 62

1.6 Bio-Hybrid Light-Harvesting Systems 64
1.6.1 Light-Harvesting Proteins in Nanotechnology 64
1.6.2 Artificially Increasing the Efficiency of Light Capture in Photosynthetic Proteins 66
1.6.3 Potential Methods of Protein-Nanoparticle Stabilisation 69

2 Experimental Procedures and Theory 73

2.1 $CuInS_2$/ZnS Quantum Dot Synthesis 73
2.1.1 Materials 73
2.1.2 $CuInS_2$ Core Growth 73
2.1.3 ZnS Shell Growth 76
2.1.4 $CuInS_2$/ZnS Cleaning 76
2.2 Formation of $CuInS_2$/ZnS Quantum Dot Nanoclusters 77
2.2.1 Materials 77
2.2.2 Aqueous Buffer Preparation 77
2.2.3 Preparation of QD-Lipid Thin Film Aliquots 78
2.2.4 Method 1 for Generating Lipid-QD Assemblies: Buffer Hydration of Thin Film 78
2.2.5 Method 2 for Generating Lipid-QD Assemblies: Cosolvent Removal by Rotary Evaporation 79
2.2.6 Method 3 for Generating Lipid-QD Assemblies: Detergent Encapsulation and Biobead Removal 80
2.3 CdTe/CdS Quantum Dot Synthesis 81
2.3.1 Materials 81
2.3.2 CdTe Core Growth 82
2.3.3 CdS Shell Growth 84
2.3.4 CdTe/CdS Cleaning 84
2.4 Protein Biochemistry 85
2.4.1 Materials 85

2.4.2 LHCII Isolation and Purification 85
2.5 Self-Assembly of Quantum Dot/Protein Bioconjugates 86
2.5.1 Materials 86
2.5.2 Crosslinking CdTe/CdS QDs to LHCII 86
2.5.3 De-salting Column Use 88
2.6 Optical Spectroscopy 88
2.6.1 Absorption Spectroscopy 88
2.6.2 Steady-State Fluorescence Spectroscopy 90
2.6.3 Fluorescence Lifetime 93
2.7 Particle Sizing 94
2.7.1 Dynamic Light Scattering 94
2.7.2 Transmission Electron Microscopy 96
2.8 Fluorescence Microscopy 98
2.8.1 Epifluorescence Microscopy 100
2.8.2 Fluorescence Lifetime Imaging Microscopy 101

3 Results: Developing the Method for Quantum Dot Nanocluster Self-Assembly 105

3.1 Motivation 105
3.2 Optimisation of Quantum Dot Core Synthesis Parameters 107
3.2.1 Introduction 107
3.2.2 Optimisation of the Seeding Time 108
3.2.3 ZnS Shell Growth 115
3.2.4 Optimising the $CuInS_2$/ZnS Cleaning Method 118
3.3 Initial Attempts to Form Quantum Dot Nanoclusters 119
3.3.1 Introduction 119
3.3.2 Attempted Nanocluster Formation by Thin Film Hydration 120
3.4 Attempted Nanocluster Formation by Cosolvent Removal 120
3.4.1 Initial Rotary Evaporation with Butanone 123

3.4.2 Surface Chemistry Alteration of the $CuInS_2$/ZnS Quantum Dots . 124
3.4.3 Stability Measurements of $CuInS_2$/ZnS QDs in THF 126
3.4.4 Attempting to Self-Assemble QD Nanoclusters Using Rotary Evaporation with THF 127
3.5 QD Nanocluster Formation by Detergent Encapsulation and Biobead Removal 129
3.5.1 Quantum Dot and Lipid Stability in Various Detergents 129
3.5.2 Stability of $CuInS_2$/ZnS QDs in Sodium Cholate Detergent 132
3.5.3 Sodium Cholate Detergent Removal Using Biobeads 133
3.6 Optimisation of the QD Nanocluster Formation Procedure 137
3.6.1 Introduction 137
3.6.2 Effect of the Lipid Choice on Nanocluster Formation 138
3.7 Conclusion 140

4 Results: Enhancing the Spectral Range of Light-Harvesting Complex II using Quantum Dots 143
4.1 Motivation 143
4.2 Introduction of LHCII to QD Nanoclusters and Investigation of Energy Transfer 145
4.3 Covalent Attachment of LHCII to QDs without Genetic Modification of Protein 147
4.3.1 Designing a QD Synthesis to Fill the Green Gap 149
4.3.2 Sample Loss/Quenching Through Use of De-salting Column 150
4.3.3 Optimising the Buffer Concentration to Achieve CdTe/CdS QD Stability 153
4.3.4 Raising the pH of the Buffer by Addition of HEPES and HEPBS . 155
4.3.5 Stability of CdTe/CdS QDs at Desired pH and Buffer Concentration 157
4.4 Optimising the Crosslinking Procedure to Achieve Energy Transfer 159
4.4.1 Introduction of the Crosslinker 159

4.4.2 Achieving Optimal Binding of the Quantum Dots to the Light-Harvesting Protein . . . 161
4.5 Future Work: Quantifying the Crosslinking of CdTe/CdS QDs and LHCII Using Polymer Microspheres . . . 168
4.6 Conclusion . . . 170

5 Results: Investigating the Structure and Photophysics of Quantum Dot Nanoclusters 172

5.1 Motivation . . . 172
5.2 Investigation into the Size and Structure of QD Nanoclusters . . . 175
5.2.1 Optical Measurements of the Samples to Be Used for Electron Microscopy . . . 175
5.2.2 Size Analysis of Colloidal $CuInS_2$/ZnS Quantum Dots . . . 177
5.2.3 Size Analysis and Structure of $CuInS_2$/ZnS Quantum Dot Nanoclusters . . . 184
5.3 Co-localisation of the Quantum Dots and Lipids . . . 187
5.3.1 Optical Spectroscopy Investigation into Energy Transfer From Lipid-Tagged Dye to $CuInS_2$/ZnS QDs . . . 188
5.3.2 Epifluorescence Investigation into Co-localisation of the Lipid-Tagged Dye and $CuInS_2$/ZnS QDs . . . 193
5.4 Investigating the Role of the Lipid Within Nanocluster Self-Assembly . . . 197
5.5 The Ensemble Photophysics of Quantum Dot Nanoclusters in Solution . . . 203
5.6 Investigating Surface-Deposited $CuInS_2$/ZnS Quantum Dot Nanoclusters at the Single-Particle Level . . . 208
5.7 Future Work: The Effect of QD Size on Nanocluster Formation . . . 216
5.8 Conclusion . . . 221

6 Conclusion and Future Outlook 224

6.1 Conclusion . . . 224
6.2 Future Work . . . 229

List of Figures

1.1 Jablonski diagram showing the excited states of a fluorescent molecule . . 22

1.2 Jablonski diagram showing donor-acceptor FRET 25

1.3 Example spectra of an energy donor and acceptor when FRET occurs . . 29

1.4 Cartoon showing the relationship between QD size and band gap. 30

1.5 Illustration of how categorisation of a material is dependant on the size of the band gap 31

1.6 Schematic of the energy-momentum relations in a direct and indirect band gap semiconductor 33

1.7 Typical spectra for a sample of colloidal QDs 40

1.8 Change in Gibbs free energy with respect to crystal size 44

1.9 Crystal growth rate dr/dt with respect to r/r_c 46

1.10 Schematic showing the various band structures of core/shell quantum dots 48

1.11 Example spectra and schematics of clustered QDs 50

1.12 Schematics and images of controlled QD clustering 53

1.13 Examples of model lipid bilayers and lipid structures 57

1.14 Structure and spectra of isolated LHCII 63

1.15 Example spectra and structures of bio-hybrid light-harvesting systems . . 68

1.16 Schematics and TEM images showing lipid association with QDs 71

2.1 Flow chart detailing the $CuInS_2$/ZnS synthesis procedure 74

2.2 Apparatus schematic for solvothermal synthesis of $CuInS_2$/ZnS quantum dots 75

2.3 Apparatus schematic for the aqueous synthesis of CdTe quantum dots . . 83

2.4 Photographs of the CdTe synthesis at various reflux times 84
2.5 Schematic of EDC/Sulfo-NHS crosslinker chemistry 87
2.6 Schematic of the FLS980 Edinburgh fluorescence spectrometer 92
2.7 Schematic of the optics within an epifluorescence microscope 101
2.8 Schematic of a fluorescence lifetime imaging microscope 103

3.1 Relationship between optical properties and seeding time for $CuInS_2$ QDs 109
3.2 Relationship between fluorescence emission peak and seeding time for $CuInS_2$ QDs 110
3.3 Time-resolved spectra showing slower decay of $CuInS_2$ QDs with increasing seeding time 114
3.4 Spectra of $CuInS_2$ and $CuInS_2$/ZnS QDs 117
3.5 Stability of lipid-tagged dye in various solvents 121
3.6 Stability measurements of $CuInS_2$/ZnS QDs in various solvents 123
3.7 Stability and spectra of $CuInS_2$ QDs with differing surface chemistries . . 125
3.8 Photographs showing stability of $CuInS_2$ QDs in co-solvent mixture . . . 128
3.9 Stability of lipid-tagged dye and $CuInS_2$ QDs in various detergents 130
3.10 Stability of 99% DOPC, 1% Texas Red DHPE after 24 hours in various detergents 131
3.11 Stability of QDs with lipid in chloroform and in sodium cholate detergent 133
3.12 Spectra of $CuInS_2$ QDs at each stage of the nanocluster self-assembly procedure 135
3.13 Cartoon showing the geometric shape and lipid curvature of DOPC and DOPG 138
3.14 Effect of lipid ratio alteration on $CuInS_2$/ZnS QD nanocluster spectra . . 139

4.1 Cartoon showing potential lipid-stabilised structures where energy transfer could be achieved 145
4.2 Resulting spectra from attempts to incorporate LHCII with QD nanoclusters 146
4.3 Simplified schematic of EDC/Sulfo-NHS crosslinker chemistry 148

4.4 Overlap of CdTe/Cds QD and LHC II spectra 151
4.5 Sample loss/quenching following use of de-salting column 152
4.6 Stability of CdTe/CdS QDs in high salt and low salt buffers 153
4.7 Stability of CdTe/CdS QDs at extremely low salt concentrations. 155
4.8 pH calibration curves used for crosslinking reaction 156
4.9 Stability of LHCII and CdTe/CdS QDs at various pH values 158
4.10 Fluorescence of CdTe/CdS QDs at each stage of the crosslinking experimental procedure 160
4.11 Effect of altering the crosslinker and CdTe/CdS QD concentrations on the QD fluorescence 163
4.12 Investigation of FRET between CdTe/CdS QDs and LHCII 166

5.1 Cartoon showing the self-assembly procedure of lipid-stabilised QD nanoclusters 174
5.2 Spectra showing alteration of optical properties for colloidal $CuInS_2$ QDs and $CuInS_2$/ZnS QD nanoclusters 177
5.3 TEM images of colloidal $CuInS_2$/ZnS QDs 178
5.4 Size distribution of colloidal $CuInS_2$/ZnS QDs following manual analysis . 179
5.5 STEM images of colloidal $CuInS_2$/ZnS QDs 180
5.6 Semi-automated analysis of colloidal $CuInS_2$/ZnS QD size 182
5.7 Size distribution of colloidal $CuInS_2$/ZnS QDs following semi-automated analysis 183
5.8 TEM/STEM images of $CuInS_2$/ZnS QD nanoclusters 185
5.9 Size distribution of $CuInS_2$/ZnS QD nanoclusters following manual analysis 186
5.10 Spectra showing co-localisation of QDs and lipids within QD nanoclusters 190
5.11 Time-resolved spectra showing the lifetime of QDs and lipids within QD nanoclusters 192
5.12 Epifluorescence microscopy control measurements of NBD-DHPE and QD nanoclusters 195

5.13 Epifluorescence microscopy showing co-localisation of QDs and lipid . . . 196
5.14 First zoomed-in epifluorescence microscopy image showing co-localisation of QDs and lipid . . . 198
5.15 Second zoomed-in epifluorescence microscopy image showing co-localisation of QDs and lipid . . . 199
5.16 Increase in QD uptake with respect to lipid concentration . . . 200
5.17 Change in QD fluorescence lifetime with respect to lipid concentration . . 201
5.18 Fluorescence intensity and fluorescence lifetime against lipid:QD molar ratio 202
5.19 Fluorescence excitation vs. emission plots comparing colloidal $CuInS_2$/ZnS QDs and $CuInS_2$/ZnS QD nanoclusters. . . . 204
5.20 Time-resolved emission spectroscopy comparison of colloidal $CuInS_2$/ZnS QDs and $CuInS_2$/ZnS QD nanoclusters . . . 206
5.21 Dual-channel images from FLIM showing individual QD nanoclusters deposited on a glass substrate . . . 209
5.22 Example of lifetime determination from captured FLIM images . . . 210
5.23 FLIM images showing both fluorescence intensity and lifetime data of selected regions of interest . . . 212
5.24 Frequency distribution of lifetimes obtained from FLIM . . . 213
5.25 Spectra of $CuInS_2$/ZnS QDs following size separation . . . 217
5.26 Fluorescence emission of size-separated $CuInS_2$/ZnS QDs . . . 218
5.27 Spectra of QD nanoclusters assembled using QDs of different sizes . . . 220

List of Abbreviations

α-DDM n-dodecyl α-D-maltoside

CCD Charge-coupled device

CdS Cadmium sulfide

CdSe Cadmium selenide

CdTe Cadmium telluride

Chl Chlorophyll

CMC Critical micelle concentration

$CuInS_2$ Copper indium sulfide

DDT Dodecanethiol

DFT Density functional theory

DLS Dynamic light scattering

DOPC 1,2-dioleoyl-sn-glycero-3-phosphocholine

DOPG 1,2-dioleoyl-sn-glycero-3-phospho-(1'-rac-glycerol)

DOPS 1,2-dioleoyl-sn-glycero-3-phospho-L-serine

DRA Diffuse reflectance accessory

EDC 1-ethyl-3-(3-dimethylaminopropyl)carbodiimide hydrochloride

EELS Electron energy loss spectroscopy

EM Electron microscopy

ETE Energy transfer efficiency

FLIM Fluorescence lifetime imaging microscopy

FPLC Fast protein liquid chromotography

FRET Förster resonance energy transfer

FWHM Full width at half maxima

HEPBS N-(2-Hydroxyethyl)piperazine-N'-(4-butanesulfonic acid)

HEPES 4-(2-Hydroxyethyl)piperazine-1-ethanesulfonic acid

HOMO Highest occupied molecular orbital

IPA Propan-2-ol

IRF Instrument response function

LED Light-emitting device

LHC Light-harvesting complex

LUMO Lowest unoccupied molecular orbital

MES 2-(N-morpholino)ethanesulfonic acid

MLV Multilamellar vesicle

MVT Micelle-to-vesicle transition

ND Neutral density

NG n-nonyl-β-d-glucoside

NIR Near-infrared

ODE Octadecene

OG n-octyl-β-d-glucoside

OLA Oleylamine

PAGE Polyacrylamide gel electrophoresis

PDI Polydispersity index

PEG Polyethylene glycol

PIE Pulsed interleaved excitation

PL Photoluminescence

PLA_2 Phospholipase A_2

PLL Poly-L-lysine

PLQY Photoluminescence quantum yield

PS Photosystem

QD Quantum dot

QY Quantum yield

RC Reaction centre

SDS Sodium dodecyl sulphate

SEC Size exclusion chromotography

SPAD Single-photon avalanche diode

STEM Scanning transmission electron microscopy

Sulfo-NHS N-hydroxysulfosuccinimide

TCSPC Time-correlated single photon counting

TEM Transmission electron microscopy

TGA Thioglycolic acid

THF Tetrahydrofuran

TOP Triostylphosphine

TOPO Triostylphosphine oxide

TR-DHPE Texas Red 1,2-dihexadecanoyl-sn-glycero-3-phosphoethanolamine

Triton X-100 4-(1,1,3,3-Tetramethylbutyl)phenyl-polyethylene glyco

UV-Vis-NIR Ultra-violet-visible-near infrared

ZnS Zinc sulfide

Chapter 1

Introduction

This introduction serves to outline the motivation for pursuing the research described in this thesis, as well as providing an extensive background to cover core topics and themes discussed in later sections. The underlying theory of fluorescence, Förster resonance energy transfer, quantum dots, lipids, and light-harvesting proteins leads to a review of the current literature surrounding the promising domains of quantum dot clustering and bio-hybrid light-harvesting systems, as novel research is presented that contributes to the field of solar harvesting, with potential secondary applications within bio-sensing.

1.1 Motivation

1.1.1 Quantum Dot Nanoclusters for Use as a Light-Harvesting Material

When hydrophobic quantum dots (QDs), such as $CuInS_2/ZnS$, are placed into aqueous suspensions, they have finite stability. QDs are known to assemble under certain conditions governed by the physicochemical environment (pH, ionic strength) and the QD surface chemistry. This can lead to the nanoparticles precipitating and falling out of solution entirely, but sometimes small and stable nanoscale clusters of quantum dots (e.g., 10-100 particles) can form, which persist and have altered ensemble and single-particle

properties to colloidal quantum dots. It is likely that these clusters will affect the many downstream applications of quantum dots, and will appear bright at the single-cluster level due to the greater number of energetically-connected particles, so it is important to understand them, as later discussed in Section 1.3. The structure and photophysics of $CuInS_2$/ZnS quantum dots within such assemblies have not yet been characterised and little is known about the excitation dynamics and energy-transfer mechanisms of small QD nanoclusters. The majority of research in this thesis focuses on designing and characterising distinct lipid-stabilised 'nanocluster' structures using $CuInS_2$/ZnS QDs, and investigating the photophysics of the QDs at the small colloidal level for use within nanocomposites or as a light-harvesting material, with emphasis on the relationship to size, energy transfer, and retainment of optical properties when deposited onto a surface. The functionality of $CuInS_2$ QD nanoclusters with respect to light harvesting will be determined as a pathway to eventually investigating the functionality of quantum dot-containing bio-hybrid light-harvesting nanocomposite materials.

1.1.2 Light-Harvesting Nanocomposite Materials

Light capture during the early stages of photosynthesis is highly efficient, although the light-harvesting proteins responsible are limited to specific biological pigments, resulting in gaps in the absorbance spectrum. QDs have been previously investigated as artificial antennas for the photosynthetic plant antenna protein light-harvesting complex II (LHCII), but energy transfer has only been achieved with genetic modification of the light-harvesting protein, as later discussed in Section 1.6. Research in Chapter 4 of this thesis focuses on supplementing the absorption of plant LHCII using QDs without genetic modification of the protein, to achieve an environment for controlled energy transfer through the development of a lipid-stabilised system. A two-stage procedure that involves using crosslinker chemistry was investigated to achieve chemical binding of the QD to LHCII before bilayer incorporation of the protein.

1.2 Absorption, Fluorescence and Förster Resonance Energy Transfer

1.2.1 Light Absorption and Fluorescence

Light absorption occurs when a photon interacts with a particle (for example, a quantum dot as described in Section 1.3) or molecule (for example, a photosynthetic pigment molecule as described in Section 1.5) and energy is transferred to an electron, which then enters an excited state. The energy of a photon is given by:

$$E = h\nu = \frac{hc}{\lambda} \tag{1.1}$$

where h is the Planck constant, ν is the frequency of the photon, c is the speed of light in a vacuum, and λ is the wavelength of the photon. Generally, a particle or molecule can absorb a photon if the photon energy corresponds to the gap between the ground state (S_0), or highest occupied molecular orbital (HOMO), and an energy level in the first (S_1) or second (S_2) excited states. High-energy photons can excite electrons from the ground state to higher-energy states ($S_0 \rightarrow S_3, S_4...$) although this typically corresponds to photons with a wavelength that is outside the visible range. Absorption of shorter wavelength, high-energy photons will result in electron excitation to higher energy levels, whereas absorption of longer wavelength, low-energy photons will lead to electron excitation to lower energy levels. If the photon has an energy that does not correspond to any transitions between energy levels, it will not be absorbed efficiently. The timescale for photon absorption and electron excitation to a higher state is on the order of femtoseconds (10^{-15} s).

For fluorescent molecules that have multiple interacting atoms and molecular orbits, each electronic energy state ($S_1, S_2...$) will be more complex and may contain many vibrational sub-states within each electronic state, broadening the energy levels available.

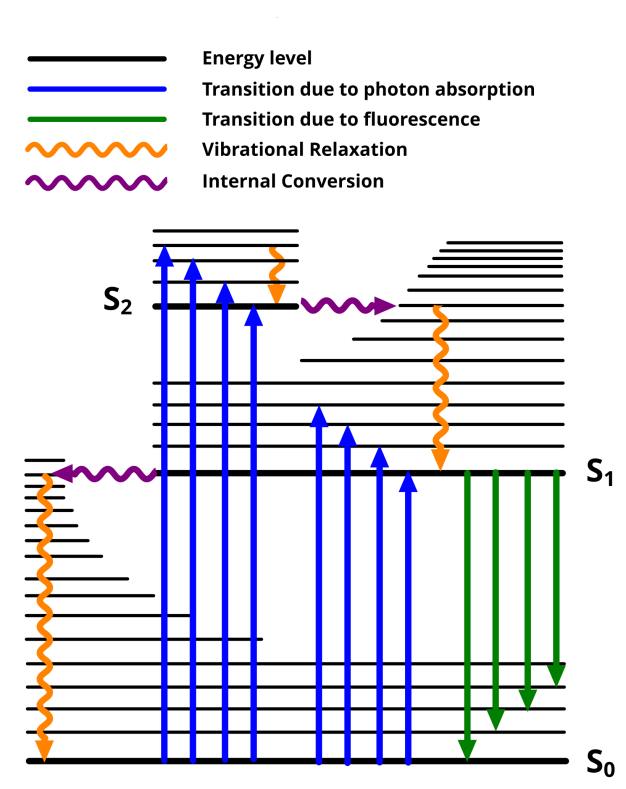

Figure 1.1: A typical Jablonski diagram showing the excited states of a fluorescent molecule and pathways for relaxation. Adapted from Edinburgh instruments F980 fluorescence spectrometer manual.

An electron may be excited to a vibrational sub-state within one electronic state by photon absorption, which occurs on the order of femtoseconds (10^{-12} s). The electron will then rapidly return to the lowest vibrational sub-state of a given electronic state, or lowest unoccupied molecular orbital (LUMO), because of the small energy gaps between sub-states. This process is called 'vibrational relaxation' where excess energy is dissipated non-radiatively as heat [1, 2]. Vibrational relaxation occurs on the order of picoseconds to hundreds of picoseconds ($10^{-12} - 10^{-10}$ s). Vibrational sub-states of one electronic orbital may also overlap with vibrational sub-states of a different electronic orbital, thus allowing non-radiative transitions downwards between electronic states in a process called 'internal conversion'. Internal conversion usually occurs on the order of tens of picoseconds to nanoseconds ($10^{-11} - 10^{-19}$ s). Finally, relaxation may occur from the lowest vibrational state in S_1 to the ground state S_0 through re-emission of

a photon, known as 'fluorescence', with a wavelength corresponding to the difference between energy levels. Fluorescence usually occurs on the order of hundreds of picoseconds and nanoseconds ($10^{-10} - 10^{-7}$ s) following excitation [3]. Due to a combination of vibrational relaxation and internal conversion, the emitted photon will be of lower energy than the absorbed photon, with the 'Stokes shift' defined as the red-shift of the absorbed photon wavelength relative to the emitted photon wavelength.

Fluorescence is a type of 'photoluminsecence' (PL), which is the emission of light from a material induced by the absorption of photons. The most common form of excited states are singlet states, where paired electrons in the ground state and excited state have opposite spin orientations, thus the decay is an allowed transition and results in short-timescale fluorescence. The other type of PL is phosphorescence, which has a long-lived PL due to an extended excited state lifetime ($10^{-1} - 10^{3}$ s). The Pauli exclusion principle forbids two electrons with the same spin to occupy the same energy level, thus when electrons in the ground state and excited state have the same spin orientation, the electron must change spin direction before returning to the ground state. These 'triplet' states, containing two unpaired electrons, are usually highly reactive and have a long lifetime so can cause damage in biological systems, thus are usually dissipated through alternative pathways [3, 4]. The allowed photon absorption and emission of a sample, with respect to energy gaps, will result in a 'spectra' for both the absorbance and PL as a function of wavelength, with the theory behind the collection of the spectra explained in the Methods section in more depth.

1.2.2 Förster Theory

Förster resonance energy transfer (FRET) is a mechanism describing the transfer of energy from a donor molecule in an excited state to an acceptor molecule to which the energy is transferred to [5, 6]. For energy in an excited state of one molecule to be transferred non-radiatively to another, three requirements must be met:

1) The donor and acceptor molecules must be within close enough proximity to experience dipole-dipole (Coulombic) coupling.

2) The transition dipole moment (electric dipole moment associated with the transition between two states) of the donor and acceptor molecule must not be perpendicularly orientated to each other and should be close to parallel.

3) The fluorescence emission spectra of the donor molecule must overlap with the excitation spectra of the acceptor molecule.

When two electromagnetic dipoles are aligned with each other and are in close proximity (i.e., within a distance of ∼10 nm), then dipole-dipole coupling can occur. If the frequency of the dipoles is similar and one of the dipoles is in the excited state (energy donor), then the dipoles can couple and energy is transferred to the non-excited dipole (energy acceptor). The excited electron in the donor molecule simultaneously relaxes to the ground state without the emission of a photon. To comply with the first law of Thermodynamics, the energy transfer from the energy donor to the energy acceptor must be energetically downhill, so energy must be lost in the transfer and not gained. Small exceptions to this occur when thermal energy (k_BT) is gained from the environment, allowing access to higher vibrational states. This process can be seen in the energy level diagram shown in Figure 1.2 A, where the electronic states of the donor and the acceptor are shown in blue and red, respectively. After initial absorption of a photon by the donor molecule, an electron is excited from the ground state $S_0{}^D$ to a vibrational state of the $S_1{}^D$ electronic state, then rapidly decays to the lowest vibrational state of $S_1{}^D$ through vibrational relaxation. FRET occurs between the coupled donor and acceptor molecules, resulting in the energy of the excited state in the donor being transferred to the acceptor molecule. In this process, the excited electron in the energy donor relaxes to the ground state without photon emission. Simultaneously, an electron is excited from the ground state of the acceptor molecule to a vibrational state in the $S_1{}^A$ excited elec-

tronic state without photon absorption. This electron then rapidly decays to the lowest vibrational state of $S_1{}^A$ through vibrational relaxation, before relaxing to the ground state $S_0{}^A$ through photon emission. As there is no absorption or emission of photons during energy transfer, and the coupling of dipoles is due to the electrostatic interactions between two vibrational states, the energy transfer is non-radiative [7–9].

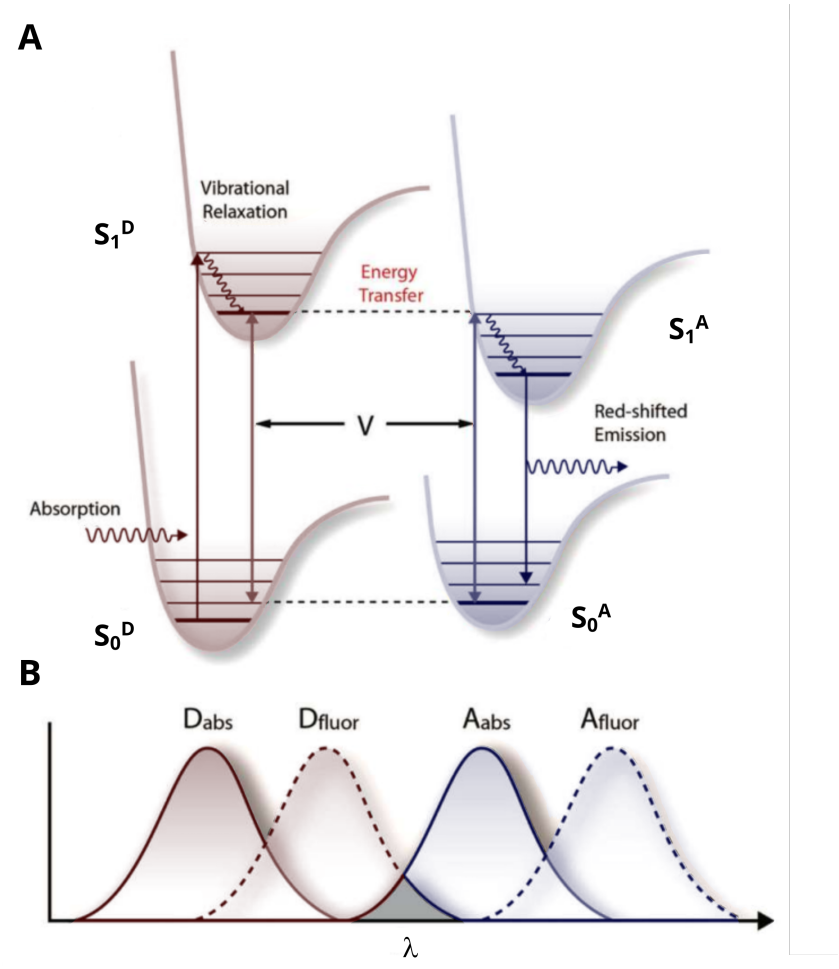

Figure 1.2: Jablonski diagram showing donor-acceptor FRET and required spectral overlap. (A) Energy level diagram showing donor to acceptor FRET. S_0^D and S_0^A are the ground states of the donor and acceptor, and S_1^D and S_1^A are the excited singlet states of the donor and acceptor, respectively. (B) The spectral conditions necessary for the donor to acceptor FRET to take place. D_{abs} and A_{abs} show the donor and acceptor absorbance, and D_{fluor} and A_{fluor} show the donor and acceptor fluorescence, respectively. The grey-shaded region is the overlap of donor fluorescence and acceptor absorbance, defined by the overlap integral J. Adapted with permission from Mirkovic *et al.* [7]. Copyright 2017 American Chemical Society.

To allow dipole-dipole coupling and downhill energy transfer, the energies of vibronic states in the donor and acceptor must be sufficiently similar; the wavelengths representing possible photon emission from the energy donor must overlap with the wavelengths of photon absorption of the acceptor. This overlap of the donor fluorescence emission and acceptor absorption is defined as the spectral overlap factor, J, which is correlated to the area of overlap between the fluorescence emission spectra of the donor and the absorption spectra of the acceptor:

$$J = \int \varepsilon(\lambda) F_D(\lambda) \lambda^4 d\lambda \tag{1.2}$$

where ε is the molar absorption coefficient of the acceptor as a function of wavelength, λ, and F_D is the normalised fluorescence emission spectrum of the donor as a function of λ. An example of donor and acceptor spectral overlap is shown by the shaded area in Figure 1.2 B.

The relative orientations of the transition dipoles are also crucial to the efficiency of energy transfer; electrostatic interactions will be maximised when dipoles are parallel and energy transfer will be most effective. Coupling is not possible for perpendicular dipoles. The relative orientation of the transition dipoles is given by the orientation factor, κ:

$$\kappa^2 = (\cos\alpha - 3\cos\beta_1 \cos\beta_2)^2 \tag{1.3}$$

where α is the angle between the planes of the dipoles, and β_1 and β_2 are the angles of each of the dipoles relative to a vector joining them. The average interaction factor has a value of $2/3$ for randomly orientated dipoles [10, 11].

The rate of energy transfer from donor to acceptor can be derived from an adaptation to Fermi's golden rule, used to define the transition rate of a quantum system:

$$k_{D\to A} = \frac{2\pi}{\hbar} |V_{DA}|^2 \delta(E_D - E_A) \tag{1.4}$$

where $\hbar$ is the reduced Planck constant, V_{DA} is the interaction energy, and $\delta(E_D - E_A)$ is the difference in state energy between the donor and acceptor, defined by the overlap integral J. The interaction energy can be defined as:

$$V_{DA} = k_e \frac{\mu_D \mu_A \kappa}{r_{DA}^3} \tag{1.5}$$

where k_e is Coulomb's constant (8.99×10^9 N m^2 C^{-2}), μ_D and μ_A are the Coulombic strengths of the donor and acceptor transition dipoles respectively, κ is the orientation factor, and r_{DA} is the distance between transition dipoles. Equations 1.4 and 1.5 can be combined to give the FRET equation for the rate of energy transfer:

$$k_{D\to A} = \frac{2\pi k_e^2}{\hbar} \frac{\mu_D^2 \mu_A^2 \kappa^2}{r_{DA}^6} J. \tag{1.6}$$

The Förster radius R_0 is defined as the critical radius between two pigments where the energy transfer is 50% efficient. This critical distance considers the rate of fluorescence from the donor in the absence of energy transfer $k_{f,D}$, equal to $1/\tau_{f,D}$ where $\tau_{f,D}$ is the donor fluorescence lifetime. The critical radius R_0 is given by:

$$R_0 = \left(\frac{2\pi k_e^2}{\hbar} \mu_D^2 \mu_A^2 \kappa^2 \tau_{f,D} J \right) = 8.785 \times 10^{-5} J k^2 n^{-4} \Phi \tag{1.7}$$

where n is the optical refractive index of the medium, and Φ is the fluorescence quantum yield of the donor in the absence of the acceptor. For FRET to take place, molecules must be separated by at least 1 nm due to the Pauli exclusion principle, which comes into effect at sub-nanometer separation and limits massive particles from occupying the same space [10]. The rate of energy transfer can also be defined with respect to the rate of the fluorescence donor, $k_{f,D}$:

$$k_{D\to A} = k_{f,D} \left(\frac{R_o}{r_{DA}} \right)^6 \tag{1.8}$$

The rate of donor-to-acceptor energy transfer $k_{D\to A}$ is proportional to r^6, thus FRET is sensitive to the distance between molecular displacement. This knowledge has been utilised in many nanotechnological applications which involve measuring when two molecules are sufficiently close for FRET to occur [12].

Finally, the energy transfer efficiency (ETE) between the donor and acceptor dipoles can be obtained with respect to the R_0 from Equation 1.9:

$$ETE = \frac{k_{D\to A}}{k_{D\to A} + k_{f,D} + k_{nr}} = \frac{R_0^6}{R_0^6 + r_{DA}^6} \tag{1.9}$$

where k_{nr} is the rate of non-radiative decay, arising from internal conversion and other non-radiative decay processes. The ETE is defined as the probability of a single energy transfer event per donor excitation event or may be expressed as a percentage efficiency when considering many events, and will be 0.5 when the separation between the donor and the acceptor is equal to R_0.

FRET can be quantified through steady-state and time-resolved fluorescence measurements, as shown in Figure 1.3. If FRET occurs between a higher-energy donor particle or molecule and a lower-energy acceptor particle or molecule, then a decrease in donor fluorescence is expected. The 'quenching' of the energy donor fluorescence is accompanied by an enhancement of the acceptor fluorescence, as seen in Figure 1.3 A. This fluorescence quenching also leads to a change in the lifetime of the energy donor (Figure 1.3 B), which will decrease in the presence of an acceptor. This is usually accompanied by an increase in the lifetime of the energy acceptor, as seen in Figure 1.3 C.

1.3 Quantum Dots

Semiconductor quantum dots (QDs) are nanocrystalline semiconductors with a diameter that is similar to or below the exciton Bohr radius (see Figure 1.4). Many characteristic

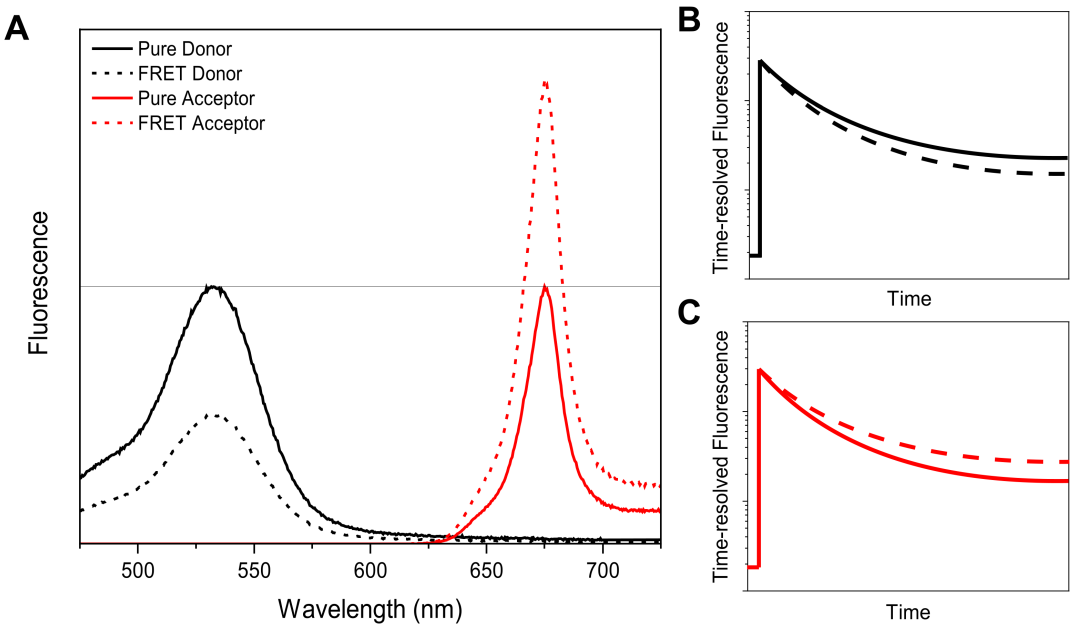

Figure 1.3: Example spectra of an energy donor and acceptor when FRET occurs. (A) Example fluorescence of an individual (*solid* line) and mixed (*dashed* line) energy donor (*black*) and acceptor (*red*). A quenching of the energy donor fluorescence and an enhancement of the energy acceptor fluorescence is expected. Example of time-resolved fluorescence spectra for (B) energy donor and (C) energy acceptor in individual (*solid* line) and mixed (*dashed* line) solution. FRET occurs between the energy donor and acceptor in the mixed sample.

properties arise from the reduction of crystal size below this critical value (typically <10 nm), including an atom-like electronic structure responsible for a tuneable PL. The term 'quantum dot' to describe colloidal semiconductor nanocrystals is derived from the three-dimensional spatial confinement experienced by charge carriers, which results in an intermediate band structure between the continuous energy bands of bulk semiconductors and the discrete quantised energy levels of a single atom [13]. Recent progress and growth within the field have led to an interest in QDs for bio-sensing [14–17] and photovoltaic devices [18–20], as well as the integration of QDs within commercial products such as display technologies [21–23]. This section introduces the properties of colloidal semiconductor QDs, discusses how these properties prove useful for light harvesting and proposes the benefits of controlled quantum dot aggregation for light-harvesting purposes.

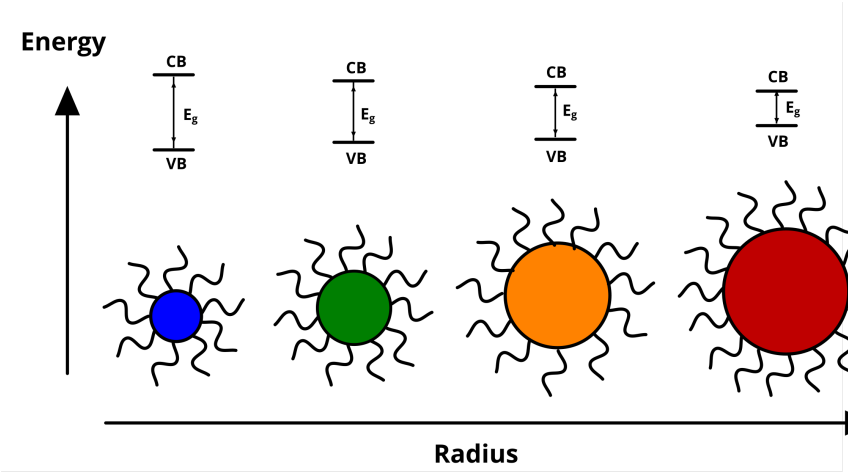

Figure 1.4: Cartoon showing the relationship between QD size and band gap. The band gap energy decreases as the QD cores increase in size (blue to red) due to the energy levels becoming less discrete, as discussed in section 1.2.2. Quantum dots are typically coated in a 'capping ligand' which allows the QD to achieve colloidal stability in a desired solvent.

1.3.1 Semiconductors and Band Gaps

Consider an isolated atom, where the energy levels are quantised. As N identical atoms are moved to within close proximity, the quantised energy levels will hybridise and split into N energy levels (electron orbitals) as an equilibrium is reached between the long-range attractive forces arising from the valence electrons and the short-range repulsive interactions between the atoms [24]. If N is sufficiently large and therefore a lattice, effectively continuous energy bands will eventually form as the electron orbitals broaden. The valence band is the lower energy band of occupied orbitals, and the conduction band is the band of orbitals that electrons are able to occupy once excited from the valence band. 'Forbidden' regions between bands in momentum space may exist, due to a difference in energy between the highest occupied state in the valence band and the lowest unoccupied state in the conduction band [24, 25]. The nature of this band gap E_g determines the electronic properties of a crystalline material. Insulators are characterised by a large band gap energy (>4 eV), with insulating properties arising due to a negligible number of free electrons occupying the conduction band. Metals have an overlapping valence and conduction band, leading to a good conducting material where

electrons in the conduction band are delocalised and highly mobile. A semiconductor is characterised by a filled valence band and a band gap energy that is between that of an insulator and a metal; slightly greater than the thermal energy at room temperature.

The Pauli exclusion principle states that no two fermions can occupy the same quantum state. For a collection of fermions at temperature T, the Fermi-Dirac equation describes the probability $f(E)$ that an electron is in the state with energy E:

$$f(E) = \frac{1}{1 + e^{\frac{E - E_F}{k_B T}}} \tag{1.10}$$

where k_B is the Boltzmann constant, T is the absolute temperature and E_F is the Fermi level, a quantification of the energy required to add an electron to a system. In the finite temperature range, where thermal energy is continuously exciting electrons within the conduction band, the occupation probability at the Fermi level $f(E_F)$ is 0.5.

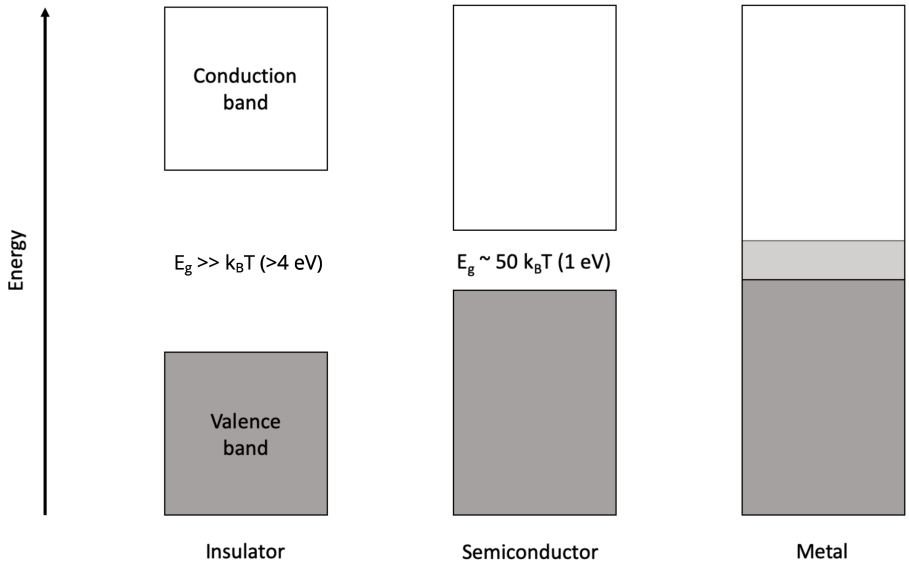

Figure 1.5: Illustration of how the categorisation of a material into an insulator, semiconductor or metal is dependant on the size of the band gap E_g. In semiconductors, a proportion of the total electrons can occupy the conduction band at finite temperatures.

The Fermi energy is defined as the highest occupied energy level of a system at 0 K (ab-

solute zero), where thermal energy is absent. Simply, this is the Fermi level at absolute zero. For a metal at 0 K, the Fermi energy exists outside the aforementioned forbidden region due to the overlapping valence and conduction bands [24]. This means the material is capable of conducting when electrons fill all available energy levels, as electrons in the conduction band have the required energy to reach the next available state, and thus move freely. For both an insulator and a semiconductor at absolute zero, the Fermi energy lies in the 'forbidden' region. In an insulator, the band gap is wide enough that electrons are unable to reach the conduction band at finite temperatures, thus are poor conductors. For the case of a semiconductor, the band gap is sufficiently narrow that at finite temperatures, carriers can be thermally excited to the unfilled conduction band via lattice vibrations [24], with respect to the Fermi-Dirac equation (1.10). Besides promotion via lattice vibration, an electron can also be promoted to an unoccupied excited state in the conduction band by photon absorption, further explained in Section 1.3.3.

If the Fermi level of a semiconductor lies directly midway between the conduction band and valence band, at the centre of the band gap, the semiconductor is intrinsic. The electronic properties of an intrinsic semiconductor can be modified by intentionally introducing impurities of a different valence to form an extrinsic semiconductor. This process is known as doping, with the added impurities acting as an electron donor or acceptor within the lattice. A semiconductor doped with electron donors is known as a 'n-type' semiconductor, where charge carriers are provided in the form of electrons to the conduction band. The Fermi level is greater than that of an intrinsic semiconductor and lies closer to the conduction band. A semiconductor doped with electron acceptors is a 'p-type' semiconductor, where added electron acceptors leave empty orbitals in the valence band, called 'holes'. Holes contain a charge of $+e$, equal and opposite to the $-e$ charge of an electron. The name 'n-type' refers to the negative charge of the electrons, whereas 'p-type' refers to the positive charge of the hole; the respective majority charge carriers. The conductivity of a semiconductor can be influenced by the relative number of electrons and holes, with an increased number of electrons leading to an increase in

conductivity. An intrinsic semiconductor contains exactly the same number of electrons and holes.

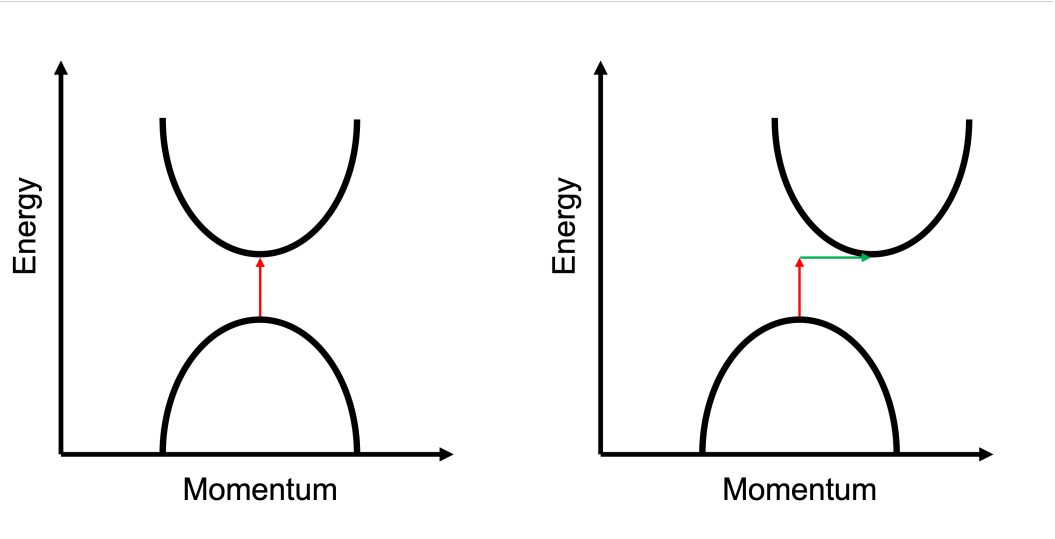

Figure 1.6: Schematic of the energy-momentum relations in a direct (left) and indirect (right) band gap semiconductor. A semiconductor with a direct band gap does not impart momentum to the crystal lattice, with all energy gained from a photon (red). In the indirect case, energy cannot shift from the highest occupied state in the valence band to the lowest unoccupied state in the conduction band without a change in momentum from a phonon (green).

The band gap of a semiconductor can be classified as being one of two basic types: a **direct** band gap or an **indirect** band gap. A semiconductor has a direct band gap if the minimal-energy state in the conduction band and the maximum energy state in the valence band lie within the same crystal lattice momentum in the energy-momentum relation (Figure 1.6 A). No momentum is imparted to the crystal during the transition between the two energy states, allowing direct absorption or emission of a photon. If the minimal-energy state in the conduction band and the maximum energy state in the valence band lie within different momentum vectors, then the band gap is indirect and a photon cannot be emitted without imparting momentum to the crystal lattice to prevent violation of momentum. This is usually done via the absorption or emission of a phonon containing a momentum equal to the difference between the electron and hole momentum.

When an electron is excited to the conduction band, a hole is left behind in the reservoir of valence electrons, containing an effective mass as well as an equal and opposite charge to that of the electron [25–27]. The opposite charge of the electron and hole means they will electrostatically attract and will be bound to one another unless provided with a large amount of kinetic energy upon excitation from a lower energy state. This electron-hole pair can be treated as a quasi-particle, called an exciton, and operates with a reduced mass determined by the following equation:

$$\frac{1}{\mu} = \frac{1}{m_e^*} + \frac{1}{m_h^*} \tag{1.11}$$

where m_e^* is the effective mass of the electron and m_h^* is the effective mass of the hole.

1.3.2 Quantum Confinement in 0-D Semiconductors

If the crystal size is reduced to the order of nanometers and the band gap increases, the mobility of electrons and holes is restricted to nanoscale dimensions due to the quantum confinement effect [28, 29]. When considering the effects of confinement with respect to excitons within semiconductors, it is useful to consider the characteristic radius for an exciton and how this is similar to the semi-classical Bohr model of an atom.

The characteristic radius of an exciton is governed by the equilibrium position between the electric potential energy of the electron and hole, and the kinetic energy of the mutual motion:

$$\frac{1}{2}\mu v^2 = \frac{1}{4\pi\varepsilon_r\varepsilon_0}\frac{e^2}{r} \tag{1.12}$$

where r is the exciton separation, e is the elementary charge, μ is the reduced exciton mass and v is the regular angular velocity of the electron-hole pair. The parameters ε_0 and ε_r represent the relative permittivity of free space and the relative permittivity of the material respectively. The Bohr model of an atom describes a quantised angular momentum $L = \mu v r$ with a minimum value $\hbar$. The characteristic Bohr radius of a

semiconductor a_0^* can be defined as the exciton separation at this minimum value:

$$a_0^* = \frac{4\pi\varepsilon_r\varepsilon_0\hbar^2}{\mu e^2} = \varepsilon_r\frac{m_e}{\mu}a_0 \tag{1.13}$$

where a_0 is the hydrogen Bohr radius and m_e is the mass of a free electron. The characteristic Bohr radius of a semiconductor is known as the exciton Bohr radius.

As the size of a semiconductor crystal is reduced below the exciton Bohr radius, excitons become spatially confined; the continuous bands associated with bulk material split into discrete states analogous to a simple atom [30]. The band gap energy increases due to the confinement energy associated with these discrete states and thus is heavily related to the size of the QD below the characteristic Bohr radius. Theoretically modelling the behaviour of confined excitons within QDs becomes difficult, as a typical CdTe or $CuInS_2$ QD contains $\sim 10^3 - 10^5$ atoms and simplifications to bulk theory are inapplicable due to a large proportion of QDs at the surface [31]. Models and computational methods have attempted to describe the optoelectronic properties of QDs through simulation, including density functional theory (DFT) approaches where attempts have been made to resolve the band structure of QDs [32], although DFT often underestimates the band gap and usually requires empirical adjustments that are too simplistic for many applications [33]. Some of the more promising developments have been made through the use of atomistic semiempirical pseudopotential theory, allowing a greater understanding of the valence and conduction band energies and carrier dynamics at the QD surface for a range of QDs and sizes [34–36].

A simplistic illustration of excitonic confinement within a QD can be shown by the 'particle in a box' model, which considers a single exciton with effective mass μ as described in Equation 1.11. The spherically symmetric potential of a QD with a radius d

can be defined as:

$$V(r,\varphi,\theta) = \begin{cases} 0, r < d \\ \\ \infty, r < d \end{cases} \tag{1.14}$$

where r is the radial distance, φ is the azimuthal angle and θ is the polar angle. This potential is the simplest spherical equivalent of the 1D 'particle in a box', with the area outside the radius d defined by an infinite potential that precludes any non-zero value of the exciton's wavefunction $\psi(r,\varphi,\theta)$. As the Hamiltonian is time-independent, the Schrodinger equation for an exciton trapped inside a spherically symmetric potential is:

$$\left[\frac{-\hbar^2}{2\mu}(\frac{\partial^2}{\partial r^2} + \frac{2}{r}\frac{\partial}{\partial r} - \frac{L^2}{\hbar^2 r^2}) + V(r)\right]\psi(r,\varphi,\theta) = E\psi(r,\varphi,\theta) \tag{1.15}$$

where $\hbar$ is the reduced Planck constant, and L^2 is the square of the angular momentum operator. The eigenvalues of L^2 can be defined as:

$$L^2\psi(r,\varphi,\theta) = R(r)L^2A(\varphi,\theta) = R(r)l(l+1)^2\hbar^2A(\varphi,\theta) \tag{1.16}$$

where the angular component of the wavefunction, $A(\varphi,\theta)$, has been separated from the radial function, $R(r)$, and the integer l is a quantum number associated with the angular momentum. Within the QD, the radial distance is such that $0 \leq r < d$, and $V(r) = 0$. Introducing a new quantum number, n, allows the Schrodinger equation to be written as follows:

$$\frac{d^2R_{n,l}}{dr^2} + \frac{2}{r}\frac{dR_{n,l}}{dr} + \left(k^2 - \frac{l(l+1)}{r^2}\right)R_{n,l} = 0 \tag{1.17}$$

where k^2 can be defined as:

$$k^2 = \frac{2\mu E}{\hbar^2}. \tag{1.18}$$

By defining the scaled variable $a = kr$, the radial Helmholtz equation can be obtained:

$$z^2\frac{d^2R_{n,l}}{dr^2} + 2z\frac{dR_{n,l}}{dr} + [z^2 - l(l+1)]R_{n,l} = 0. \tag{1.19}$$

When solving the radial Helmholtz equation in spherical coordinates, the two linearly independent solutions are called the spherical Bessel functions of the first and second kind, $j_l(z)$ and $y_l(z)$. The $y_l(z)$ functions are not square integrable at $r = 0$, and tend to $-\infty$, therefore the radial wavefunction is proportional to $j_l(z)$ is definable:

$$j_l(z) = z^l \left(\frac{-1}{z}\frac{d}{dz}\right)^l \left(\frac{\sin z}{z}\right) \tag{1.20}$$

The spherical Bessel functions can be matched with the zero amplitude wavefunction outside of the QD region, where the potential is infinite for $r \geq d$. The Bessel functions are spherical in nature, therefore pass through zero many times. A value of k is chosen so that $z = kd$ corresponds to a zero of the spherical Bessel function $j_l(z)$, allowing the value of the wavefunction to reach zero as $r = d$. The nth zero for the first spherical Bessel function can be written as $z_{n,l}$, thus for positive integer values of n:

$$kd = \sqrt{\frac{2\mu E_{n,l}}{\hbar^2}}d = z_{n,l} \tag{1.21}$$

Thus, the allowed energy levels of a particle trapped in an infinite spherical potential well can be obtained by combining with Equation 1.20 to give:

$$E_{n,l} = \frac{z_{n,l}^2 \hbar^2}{2\mu d^2}. \tag{1.22}$$

Inputting the integer values of the lowest energy state, where $n = 1$ and $l = 0$, gives $z_{l,n} = \pi$, corresponding to the first excited S_1 state. The energy required to reach this first excited state in a QD is the band gap energy, given by the equation: 1.20 to give:

$$E_{g,QD} = E_{g,bulk} + \frac{\pi^2\hbar^2}{2\mu d^2} - \frac{1.786e^2}{2\epsilon d} \tag{1.23}$$

where the final term accounts for the electrostatic attraction between the electron and the hole [37]. The final term is inversely proportional to the QD diameter d, so will serve to reduce the band gap as the QD size increases, but only has a significant contribution

compared to the confinement term for very large QDs. The key result in explaining the strong size dependence of the energy of small-size QDs comes from the confinement term itself, specifically the inverse-square relationship between the confinement term and the particle diameter. This relationship is particularly useful as it is known that the QDs grow larger over time during QD synthesis, as discussed in Section 1.3.5, so this size-energy relationship can be used to estimate that longer synthesis times should lead to QDs with a lower energy gap (i.e., longer absorption wavelengths). Thus, particular desirable optical properties can be achieved by varying synthesis parameters.

1.3.3 Photon Absorption Capabilities of Quantum Dots

As discussed in Section 1.2.1, an electron can be promoted from the valence band to an unoccupied excited state in the conduction band due to incident photon excitation, leaving a hole behind in the valence band with an effective mass as well as an opposing charge to that of the electron. For reliable excitation, the photon must have an energy greater than the band gap $E = \hbar\omega \geq E_(g, QD)$ for the electron to transition from the valence band to the conduction band.

To calculate the absorption of a material, the linear absorption coefficient α of a bulk material is commonly used. This is usually calculated from Fermi's Golden rule [38], which gives the probability of transition from an initial state $|i\rangle$ to an excited state $|f\rangle$:

$$\Gamma_{i\to j} = \frac{2\pi}{\hbar} + |\langle f|H'|i\rangle|^2 \rho \tag{1.24}$$

where $\Gamma_{i\to j}$ is the transition probability, H' represents the interaction between light and electron states, and ρ is the density of the final electronic states. The value of $|\langle f|H'|i\rangle|$ varies with the material, and is related to the interband momentum matrix element. To understand the absorption of a quantum dot, which is neither a perfect 0-D nor bulk 3-D material, a different approach must be taken. Derived from the spherical infinite

potential well model, the density of states for a 0-D material can be expressed as:

$$N_{0D}(E) = \frac{1}{V_{QD}} \sum_{n,l} (2l+1)\delta(E - E_n) \tag{1.25}$$

where V_{QD} is the geometric volume of a single QD, and E_n are the energy levels with a degeneracy l. The volume of the QD can be obtained by averaging the volumes in a single batch to account for polydispersity. Sun and Goldys used the envelope function approximation [39] to derive the linear absorption coefficient $\alpha_{QD}(\hbar\omega)$ of a single QD, assuming the lattice constant and therefore momentum matrix element E_p for a QD and bulk semiconductor are identical:

$$\alpha_{QD}(\hbar\omega) = \frac{\pi e^2 E_p \alpha_p}{2 m_e c n_r \varepsilon_0 \omega} \frac{1}{V_{QD}} \sum_{n,l} (2l+1)\delta(\hbar\omega - E_{nl}). \tag{1.26}$$

Here, e is the elementary charge, α_p is the average over polarisation directions for incident light (2/3 if the light is unpolarised), m_e is the mass of an electron, c is the speed of light in a vacuum, n_r is the refractive index for the QD material, and ε_0 is the permittivity of vacuum. The QD size polydispersity leads to a distribution of quantised energies of width ΔE_{nl} [40, 41], thus, a Gaussian distribution can be used to replace the delta function:

$$\alpha_{QD}(\hbar\omega) = \frac{\pi e^2 E_p \alpha_p}{2 m_e c n_r \varepsilon_0 \omega} \frac{1}{V_{QD}} \sum_{n,l} \frac{(2l+1)}{E\sqrt{2\pi}\Delta E_{nl}} \exp\left(-\frac{(\hbar\omega - E_{nl})^2}{2\Delta E_{nl}^2}\right) \tag{1.27}$$

The molar absorption coefficient can be derived from the linear absorption coefficients for a homogeneous solution of QDs using the Beer-Lambert law, and measures how strongly the QDs absorb light at a particular wavelength. It is defined and expressed as a function of photon energy E:

$$\varepsilon(E) = \frac{N_A V_{QD} \alpha_{QD}(E)}{\ln(10)} \tag{1.28}$$

where N_A is Avogadro's number. This is more useful for colloidal QDs in solution with a relatively low molar concentration.

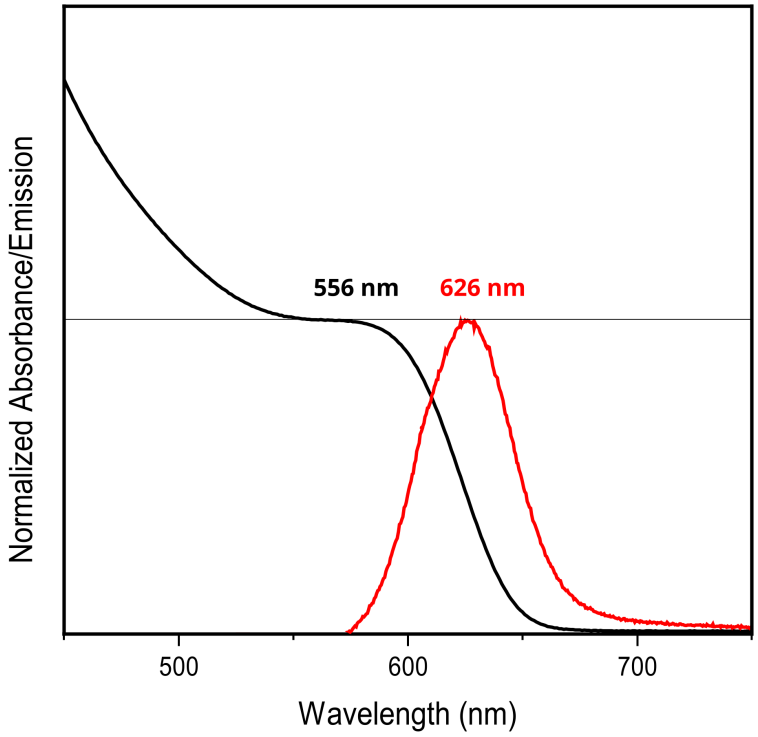

Figure 1.7: Typical spectra for a sample of colloidal QDs. The absorption is shown by the *black* line, where the first excitonic absorption peak at 556 nm corresponds to the first S_1 excitation. This absorption increases as the wavelength decreases, corresponding to the greater number of available states at higher energies. The fluorescence is shown by the *red* line, and has a fluorescence emission peak of 626 nm.

The QD states are intermediate between bulk semiconductors and discrete atoms, with the QD states being more discrete at low excitation energies. As the excitation energy is increased, the states become similar to excitation bands as the discrete states exist closer together, thus the absorption increases at shorter wavelengths. The first exciton absorption peak (see Figure 1.7), commonly referenced during QD size and molar absorption coefficient calculations, represents the S_1 excitation and provides information on the polydispersity of a sample, with a defined peak representing a monodisperse sample. If colloidal QDs have a deficit-rich crystal structure or are polydisperse (varied QD size resulting in varied QD band gaps), they usually display broad excitation and fluorescence emission characteristics.

1.3.4 Excited State Dynamics of Quantum Dots

When a QD absorbs a photon that has an energy greater than the band gap energy E_g, the QD is classed as being in the excited state, where the energy of the promoted electron lies above the conduction band minimum and the hole lies below the valence band maximum. Electrons in the excited state decay rapidly to the band edge due to phonon scattering, populating the lowest electronic states in the conduction band [42]. The corresponding holes in the valence band relax to the valence band maximum in a process called thermalisation. In bulk semiconductors, the energy states are continuous, therefore hot exciton cooling (the nonradiative relaxation of an excited electron/hole pair to the band edge) occurs on the order of hundreds of femtoseconds [43]. In QDs, however, the energy bands separate into discrete states as the size decreases, with the energy separation increasing with confinement. As the QD size decreases for a given material, the energy separation becomes larger than typical acoustic phonon energies, leading to a 'phonon bottleneck' where direct thermalisation is prevented, and the need for precise resonance between the phonon energy and transition energy results in an increase in carrier relaxation times [44, 45]. It was expected that the 'phonon bottleneck' would lead to an increase in carrier relaxation times for smaller QDs, however, short lifetimes on the order of picoseconds (10^{-12}) suggests additional mechanisms for relaxation must be responsible [46, 47].

When a hole in the Nth shell is filled by an electron from the (N + 1)th shell, this leads to an impartation of the transition energy via the emission of an electron in the (N+2)th shell and is termed the Auger effect. Auger processes, like the one described, can contribute to breaking the 'phonon bottleneck' by allowing the exchange of energy between electrons and holes, making additional relaxation channels available [46, 48, 49]. Holes relax more quickly than electrons as energy levels are denser in the valence band, therefore an Auger transfer of energy from excited state electrons to holes that have relaxed to the valence band maximum via phonon emission can take place. The photon

emitted from electron decay has an energy that corresponds to the difference between the energies of the electron and hole, which is typically from the conduction band minimum to the valence band maximum in the absence of intra-gap states.

As well as radiative relaxation by way of Auger transfer of energy, structural defects can also contribute to breaking the 'phonon bottleneck'. Due to the small size of QDs, the majority of the constituent atoms are located at the surface, regardless of the shape [31]. Surface effects from the large surface-to-volume ratio have a prominent role in the electron decay from the excited state within QDs, with defects formed during the synthesis causing 'trapped' electrons to become spatially delocalised, or 'shallow', with a rapid depopulation. Shallow trap states are usually found within the vicinity (a few k_BT) of the band edges [50], where under-coordinated atoms contain unpaired valences, or unsaturated 'dangling bonds', at the edge of the crystal structure. Usually, most surface atoms are passivated via binding to stabilising molecules called 'ligands', although steric limitations usually dictate that 'dangling bonds' will remain present on a number of atoms. These 'dangling bonds' are a source of 'trap' states that are attributed to non-radiative recombination and undesirable losses in photoluminescence quantum yield (PLQY), where energy is transferred to a conduction band electron instead of a photon [51–53]. Internal point defects related to chemical/structural deviations from the ideal crystal structure can give rise to 'deep' intra-gap trap states that are spatially localised and can also provide alternative recombination pathways [54, 55]. Deep trap states lie further from the band edges (several k_BT) [50], and are usually found in defect-tolerant materials and experience much longer lifetimes, contributing to efficient radiative recombination of excitons.

1.3.5 Thermodynamics of Colloidal Quantum Dot Syntheses

Many applications of QDs require a specific range of wavelengths for photon absorption and emission, which can be tuned during QD synthesis. A 'bottom up' fabrication technique is often employed to synthesise QDs in large batches while attaining a high level

of control over the QD size and polydispersity [56]. The seminal 'bottom up' synthesis involved pyrolysis of organometallic reagents through injection into a hot coordinating solvent, allowing nucleation sites to form and permit the growth of monodisperse nanocrystals [57].

A nucleation event results in a transition to the crystal phase from the solution phase and usually occurs when multiple monomers overcome an energetic barrier, assembling into a thermodynamically stable cluster. The thermodynamics of the initial nucleation event can be modelled using classical nucleation theory when considering the formation of spherical colloidal particles [58]. The change in free energy associated with nucleation is given by:

$$\Delta G = n(\mu_c - \mu_s) + 4\pi r^2 \gamma \tag{1.29}$$

where n is the number of atoms in the crystal nucleus, μ_c and μ_s are the chemical potentials of the crystal and solution phase respectively, γ is the surface tension, and $4\pi r^2$ is the surface area of the cluster where r is the radius. The second term of the equation represents the surface energy associated with the crystal-solution interface. By accounting for the volume and number of atoms per unit volume N of the nanocrystal:

$$\Delta G = \frac{4\pi}{3} N r^3 (\mu_c - \mu_s) + 4\pi r^2 \gamma \tag{1.30}$$

Typically, $\mu_c - \mu_s$ gives a small, negative value, therefore the barrier to nucleation is dependent on the surface energy. Initially, the change in free energy will be positive and the crystal will be unstable, but as the crystal grows and reaches a critical radius r_c, a stable interface is created between the cluster and the surrounding medium (Figure 1.8).

The value of r_c can be determined through differentiation of ΔG with respect to the cluster radius to obtain the maxima:

$$\frac{d\Delta G}{r} = 4\pi N r_2 (\mu_c - \mu_s) + 8\pi r \gamma = 0. \tag{1.31}$$

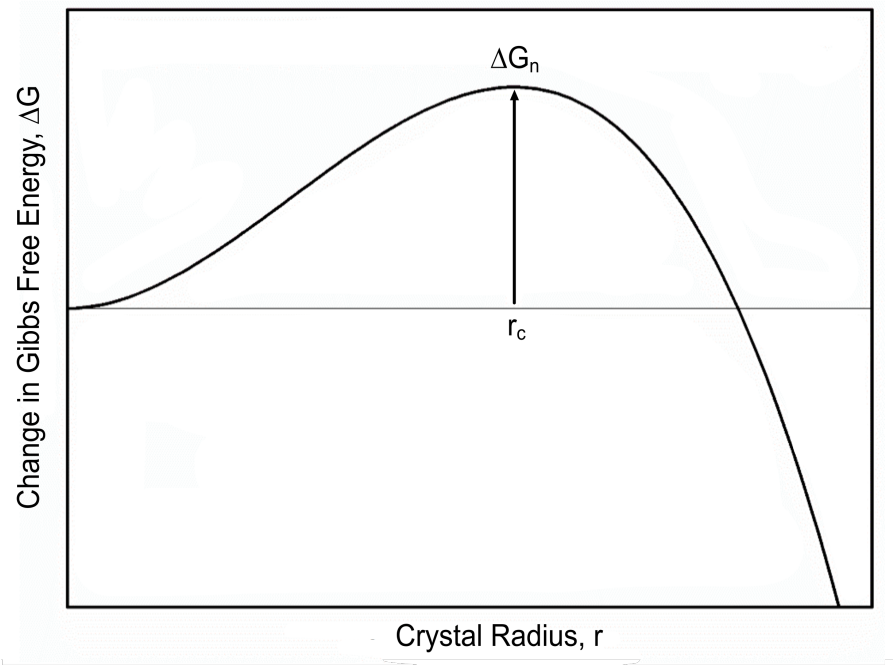

Figure 1.8: Graph to show the change in Gibbs free energy with respect to crystal size. Above the critical crystal size r_c, crystals are stable as an increase in size leads to a net decrease in free energy. ΔG_{nuc} is the free energy required for nucleation.

Rearranging gives the critical radius where the concentration of monomers in solution reaches an equilibrium:

$$r_c = \frac{-2\gamma}{N(\mu_c - \mu_s)}. \tag{1.32}$$

The nucleation energy ΔG_n is the free energy change required to obtain r_c (Figure 1.8), and is dependent on the temperature of the reaction [59]. To achieve nucleation at reasonable temperatures, many variables can be modified including the solvent, concentrations of precursors, and the concentration of ligands that are responsible for the coordination of precursor ions in solution and affect solubility.

Above the critical radius, it will be more energetically favourable for monomers to adsorb onto the surface of the crystal than to stay in solution [60]. The rate of growth is dependent on the diffusion of monomers towards the nanocrystal from the solution. For

classical crystal growth, a model of monomer diffusion can be provided by Fick's law:

$$J = 4\pi x^2 D \frac{dC}{dx} \tag{1.33}$$

where J is the total flux of monomers passing through a spherical plane with radius x [61]. The plane surrounds a crystal of radius r, with D being the diffusion coefficient and C the concentration at distance x. This can be rewritten for a nanoparticle in solution:

$$J = \frac{4\pi D r(r+\delta)}{\delta}(C_s - C_i) \tag{1.34}$$

where δ is the distance from the particle surface to the concentration of monomers in the solution C_s, and C_i is the concentration of monomers at the interface [62]. The flux J is constant irrespective of the radius of the place x, thus integration of the concentration C with respect to x from the crystal surface to the bulk solution gives:

$$J = 4\pi D r(C_s - C_i). \tag{1.35}$$

Considering the diffusion of monomers to the surface as a limiting factor, the particle growth with respect to time is given by:

$$\frac{dr}{dt} = \frac{D\nu}{r} 4\pi r^2 k(C_i - C_r) \tag{1.36}$$

where ν is the molar volume of the crystal and C_r is the solubility of the nanoparticle. C_r is not size-dependent, thus the Gibbs-Thompson equation can be considered:

$$C_r = C_s \exp\left(\frac{2\gamma\nu}{r k_B T}\right) \tag{1.37}$$

where k_B is the Boltzmann constant and T is temperature. Combining Equations 1.36 and 1.37 helps to explain the differences in nanoparticle size during growth:

$$\frac{dr}{dt} = \frac{2\gamma D \nu_2 C_s}{r k_B T}\left(\frac{1}{r_c} - \frac{1}{r}\right) \tag{1.38}$$

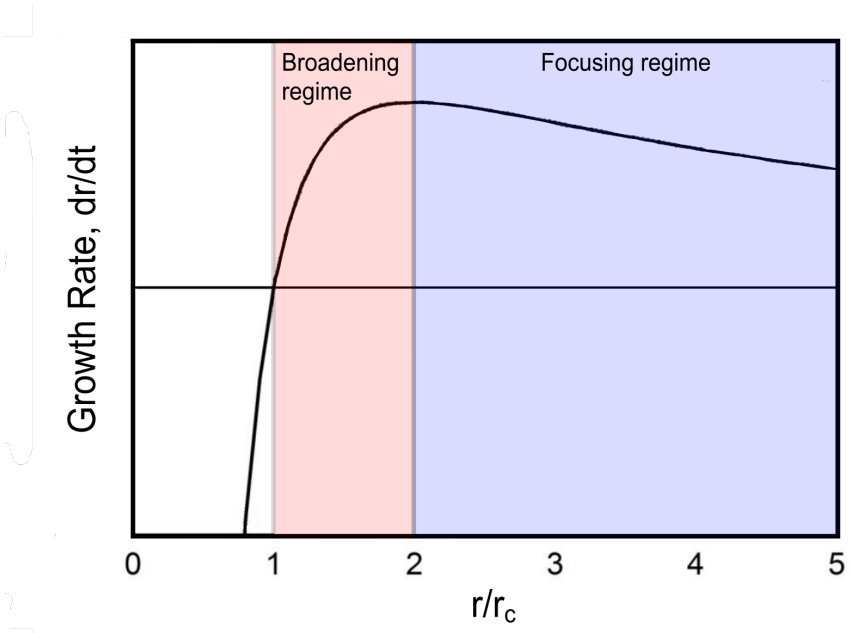

Figure 1.9: Graph to show the growth rate dr/dt with respect to r/r_c. The size-broadening regime occurs when $r_c < r < 2r_c$ and the size-focusing regime occurs when $r > 2r_c$.

where r_c is the critical radius where the concentration of monomers in solution reaches an equilibrium. This temperature-dependent growth rate is known as Ostwald ripening and explains the limit on crystal size as the concentration of precursor materials decreases. As the concentration of monomers decreases, μ_s will decrease and r_c will increase. Ostwald ripening suggests that smaller crystals ($r < r_c$) will shrink and larger crystals ($r > r_c$) will grow (Figure 1.9). If $r = r_c$, the crystal growth rate will be zero. The maximum growth rate can be defined as $r = 2r_c$, where smaller crystals will grow faster than large crystals, leading to a size-focusing of the crystals and a narrow size distribution at the expense of nanoparticle concentration (Figure 1.9). This is generally achieved by continuous injection of precursor to preserve the monomer concentration [63].

As discussed in Section 1.3.4, QDs contain surface 'trap' states that are associated with a non-radiative combination of excitons. Unwanted surface defects can be passivated through the addition of a 'shell' of a distinct semiconductor material containing a dif-

ferent band gap to the core material, increasing the photoluminescence of the material. The electronic properties of QDs are strongly influenced by the offset between the core and shell band offset, with examples shown in Figure 1.10.

If the band gap of the shell is much wider than that of the core, then a type-I behaviour is observed where the exciton is confined to the core, identical to shell-less QDs. The shell serves to passivate the 'dangling' bonds that are present in atoms at the QD surface, which usually results in a quantum yield increase as the number of non-radiative pathways for decay is reduced [64]. Zinc sulfide (ZnS) is generally used as a shell material during type-I QD synthesis due to containing a lattice that is closely matched with common QD core materials, in addition to a wider band gap and oxidation resistance. $CuInS_2$/ZnS core/shell QDs display type I behaviour. The band alignment is type II when one of the charge carriers of any given exciton is localised to the core, and the other is localised to the shell. This usually results in a suppression of Auger recombination and results in longer recombination lifetimes and a red-shift in emission when compared to core-only QDs, with localisation of a charge carrier to the shell allowing efficient charge extraction. Cadmium sulfide (CdS) can be used as a shell material for type-II QDs, although shell thickness can dictate the QD type [65, 66]. CdTe/CdS core/shell QDs display type II behaviour.

One final parameter that is significant during the QD synthesis is the capping ligand, which primarily serves to provide colloidal stability and prevent QD agglomeration while controlling growth [67], but can also aid the attainment of particle morphology and crystal structure along with the solvent. In many hydrophobic QD syntheses, long-chain thiolated surfactants are typically used because they act as a stabilising ligand and also provide a source of sulfur for the nanoparticles during core and shell growth while acting as one of the reaction solvents [68, 69]. A large ($\times$1000) molar excess of thiol promotes a complete surface ligand coverage of the QD, thus provides sufficient colloidal stability in hydrophobic environments.

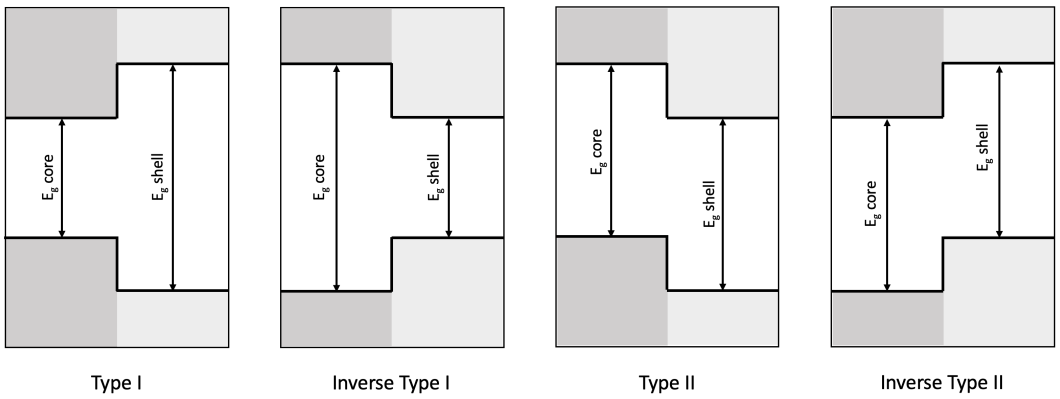

Figure 1.10: Schematic showing the various band structures of core/shell quantum dots. In type I core/shell QDs, the electron and hole are energetically confined to the core. In type II core/shell QDs, the electron is confined to the shell and the hole to the core. E_g is the band gap energy.

1.3.6 Current Knowledge of QD Clustering and Aggregation

Hydrophobic QDs are highly unstable when placed into aqueous suspensions unless they are encapsulated by a more hydrophilic (or amphiphilic) material (such as polymers). QDs can assemble into clusters of several particles under certain conditions governed by the physicochemical environment, including the choice of solvent/buffer, the temperature, and the surface chemistry of the QD [70–74]. Often this can leads to extremely large aggregates containing hundreds of nanoparticles, which become unstable and eventually precipitate out of the solution, but sometimes relatively small and stable nanoscale clusters of QDs (e.g., 10-100 particles) can form. These 'nanoclusters' persist and have altered ensemble and single-particle properties to colloidal QDs. It is likely that QD clustering and aggregation will affect the many downstream applications of QDs, so it is important to understand them and control their size.

FRET between QDs is important within many optoelectronic devices. In QD photovoltaics, FRET between QDs usually leads to energy loss and is undesirable [75], as is the case with core-only QD FRET in light-emitting devices (LEDs) where energy is distributed to non-luminescent QDs where they recombine non-radiatively [76, 77].

However, in core-shell QD arrays, FRET can provide a route to QD excitation and high-brightness QD LED devices which were otherwise hindered through poor charge injection [22]. Investigation into FRET between QDs was first completed on dried samples within the Bawendi group, where aggregation was achieved through thin-film deposition of Cd QDs [78, 79]. These seminal investigations theorised that FRET occurred within the inhomogeneous size distribution of QDs [22], specifically energy transfer from small, higher energy QDs to larger, lower energy QDs when co-localised. Later experiments within the Klimov group investigated monodisperse (7% size distribution) QDs deposited in layers [80], where energy transfer was again seen from 'blue' to 'red' QDs across an energy gap of tens of meV (Figure 1.11 A/B). A fast nanosecond decay from FRET was observed when exciting high-energy QDs on the blue side of the fluorescence emission band, with the QD lifetime showing size-dependence and increasing in redder QDs which typically acted as energy acceptors, ruling out indirect coupling via photon re-absorption. Similar findings were observed in linear 1D arrays of CdTe QDs (size distribution of 10-15%) that were self-assembled through dipole-dipole attraction, where the PL spectrum of QDs in the linear chain was red-shifted compared to individual QDs with an identical absorbance [81]. A shorter lifetime was also observed in the linear chain QDs, again suggesting FRET from smaller QDs (energy donors) to larger QDs (energy acceptors). More recently, investigations into FRET between Cd-free $CuInS_2$/ZnS QDs deposited on a thin film have been studied [82], where the red-shift in PL was found to be dependant on the cluster size. Larger aggregates were also found to have a slower decay in the fluorescence lifetime than smaller aggregates, resulting from a higher frequency of non-radiative energy transfer from smaller to larger QDs.

In solution, FRET between colloidal QDs is more difficult to achieve because the average distances between QDs will typically be much larger, simply because the particles are dispersed in a 3-D volume. Furthermore, the individual QDs may be coated with organic layers composed of polymers, thiols and phospholipids to maintain colloidal stability while preventing aggregation [72, 83, 84], which increases the distances further.

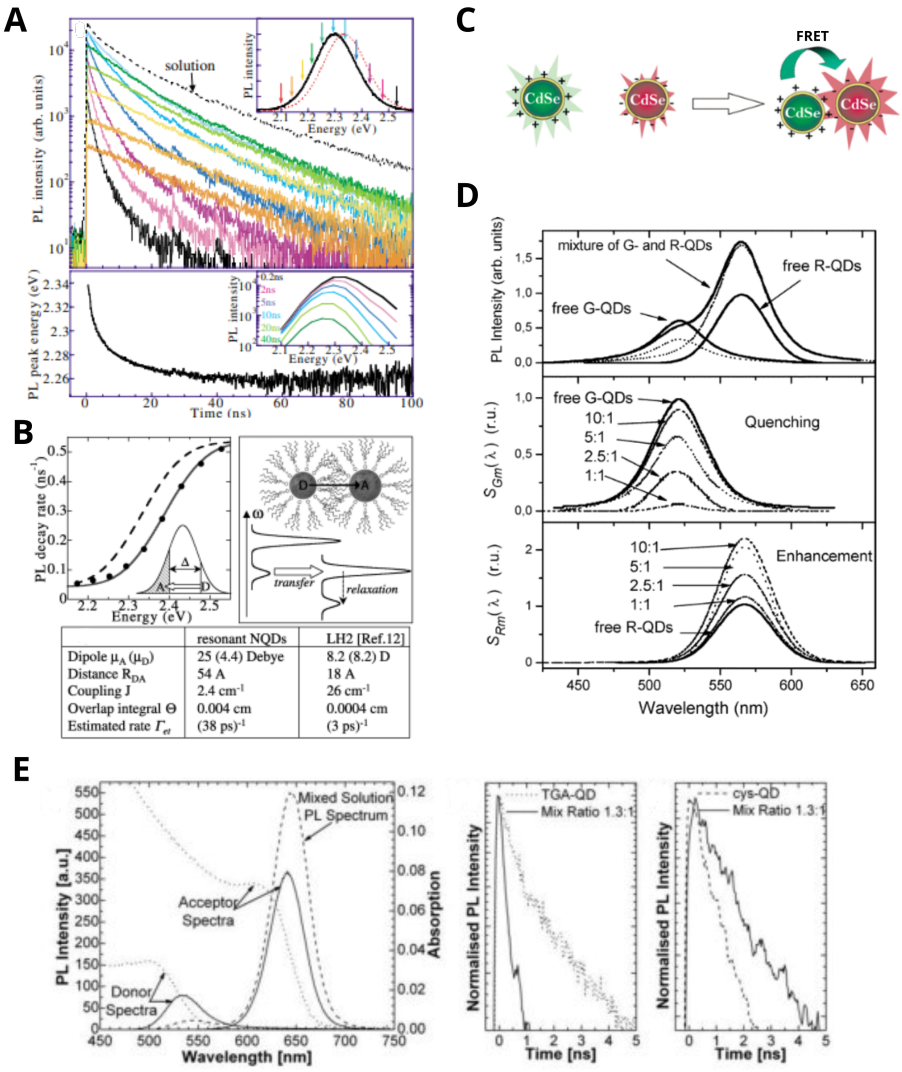

Figure 1.11: Example spectra and schematics of clustered QDs. (A) Top: PL decays obtained from a dense film of CdTe/CdS quantum dots at energies specified in the inset, which displays the PL of QDs in film (solid) and solution (dashed). Bottom: dynamic red-shift of the peak fluorescence emission. (B) Top left: PL decay rate vs energy for QDs with no gap between them (dashed) and a 5 meV gap (solid). Top right: FRET between QDs that are spatially separated by an 11 Å gap. Bottom: Typical Förster parameters for resonant QDs. (A) and (B) adapted with permission from Crooker *et al.* [80]. Copyright 2002 by the American Physical Society. (C) Schematic to show electrostatic attraction of QDs with opposite surface chemistries. (D) Top: PL intensity of aqueous red R and green G QDs individually and mixed (solid), with deconvolution (dashed). Middle: quenching of the green 'donor' QDs with the changing donor:acceptor concentration. Bottom: enhancement of the red 'acceptor' QDs with the changing donor:acceptor concentration. (C) and (D) adapted with permission from Wargnier *et al.* [71]. Copyright 2004 American Chemical Society. (E) Left: PL of the individual (solid) and mixed (dashed) donor/acceptor QDs in solution showing acceptor enhancement. The dotted line represents QD absorption. Middle: Time-resolved PL measurements of donor QDs in pure (dotted) and mixed (solid) solution. Right: Time-resolved PL measurements of acceptor QDs in pure (dotted) and mixed (solid) solution. (E) adapted from Higgins *et al.* [73].

These larger effective particle diameters are likely to limit the effectiveness of QD-QD FRET and may prohibit certain FRET-based applications such as bio-sensing [85, 86]. One of the first instances of QD aggregation in solution came through the utilisation of oppositely-charged QDs, where electrostatic attraction promoted the aggregation of positively-charged 'green' and negatively-charged 'red' core/shell CdSe/ZnS QDs (518 nm and 563 nm fluorescence emission maxima respectively) [71], shown in Figure 1.11 C/D. The composition of the assemblies was unknown, but a combination of experimental and simulation data demonstrated that FRET was a primary interaction between donor and acceptor QDs. Similar experiments attempted to quantify resulting structures through transmission electron microscopy (TEM) as well as investigate various donor/acceptor QD ratios (Figure 1.11 E), and while the percentage of donor quenching and acceptor enhancement was successfully calculated, it was noted that TEM data may not be representative of solution aggregation [73].

Reversible aggregation of QDs in solution has also been achieved through mixing concentrations of coordinating and non-coordinating solvents [70], where CdSe clusters with an average diameter of 27 nm were formed from 2-5 nm QDs. The PL of the QD clusters was found to be heat-sensitive, with a red-shift and quenching of the PL observed with an increase in temperature. It was suggested that FRET, as well as reversible thermal trapping of electrons, was responsible for the shift, although understanding of the interfacial interactions was limited. A similar method was used to investigate the energy transfer between two distinct populations of QD (3.5 nm and 7.3 nm diameters), where aggregation was achieved in solution through alteration of the solvent polarity. A quenching in the smaller QD donors' fluorescence intensity and an enhancement of the larger QD acceptors' fluorescence intensity was observed, although the cluster size ranged from 500 nm to micrometres and was uncontrolled [87]. The energy transfer mechanisms between hydrophilic QDs aggregated via solvent alteration have more recently been theorised through computer simulations of energy transfer within clusters of cadmium selenide colloidal QDs [88]. Subsequent investigations were completed [89–91],

although little control over cluster size was reported, and the clusters likely do not have any surface functionality due to aggregation that is reliant on alteration of the solvent polarity.

Control of cluster size has been achieved by Li *et al.* using large 16 nm diameter hydrophobic CdSe/ZnS QDs (Figure 1.12 B1) encapsulated within a fluorescent lipid micelle to act as a probe [92]. The intention of the study was to use a phospholipase A_2 (PLA_2) enzyme to release a lipid dye that would otherwise be quenched as an energy donor for FRET (Figure 1.12 A), with large 100 nm clusters obtained (Figure 1.12 B2). The fluorescence of the NBD lipid was initially quenched by the QD clusters, with the fluorescence restored upon lipid digestion by the enzyme, however, the dye-QD and QD-QD energy transfer dynamics were not reported. Finally, QD coupling has been controlled through the use of covalent bonding in combination with solvent alteration (Figure 1.12 C), where a network of crosslinked CdSe QDs was achieved [93, 94]. These were then deposited as a layer of structures to form QD arrays where the energy transfer mechanisms of dried samples were investigated.

One limitation of the studies into QD clustering and aggregation is the types of QD used, where the majority of studies used toxic Cd-based QDs. A shift to non-toxic QDs should be considered, as later explained in Section 1.3.7. The QD-QD energy transfer mechanisms for non-toxic QDs would need investigating, and control of the cluster size in solution could also be optimised. Further advancements could aim for a structure that maintains a consistent size in an aqueous solution as well as on a solid surface (e.g., following thin-film deposition) which could be achieved through the utilisation of phospholipids to stabilise QD aggregates, similar to the controlled aggregation proposed by Li *et al.* Finally, assembling smaller clusters of QDs would increase the surface-to-volume ratio, with more QDs situated at the surface of the cluster leading to optimal cluster absorption and ultimately brighter clusters [82].

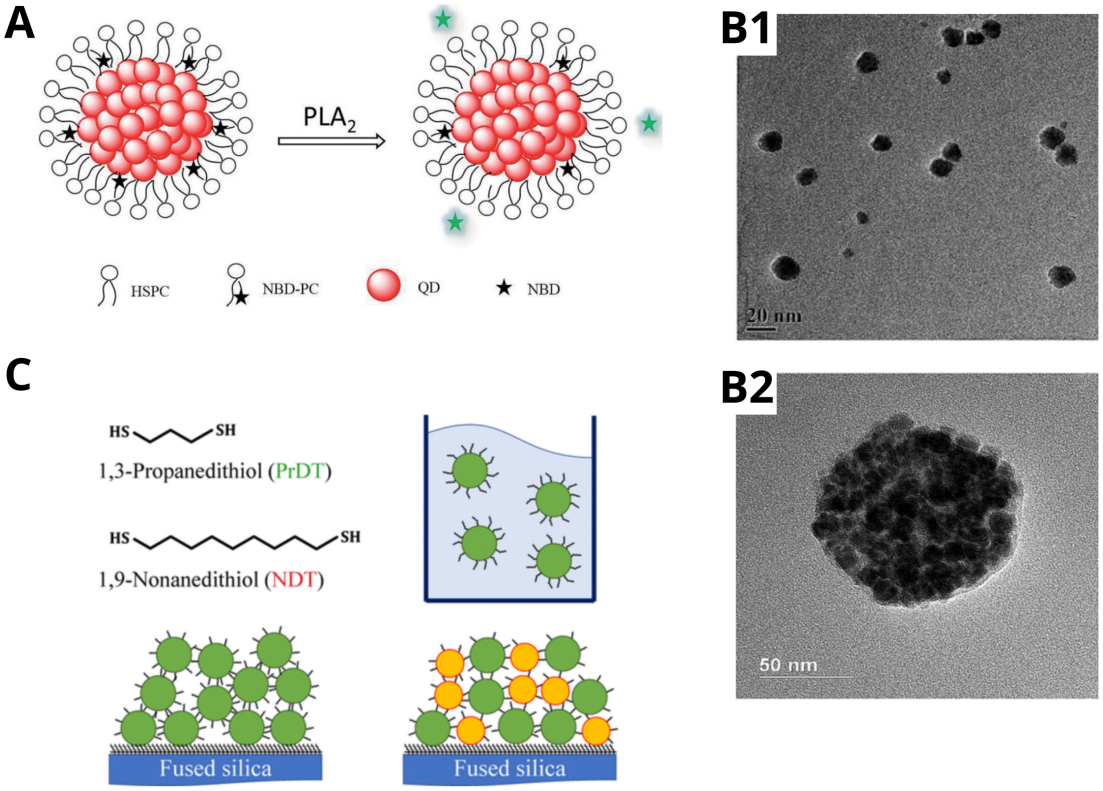

Figure 1.12: Schematics and images of controlled QD clustering. (A) Schematic showing lipid-encapsulated clusters of CdTe QDs and principle for dye activation using PLA_2. (B1) TEM image of CdTe QDs with 16 nm mean diameter and (B2) TEM image of a phospholipid-encapsulated cluster of CdTe QDs. (A) and (B) adapted with permission from Li *et al.* [92]. Copyright 2016 The Royal Society of Chemistry. (C) Top left: The structure of alkanethiol molecules used to achieve crosslinking. Top right: Single-sized QDs in solution. Bottom left: Disordered structure of covalently-coupled single-sized QDs. Bottom right: Disordered structure of covalently-coupled QDs consisting of two different sizes. (C) adapted with permission from Cohen *et al.* [94]. Copyright 2018 American Chemical Society.

1.3.7 Quantum Dot Choice

Widely used cadmium (Cd) QDs are considered toxic because of the oxidation of chalcogenide atoms (Se and S) by O_2 from the air, which forms oxides (SeO_2 and S_4^{2-}) that desorb from the surface of the QD [95, 96]. This results in the remaining free reduced Cd atoms seeping from the core of the QD. The rate of this process is increased upon exposure to Cd-binding chloride ions as well as ultraviolet light [96, 97]. $CuInS_2$ QDs provide a less-toxic alternative to Cd-based QDs, as toxic ions are not released from the core upon oxidation [69]. Currently, there is a drive to reduce the use of heavy metals in electronic devices, with commercial use of such metals in applications restricted by legislation worldwide, meaning that even devices containing Cd QDs for non-biological applications need to consider the use of less toxic materials. $CuInS_2$ QDs are well-characterised with respect to the excited state mechanics and recombination mechanisms [98–101], as well as the size of the QDs in relation to the fluorescence emission peak and molar absorption coefficient [102]. Studies comparing the photoluminescence of $CuInS_2$ QDs with varying Cu:In ratios have shown that the formation energy of In_{Cu} and V_{Cu} defects (copper vacancies) in Cu-deficient QDs is lower than in stoichiometric $CuInS_2$ QDs [103], resulting in Cu-poor QDs displaying a higher PLQY than their stoichiometric counterparts [55, 100, 104, 105]. The elemental distribution of Cu and In within stoichiometric solvothermal-synthesised chalcopyrite $CuInS_2$ QDs has also been imaged using STEM-EELS mapping to investigate the characteristic photophysical properties of $CuInS_2$ QDs, with the spatial separation of Cu and In consistent with a large population of Cu_{In} antisite defects, supporting intraband electronic states involved in radiative recombination of excitons [99].

Single-particle analysis of $CuInS_2$/ZnS QDs has been difficult due to the phenomenon of 'blinking' – random fluctuations in the QD photoluminescence resulting in long off periods with short emission bursts, giving rise to large signal fluctuations and low photon counts which makes characterisation difficult[106, 107]. A recent investigation into

the single-particle analysis of $CuInS_2$/ZnS QDs has managed to reduce blinking via the growth of a thick ZnS shell to passivate trap states that are otherwise involved in non-radiative recombination of excitons [104]. It was determined that the broad fluorescence emission spectra of $CuInS_2$/ZnS are not solely due to the polydispersity of the QDs, but the location of the emissive defect within the QD, where a shorter lifetime is expected for a centrally located defect and a longer lifetime expected for a peripherally-located defect. The photoluminescence of $CuInS_2$ QDs can be enhanced ~40-fold with the addition of a ZnS shell, which also leads to a blue shift of the PL spectrum due to the cationic exchange between $CuInS_2$ and ZnS lattices [108]. This is the result of a semi-alloyed $CuInS_2$/ZnS particle where Cu^+ and In^{3+} cations are exchanged with Zn^{2+}, as opposed to a typical core/shell structure with a well-defined boundary. $CuInS_2$/ZnS QDs have broad excitation spectra and can be tuned to compliment the absorption range of many other optically-active components of potential nanotechnological devices, while also displaying long lifetimes, broad fluorescence emission spectra due to the polydispersity in size, and a large Stokes shift when compared to CdSe QDs, for example [68]. This suggests that QDs may act as good FRET energy donors if the energy acceptor satisfies the criteria outlined in Section 1.2.2.

1.4 Lipids

1.4.1 Common Structures and Compositions of Lipids and Detergents

Lipids are amphiphilic molecules consisting of a hydrophilic head group and two hydrophobic fatty acyl tails. As lipids are amphiphilic in nature, they will self-assemble to reduce the system's free energy when in a polar solvent by minimising the exposure of the hydrophobic tails to the solvent and maximising the exposure of the hydrophilic heads of the lipids [109, 110]. The resulting structures are dependent on the effective curvature of the lipid with respect to the lipid head and tail groups [111]. If the effective head group is wider than the effective tail, spherical structures will tend to form, with the tails aggregating together and the heads exposed to the surrounding solvent

(Figure 1.13 A). These spherical structures, termed 'micelles', commonly form during the self-assembly of detergents, which are single-chain amphiphilic molecules containing a single hydrophobic fatty acyl tail and a hydrophilic head. The self-assembly to form micelles only occurs when the detergent is above a critical concentration, termed the critical micelle concentration (CMC), where it is energetically favourable for molecules to self-associate to reduce the exposure of the hydrophobic tails to the polar environment [112]. If the effective head group and the effective tail group are of equal or similar width, then lipids will form planar lipid bilayers (Figure 1.13 B), where two layers of lipid are arranged with tails facing each other and heads exposed to the polar aqueous solution to minimise exposure to the solvent [109, 110]. Bilayers have a natural curvature that is dependant on the lipid, which can lead to the formation of large spheres called 'liposomes' or 'lipid vesicles' (Figure 1.13 C) that separate an aqueous core from an aqueous solvent with one (unilamellar) or multiple (multilamellar) lipid bilayers [113, 114]. The size of a formed liposome is often dependent on the curvature of the lipid.

The chemical composition of lipids dictates the assembled structure and the manner in which they interact with each other. A typical lipid consists of a polar head group that is connected to 1-3 fatty acid tails via a glyceral backbone or similar sugar scaffold. The fatty acid tails usually consist of a carboxylic acid (or other acyl) with an aliphatic chain of carbon atoms. Fatty acids are either 'saturated' or 'unsaturated', where the tail contains at least one carbon-carbon double bond that causes the chain to be bent. The number of carbon atoms and double bonds in the fatty acid tail can be denoted by a pair of numbers X:Y, where the first number represents the number of carbons and the second number represents the number of double bonds. The head group of the lipid is the hydrophilic portion of the molecule and often contains a phosphate group, with this class of lipid known as a phospholipid. A common, and well-studied phospholipid is the zwitterionic 1,2-dioleoyl-sn-glycero-3-phosphocholine (DOPC), which is shown in Figure 1.13 D, and is used to form model lipid membranes as it readily assembles into liposomes which can be deposited onto a surface [115]. DOPC contains a phosphate and

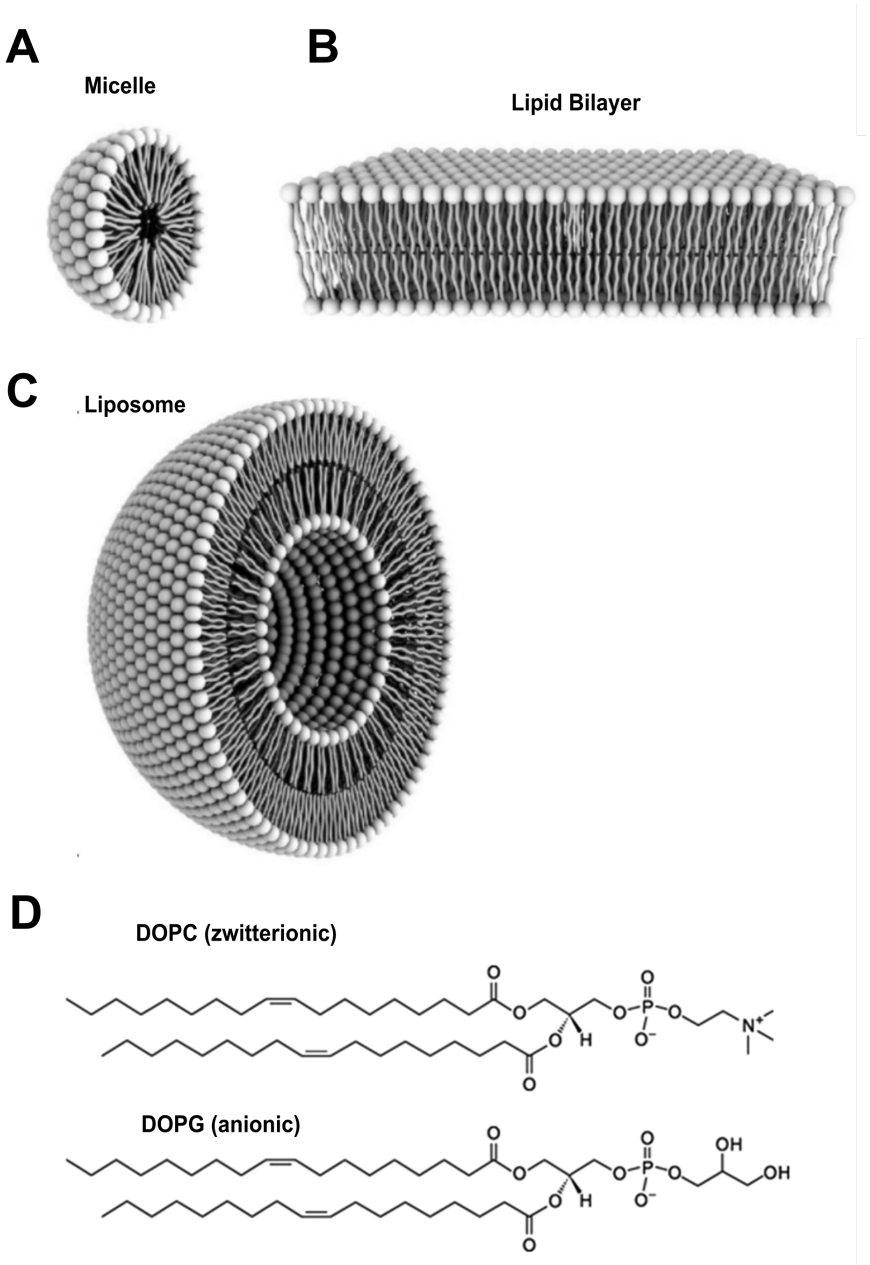

Figure 1.13: Examples of model lipid bilayers and lipid structures. Structure of (A) a micelle, (B) a lipid bilayer and (C) a liposome. White circles represent hydrophilic lipid headgroups and grey represents hydrophobic lipid tails. Adapted from Bitounis *et al.* [111] (D) Chemical structure of DOPC and DOPG.

choline head group that is connected to two 18:1 fatty acid tails via glycerol and ester bonds. A second, well-studied phospholipid of potential use is 1,2-dioleoyl-sn-glycero-3-phospho-(1'-rac-glycerol) (DOPG), which contains a negatively charged head group and therefore a large effective head group due to electrostatic interactions. Integration of the anionic DOPG into DOPC liposomes will increase the lipid curvature, depending on the DOPG:DOPC molar ratio, allowing the possibility of size control of the self-assembled lipid structure.

1.4.2 Model Environments for Membrane Proteins

To effectively study the properties of lipids and/or membrane proteins in a native-like lipid environment, model lipid membranes can be formed in vitro. Lipid bilayers can be prepared from specifically selected lipids that self-assemble into nanoscale structures which are stable in aqueous solutions. There are numerous ways that this can be achieved, such as the gradual hydration of lipids dried onto a surface [116], through disrupting aggregates of liposomes in solution by applying a force through sonication [117], or by solubilising lipids into detergent micelles and gently removing the detergent [118]. All of these methods involve breaking up any preformed aggregates of lipids, allowing self-assembly into various structures. Once formed, these model lipid bilayers can then be used as a platform to study proteins and their function by incorporating proteins during self-assembly to form 'proteoliposomes'. Membrane proteins are typically solubilised using detergent micelles during the isolation and purification procedures that extract them from natural membranes. When lipid is present, proteoliposomes can be formed through the removal of the detergent, allowing reconstitution of the membrane proteins into lipid bilayers, which is often done by rapidly diluting the protein solution to lower detergent concentration or by the gradual removal of detergent using porous polystyrene bead adsorbents [119]. Adsorption of the detergent reduces the concentration below the CMC causing micelles to disassociate, with membrane proteins then able to reconstitute into lipid bilayers to minimise free energy by removing their hydrophobic regions from contact with the polar solvent. These proteoliposomes can then be stud-

ied in solution [120] or tethered to a surface for fluorescence microscopy measurements [121, 122]. Research utilising proteoliposomes includes studies of in-membrane protein aggregation [123], lipid-protein interactions [123, 124], and energy transfer between dyes and proteins [120, 125].

1.4.3 Lipids and the Potential for Association with Quantum Dots

A modular, lipid-stabilised system could provide a stable environment for controlled energy transfer between hydrophobic QDs in an aqueous environment, while also allowing a greater understanding of the fundamental underlying photophysical processes involved. The introduction of lipids for nanoparticle stabilisation also introduces the potential of self-assembly, bypassing the need to alter solvent polarity in order to achieve controlled QD clustering. Lipids are known to have the potential to associate with nanoparticles containing hydrophobic surface chemistry, such as the clustered CdTe QDs encapsulated by lipids described in Section 1.3.6 [92]. Attempts have also been made to associate hydrophobic QDs with lipid vesicles [126–128], which may be beneficial in providing a stable environment for investigating FRET between QDs and photosynthetic pigment molecules, detailed comprehensively in Chapter 1.6.

1.5 Light-Harvesting Proteins

The photosynthetic structure of plants is the result of over three billion years of evolution to optimise the efficiency of capturing and converting solar energy into electrochemical energy [129]. The visible light spectral region (400 to 700 nm) accounts for a significant proportion (∼43%) of the total solar irradiance, with the remainder covered by low-energy infrared (IR) radiation (∼52%) and high-energy ultraviolet (UV) radiation (∼5%) [130].

1.5.1 Light Harvesting in Photosynthetic Systems

Photosynthetic systems consist of many pigments that are arranged in such a way that energy can be captured from sunlight and then transferred efficiently via FRET to reaction centres (RCs), where photochemical reactions can take place. Chlorophylls are the most common pigments in plants, and are arranged in and around photosystems so they can absorb an incident photon of light to form an exciton; an excited electronic state as discussed in Section 1.2. Chlorophyll (Chl) molecules consist of a planar 'head group' containing a central magnesium atom ligated by four nitrogen atoms, each forming part of a cyclic pyrrole ring with four carbon atoms. The four pyrrole rings provide a delocalised π bond, called a macrocycle, to allow various vibrational energy states across the molecule. Chl molecules are also comprised of a hydrocarbon 'tail' which provides stability and allows incorporation into complex structures, such as proteins. Chl *a* is the most common type of chlorophyll in photosynthetic systems and has a strong absorbance in the visible wavelength regions of 380 - 450 nm (Soret band) and 625 - 725 nm (Q_y peak), with a weaker absorption peak between 550 - 600 nm (Q_x peak). Electrons promoted to the lowest-energy (Q_y) electronic excited state ($S_0 \rightarrow S_1$) are relatively stable with a $\sim$4 ns lifetime, therefore the Q_y state is effective for the transfer of excitation energy to other pigments. Electrons promoted to the higher-energy Soret (B_x and B_y) excited states ($S_0 \rightarrow S_2$) and the Q_x excited state ($S_0 \rightarrow S_1$) are less stable and will relax to the Q_y state via internal conversion and vibrational relaxation within picoseconds.

As well as chlorophylls, other pigments such as carotenoids are also present in photosynthetic systems to maximise the absorption range of the protein. Carotenoid molecules consist of many double bonds which provide a delocalised π bond system that spans the molecule. The most common carotenoid in plants is lutein, which contains cyclic carbon rings at either end of the molecule to further extend the π bond system. Carotenoids typically absorb strongly in the 400 - 500 nm visible wavelength region, where electrons are promoted from $S_0 \rightarrow S_2$ and the associated manifold of vibrational energy levels.

Due to the symmetry of the elongated carotenoid molecules, the $S_0 \rightarrow S_1$ transition is 'forbidden' and does not occur under normal conditions in nature. This means the internal conversion from $S_2 \rightarrow S_1$ is very efficient and occurs on a femtosecond timescale, with $S_1 \rightarrow S_0$ internal conversion also efficient due to the 'forbidden' nature of the S_1 state. Carotenoids have multiple roles in photosynthetic systems:

1) Energy absorbed by the carotenoids in the 400 - 500 nm range can be transferred to chlorophylls for eventual use in photochemical reactions.

2) Carotenoids can quickly dissipate electron energy as heat through internal conversion and vibrational relaxation, making them crucial for rapid quenching of potentially damaging chlorophyll triplet states in the event of multiple excitations in a short period.

3) Carotenoids are important in stabilising the 3-D structure of many pigment-protein complexes [10].

Photosystems (PS) and their respective light-harvesting complexes (LHC) are crucial to the first stages of photosynthesis and are responsible for the absorption of light and the transfer of energy and electrons. The pigments in these proteins are arranged in such a way as to increase the spatial and optical area available for light harvesting and then to transfer this energy via FRET to RC subunits, where electron transfer eventually leads to productive chemistry [131]. Solar energy is dilute and diffuse, with photon absorption by individual chlorophylls occurring relatively infrequently: on average only once every $\sim$100 µs [10]. As multiple cycles of photon absorption, photochemistry and electron transfer are required for water-splitting in the PSII RC, relying on the absorption of these chlorophylls alone would result in a rate of water splitting that fell well below the maximum capable rate that PSII RCs are capable of (once per 300 ps) [132]. For maximum efficiency, aptly-named 'antenna' proteins and photosystems are organised into

light-harvesting supercomplexes consisting of a photosystem and multiple LHCs, where they act to increase the effective absorption area of the RC in a similar principle to a satellite dish. The antenna proteins and photosystems are organised in such a way that the pigments which absorb the highest energy photons are situated furthest away from the RC and the chlorophylls that absorb the lower-energy photons are situated towards the centre. It would be inefficient to have many RCs spread out as the low photon flux would result in RC inactivity for a large proportion of the time. Carotenoids, which are situated furthest away from the RCs, are able to absorb high-energy photons and transfer that energy 'downhill' to the chlorophylls, which have lower associated energy levels. The chlorophyll pigments have similar associated energy levels, so are able to transfer energy to each other within PSs and LHCs, including to 'special pairs' of chlorophylls (P680) located in the photosystem RCs that are responsible for electron transfer to other electron carriers. FRET can occur between all chlorophyll pigments in the proteins, meaning electrons are effectively delocalised throughout the entire system (small uphill energy transfer is attainable at room temperature due to vibrations and heat, k_BT) [7]. This allows energy absorbed by any pigment to eventually be transferred to the RCs.

1.5.2 Light-Harvesting Complex II

The light Harvesting Complex II (LHCII) of plants is the most abundant antenna complex in nature. Initially discovered in 1993, LHCII is located within a complex system of bio-membranes called the thylakoid and acts as the major light-harvesting antenna of PSII [133–137]. In 1994, electron crystallography was used to determine the first structural model for LHCII to a maximum resolution of 3.4 Å [138]. The next significant updates to this structural model were achieved using x-ray crystallography in the mid-2000s, further increasing the resolution to 2.5 Å as shown in Figure 1.14 A/B [139–141]. In nature, LHCII functions in both a monomeric form and in a trimeric form, with subtle differences in the structure and absorption spectra [142, 143]. Both monomers and trimers are found in the dimeric PSII-LHCII supercomplex, with monomers labelled

CP29, CP26 and CP24 [144]. Each monomer of LHCII contains three transmembrane alpha helices, 8 chlorophyll a, 6 chlorophyll b, 4 carotenoids and 2 bound lipids [140]. There are three isoforms of the LHCII polypeptides, each of which is produced from separate genes: Lhcb1, Lhcb2 and Lhcb3. These combine to make up the trimeric complex [145]. Lhcb1 and Lhcb2 are very similar, while Lhcb3 differs due to its lack of phosphorylation sites and one less chlorophyll b pigment. It is thought that Lhcb1 and 2 act as the main antenna complexes and Lhcb3 contains the lowest energy chlorophyll that acts as an intermediate between Lhcb1, Lhcb2 and PSII in the FRET energy transfer chain [146].

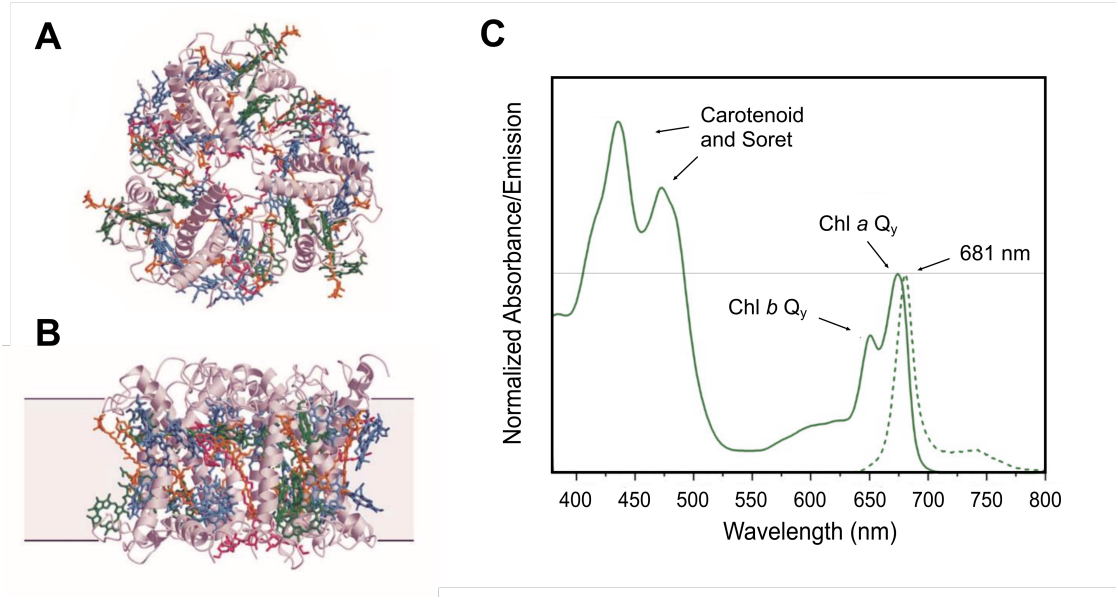

Figure 1.14: Structure and spectra of isolated LHCII. (A) Top view of the LHCII trimer from the stromal side and (B) side view of LHCII trimer protruding from a 3.5 nm bilayer (black lines) by 1.3 nm on the stromal side (top) and by 0.8 nm on the lumenal side (bottom). Grey - alpha helix, blue - chlorophyll *a*, green - chlorophyll *b*, orange - carotenoid, pink - lipids. Adapted with permission from Standfuss *et al.* [140]. Copyright 2005 European Molecular Biology Organization. (C) Absorption and fluorescence emission of isolated LHC II in detergent. The absorption is normalised to Chl *a* Q_y peak and the fluorescence is normalised to the 681 nm peak.

Both monomers and trimers of LHCII have strong absorption in the blue region of the visible spectrum (400 - 500 nm) due to densely-packed pigments of chlorophyll a/b and carotenoids, which provide for photon absorption at the chlorophyll Soret and carotenoid

$S_0 \rightarrow S_2$ transitions, respectively (Figure 1.14 C, solid green line). LHCII also has a strong absorption in the red spectral domain (650 - 700 nm) due to the Q_y transitions of chlorophyll *a* and *b*. The energy absorbed by the pigments in the LHC II antenna protein is transferred downhill via FRET to the 'terminal' chlorophyll *a* molecules, where energy is equilibrated to the lowest level (corresponding wavelength of ∼680 nm) for fluorescence or transfer to PSII. Under normal conditions in nature, the majority of energy is transferred to PSII in a few picoseconds on average [147]. For isolated LHCII trimers (no PSII present), a single fluorescence emission peak at 681 nm is observed, corresponding to emission from a single type of pigment (Figure 1.14 C, dotted green line). The peak has a full width at half maxima (FWHM) of ∼50 nm and a minor shoulder between 700 - 750 nm due to various vibrational sub-states.

1.6 Bio-Hybrid Light-Harvesting Systems

1.6.1 Light-Harvesting Proteins in Nanotechnology

When considering available carbon-neutral energy sources, solar is among the most promising. Energy from the sun strikes the surface of the Earth at a rate of ∼120 000 TW, significantly surpassing the rate of world-marketed energy consumption [130, 148, 149]. There are, however, limitations to solar energy that must be overcome before it can be considered as a long-term replacement of fossil fuels. Solar energy is diffuse (∼1 kW/m^2) and diurnal, meaning the energy must be efficiently captured and stored in a cost-effective manner [130]. Photosynthesis is an example of energy capture and storage on a wide scale, where energy is stored in the biomass of phototrophic organisms at a rate of ∼120 TW [150]. The overall efficiency in converting solar energy into chemical energy in carbohydrates by photosynthesis in plants does not exceed 1-3% [151, 152], however, the photon absorption and excitation energy transfers that occur during the early stages of photosynthesis are highly efficient at ∼95% [153]. In comparison, industrial silicon solar cells are ∼20% efficient at converting incoming solar energy to electricity via the photovoltaic effect, with a theoretical maximum efficiency of 47.7% [154]. If the prin-

ciples of the early stages of photosynthesis could be replicated or incorporated with synthetic constructs to replace or enhance current technologies, the challenge of total fossil fuel replacement may finally be both achievable and affordable [155].

When considering existing light-harvesting proteins for integration into human-made devices, LHCII is among the most promising; LHCII features a particularly high density of pigments with a 0.3 M concentration of Chl per LHCII monomer [140] which cannot be replicated in organic solvents without significant concentration quenching of excited Chl [129, 156]. When nanopattern-deposited onto glass, LHCII trimers have been shown to retain their high photon absorption and fluorescence properties, with reversibility between fluorescent and quenched states achieved through controlling the stabilising detergent concentration [157]. Previous studies have also shown that nanopatterned light-harvesting proteins are capable of long-range (micrometre) energy transfer through an efficient coupling of bacterial LH proteins [158], suggesting potential applications of light-harvesting proteins following surface deposition. With respect to electrical current production and the interaction of light-harvesting proteins with electrodes, an enhancement of photocurrent production using light-harvesting proteins was first obtained through multilayer deposition of plant PSI into an electrochemical system [159]. Further to this, isolated reaction centre/light-harvesting 1 (RC-LHI) complexes from bacteria have been shown to retain up to 32% of their energy transfer efficiency when a densely-packed monolayer was deposited on an electrode using the Langmuir-Blodgett method to control orientation [160]. This 32% retained efficiency suggests promise in replicating the efficient energy transfer processes that occur during the early stages of photosynthesis as well as promising applications for light-harvesting proteins with respect to bio-sensors and bio-solar cells.

1.6.2 Artificially Increasing the Efficiency of Light Capture in Photosynthetic Proteins

While light capture in photosynthetic systems is efficient, the light-harvesting proteins responsible in both plants and bacteria are limited to specific biological pigments, resulting in gaps in the absorbance spectrum [153]. Bio-hybrid light-harvesting systems involve the use of artificial light antennae to absorb photons of energy from regions of poor absorption and then transfer the energy to the light-harvesting protein, increasing the effective absorption cross-section of light-harvesting proteins. This extends to LHCII, where energy capture can be improved by filling the 500 - 600 nm 'green gap' present in the major network of pigment molecules found in plants; in the green spectral domain, LHCII has a low absorption when compared to the blue and red spectral domains. This 'green gap' is not just limited to plants; certain algae are also predominately made of Chl a/b pigments, with the green gap giving rise to the green colour of leaves and green algae. In some environments where sunlight is limited, natural photosynthetic organisms have evolved to fill this green gap; red wavelengths of light are absorbed within the first few metres of water, therefore organisms living at depths below 10 m have an abundance of carotenoids which absorb across the 500 - 650 nm range [161]. As well as carotenoids, cyanobacteria and red algae also have an abundance of phycobilins, absorbing strongly between 550 - 650 nm, also covering the green gap [162]. The use of these alternative pigments to chlorophyll/carotenoid allows these deep-water organisms to broaden their light-harvesting abilities because it would be extremely limiting if they could only absorb photons below 500 nm.

As discussed, fluorophores absorb light at a specific wavelength and re-emit the light with reduced energy at a longer wavelength, characterised by their absorption and fluorescence emission spectra. Energy can be transferred from a synthetic fluorophore to a light-harvesting protein via FRET to fill gaps in the absorption spectra, thus increasing the absorption cross-section of the photosynthetic protein [129, 163–165]. The first

instance of artificially filling the green gap of LHCII was completed by Gundlach *et al.*, where site-specific covalent attachment of Rhodamine Red dyes to LHCII was achieved by crosslinking a maleimide derivative of the dye to a reactive cysteine residue of the protein [129]. The majority of the Rhodamine Red excitation energy was transferred to the chlorophylls when attaching a single Rhodamine Red dye, supported by an almost 100% quenching of the donor fluorescence intensity and an increase in LHCII fluorescence intensity. Covalently attaching three Rhodamine Red dyes further increased the absorption of LHCII by enhancing the 573 nm absorption peak of the dye, leading to a two-fold increase in LHCII fluorescence, thus partially filling the green gap of LHCII (Figure 1.15 A). One limitation of this research was that covalently attaching fluorophores to modified proteins is intensive (requires specific genetics for each protein), and it may be uneconomical to replicate on a sizeable scale. Recently, a modular approach has been developed by Hancock *et al.* where model lipid membranes have been used to provide a stable environment for energy transfer while controlling the concentrations of incorporated lipid-linked Texas Red dyes and plant LHCII (Figure 1.15 B-E). A 94% energy transfer efficiency was achieved with a three-fold enhancement of LHC II fluorescence when exciting in the 'green gap', with the functionality being retained when deposited onto a surface as a thin film. Dyes have also been shown to be effective in enhancing the spectral range of bacterial light-harvesting complexes [125, 166], showing the flexibility of light-harvesting proteins in interacting with various chromophores to enhance the absorption cross-section. This research also shows that the use of lipids to stabilise light-harvesting proteins would be beneficial in retaining energy transfer efficiency and functionality when depositing bio-hybrid light-harvesting materials onto a surface.

One disadvantage of using fluorescent dyes is that the absorption maxima is relatively narrow and fixed, meaning the absorption band can only be altered by using different dyes. To address the limitation of the fixed absorption maxima, narrow spectral windows and lack of photostability when using fluorescent dyes, QDs have been investigated for use as artificial light antennas [126, 167, 168]. The transfer of energy from an artificial

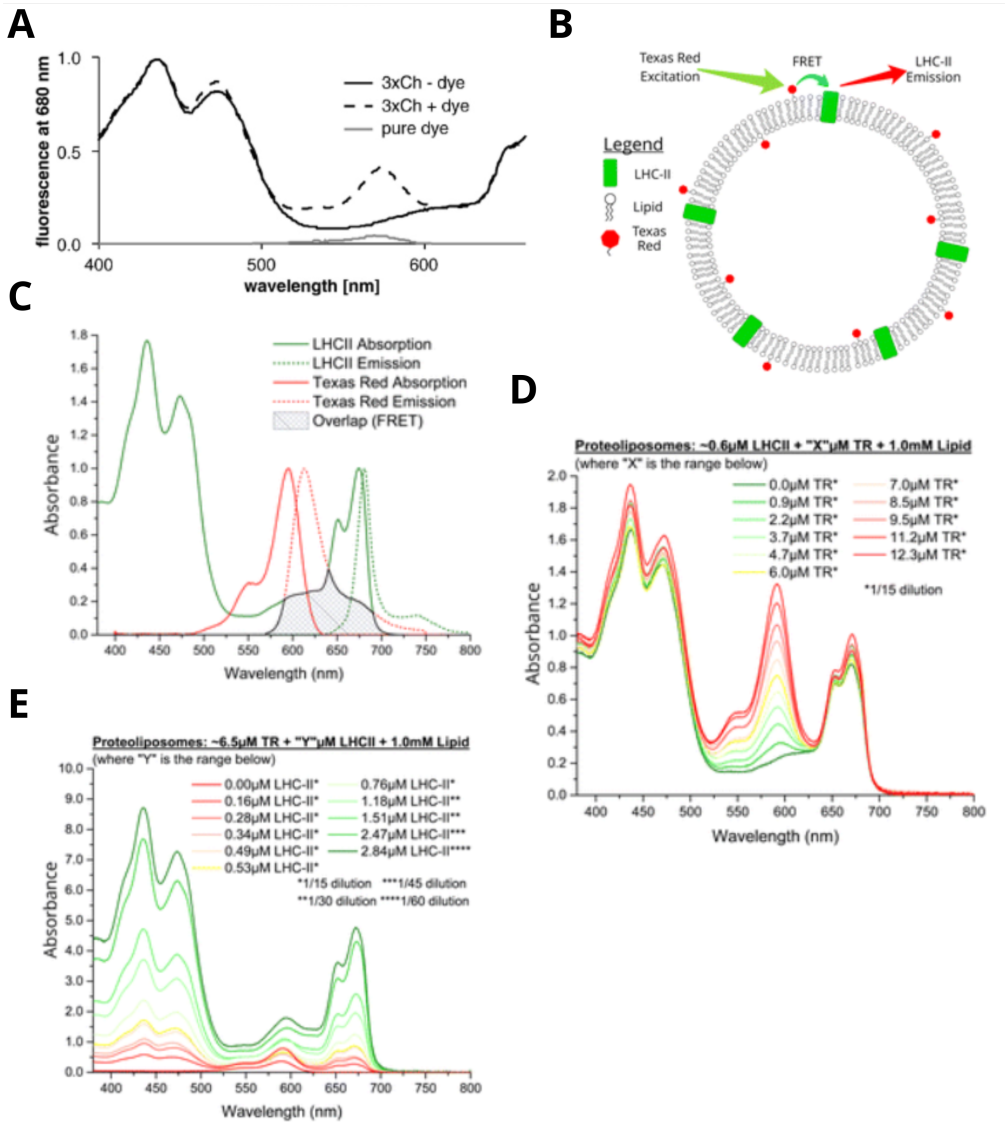

Figure 1.15: Example spectra and structures of bio-hybrid light-harvesting systems. (A) Selective LHCII fluorescence excitation spectra of isolated LHCII monomers (*solid black* line), isolated Rhodamine Red dye (*solid grey* line) and LHCII-Rhodamine Red complex (*dashed* line), adapted with permission from Gundlach *et al.* [129]. Copyright 2009 Elsevier B.V. (B) Schematic of proteoliposome concept with indicated energy transfer directions. (C) Absorbance (*solid* line) and fluorescence (*dotted* line) of LHCII (*green*) and Texas Red (*red*), showing overlap of the energy donor fluorescence and energy acceptor absorbance (grey). Ensemble spectra of proteoliposomes showing modular control of (D) Texas Red and (E) LHCII concentration. (B-E) adapted from Hancock *et al.* [120].

light antenna donor to a light-harvesting protein acceptor using QDs was first studied by Nabiev *et al.*, where Cd-based QDs were found to successfully transfer energy to coupled photosynthetic RCs via FRET [168]. The transfer of energy, evidenced by a reduction in the QD lifetime and an increase in the RC fluorescence, affirms the potential for QDs to be used as an energy donor as a replacement for fluorescent dyes. Lower-energy QDs are also efficient at accepting energy provided by a photosynthetic protein donor, as evidenced by Werwie *et al.*, where quenching of LHCII was observed when individually bound to CdTe QDs [167]. The photoluminescence of the QDs was further enhanced by attaching fluorescent dyes that absorb in the 'green gap' of LHCII, showing that both dyes and photosynthetic proteins could supplement QD absorption if the system is able to transfer energy downhill via FRET. Most recently, a three-part system of QDs, plant LHCII and bacterial RCs was combined to achieve downhill energy transfer [169], a progression of a simpler two-part system containing bacteria RCs and QDs [170]. LHCII was the energy donor, with the energy transferred either to the RCs directly, or indirectly via the CdTe QD, with both proteins genetically modified with histidine tags to bind to the QDs to link all three components together. Similarly to initial studies using dyes, the issue of uneconomical genetic modification to covalently attach QDs and proteins is still present. If the incorporation of QDs with lipids could be achieved within an artificial bio-membrane environment to create a modular system, or if QDs could be covalently attached to light-harvesting proteins without genetic modification, then the barrier of intensive bioconjugate attachment could be overcome.

1.6.3 Potential Methods of Protein-Nanoparticle Stabilisation

A modular, lipid-stabilised system would provide a stable environment for controlled energy transfer, while also allowing a greater understanding of the fundamental underlying photophysical processes involved [120, 171]. The inclusion of a lipid also introduces the potential of self-assembly, bypassing the need for genetically modified proteins in order to achieve bioconjugate energy transfer.

Hydrophobic CdSe QDs have been successfully incorporated into a liposome with the photosynthetic RCs isolated from *Rhodobacter sphaeroides* using a developed 'micelle-to-vesicle transition' (MVT) method [126]. The MVT method involves removing detergent from phospholipid-containing mixed micelles, inducing liposome formation. The initial stabilising ligands on the CdSe/ZnS QDs are triostylphosphine (TOP) and triostylphosphine oxide (TOPO), with the TOPO surface capping replaced by alkyl thiols to increase hydrophobic interlocking and interdigitation between the QD shells and the hydrophobic tails of the ligand. The QDs were then dispersed in water with the desired phospholipids to create micelles by means of a detergent solution (Figure 1.16 A) before QD-liposomes were assembled by removing detergent molecules via size exclusion chromatography (SEC). To assemble QD-RC liposomes, a detergent-stabilised stock RC solution was added to the micellar solution and then shaken vigorously. Above a certain QD concentration, it was unfavourable for liposomes to form and more favourable for QDs to cluster, potentially allowing manipulation of the resulting structure through alteration of the QD concentration. Unfortunately, no energy transfer was observed between QDs and RCs at the maximum QD concentration, suggesting the bilayer was sparsely packed with QDs that did not lie within the critical distance from the RC for FRET to occur. If a sufficient concentration of QDs cannot be packed into the bilayer without collapsing the liposome, bilayer incorporation of QDs may not provide a pathway for progression.

In a separate study, $CuInS_2$/ZnS QDs were successfully incorporated into the lipid bilayer by Tanaka *et al.* [127], where QDs were embedded inside nanotubules formed from liposomes. The method involved the direct re-hydration of dried-down lipids and QDs into an aqueous buffer. A short nonanethiol ($C_9H_{20}S$) ligand was used when synthesising the $CuInS_2$/ZnS QDs to reduce the nanoparticle diameter to 4.1 nm, a reduction of 0.6 nm compared to syntheses using dodecanethiol ($C_{12}H_{26}S$). The incorporation of larger QDs (>6 nm) was unsuccessful, suggesting the nonanethiol stabilising ligand may be beneficial in decreasing the QD size for bilayer insertion. This study focused on lipid and QD assembly, and did not attempt to incorporate photosynthetic proteins. The

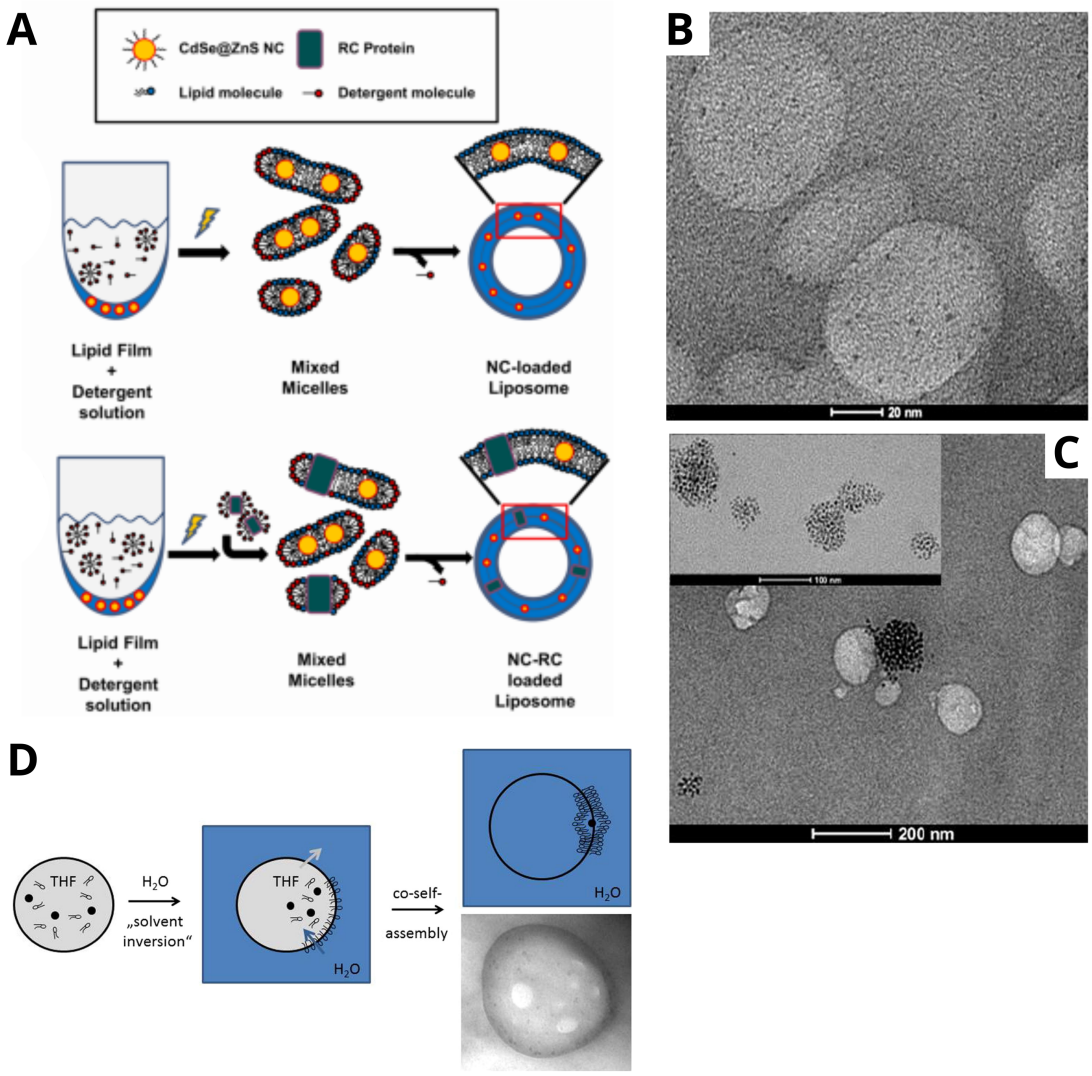

Figure 1.16: Schematics and images showing lipid association with QDs. (A) Schematic of the micelle-to-vesicle transition method. Detergent is added to a dried film of QDs and lipids (top) or QDs, RCs and lipids (bottom) to form mixed micelles, with QD-liposomes (top) or QD-RC-liposomes (bottom) formed as the detergent is removed. Adapted with permission from De Leo *et al.* [126]. Copyright 2014 American Chemical Society. (B) TEM image of 4.5 nm nanoparticles incorporated into POPC liposomes. (C) TEM image of lipid assembly using 8.3 nm nanoparticles, which yielded unloaded lipid vesicles co-existing with nanoparticle-loaded lipid droplets. (D) Schematic for co-solvent removal method used to incorporate nanoparticles into liposomes. A co-solvent of THF and water was formed, with liposomes self-assembling at the solvent-water interface as the solvent is evaporated. (B-D) adapted with permission from Bixner and Reimhult [128]. Copyright 2015 Elsevier Inc.

QD-liposome stability degrades significantly over a period of days, and it is also unclear whether the QDs were located inside the bilayer or tagged to the outside, which is a concern when accounting for the QD being located within the Förster radius of a photosynthetic protein that must be embedded within the lipid bilayer. This may also explain the poor stability observed. Finally, an alternate method has been successful in incorporating a different type of nanoparticle (iron oxide) into a lipid bilayer (Figure 1.16 B-D); a dried lipid-nanoparticle mixture was dissolved in tetrahydrofuran (THF) then added dropwise to a buffer, forming liposomes as the THF is evaporated under nitrogen over a 24 hour period [128]. While QDs were not used for incorporation, this 'co-solvent removal' method could be applied to QDs if colloidally stable in THF.

To summarise, the three aforementioned bilayer incorporation methods do not provide evidence of a high bilayer uptake of nanoparticles, and the quantity of QDs required for optimal energy transfer within the bilayer remains uncertain. One theoretical way to circumvent the need for QD incorporation into lipid bilayers would be to take advantage of the high number of amino acids present in the N-terminal of LHCII [172, 172–176], the site of chemical modification and attachment of histidine tags from the previous studies discussed [129, 167, 168]. The N-terminal is universally present in all proteins and provides a site of a free-amine group that is usually exposed and accessible [177]. A zero-length chain crosslinker, such as EDC/sulfo-NHS, would allow direct binding of hydrophilic QDs with a carboxyl surface chemistry and LHCII through the formation of N-substituted carbodiimides [178, 179]. The LHCII could then be incorporated into the native bilayer environment of a liposome, while the hydrophilic QDs remain stable in the aqueous environment surrounding the newly-formed proteoliposome while covalently attached to the LHCII. The use of a zero-length chain crosslinker and a short-chain stabilising ligand on the QD would mean the crosslinked QD and LHCII lie within the critical distance for energy transfer, thus successfully filling the 'green gap' of LHCII and increasing the cross-sectional absorbance of the photosynthetic protein.

Chapter 2

Experimental Procedures and Theory

2.1 $CuInS_2$/ZnS Quantum Dot Synthesis

The $CuInS_2$/ZnS synthesis was adapted from a solvothermal method in octadecene (ODE) [99, 102], developed within the group. The synthesis consists of three stages; the initial $CuInS_2$ core growth, the addition of a ZnS shell, and finally the cleaning and storage of the $CuInS_2$/ZnS QDs.

2.1.1 Materials

Indium(III) acetate (99.99%), copper(I) iodide (99.999%), octanethiol (≥98%, nonanethiol (≥95%), 9-mercapto-1-nonanol (nonanol, ≥95%), dodecanethiol (DDT, ≥98%), zinc stearate (90%) and octadecene (ODE, 90%) were purchased from Sigma Aldrich.

2.1.2 $CuInS_2$ Core Growth

The chemical synthesis of QDs is a long multi-step procedure and an overview of the stages involved in shown in the flow chart in Figure 2.1. Each stage is described in detail below.

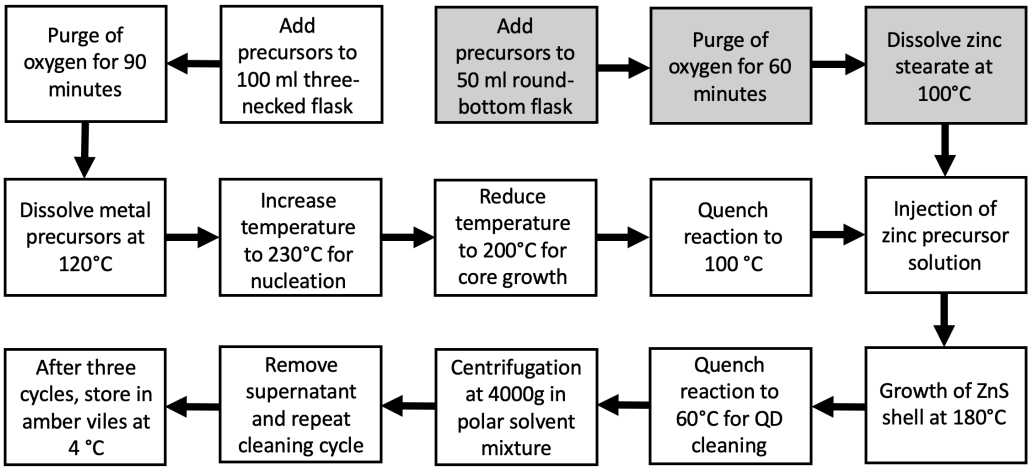

Figure 2.1: Flow chart detailing the $CuInS_2$/ZnS synthesis procedure. The white boxes represent the quantum dot core synthesis procedure and the grey boxes represent the simultaneous shell-growth preparation until injection of the zinc precursor solution.

Although many copper and indium precursors are compatible with this solvothermal method, indium (III) acetate and copper (I) iodide were specifically chosen for their demonstrated solubility and reactivity [180]. Typically, 0.25 mol (47.5 mg) of copper iodide and 0.25 mol (73.0 mg) of indium acetate were added to a 100 mL three-necked flask with 6 mL of octadecene (ODE) and a 4 mL molar excess of thiolate ligand. The thiolate ligand is added in a vast molar excess to the copper iodide and indium acetate precursors to provide a source of sulfur as well as the stabilising ligands for the resulting $CuInS_2$/ZnS QDs. Acting as the reaction solvent, the large molar excess provided promotes good colloidal stability through a complete surface ligand coverage [68, 69]. The introduction of a high-boiling point solvent, such as ODE, increases solubility and the speed of monomer production during the dissolution of metal precursors. The choice of solvent is also crucial to the final crystal structure of the $CuInS_2$ QDs, with ODE coordinating the formation of a tetrahedral zinc-blend phase and the presence of oleylamine (OLA) or trioctylphosphine oxide (TOPO) contributing to the formation of spherical wurtzite $CuInS_2$ QDs [180, 181]. A final volume of 10 mL was chosen to allow sufficient submersion of the temperature probe for an accurate temperature reading. The

flask was then attached to a condenser reflux column (Figure 2.2) inside a fume hood to mitigate any risks arising from elevated temperature and the release of potentially-toxic gases. The mixture was degassed with argon gas and stirred at room temperature under a protective atmosphere for 90 minutes to remove oxygen from the system and prevent the formation of oxygen-sulfur antisite defects.

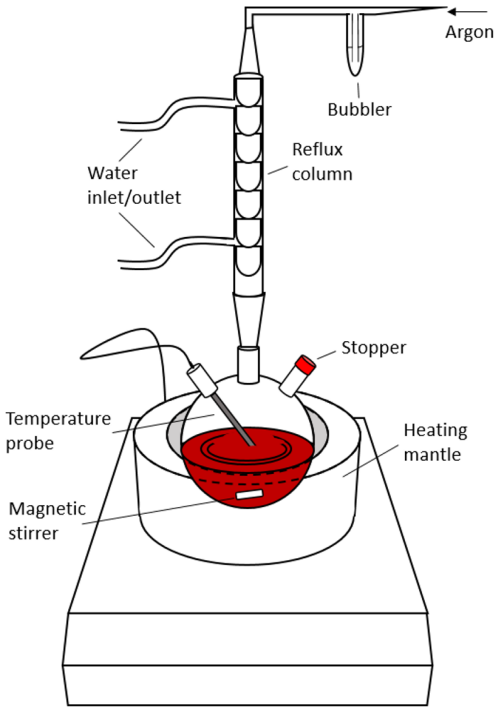

Figure 2.2: Apparatus schematic for solvothermal synthesis of $CuInS_2$/ZnS quantum dots.

After purging the system of oxygen, the temperature was raised to 120 °C for 30 minutes to dissolve the powder metal precursors and form metal-thiolate complexes [180], which act as the monomers for nucleation. Once dissolved, the solution changes from a cloudy to a clear yellow colour. The temperature can be increased slowly to 150 °C to maximise the fraction of reagents forming monomers before nucleation occurs. Once a high concentration of metal-thiolate complexes is present and the solution is perfectly clear, the temperature was increased above 230 °C to start nucleation of the nanoparticles, indicated by an almost instantaneous colour change from yellow to red. Following nu-

cleation, the temperature was lowered to 200 °C for the growth phase, with a blood-red colour change indicative of reduced confinement and the formation of nucleation sites. During the growth phase, the absorption band is red-shifted towards that of the bulk material, confirming an increase in nanocrystal size. After a predetermined seeding time, relative to the fluorescence emission peak of the cores, the flask was submerged in an ice-water bath to arrest core growth. An ice-water bath was used to rapidly quench the reaction as a slow cooling process is detrimental to the size-dispersion of the QDs. When a ZnS shell was desired, the $CuInS_2$ QD cores were quenched and then returned to the heating mantle at a temperature of 100 °C (this low temperature ensures no further core growth), with the synthesis proceeding as described in the next section.

2.1.3 ZnS Shell Growth

For the growth of a ZnS shell, 0.5 mol (307mg) zinc stearate was added to 2 ml ODE and 2 ml nonanethiol in a 50 mL flask and flushed with argon for 60 minutes. A molar excess of the thiolated ligand is again used to provide a source of sulfur as well as the stabilising ligand for the $CuInS_2$/ZnS QDs. The mixture was then heated to 100 °C under continuous stirring for 30 minutes to dissolve the zinc stearate powder, with the ZnS precursor then injected into the $CuInS_2$ QD core solution, still at 100 °C. The combined solution was refluxed at 180 °C for 1 hour, at which point the reaction was rapidly quenched in an ice-water bath to arrest shell growth. Finally, the QD solution was extracted from the flask and transferred to a 60 °C water bath in preparation for cleaning.

2.1.4 $CuInS_2$/ZnS Cleaning

To clean the newly synthesised $CuInS_2$/ZnS QDs and remove excess precursor, the unrefined solution was diluted tenfold in a 10:5:1 acetone:methanol:chloroform polar mixture to promote precipitation of the QDs. The polar QD mixture was centrifuged at 4000 g for 15 minutes at 30 °C, with the supernatant discarded and the resulting pellet re-suspended in a minimal amount of chloroform. 20 ml of acetone and 10 ml methanol (or enough to

maintain the 10:5:1 acetone:methanol:chloroform ratio) were added and the centrifugation process was repeated a further two times, with the final pellet re-suspended in 20 ml of chloroform and stored in a protective amber glass vial. Alternatively, other ratios of organic solvents were trialled for their ability to precipitate QDs (as stated in Chapter 3).

2.2 Formation of $CuInS_2$/ZnS Quantum Dot Nanoclusters

Three different techniques were trialled in an attempt to control the clustering of hydrophobic $CuInS_2$/ZnS QDs through lipid stabilisation. A mixed thin film of lipid and $CuInS_2$/ZnS QDs at various lipid:QD mol/mol ratios were required for all methods, obtained by drying under nitrogen flow.

2.2.1 Materials

4-(1,1,3,3-Tetramethylbutyl)phenyl-polyethylene glycol (Triton X-100), n-dodecyl α-D-maltoside (α-DDM), n-octyl-β-d-glucoside (OG) and n-nonyl-β-D-glucoside (NG) were purchased from Generon. 1,2-dioleoyl-sn-glycero-3-phosphocholine (DOPC) and 1,2-dioleoyl-sn-glycero-3-phospho-L-serine (DOPS) were purchased from Avanti Polar Lipids as lyophilised solids. Texas Red 1,2-dihexadecanoyl-sn-glycero-3-phosphoethanolamine (TR-DHPE) was purchased as a solid from Life Technologies. Methyl acetate ($\geq$99%) and butanone ($\geq$99%) were purchased from Fischer Scientific (UK). Tetrahydrofuran (THF, $\geq$99.5%) and 4-(2-Hydroxyethyl)piperazine-1-ethanesulfonic acid (HEPES, $\geq$99.5%) were purchased from Sigma Aldrich.

2.2.2 Aqueous Buffer Preparation

All buffers were prepared as stock solutions, typically 1 M, by weighing solids to $\pm$1 mg accuracy and dissolving in ultrapure water. All water used was deionised and filtered by a milli-Q water purification system. Buffers were purified through 0.22 µm syringe filters (Millipore) before use and typically stored at 4 °C. pH buffers were prepared to

be within 0.1 of the intended final pH by the dropwise addition of 1-10 M hydrochloric acid or sodium hydroxide.

2.2.3 Preparation of QD-Lipid Thin Film Aliquots

DOPC was suspended in chloroform to give a 20 mg/ml solution, and then the desired ratio of $CuInS_2$/ZnS QDs (in chloroform) was then added to the aliquots in pre-determined volumes calculated from the stock optical density (OD) and molar absorption coefficient calculated from the fluorescence emission peak. 1.75 ml screw-top glass vials (SLS) were used for aliquot preparation and subsequent hydration for all methods of generating lipid-QD assemblies unless stated. The aliquots were vortexed (15 seconds) multiple times to disperse and mix before drying. If the stability of the lipids was to be monitored, 0.5% w/w Texas Red/BODIPY/NBD dye was added. BODIPY or NBD was used alongside the QDs in the place of Texas Red to circumvent an overlap of fluorescence emission peaks.

To dry, the mixture of lipids and QDs in chloroform was placed under a gentle flow of dry nitrogen gas for 20 minutes before the flow rate was increased. After 20 minutes of chloroform evaporation under the strong nitrogen flow, the vials of mixed lipids and $CuInS_2$/ZnS QDs were placed inside a desiccator under foil at room temperature to remove any residual traces of chloroform. The samples were stored under foil to protect the $CuInS_2$/ZnS QDs and fluorescent dyes from photobleaching. After $\sim$6 hours, the mixed thin films were ready to be used or were stored at -80 °C under argon gas until use.

2.2.4 Method 1 for Generating Lipid-QD Assemblies: Buffer Hydration of Thin Film

The buffer hydration method used probe sonication to provide the energy needed to break down multilamellar vesicle (MLV) aggregates into unilamellar structures. The mixed film of QDs and lipids should disperse upon hydration with buffer, with low

concentrations of QDs theoretically being incorporated in the bilayers of multilamellar aggregates. It was hoped that controlled QD-nanoclusters would form by increasing QD concentration, with the QDs encapsulated by the lipid once broken down.

Aliquots of DOPC and $CuInS_2$/ZnS thin film were hydrated with 1 ml of 50 mM HEPES buffer (pH 7.5) then bath sonicated (10 minutes) and vortexed (30 seconds) to disperse the QDs and form MLV aggregates. The bath sonication and vortex technique was repeated a further three times before the sample was transferred to a temperature-controlled hollow glass container maintained at 4°C to prevent sample evaporation during probe sonication. The sample was subject to a continuous 15-minute probe sonication, sufficient enough to break down MLVs into lipid-stabilised QD nanoclusters.

During probe sonication, microscale fragments of the titanium tip were expected to detach and enter the sample. These impurities needed to be removed as they could interfere with spectroscopy measurements, thus the sample was transferred to a 1.5 ml microcentrifuge tube and span at 4000 g to remove large aggregates. 900 μl of the sample was extracted (the supernatant), with the remaining 10% containing the titanium fragments (in a pellet). The resulting samples were characterised immediately after centrifugation, and stored in the dark at 4°C when not in use.

2.2.5 Method 2 for Generating Lipid-QD Assemblies: Cosolvent Removal by Rotary Evaporation

The cosolvent removal method attempts to achieve controlled QD clustering via solvent removal and is based on a method previously used by Bixner and Reimhult [128] where the nanoparticle concentration was increased to promote micelle formation. During rotary evaporation, the chosen solvent should act as a cosolvent scaffold for the lipids and QDs, increasing the solubility before the lipid-stabilised QDs are forced into their final assembly as the solvent is removed.

Aliquots of dried lipid and $CuInS_2$/ZnS QD thin film were solubilised in 1 ml of the desired solvent and briefly bath sonicated/vortexed until the sample was dispersed (to the extent it was possible). The solution was then added dropwise to 10 ml of 50 mM HEPES buffer (pH 7.5) in a 20 ml glass vial under constant stirring (magnetic stir bar rotation at 100 rpm). The mass of the sample was measured to monitor solvent loss after removal, then transferred to a 50 ml 19/26 mm neck round-bottom flask. The flask was then attached to a rotary evaporator, suspended in a water bath set at 60 °C with the cooling water temperature inside the condenser set to 20 °C. The pressure inside the flask was reduced to lower the boiling point of the solvent to 40 °C, and the 50 ml flask was rotated at 200 rpm to increase the effective surface area. Once the solvent evaporates, it is captured by the condenser and collected in a receiving flask, with QD-nanoclusters expected to form in the liquid remaining in the flask as the cosolvent is removed and solubility decreases. The 50 ml flask with the sample was removed and weighed, allowing an estimation for the amount of evaporated solvent to be calculated (for successful removal this should equal or exceed the volume of the organic solvent in the original mix). QD-nanoclusters were characterised immediately after rotary evaporation, and stored in the dark at 4°C when not in use.

2.2.6 Method 3 for Generating Lipid-QD Assemblies: Detergent Encapsulation and Biobead Removal

The QD detergent encapsulation method is similar to methods used within the research group when incorporating LHC II into lipid bilayers to form proteoliposomes, with QDs replacing the protein. The samples were solubilised with a high concentration of detergent, then incubated with hydrophobic absorbent beads termed 'Biobeads' (SM-2 Resin, from Bio-Rad) which are established to remove detergent molecules selectively over lipids. This should allow QD-nanocluster formation via self-assembly as the detergent is removed.

To de-gas, 5g of Biobeads were added to a 20 ml amber vial with 10 ml of Milli-Q.

The amber vial was placed inside a Duran flask attached to a vacuum pump, with entrapped air being removed from the Biobeads using an ultrasonic bath. After 10 minutes the Biobeads solution was removed from the Duran flask, ready to use.

Aliquots of DOPC and $CuInS_2$/ZnS thin film were solubilised with 1 ml of 4% w/v detergent in 50 mM HEPES/100 mM NaCl (pH 7.5), then were bath sonicated (30 minutes) and vortexed (30 seconds) to disperse and form lipid-stabilised QD clusters. The bath sonication and vortex technique was repeated a further three times followed by probe sonication used to further break down the QD aggregates. The samples were subjected to twenty 5-second pulses of probe sonication before being transferred back to the vials. Samples were added to 1.5 ml microcentrifuge tubes containing the Biobeads, which were then placed in a pinwheel rotator to mix the solution during incubation. Four incubation cycles with increasing quantities of Biobeads (100 mg/ml, 200 mg/ml, 400 mg/ml and 400 mg/ml) for 45 min, 45 min, 45 min and ~16 hours, respectively, were used to remove the detergent and promote self-assembly. QD-liposomes were characterised immediately after the final biobead incubation, and stored in the dark at 4°C when not in use.

2.3 CdTe/CdS Quantum Dot Synthesis

The synthesis method of hydrophilic thioglycolic acid (TGA)-stabilised CdTe/CdS core/shell QDs was based on a method from within the group, adapted from literature methods [182, 183].

2.3.1 Materials

Thioglycolic acid (≥99%) and cadmium perchlorate hydrate (99.9%) was purchased from Merck. Sodium hydroxide (≥98%), propan-2-ol (≥99%) and thiourea (≥99%) was purchased from Sigma-Aldrich. Aluminium telluride was provided by ABSCO Limited and stored under N_2 atmosphere. Sulfuric acid (≥98%) was purchased from Fisher Scientific.

All aqueous solutions were prepared with MilliQ-grade ultrapure water.

2.3.2 CdTe Core Growth

Typically, 0.985 g cadmium chlorate hexahydrate was dissolved in 100 ml ultrapure water at a 50 mM concentration. 400 µl TGA was added under stirring to obtain a TGA:Cd^{2+} ratio of 1:4, turning the solution turbid via the formation of insoluble Cd^{2+}-TGA complexes. Aqueous sodium hydroxide (NaOH) at a concentration of 1 M was added dropwise to raise the pH to 11.2, allowing deprotonation of the TGA, therefore, promoting solubilisation of the Cd^{2+}-thiolate complexes, forming a clear and colourless solution. The solution was then added to a three-necked flask which was attached to a condenser reflux column inside a fume hood, before being degassed with nitrogen gas and stirred at room temperature under a protective atmosphere to prevent oxidation and the formation of poor-quality QDs. Lumps of aluminium telluride (Al_2Te_3) weighing 0.2 g were added to a separate flask, which was then connected to the same argon supply to remove any oxygen present. After 60 minutes of purging the system of oxygen, 20 ml of degassed 0.5 M sulphuric acid (H_2SO_4) was injected into the Al_2Te_3 lumps to produce H_2Te gas, which passes through the cadmium precursor solution with the flow of nitrogen.

The formation of CdTe nanocrystal seeds is indicated by a colour change to a deep red colour, with the H_2Te gas flow being stopped after a period of two minutes. The amount of tellurium that gets dissolved in the solution is difficult to control and is dependent on the rate of nitrogen flow and observation of a colour change of the solution, therefore a cadmium excess is present which limits the QD size. The CdTe seeds were grown into QDs by heating and stirring under reflux at 100 °C, with a nitrogen atmosphere achieved at positive pressure evidenced via an oil bubbler. As the QDs grow, the fluorescence transitions from a 520 nm emission (green) after 2 minutes to a 650 nm emission (red) over a period of days. Figure 2.4 shows the colour of the CdTe cores upon excitation of a UV-A 365 nm wavelength UV torch, used to monitor the reaction. The reaction was stopped once cores had grown to the desired size by submerging the flask

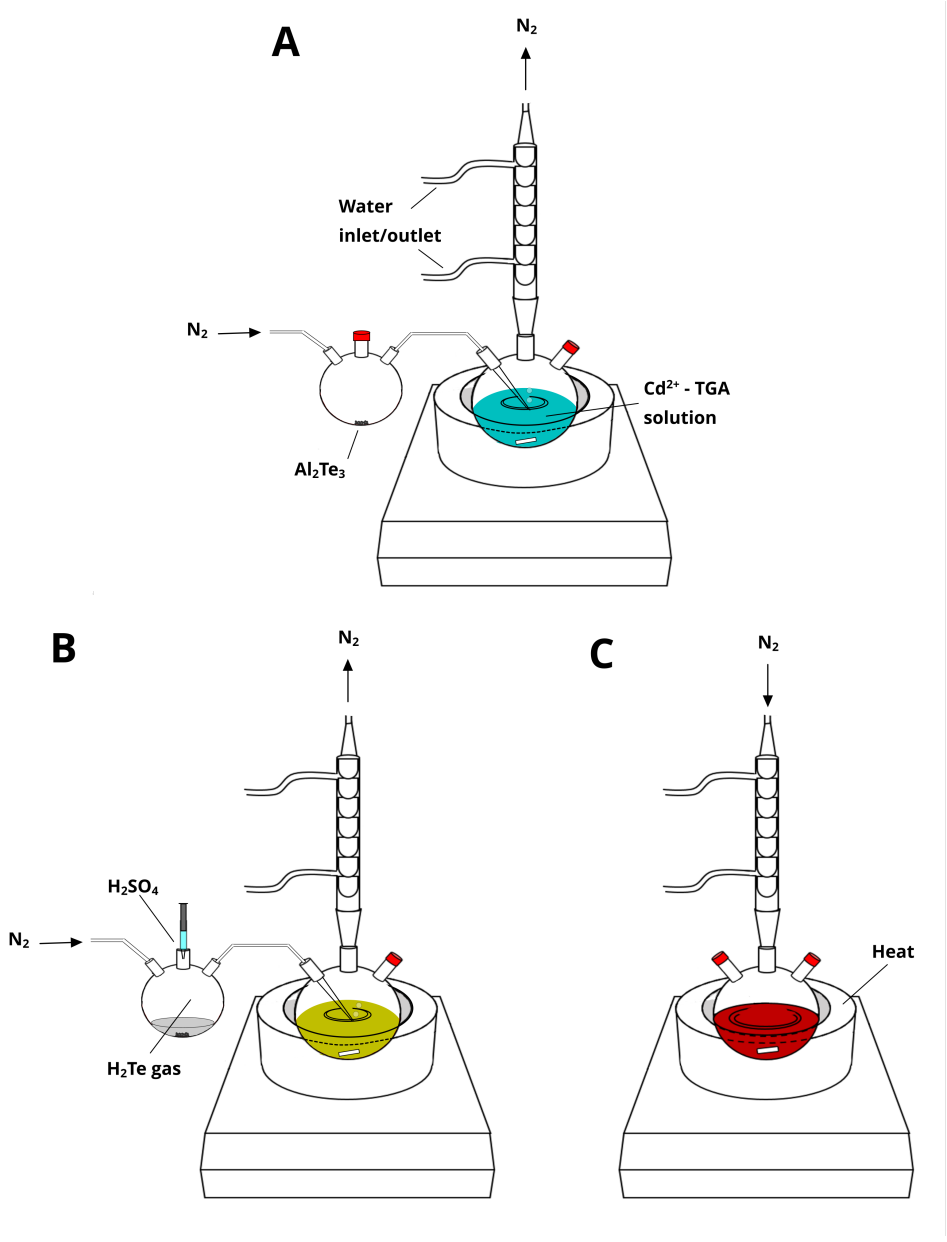

Figure 2.3: Apparatus schematic for the aqueous synthesis of CdTe quantum dots. (A) The solution is degassed using nitrogen. (B) H_2SO_4 is injected into the flask containing the lumps of Al_2Te_3, with the evolved H_2Te gas bubbled through the Cd^{2+} - TGA solution to form CdTe complexes. (C) The resulting precursor solution is heated to 100 °C under reflux, promoting CdTe QD nucleation and growth.

in a room-temperature water bath to arrest core growth.

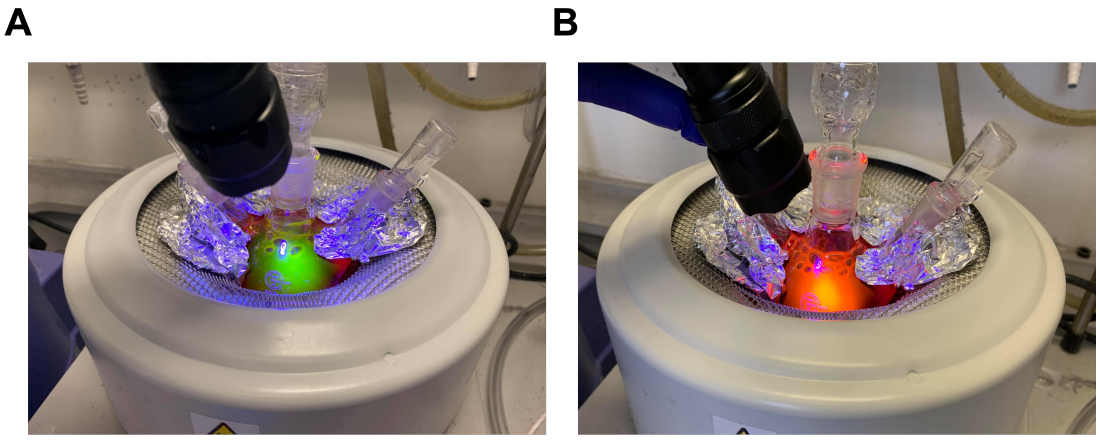

Figure 2.4: Photographs of the CdTe synthesis at various reflux times. Image of the CdTe core growth after (A) 2 minutes of seeding and (B) 18 hours of seeding. The QDs are excited with a 365 nm UV torch used to monitor the reaction.

2.3.3 CdS Shell Growth

The excess Cd^{2+}-thiolate complexes from CdTe core growth are utilised to grow a CdS shell, forming CdTe/CdS core/shell QDs. 200 mg thiourea was dissolved in 2 ml of ultrapure water, then added to the CdTe QD solution in enough volume to achieve a rough Cd:S ratio of between 1 - 3. The pH was then raised to 11.2 to ensure solubility of the excess Cd precursor before the temperature was raised to 100 °C. Shell growth was completed under reflux for 60 minutes before quenching the reaction in a room-temperature water bath to arrest growth. The QD solution was stored as-synthesised at 4°C until use.

2.3.4 CdTe/CdS Cleaning

The CdTe/CdS QDs are very stable in the unrefined solution, although this contains unreacted precursor materials and byproducts, as well as a high salt concentration, so QDs need to be purified before use. The QDs were cleaned by centrifugation and precipitation using propan-2-ol (IPA), which served as a solvent that promoted aggregation and precipitation of the QDs through instability and also dissolved byproducts of the

reaction. The QD solution became immediately cloudy upon the addition of IPA at a 2:1 ratio of IPA to unrefined QD solution, at which stage the QDs were microcentrifuged at 5000 g for 5 minutes to obtain a pellet. The supernatant was then removed and the QDs were re-suspended in the same volume of ultrapure water as the starting volume, where the QDs remain completely stable for a minimum of 3-4 days. QDs were cleaned as needed, with typical QD volumes between 150 - 450 µl, and were immediately used within hours.

2.4 Protein Biochemistry

2.4.1 Materials

Spinach leaves were purchased from the local supermarket. n-dodecyl α-D-maltoside (α-DDM, $\geq$99%) was purchased from Generon.

2.4.2 LHCII Isolation and Purification

Trimeric LHCII complexes were biochemically purified directly from spinach leaves using a previously established procedure by Hancock *et al.* [120], adapted from the procedures of the Johnson group [184]. A brief description of the isolation procedure is as follows: spinach leaves were macerated using a blender, chloroplasts were osmotically lysed and then thylakoid membranes were solubilised with 0.5% α-DDM. Thylakoid membrane proteins were isolated using continuous sucrose density gradients in 20 mM HEPES (pH 7.5), 0.03% α-DDM (8-13% w/w sucrose) and ultracentrifuged at 100,000 g for 36 hr at 4°C. The dense green band of LHCII trimers was collected and concentrated using a 30 kDa Amicon Ultra centrifugal filter. LHCII trimers were further purified using high-resolution size exclusion chromatography using a 16/600 Superdex 200 prep grade column and an AKTA Prime FPLC system in the buffer 20 mM HEPES, 150 mM NaCl, 0.03% α-DDM (pH 7.5). Appropriate eluted fractions were pooled and concentrated. Finally, LHCII trimers were at a concentration of $\sim$100 nM, corresponding to an absorbance of $\sim$20 at 675 nm estimated by absorption spectroscopy, in a final buffer of

20 mM HEPES (pH 7.5) and estimated 0.3% α-DDM. SDS-PAGE and Native-PAGE confirmed protein purity and oligomerisation state. Purified LHCII trimers were stable at 4 °C for many months and were used as needed.

Note on contributions: All LHCII isolation, purification and characterisation was completed by Dr Ashley Hancock.

2.5 Self-Assembly of Quantum Dot/Protein Bioconjugates

To form QD/LHCII bioconjugates, a zero-length chain crosslinking method generally used to crosslink two proteins with available carboxyl and amine functional groups was modified for use with QDs (Figure 2.5). CdTe/CdS QDs with a TGA stabilising ligand were chosen as they would provide many carboxylic acid functional groups for carbodiimide crosslinking, where EDC and sulfo-NHS would allow binding to one of the ~100 amino acids located in the N-terminal of LHCII [172–176]. TGA is also a ligand with a small-length carbon chain, allowing optimal FRET between zero-length chain crosslinked QDs and proteins as the distance would lie well below the Förster radius at which energy transfer is 50% efficient. A schematic of the reaction is shown below (Figure 2.5).

2.5.1 Materials

1-ethyl-3-(3-dimethylaminopropyl)carbodiimide hydrochloride (EDC) and N-hydroxysulfosuccinimide (sulfo-NHS) were purchased from Thermo Fisher Scientific. CdTe/CdS QDs were prepared as described in Section 2.3. LHCII was prepared as described in Section 2.4.

2.5.2 Crosslinking CdTe/CdS QDs to LHCII

Typically, CdTe/CdS QDs were cleaned and suspended in ultrapure water, with the volume dependent on the desired sample concentration and quantity. Stocks of EDC and sulfo-NHS were prepared by hydrating 3.8 mg EDC in 1 ml ultrapure water at a

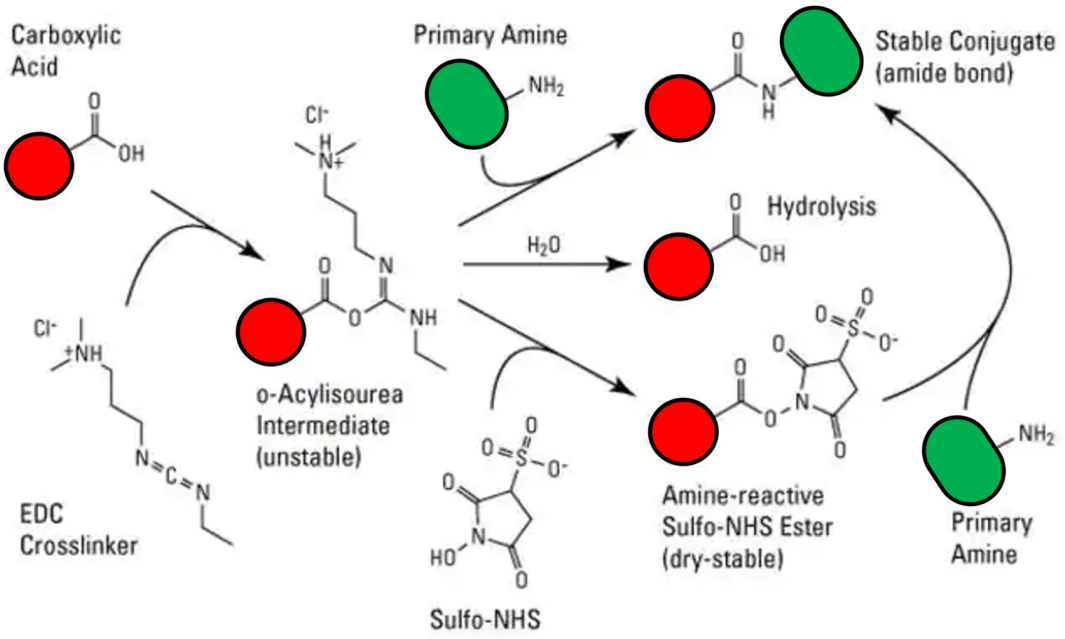

Figure 2.5: Schematic of EDC/Sulfo-NHS crosslinker chemistry. TGA-capped CdTe/CdS QDs are shown in red and plant LHCII is shown in green. Schematic adapted from Sulfo-NHS user guide [185].

concentration of 20 mM and 10.9 mg sulfo-NHS separately in 0.5 ml ultrapure water at a concentration of 50 mM. QDs, 50 µl EDC, 50 µl sulfo-NHS and ultrapure water were added to 100 µl concentrated (50 mM) 2-(N-morpholino)ethanesulfonic acid (MES) buffer at pH 6.0 in a 5 ml amber glass vial (Agilent) to give a final concentration of 0.5 µM QDs, 1mM EDC, 2.5 mM sulfo-NHS and 5 mM MES at a 1 ml volume. The excess of crosslinker is approximately $\times 10$ greater than the total number of available binding sites of the CdTe/CdS QDs, modified from a $\times 10$ excess of available carboxyl functional groups on the protein. The reactants were allowed to interact for 15 minutes under stirring, allowing the initial formation of unstable o-acylisourea intermediates at pH 6.0.

The pH was then raised to 7.5 by the addition of concentrated 50 mM HEPES buffer (pH 8.3) to allow the formation of semi-stable amine-reactive sulfo-NHS esters on the CdTe/CdS QDs, with LHCII in 0.1% α-DDM introduced at an equal concentration to

the QDs. The volume was increased to 2 ml with ultrapure water and 0.1% α-DDM detergent to stabilise the LHCII, with the bioconjugation taking place over a period of 2 hours under stirring. To quench the active NHS esters, 50 mM HEPBS (pH 9.0) was added to raise the pH of the crosslinking solution to pH 8.6. The NHS esters have a quenching half-life of 10 minutes at pH 8.6, therefore 99% of active esters will be quenched after a period of 67 minutes. Samples were diluted $\times 2$ in ultrapure water for characterisation.

2.5.3 De-salting Column Use

Before use, desalting columns were centrifuged at 1000g for 2 minutes to remove the storage solution, then 1 ml of ultrapure water was passed through the column before discarding to ensure full removal of the storage solution before the addition of the sample, as per the user guide [186]. Then 1 ml of sample (CdTe/CdS QDs or LHCII with 0.1% α-DDM) in ultrapure water was added to the desalting column before the sample was spun at 1000 g for 3 minutes, with the final sample retained in the collection tube for characterisation.

2.6 Optical Spectroscopy

This section describes the techniques and theory used to determine the absorbance, steady-state fluorescence and lifetime characteristics of investigated samples.

2.6.1 Absorption Spectroscopy

Ultra-violet/visible/near-infrared (UV-Vis-NIR) absorption spectroscopy is a steady-state technique used to measure how a sample absorbs light as a function of wavelength. Absorption spectroscopy can measure changes in a material's absorbance that arise due to differing photon absorption efficiencies with changing wavelength, common in systems such as light-harvesting proteins that consist of multiple chromophores. Absorption spectroscopy is also ideal for determining the optoelectronic properties of QDs, as many of

the electronic transitions lie within this energy range of the electromagnetic spectrum. Importantly, the measured absorbance absorption is a result of all excitation events and not just those resulting in radiative decay, unlike steady-state fluorescence spectroscopy. The concentration of a sample is proportional to the absorbance and can be determined if the molar absorption coefficient (constant conveying strength of light absorption for a particular substance at a particular wavelength) and path length are known. The molar concentration (C) can be determined from the Beer-Lambert law:

$$A = \varepsilon(\lambda) l C \tag{2.1}$$

where A is the sample absorbance, $\varepsilon(\lambda)$ is the molar absorption coefficient as a function of wavelength λ, and l is the optical path length of the sample during spectroscopy. The molar absorption coefficient of QDs is dependant on both the QD material and size and can be empirically estimated from steady-state fluorescence [102] and absorption spectroscopy measurements [101, 187].

A UV-Vis-NIR dual beam spectrometer uses a white light lamp to provide a range of controllable wavelengths for spectroscopy. A monochromator is used to separate the polychromatic white light using a series of concave mirrors and a diffraction grating, allowing the absorbance to be measured as a function of wavelength. The single beam of controlled light is divided into two using a beam-splitter before each beam heads through identical cuvettes to the photodetectors. One cuvette will contain the sample, with the other containing a 'blank' which holds the solvent or buffer the sample of interest is dispersed in. Through knowledge of the path length of the beam through the sample (typically 1 cm), the intensity of the absorbance can be measured by subtracting the intensity of light transmitted through the blank from the intensity of light transmitted through the sample, giving an intensity difference representative of the amount of light absorbed by the sample at a given wavelength, independent of the solvent or buffer. The use of the dual beam function accounts for changes in absorption due to the fluctuations

in the intensity of the lamp and also negates any changes in the absorbance of the dispersion medium over the period of characterisation.

Cuvette-based absorption spectroscopy measurements were taken using an Agilent Technologies Cary 5000 UV-Vis-NIR absorption spectrophotometer. To reduce scattering when characterising lipid-stabilised QD-nanocluster samples, a Cary diffuse reflectance accessory (DRA) was used, otherwise known as an 'integrating sphere'. The integrating sphere is designed to collect reflected and transmitted radiation via a non-selective diffuse reflector, with an integrated signal then presented to the photodetector. Absorption measurements were performed using either a 10 × 10 mm quartz cuvette for QD characterisation in chloroform or a 10 × 10 mm plastic cuvette for QD-nanocluster and QD-protein bioconjugate characterisation in buffer. The samples were diluted to an absorbance of 0.1 at 400 nm to avoid inner filter effects before absorbance measurements were taken. Scans were completed within a 300 - 800 nm wavelength range with baseline correction completed using the base solvent/buffer.

2.6.2 Steady-State Fluorescence Spectroscopy

Steady-state fluorescence spectroscopy, also termed photoluminescence (PL) spectroscopy, is a technique used to measure the properties of fluorescence emission at a specific wavelength, following excitation at a different wavelength. In fluorescence spectroscopy, a white light lamp is used to provide a range of controllable wavelengths for spectroscopy, with an adjustable monochromator used to select a wavelength of excitation. The 'slit width' defines the range of wavelengths of the beam of light, and represents the physical opening of the slits within the monochromator, altering the intensity of light. A collimated beam of unpolarised light then passes through an iris that allows mediation of the beam intensity, exciting the sample continuously throughout the measurement. The emitted light is then collected at a 90° angle from the excitation beam, passing through a second adjustable monochromator that gives control of a second adjustable slit, allowing a defined range of wavelengths to reach the detector. The detector records the

fluorescence intensity of the defined excitation and emission wavelengths. To account for fluctuations in the excitation intensity, as well as wavelength-dependent intensity changes arising from an imperfect light source, a reference signal is measured directly from the excitation.

Typically, fluorescence scans can be obtained in two domains using a standard steady-state fluorescence spectrometer:

1) Fluorescence emission spectroscopy: the excitation wavelength is fixed by the first 'excitation' monochromator, while the emission intensity as a function of wavelength is measured through the scanning of the second 'emission' monochromator. The resulting spectrum is known as the 'emission spectrum'.

2) Fluorescence excitation spectroscopy: the emission intensity is collected at a set wavelength by use of the second 'emission' monochromator, while the excitation wavelength is varied. The resulting spectrum is known as the 'excitation spectrum'.

These can be combined to obtain a 2-D spectrum showing the fluorescence excitation vs. emission measurements, as utilised when investigating the optical properties of QD-nanoclusters in Chapter 5.

Cuvette-based steady-state fluorescence spectroscopy was performed using an Edinburgh Instruments FLS 980 spectrophotometer that was equipped with dual excitation monochromators and duel emission monochromators (Figure 2.6). Spectroscopy was performed using either a 10 × 10 mm quartz cuvette or a 10 × 10 mm plastic cuvette, as described previously. The sample of absorbance of 0.1 at 400 nm was transferred to FLS 980 immediately after absorption spectroscopy measurements. Samples were characterised at 20 °C using a thermoelectrically-cooled cuvette holder (Quantum

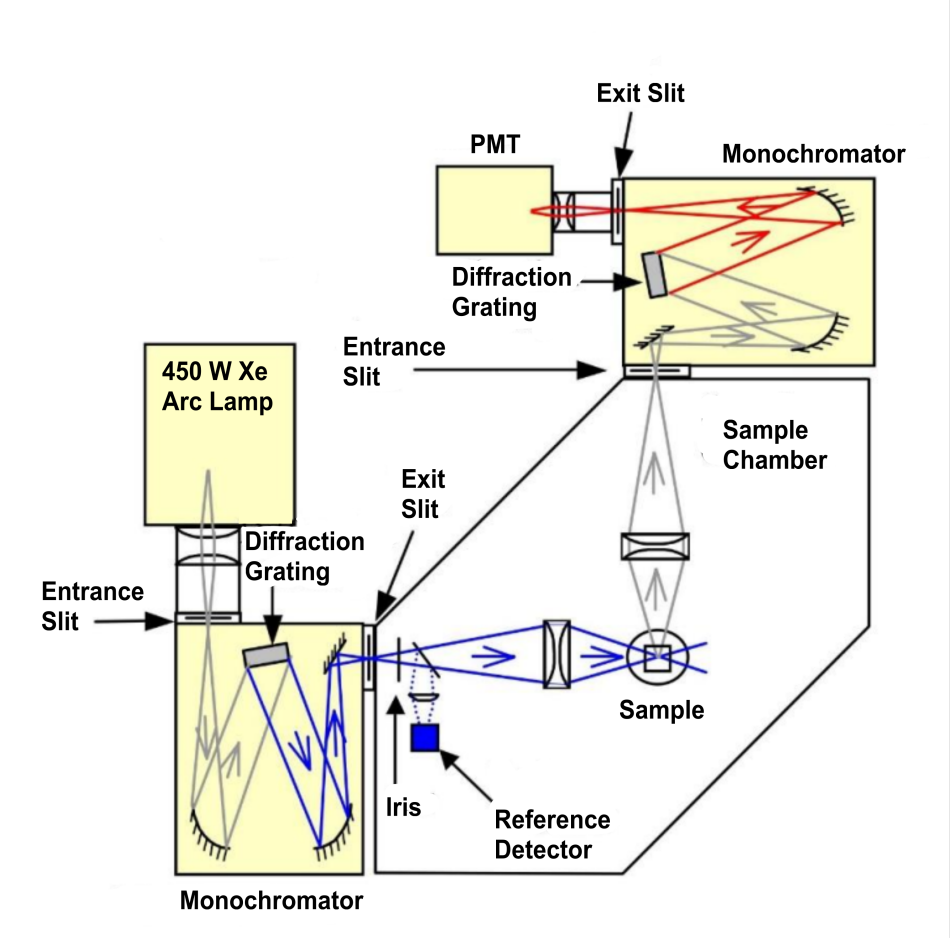

Figure 2.6: Schematic of the FLS980 Edinburgh fluorescence spectrometer. Adapted from the Edinburgh Instruments FLS980 fluorescence spectrophotometer manual.

Northwest TC 1 Temperature Controller). Excitation was achieved using a 450W Xenon arc lamp and detection using a red-sensitive photomultiplier tube module (Hamamatsu R928 PMT). Fluorescence emission scans were completed on the $CuInS_2$/ZnS QDs using a 500 nm excitation wavelength and collecting between 540 - 800 nm using a 2 nm bandwidth excitation slit and a 1 nm emission slit for the majority of measurements unless stated. The bandwidth of the excitation and emission slits were increased to 4 nm and 2 nm respectively for lipid-stabilised QD-nanocluster emission scans to provide a greater signal. Data acquisition parameters were 1 nm steps, integrating 0.1 s/step with five scans averaged to reduce noise.

2.6.3 Fluorescence Lifetime

The average lifetime of fluorescent samples such as light-harvesting proteins and QDs is determined using the time-correlated single photon counting (TCSPC) spectroscopic technique. High-frequency pulsed laser sources allow a cuvette-based sample to be excited with a short (∼100 ps) initial pulse at a defined wavelength, with photons recorded using a highly sensitive, time-accurate photomultiplier detector. The time between the initial pulse and the first detection of an emitted photon from the sample is recorded through a combination of the photomultiplier detector and fast electronics, for a large number of pulses, with a histogram built up with the respective decay times. The frequency of laser pulses can be altered and was typically chosen based on the type of sample, with the time between pulses set to allow decay from the excited state before a subsequent pulse is sent. The histogram will take the shape of an exponential decay, with the frequency density of each bin proportional to the probability of detecting the emission at the corresponding time after excitation. The most probable time of emission is immediately following excitation, as the maximum number of fluorophores will be in the excited state, and will therefore be most likely to fluoresce. The probability decreases with time as more excited states have depopulated, and will continue to do so.

Measurements were stopped when the largest histogram bin reaches a predetermined number of counts, decided by the user. The histogram plot can be described as a sum of exponential decays, with the number of time constants dependent on the fluorophore being measured:

$$I = \sum_i A_i e^{-\frac{t}{\tau_i}} \tag{2.2}$$

where I is the intensity, τ_i are the time constants with A_i being the associated amplitudes, and t is the time. The fluorescence lifetime of a sample represents the time required for the excited state population to decrease to $1/e$ of its maximal level and is a measure of the stability of the excited state under the conditions of characterisation. Known as the amplitude-weighted mean lifetime τ_{av}, it is calculated by averaging the

amplitude-weighted time constants from a multi-component fit. Each component usually represents a radiative decay pathway, but excited state dynamics are complex in ensemble QDs due to various factors such as polydispersity, therefore a sample of QDs may have a vast number of recombination processes with only the main pathways of decay identifiable.

Cuvette-based fluorescence lifetime measurements were performed using an Edinburgh Instruments FLS 980 spectrophotometer within a 10 × 10 mm quartz cuvette or 10 × 10 mm plastic cuvette. Samples were characterised at 20 °C using a thermoelectrically-cooled cuvette holder with magnetic stirring capabilities (Quantum Northwest TC 1 Temperature Controller) and were stirred during lifetime measurements to prevent photobleaching. Excitation was achieved using a 473 nm pulsed diode laser (Edinburgh Instruments EPL-475, pulse width ∼100 ps), with the frequency adjusted depending on the expected lifetime of the sample. A built-in neutral density (ND) filter wheel was applied to the pulsed laser, allowing excitation power to be set as desired. Finally, a high-speed red-sensitive photomultiplier tube module (Hamamatsu H10720-20 PMT) was used for detection. Decay curves were fitted using the accompanying software for the Edinburgh FLS 980. The instrument response function (IRF) was obtained by measuring scattered excitation light using a dilute solution of colloidal silica (LUDOX) with a width of ∼270 ps, which was fitted with obtained traces.

2.7 Particle Sizing

2.7.1 Dynamic Light Scattering

Dynamic light scattering (DLS) is a light scattering technique that uses a laser to measure the Brownian motion of nanoscale to microscale particles suspended in solution, allowing the hydrodynamic radius to be estimated. Brownian motion is the random movement of particles suspended in a solution due to collisions with other surrounding particles, and

can be determined from the following equation:

$$\bar{x^2} = 2Dt \tag{2.3}$$

where $\bar{x^2}$ is the mean squared displacement, D is the diffusivity and t is the time. The particle radius can be extracted from the diffusivity if the viscosity of the solute is known:

$$D = \frac{RT}{6\pi\eta r N_A} \tag{2.4}$$

where R is the universal gas constant (8.314 J mol^{-1} K^{-1}), T is the temperature, η is the viscosity of the solute, r is the particle radius, and N_A is Avogadro's number (6.022×10^{23} mol^{-1}).

Light from the laser is diffracted when passing through the sample and interacting with the particles, forming a speckle pattern which is measured by a charge-coupled device (CCD). This speckle pattern, which changes when particles diffuse through the sample, is measured at nanosecond intervals. The rate of change of the speckle pattern can be calculated by fitting the data to an autocorrelation function, which is a measure of the random movement of particles within the sample. This means the particle radius can be determined through the measurement of time-dependent fluctuations in scattered light intensity, with the rate of fluctuations relative to the rate of diffusion of a particle through the solvent. Smaller particles have a faster diffusion, therefore cause more rapid fluctuations in the scattered light intensity than larger particles. The second-order autocorrelation function generated from the recorded intensity trace is given by the following equation:

$$g^2(q;\tau) = \frac{\langle I(t)I(t+\tau)\rangle}{\langle I(t)\rangle^2} \tag{2.5}$$

where $g^2(q;\tau)$ is the second-order autocorrelation function at a given wave vector, q, and delay time, τ, with I representing the intensity. At short time intervals, the correlation is high as the particle is unable to diffuse a great distance. The correlation decays

exponentially at the time delays become longer, with no correlation between the initial and final intensity after long periods of time. The first-order correlation function can be related to the second using the Siegert equation:

$$g^2(q;\tau) = 1 + \beta[g^1(q;\tau)]^2 \tag{2.6}$$

where the first part of the sum relates to the baseline value and β is a correction factor that depends on the alignment of the laser beam within the setup. The first-order autocorrelation function can be treated as a single exponential decay for monodisperse populations but should be treated as a sum of exponential decays corresponding to each species for a polydisperse population.

DLS size distribution measurements on QD-nanoclusters were performed using a Malvern ZetaSizer Nano. QD-nanoclusters were suspended in HEPES buffer at low concentrations using an 80 µl disposable polystyrene cuvette (BRAND). Samples were irradiated by a 633 nm monochromatic HeNe laser, which is scattered in all directions from particles undergoing Brownian motion. The scattered light was recorded at a 173° backscatter angle, with at least three measurements taken for each sample to provide a size distribution and polydispersity index (PDI). All samples were characterised at 20 °C.

2.7.2 Transmission Electron Microscopy

Electron microscopy is a technique that uses electrons to illuminate a sample as opposed to photons, thus allowing imaging below the classical diffraction limit of optical microscopy. The diffraction limit of visible light, and therefore the best resolution of an optical microscope, is defined by the Abbe limit:

$$d = \frac{\lambda}{2n \sin\theta} \tag{2.7}$$

where d is the limit of resolution, λ is the wavelength of light, n is the refractive index of the medium, θ is half of the lens convergence angle and $n \sin \theta$ represents the numerical aperture. The highest theoretical resolution that can be achieved for visible light ($\lambda \sim 550$ nm) will be 275 nm, assuming the lens convergence angle was 180° and the numerical aperture of the lens, $n \sin \theta$, is 1.0. Most nanomaterials, including QDs and lipid-stabilised QD nanoclusters, have a size on the order of nanometres to tens of nanometres in diameter, therefore optical microscopes are clearly insufficient for resolving the size of these structures.

For massive particles, such as electrons, the de Broglie wavelength λ can be defined by the equation:

$$\lambda = \frac{h}{p} \tag{2.8}$$

where h is Planck's constant and p is the momentum of the particle. Electron microscopes benefit from a much shorter de Broglie wavelength from electrons as they are travelling with high momentum, theoretically allowing resolution on the picoscale. In reality, modern electron microscopes can achieve resolution with a diffraction limit of $\sim$ 1 Å due to the objective lens system. Electrons are emitted from an electron gun and are accelerated across a potential difference before being focused into a small, coherent beam using a condenser lens. Electron microscopes that can achieve a higher electron accelerating voltage able to obtain a higher resolution. The beam then hits the specimen, where electrons will either scatter upon interaction with a dense medium, such as an atomic nucleus or will be transmitted through the sample. The transmitted electrons are then focused through an objective lens onto a CCD, where an image is generated based on the transmitted electron intensity, which will be lower where scattering has occurred.

Initial TEM measurements of lipid-stabilised QD nanoclusters were taken on an FEI Technai 12 microscope with a 120 keV accelerating voltage, a Lanthanum Hexaboride

(LaB6) filament and Gatan UltraScan 4000 CCD camera. Samples were prepared as described in Chapter 2.2.6 and were diluted ×100 in 50 mM HEPES (pH 7.5) 100 mM NaCl for deposition on carbon-coated TEM grids (made at the University of Leeds Astbury Centre EM Facility). Grids were glow-discharged to remove hydrocarbon contaminations that may cause accumulation of charge, then 5 µl of the sample was deposited onto the grid and incubated for 1 minute. Samples were washed using 50 mM HEPES (pH 7.5) 100 mM NaCl, wicking-off excess sample and buffer with filter paper before air-drying at room temperature. Size analysis was completed using ImageJ analysis software (v.2.9.0, open source).

To obtain higher-resolution images of colloidal $CuInS_2$/ZnS QDs and lipid-stabilised QD nanoclusters, TEM measurements were taken on an FEI Titan3 Themis 300 microscope with a 300 keV accelerating voltage, X-FEG electron source, S-TWIN objective lens and a Gatan OneView 4K CMOS digital camera. QD nanoclusters were prepared as described above, with colloidal QDs in chloroform prepared on thinner graphene-oxide TEM grids containing a single monolayer of oxidised graphite to increase electron transmission and therefore image resolution. $CuInS_2$/ZnS QDs in chloroform were diluted to a 70 nM concentration, then 2 µl were drop-deposited onto the graphene-oxide TEM grids and left to air-dry at room temperature. Size analysis was completed in ImageJ and is detailed in Chapter 5.2.

Note on contributions: FEI Titan3 Themis 300 TEM data was collected by Dr Zabeada Aslam from the Leeds Electron Microscopy and Spectroscopy Centre (LEMAS) and analysed by the author of this thesis.

2.8 Fluorescence Microscopy

The substrates used when characterising samples using fluorescence microscopy techniques were 50 x 25 mm glass coverslips (#1.5 thickness), made hydrophilic by a 30-

minute incubation in a 3:1 mixture of sulfuric acid (H_2SO_4) to hydrogen peroxide (H_2O_2), otherwise known as 'piranha solution'. Piranha cleaning is a highly oxidising reaction, therefore hydroxylates the glass surface as well as removing most organic matter, rendering the surface hydrophilic. The piranha-cleaned coverslips were then rinsed ×10 with ultrapure water and were then stored in ultrapure water at room temperature until use, usually within a 1-2 day period. Before use, cleaned glass coverslips were removed using clean tweezers and dried with a nitrogen gun, then hydrophobic adhesive imaging spacers (0.12 mm depth, 9 mm diameter, Grace Bio-Labs) were attached to dry substrates to confine a droplet of buffer for an open sample setup, allowing buffer exchanges. When imaging dried samples such as colloidal QDs, imaging spacers were not used and low volumes of dilute samples were drop-cast (dried) onto substrates. Samples were incubated with the glass immediately after drying substrates to avoid substrate contamination.

To ensure effective attachment of the lipid-stabilised QD nanoclusters to the coverslip, positively-charged poly-L-lysine (PLL) (Sigma, mol wt 30 000 - 70 000) was used to enhance electrostatic interaction between the negatively-charged DOPG lipid within the sample and the negatively-charged substrate. 100 µl of 0.1% w/v PLL was incubated with the clean glass for 30 minutes before being washed off with ten changes of ultrapure water to remove excess PLL, before drying on a hot plate at 40 °C. Meanwhile, lipid-stabilised QD nanoclusters were diluted serially (×1, ×10, ×100 or ×250 diluted, initial concentration of 5 mg/ml lipid) using 10 mM HEPES, 20 mM NaCl (pH 7.5), with low concentrations of the buffer used to promote interactions between the sample and the positively-charged PLL. Once the substrate was dry, 100 µl of QD nanoclusters at the desired concentration (×250 diluted for FLIM measurements) were incubated with the PLL-coated (or piranha-cleaned) coverslips for 15 minutes. Samples were then washed ×10 with 10 mM HEPES, 20 mM NaCl (pH 7.5), before three final washes in a higher-concentration 50 mM HEPES, 100 mM NaCl (pH 7.5) buffer to maintain consistency between microscopy and spectroscopy conditions.

2.8.1 Epifluorescence Microscopy

Epifluorescence microscopy is a technique where a light source, usually an incandescent lamp, is used to excite a sample, with the emission being collected along the same path as the excitation light (see Figure 2.7). Multiple fluorescent components can be imaged within the same sample through the use of filters, allowing control of the excitation wavelengths that reach the sample as well as the wavelengths of emitted light that are collected. A dichroic mirror is a device that reflects short wavelengths, but allows transmission of longer wavelengths, and can be coupled with the excitation and emission filters to create 'filter cubes'. These are designed to excite and collect fluorescence emission from certain fluorophores by blocking light that lies outside of the specified excitation wavelength range and emission range. This can allow investigation into the co-localisation of two or more fluorescent components of the same sample if they have excitation and emission parameters that align with the interchangeable filter cubes of the epifluorescence microscope.

Within the epifluorescence microscope, a mercury lamp emits white light, which is passed through a mechanical aperture that can open or close to control the width of the excitation beam or prevent light from exciting the sample completely. The beam then passes through the excitation filter to the dichroic mirror, which reflects the beam 90° through an objective lens which is focused on the fluorescent sample. The sample emission is collected through the objective lens and then transmitted through the dichroic mirror and emission filter towards the CCD detector. The resolution of the epifluorescence microscope is limited by the Abbe limit, therefore can be no greater than $\sim$ 275 nm for green light.

Epifluorescence microscopy was performed on a Nikon E600 microscope equipped with an Andor Zyla 4.2 sCMOS detector and filter cubes (‘blue’ filter: excitation 450-475 nm, dichroic 500 nm, emission 650-800 nm; ‘green’ filter: excitation 540-580 nm, dichroic 595

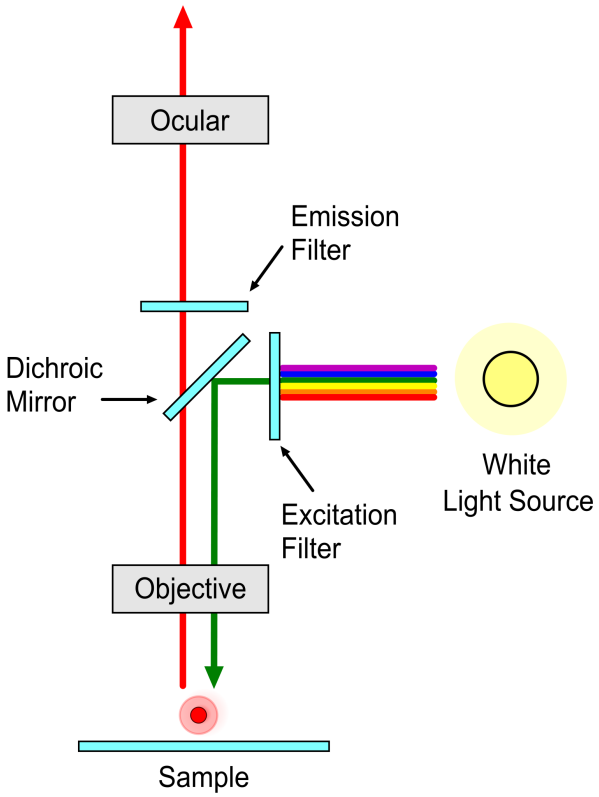

Figure 2.7: Schematic of the optics within a Nikon E600 epifluorescence microscope. Adapted from ThorLabs user manual.

nm, emission 600-660 nm). Images were taken using a ×40 air objective (N.A. 0.6) and a ×100 oil objective (N.A. 1.25). The oil lessens the difference between the refractive index of the lens and the refractive index of the observation media, reducing the effects of aberration and improving the achievable resolution limit. The range of exposure times was between 300 ms - 1s depending on the sample, and appropriate neutral density (ND) filters were inserted for reduction of the light entering the lens for an optimal signal-to-noise ratio.

2.8.2 Fluorescence Lifetime Imaging Microscopy

Fluorescence Lifetime Imaging Microscopy (FLIM) is a technique that records the fluorescence lifetime obtained from TCSPC measurements on individual pixels to build up an image that provides both the fluorescence intensity and lifetime of a sample (see

Figure 2.8). A pulsed laser is used as an excitation source, which passes through an excitation filter to select the range of excitation wavelengths. The laser then passes through a mechanical aperture to a magnifying objective lens, before scanning across the sample stage similar to confocal laser scanning microscopy. The sample emission is transmitted through a dichroic mirror which isolates the desired emission wavelength range, then through an emission filter towards a single PMT detector. If two fluorophores are being imaged simultaneously, then two excitation sources can be utilised through the use of multiple pulsed lasers, with the emission being directed through a beam splitter towards two separate emission filters with two detection channels. Decay curves are built up for each measured fluorophore, with TCSPC measurements recording the time between each excitation pulse sent and the emission received by the detectors, as explained in Chapter 2.5.3. A decay curve is built up in every pixel for each fluorophore being characterised, allowing an image to be formed containing both the fluorescence lifetime and intensity.

FLIM was performed on a PicoQuant GmbH Microtime 200 time-resolved confocal fluorescence microscope. Samples were placed within an Olympus IX73 inverted optical microscope, acting as a sample holder, with light from a pulsed laser passing into and exciting various filter units for excitation, laser scanning and emission detection. A small portion of the beam is deflected towards a photodiode to provide an average power readout for the excitation source before reaching the objective lens, with the main excitation laser reflected toward the sample by a 488/561 (dual band) dichroic mirror. An Olympus UPlanSApo $\times$60 water objective (N.A. 1.2) focuses the beam. The excitation sources, PicoQuant LDH 485 nm and LDH 561 nm laser heads were driven in Pulsed Interleaved Excitation (PIE) mode by a PicoQuant PDL 828 Sepia II burst generator module. The pulse rates for the LDH 485 nm and LDH 561 nm lasers were 20 MHz and 1 MHz respectively. To maintain the shortest possible pulse FWHM and provide the best temporal resolution, the voltage supplied to each laser was set at the minimum required to allow lasing and was kept constant for all measurements. The laser power was set to the desired output (500 AU for 485 nm laser and 1000 AU for 561 nm laser)

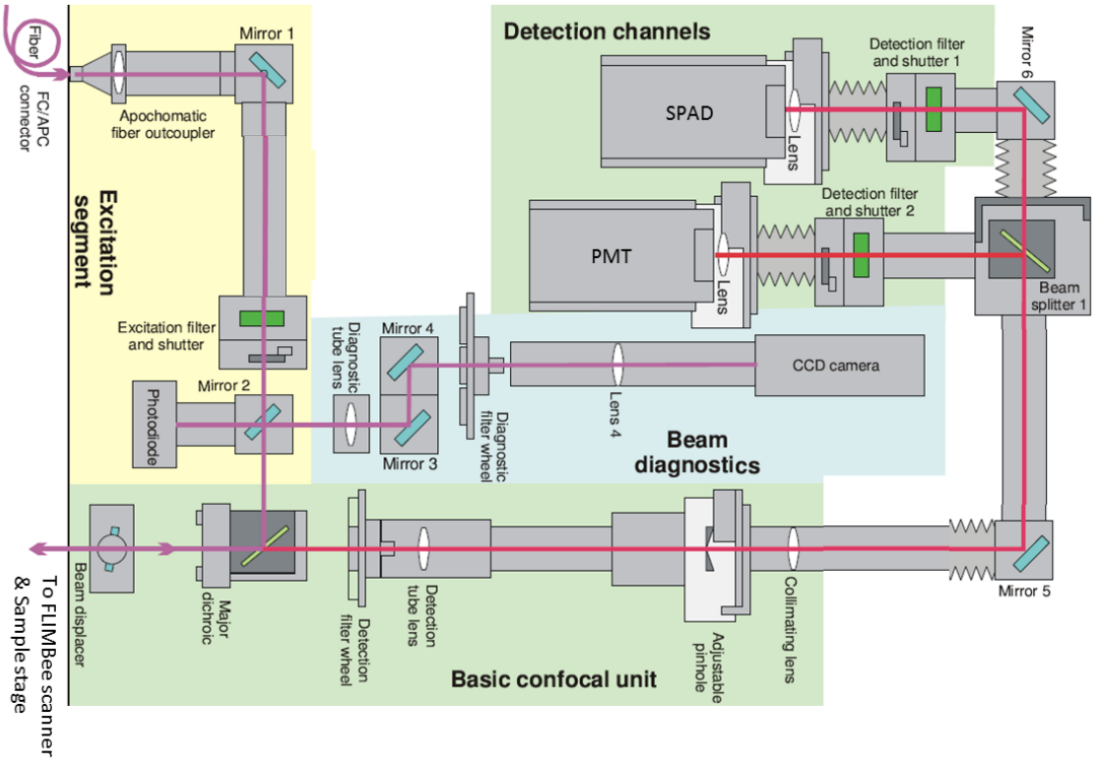

Figure 2.8: Instrument schematic for the FLIM system. Adapted from the Picoquant (GmbH) user manual.

using a combination of neutral density filters and a micro-blade cut-off that partially blocks the laser beam. It is estimated that the transmission efficiency is ~85% at the 485 nm and 561 nm excitation wavelengths for excitation power calculations. The pulse widths for the LDH 485 nm and LDH 561 nm lasers were 90 ps and 70 ps respectively.

The sample emission was collected through the same objective lens and then transmitted through the dichroic mirror towards a detection arm of the optical path. The NBD emission and $CuInS_2$/ZnS QD emission were separated by a T635-LPXR filter in a beam splitter that split the emission between two detectors. Fluorescence emission wavelengths shorter than 635 nm were directed through a 520/35 emission filter before being detected by a hybrid PicoQuant PMT detector. Fluorescence emission wavelengths longer than 635 nm, were directed through a 690/70 emission filter before being detected by a PicoQuant single-photon avalanche diode (SPAD) detector. With

this detector setup, the PMT was optimised to collect emission from the NBD dye and the SPAD was optimised to collect fluorescence emission for the QDs. Timing electronics were a PicoQuant TCSPC TimeHarp 260 module.

The PIE beam was directed across the sample using a Picoquant "FLIMBee" mirror-based galvanometer scanner. FLIM measurements were generally taken for 256 x 256 pixels across a high magnification 5 x 5 µm field of view when isolating individual lipid-stabilised QD nanoclusters, expanding the field of view to 50 x 50 µm and selecting regions of interest when collating the average lifetime measurements for multiple particles. The total TCSPC collection time was 1 µs for the $CuInS_2/ZnS$ QD channel with a bin size of 800 ps, and the collection time was 50 ns for the NBD channel with a bin size of 25 ps. Analysis of fluorescence decay curves was performed using inbuilt fitting functions in the PicoQuant GmbH SymPhoTime software to fit a bi-exponential decay that was re-convoluted with measured IRFs. A good fit was confirmed when residuals were minimised, and χ^2 was $\sim$1. When analysing the sample lifetimes, the amplitude-weighted mean lifetime, which reflects the quenching of the energy donor due to FRET, was chosen over the intensity-weighted average lifetime, which corresponds to the real average arrival time of the photons, to allow the FRET efficiency to be calculated.

Note on contributions: FLIM data was collected and analysed by Dr Ashley Hancock with sample preparation completed by the author of this thesis.

Chapter 3

Results: Developing the Method for Quantum Dot Nanocluster Self-Assembly

3.1 Motivation

When hydrophobic QDs, such as dodecanethiol-functionalised $CuInS_2$/ZnS nanoparticles, are placed into aqueous suspensions, they are highly unstable. QDs can assemble into clusters of several particles under certain conditions governed by the physicochemical environment (pH, ionic strength, etc.) and the QD surface chemistry. Sometimes this can lead to the nanoparticles precipitating, but sometimes relatively small and stable nanoscale clusters of QDs (e.g., 10-100 particles) can form which persist and have altered properties compared to individual colloidal QDs. It is likely that the occurrence of these clusters will affect the many downstream applications of QDs, so it is important to understand them and control their size.

The research presented in this chapter focuses on creating and optimising a system where $CuInS_2$/ZnS QDs are controllably assembled into distinct 'nanocluster' structures. The

structure and photophysics of $CuInS_2$/ZnS QDs within small nanocluster assemblies have not yet been characterised and little is known about the excitation dynamics and energy transfer mechanisms of small QD nanoclusters. Energy transfer between hydrophilic cadmium selenide QDs that were induced to aggregate via solvent alteration has been investigated by other groups [89, 90], although little control over cluster size has been reported. Control of cluster size has been achieved by researchers using hydrophobic QDs encapsulated within a fluorescent lipid micelle to act as a probe [92]. The intention of that study was to use a phospholipase A_2 (PLA_2) enzyme to release a lipid dye that would otherwise be quenched as an energy donor for FRET to the QDs acting as energy acceptors. However, the energy transfer dynamics from the dye to the QDs and between the QDs themselves were not reported. This is an area of interest for this chapter.

To investigate the structure and energy transfer mechanisms of colloidal QD assemblies, first, the controlled synthesis procedure must be optimised. The first goal of this chapter was to attain consistent and repeatable $CuInS_2$/ZnS QDs with bright and stable core/shell QDs to prevent non-radiative recombination of excitons. The photoluminescence of $CuInS_2$ QDs is enhanced ~40-fold with the addition of a ZnS shell, which also leads to a blue shift of the PL spectrum, the result of a semi-alloyed $CuInS_2$/ZnS particle as opposed to a typical core/shell structure with a well-defined boundary due to the cationic exchange between $CuInS_2$ and ZnS lattices [108]. $CuInS_2$/ZnS QDs have relatively broad excitation bands and can be tuned to compliment the absorption of many light-harvesting proteins, while also displaying long fluorescence lifetimes, broad fluorescence emission spectra and a large Stokes shift when compared to CdSe QDs [68].

Once a controllable $CuInS_2$/ZnS QD synthesis has been achieved, the second goal was the development of a consistent method for generating a controlled cluster of QDs. The clusters need to be stable for long periods of time to allow full characterisation of the optical properties and should maintain their structure when deposited on a surface. If the clusters are too large, it is likely that precipitation would occur, causing

large-scale agglomeration of QDs which should be avoided. The third goal, once a nanocluster self-assembly procedure had been developed, was to understand and compare the photophysics and mechanisms of energy transfer of $CuInS_2$/ZnS QDs within nanoclusters to that of colloidal $CuInS_2$/ZnS QDs, with emphasis on the relationship to size, structure, and long-term stability. The functionality of $CuInS_2$ QD nanoclusters as a light-harvesting material will be determined as a pathway to eventually investigating the functionality of QD-containing bio-hybrid light-harvesting nanocomposite materials.

3.2 Optimisation of Quantum Dot Core Synthesis Parameters

3.2.1 Introduction

A consistent quantum dot synthesis was desired with (1) bright QDs, (2) a narrow band of fluorescence emission, and (3) a high batch yield to allow a full experimental investigation using the same QD stock. Syntheses of QD cores were carried out following the general synthesis method outlined in Chapter 2.1, based on a solvothermal method using thiolate ligands [99].

To obtain a QD synthesis with a high yield and a large relative fluorescence, the seeding time must be optimised. A synthesis temperature of 200°C was chosen to maximise the uniformity and yield while still giving control over the fluorescence emission peak position. Alteration of the alkanethiol ligand can have an effect on the optical properties of QDs [188], therefore the relationship between synthesis time and the first excitonic absorption/emission peaks) must be investigated to obtain a tunable synthesis using shorter-length ligands such as octanethiol and nonanethiol as opposed to DDT. To increase the brightness of the $CuInS_2$ core QDs, a ZnS shell must be grown to passivate surface trap states involved in the non-radiative recombination of excitons [189, 190], increasing the likelihood of radiative decay. The addition of a ZnS shell leads to a blue-

shift in the fluorescence emission peak of the QDs, attributed to a size reduction in the $CuInS_2$ cores due to cationic exchange between the $CuInS_2$ and ZnS lattices [108], and should be accounted for when seeding the $CuInS_2$ cores. Finally, the use of a shorter-length ligand during reflux may lead to a slight increase in QD polarity, therefore the $CuInS_2$/ZnS QD cleaning procedure may require modification to successfully promote QD instability and subsequent precipitation when removing chemical precursors and by-products following synthesis. These challenges will be addressed within Section 3.2 to achieve $CuInS_2$/ZnS QDs that would be optimal for achieving QD-QD energy transfer within lipid-stabilised nanoclusters.

3.2.2 Optimisation of the Seeding Time

The nanoparticle seeding time is the period of core growth following nucleation, where the fluorescence emission peak position of the $CuInS_2$ cores increases in wavelength over time due to the quantum confinement effect, as discussed in Chapter 1.3.2. The band gap decreases as the size of the particle increases over time, meaning that lower-energy photons will be emitted for longer synthesis periods. The $CuInS_2$ cores increase in size as the synthesis takes place and more material is added to the cores through Ostwald ripening, where small particles dissolve and redeposit on the surface of larger crystals as described in Section 1.3.5. The relationship between seeding time and fluorescence emission peak position was expected to be linear, and obtaining a reference for the timing of core growth was a crucial first step for developing a systematic $CuInS_2$/ZnS synthesis procedure that produces a controllable fluorescence emission peak wavelength.

Figure 3.1 A shows the results of a synthesis where 100 μl aliquots were extracted from the 10 ml stock solution at defined time points during a $CuInS_2$ core synthesis, with five-minute intervals. The image is a photograph of the vials containing 16 such samples where the change in colour of the QDs is evident, from a pale orange to dark red. This protocol allows the position of the fluorescence emission peak of the $CuInS_2$ cores to be characterised while minimising an alteration in the rate of reaction arising through a

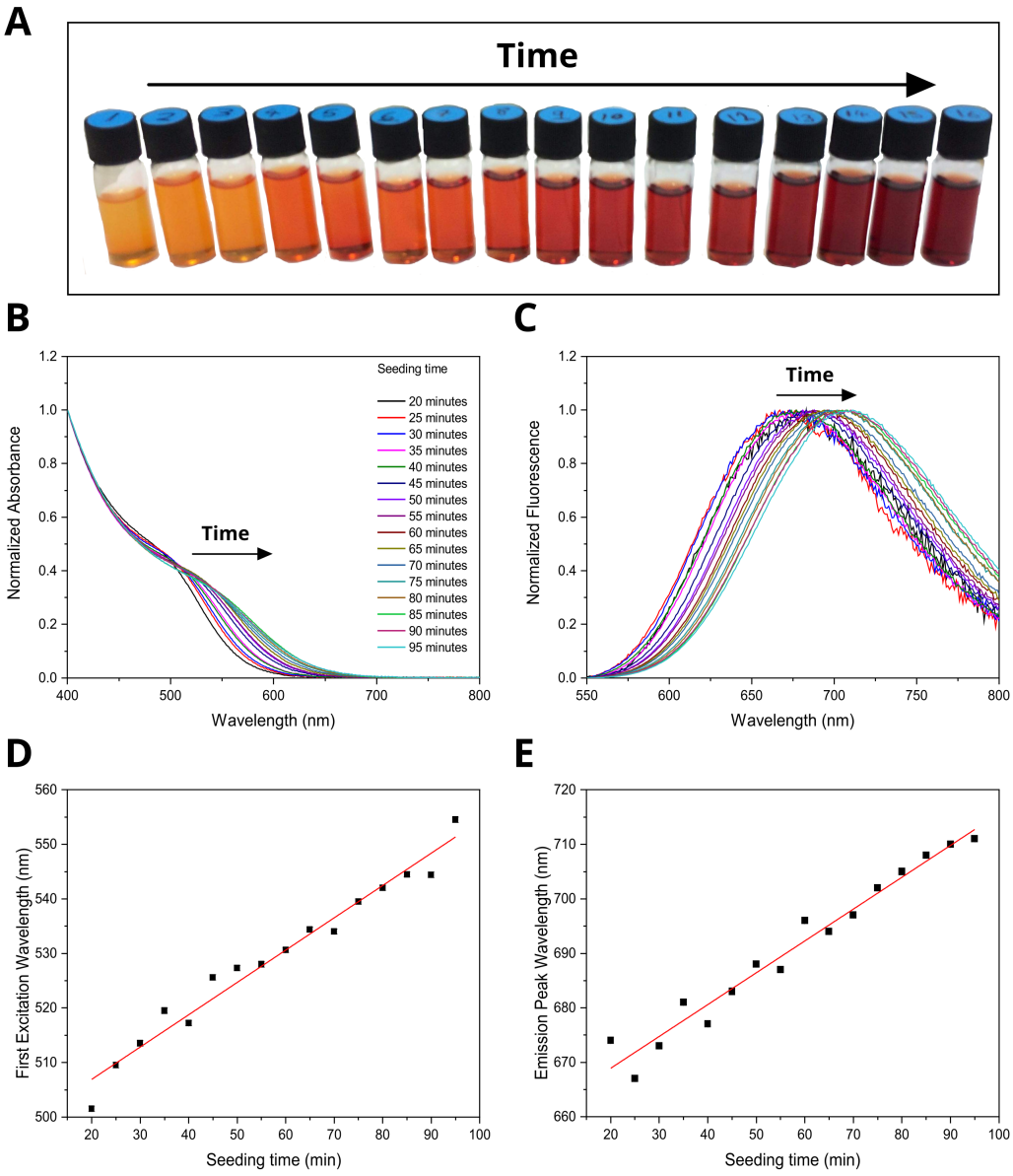

Figure 3.1: Spectra showing relationship between optical properties and seeding time for $CuInS_2$ QDs. Measurements were taken from aliquots of a single synthesis. (A) Control of synthesis is shown by a gradual colour change of samples taken between 20 minutes and 95 minutes at five-minute intervals. 1 = 20 min - 16 = 95 min. Samples were diluted in 1.5 ml chloroform. (B) Normalised (400 nm) absorption spectra of nonanethiol-capped $CuInS_2$ QD cores in chloroform showing an increase in the first excitation peak with increasing seeding time. (C) Normalised steady-state fluorescence emission spectra (λ_{ex} = 500 nm) of nonanethiol-capped $CuInS_2$ QD cores in chloroform showing an increase in emission peak wavelength with increasing synthesis time. (D) A plot of steady-state emission peak wavelength against seeding time for nonanethiol-capped $CuInS_2$ QD cores in chloroform. The data points were fit to a linear increase equation with the formula $y = mx + c$, where $m = 0.61 \pm 0.03$ and the Pearson correlation coefficient was 0.986. (E) A plot of first excitonic absorption wavelength against seeding time for nonanethiol-capped $CuInS_2$ QD cores in chloroform. The data points were fit to a linear increase equation with the formula $y = mx + c$, where $m = 0.59 \pm 0.03$ and the Pearson correlation coefficient was 0.983.

reduction in the volume of the sample, as only 1% of the initial volume is extracted each time. A plot of the absorbance, normalised at a wavelength of 400 nm to capture peak shifts (Figure 3.1 B), shows an increase in the absorbance peak wavelength with core seeding time, with the absorbance peak corresponding to the first excitation wavelength of the quantum dot. As the first excitation peak in the absorbance spectra can be quite broad, determining the local minimum from the second derivative is the most reliable method of finding the excitation position. The normalised fluorescence emission spectra of the same samples of $CuInS_2$ cores extracted at five-minute intervals are shown in Figure 3.1 C, with an increase in the wavelength observed as the synthesis time increases.

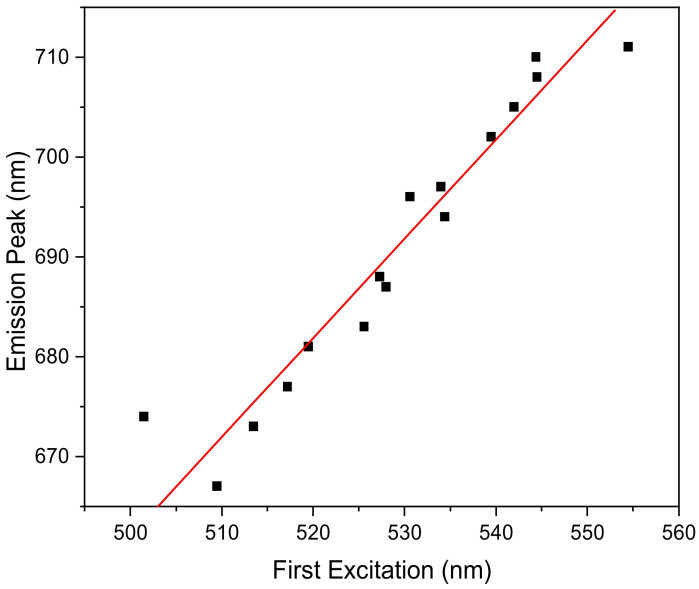

Figure 3.2: Relationship between fluorescence emission peak and seeding time for $CuInS_2$ QDs. The initially-linear relationship between steady-state fluorescence emission peak wavelength and first excitation wavelength for nonanethiol-capped $CuInS_2$ QD cores in chloroform with a gradient of 0.99 ± 0.08 (red line).

Plotting the first excitation transition, as detected from the second derivative of absorbance spectra, against the core seeding time (Figure 3.1 D) gives an initial linear relationship and shows an increase in the first excitation wavelength with seeding time. A Pseudo-Voigt fit was chosen to analyse the fluorescence emission maxima, using a

linear combination of a Lorentzian curve and a Gaussian curve to approximate the Voigt profile. Pseudo-Voigt fits are regularly used to fit fluorescence emission spectra of QDs as the combination of the Lorentzian and Gaussian functions can be tailored to the specific peak shape. The fluorescence emission peak wavelength can also be plotted against the seeding time (Figure 3.1 E) and shows a linear increase over time. The size-dependant red-shift agrees with the literature [68, 102], meaning both graphs can be used as a reference for tuning the optical properties of the $CuInS_2$/ZnS QDs in future syntheses. Both the absorbance peak and fluorescence emission peak wavelength would be expected to plateau with increasing seeding time as the QDs approach the size limit at which quantum confinement effects can be observed ($\sim$ 8nm due to a Bohr exciton radius of 4.1 nm), but the size of the QDs synthesised remain well below this value [191]. The fluorescence emission peak wavelength is shown to increase from 683 nm after 20 minutes of core growth to 711 nm after 90 minutes, with a total wavelength shift of 28 nm in 75 minutes and an average shift of 1 nm every 160 seconds. This allows precise control of the fluorescence emission peak position during synthesis and allows $CuInS_2$/ZnS QDs to be synthesised with desired optical properties.

The relative fluorescence, calculated by dividing the maximum fluorescence intensity by the absorbance at 400 nm, is shown to increase as the core seeding time increases. This is representative of the quantum yield (QY), showing that the fluorescence is increasing as more material is added to the cores through Ostwald ripening (Table 3.1). FWHM measurements show that the fluorescence emission spectra for the $CuInS_2$ cores are fairly broad (130 - 140 nm for most samples) in comparison to the $CuInS_2$/ZnS QDs after core concentration (cation exchange during shell formation which results in a reduced core size) with the addition of the shell ($CuInS_2$ 65 mins) [68], suggesting the QDs have a fair distribution of sizes.

The Stokes shift of QDs is used to characterise the red-shift of the fluorescence emission spectra with respect to the absorption spectra and can be defined as the difference

Optical Properties of $CuInS_2$ and $CuInS_2$/ZnS Quantum Dots					
Sample	Emission (nm)	First Excitation (nm)	Stokes Shift (nm)	FWHM (nm)	Relative Fluorescence ($\times 10^4$)
$CuInS_2$ 20 mins	680 ± 1	501 ± 1	173 ± 1	154 ± 1	7.11 ± 0.2
$CuInS_2$ 25 mins	673 ± 1	510 ± 1	158 ± 1	142 ± 1	11.2 ± 0.2
$CuInS_2$ 30 mins	674 ± 1	514 ± 1	160 ± 1	138 ± 1	14.1 ± 0.2
$CuInS_2$ 35 mins	679 ± 1	520 ± 1	162 ± 1	133 ± 1	26.1 ± 0.3
$CuInS_2$ 40 mins	678 ± 1	517 ± 1	160 ± 1	135 ± 1	24.1 ± 0.3
$CuInS_2$ 45 mins	685 ± 1	526 ± 1	157 ± 1	135 ± 1	26.6 ± 0.3
$CuInS_2$ 50 mins	689 ± 1	527 ± 1	161 ± 1	133 ± 1	61.9 ± 0.4
$CuInS_2$ 55 mins	691 ± 1	528 ± 1	159 ± 1	133 ± 1	67.3 ± 0.4
$CuInS_2$ 60 mins	694 ± 1	531 ± 1	165 ± 1	133 ± 1	91.5 ± 0.4
$CuInS_2$ 65 mins	696 ± 1	534 ± 1	160 ± 1	134 ± 1	104 ± 1
$CuInS_2$ 70 mins	699 ± 1	534 ± 1	163 ± 1	135 ± 1	117 ± 1
$CuInS_2$ 75 mins	703 ± 1	540 ± 1	163 ± 1	138 ± 1	138 ± 1
$CuInS_2$ 80 mins	704 ± 1	542 ± 1	163 ± 1	138 ± 1	165 ± 1
$CuInS_2$ 85 mins	707 ± 1	545 ± 1	164 ± 1	138 ± 1	197 ± 1
$CuInS_2$ 90 mins	708 ± 1	544 ± 1	166 ± 1	139 ± 1	204 ± 1
$CuInS_2$ 95 mins	710 ± 1	555 ± 1	157 ± 1	139 ± 1	232 ± 1
$CuInS_2$/ZnS 65 mins	646 ± 1	527 ± 1	119 ± 1	122 ± 1	4910 ± 10

Table 3.1: Optical properties of $CuInS_2$ with increasing seeding time and comparison to $CuInS_2$/ZnS QDs. Fluorescence emission peak, first excitation peak, Stoke's shift, full width at half maximum (FWHM) and relative fluorescence (emission peak over the absorbance at 400 nm) obtained for $CuInS_2$ cores from the 16-aliquot seeding experiment ($CuInS_2$ C9 20 mins - $CuInS_2$ C9 95 mins) and a $CuInS_2$/ZnS core-shell synthesis with a 65-minute core seeding time and 1-hour shell-growth.

between the fluorescence emission peak wavelength and the first excitation wavelength. The Stokes shift is unusually large in $CuInS_2$ core QDs compared to other QDs, showing a weak size-dependence consistent with trap state emission [68, 102], and is expected to be similar across all extracted samples due to material dependency. If the Stokes shift is consistent (i.e. no/weak size dependence), then a plot of the fluorescence emission peak wavelength against the first excitation wavelength is expected to give a linear fit due to the quantum confinement effect linking the absorbance and fluorescence emission to the QD size [101, 102, 192, 193], as described in Chapter 1.3.2. The energy difference between the absorption and fluorescence emission energies ($\Delta E = E_A - E_E$) is such that

the difference in wavelength is given by:

$$\Delta\lambda = \frac{hc}{E_A} - \frac{hc}{E_E}, \tag{3.1}$$

with a proportional increase in wavelength expected for small QD sizes when considering the confinement term in Equation 1.23, before plateauing as the QD size increases significantly. Figure 3.2 does show this trend with a gradient of 0.99 ± 0.08, suggesting that the chemical synthesis was successful and the $CuInS_2$ QDs have the expected optical properties varying with their size.

Time-resolved fluorescence measurements of five $CuInS_2$ core samples covering the range of synthesis times were also taken (Figure 3.3 A/B). The excited state decay becomes slower, shown as a shallower exponential decay function, as seeding time increases, with the surface-to-volume ratio decreasing as the $CuInS_2$ cores increase in size, thus slightly reducing the trap-state decay pathway contribution described in Chapter 1.3.4. The lifetimes of these $CuInS_2$ QDs (no shell) are significantly shorter than the equivalent core-shell QDs due to the presence of surface trap states, which would be passivated by a ZnS shell thus reducing the number of possible pathways for electron decay [189, 190].

The decay components can be analysed in detail when fitting the tail to a tri-exponential, as seen in Table 3.2. The τ_1 component, believed to represent decay to surface trap-states that are involved in non-radiative recombination of excitons [189, 190], is increasing in size and decreasing in intensity, meaning the contribution of surface trap-states to the lifetime of the QDs is decreasing (Figure 3.3 C/D, black lines). As previously mentioned, this is likely due to the surface-to-volume ratio decreasing as the particles increase in size from Ostwald ripening. The τ_2 component, thought to represent recombination from the conduction band to impurities within the lattice [68, 190], increases in size and increases in intensity, with the band gap decreasing in size as the particles increase in size (Figure 3.3 C/D, red lines). The final τ_3 component, believed to represent Auger recombination

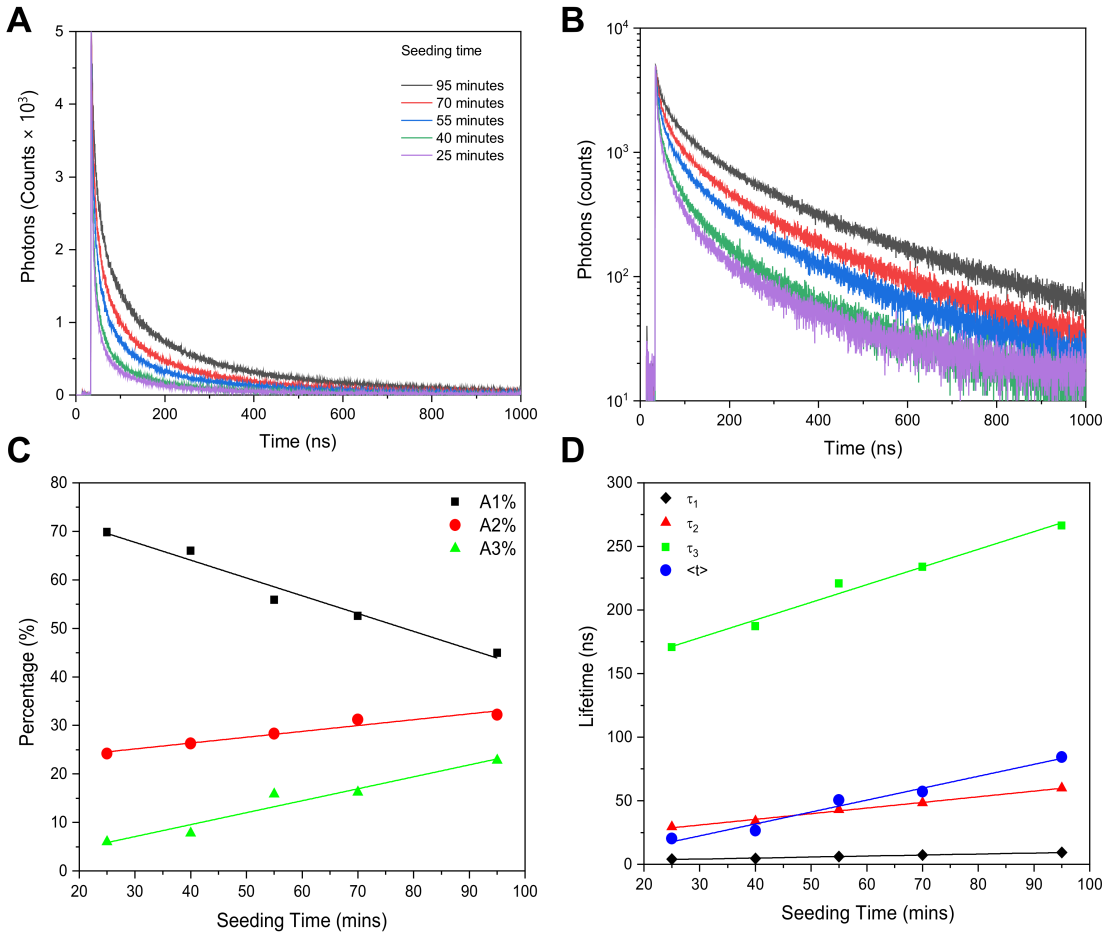

Figure 3.3: Time-resolved spectra showing slower decay of $CuInS_2$ QDs with increasing seeding time. (A) linear and (B) logarithmic time-resolved fluorescence decay curves (λ_{ex} = 473 nm, λ_{em} = 690 nm) from nonanethiol-capped $CuInS_2$ QD cores in chloroform. (C) Time components (τ_1 (black), τ_2 (red) and τ_3 (green)) and average lifetime <t> (blue) extracted from the time-resolved fluorescence decay curves of nonanethiol-capped $CuInS_2$ QD cores in chloroform. (D) Percentage of overall lifetime contribution calculated from amplitude measurements. A1% (black) represents the contribution from the τ_1 component, A2% (red) from τ_2 and A3% (green) from τ_3.

[98], also increases in size and intensity as the particle seeding time increases (Figure 3.3 C/D, green lines), similar to the τ_2 component. The overall amplitude-weighted lifetime significantly increases from 20.1 to 84.3 ns representing the significantly more stable excited states in the larger QDs. As the seeding time decreases and the core size increases, it is expected that the contributions from the τ_2 and τ_3 components will surpass the τ_1 contribution to the $CuInS_2$ lifetime.

Lifetime Components and Contributions							
Sample	τ_1 (ns)	A_1 (%)	τ_2 (ns)	A_2 (%)	τ_3 (ns)	A_3 (%)	<t> (ns)
$CuInS_2$ 25 mins	4.01 ± 0.01	69.8 ± 0.1	29.4 ± 0.1	24.2 ± 0.1	170.7 ± 0.1	6.04 ± 0.01	20.1 ± 0.3
$CuInS_2$ 40 mins	4.61 ± 0.01	66.0 ± 0.1	33.0 ± 0.1	26.2 ± 0.1	187.1 ± 0.1	7.77 ± 0.01	26.5 ± 0.3
$CuInS_2$ 55 mins	6.04 ± 0.01	55.9 ± 0.1	43.0 ± 0.1	28.3 ± 0.1	220.7 ± 0.1	15.8 ± 0.01	50.5 ± 0.4
$CuInS_2$ 70 mins	7.36 ± 0.01	52.6 ± 0.1	48.4 ± 0.1	31.2 ± 0.1	233.8 ± 0.1	16.3 ± 0.1	57.0 ± 0.4
$CuInS_2$ 95 mins	9.34 ± 0.01	45.0 ± 0.1	59.9 ± 0.1	32.2 ± 0.1	266.2 ± 0.1	22.8 ± 0.01	84.3 ± 0.5
$CuInS_2$/ZnS 65 mins	18.9 ± 0.1	16.1 ± 0.1	112 ± 1	36.4 ± 0.1	330 ± 1	47.5 ± 0.1	200.7 ± 0.6

Table 3.2: Deconstruction of the tri-exponential decay of $CuInS_2$ and $CuInS_2$/ZnS QDs from time-resolved fluorescence lifetime measurements. The $CuInS_2$ core samples ($CuInS_2$ C9 25 mins - $CuInS_2$ C9 95 mins) were selected from the 16-aliquot seeding experiment and the $CuInS_2$/ZnS sample is taken from a core/shell synthesis with a 65 minute core seeding time and 1 hour shell growth.

3.2.3 ZnS Shell Growth

To increase the fluorescence emission intensity of the $CuInS_2$ QDs, a zinc sulfide shell was added after the $CuInS_2$ core synthesis in order to passivate the surface trap states that are involved in non-radiative recombination of excitons. A blue-shift of the fluorescence emission maxima was anticipated after ZnS shell growth, due to the expected cationic exchange between the $CuInS_2$ and ZnS lattices [108]. This should be accounted for when synthesising the $CuInS_2$ cores if a specific fluorescence emission wavelength is required for the final nanoparticle sample. It is likely that the $CuInS_2$/ZnS QD has a semi-alloyed structure as opposed to a 'core-shell' structure with a well-defined boundary, with a band-gap increase expected as the size of the core decreases [99]. The first excitation peaks of the $CuInS_2$ and $CuInS_2$/ZnS QDs before and after shell growth were analysed from normalised absorbance spectra (Figure 3.4 A). The location of the peaks

was found by determining the local minimum of the second derivative due to the broad nature of the absorption spectra. The first excitation peak of the $CuInS_2$ QDs with no shell was found to be 534 nm, with the peak slightly blue-shifting to 527 nm with the addition of a ZnS shell, in agreement with our expectations. Figure 3.4 B shows the steady-state fluorescence emission spectra of the $CuInS_2$ QDs before and after a one-hour ZnS shell-growth, with ∼38-fold increase in fluorescence observed after correcting the $CuInS_2$ core sample for changes in concentration. The Stokes shift was found to decrease from 162 nm to 119 nm after shell growth, explained by the band gap of the ZnS shell being significantly larger than that of the $CuInS_2$ core, allowing type I band-alignment as shown in Figure 1.10, where excited electrons and holes are completely confined in the core region [194, 195]. Type I band alignment, when the band gap of the core is smaller than and falls within the band gap of the shell, usually provides long-term stability and a significantly higher quantum yield at the expense of a smaller Stokes shift [196]. A large Stokes shift is present in core-only QDs due to the radiative decay involving a transition from the quantised conduction band to intra-gap trap states [68], which are subsequently passivated with the addition of a ZnS shell. The energy difference related to the Stokes shift for the core-only QDs is 51.5 meV, with the energy at the first excitonic absorption peak and fluorescence emission maxima calculated to be 2.32 eV and 1.81 eV, respectively. For the core/shell QDs, the Stokes shift energy difference decreased to 43.3 meV, as expected, with the energy at the first excitonic absorption peak and fluorescence emission maxima calculated to be 2.35 eV and 1.92 eV, respectively.

Figure 3.4 C shows the normalised fluorescence emission spectra (λ_{ex} = 500 nm) of both $CuInS_2$ and $CuInS_2$/ZnS samples, with the 40 nm blue-shift observed agreeing with values from the literature at similar shell-growth times [99]. A narrowing of the fluorescence emission spectrum is also seen, with the FWHM decreasing from 130 nm to 120 nm with the addition of a shell due to size-focusing of the QDs through Ostwald ripening during shell growth [99]. The FWHM of the $CuInS_2$ cores being 130 nm also confirms the pre-

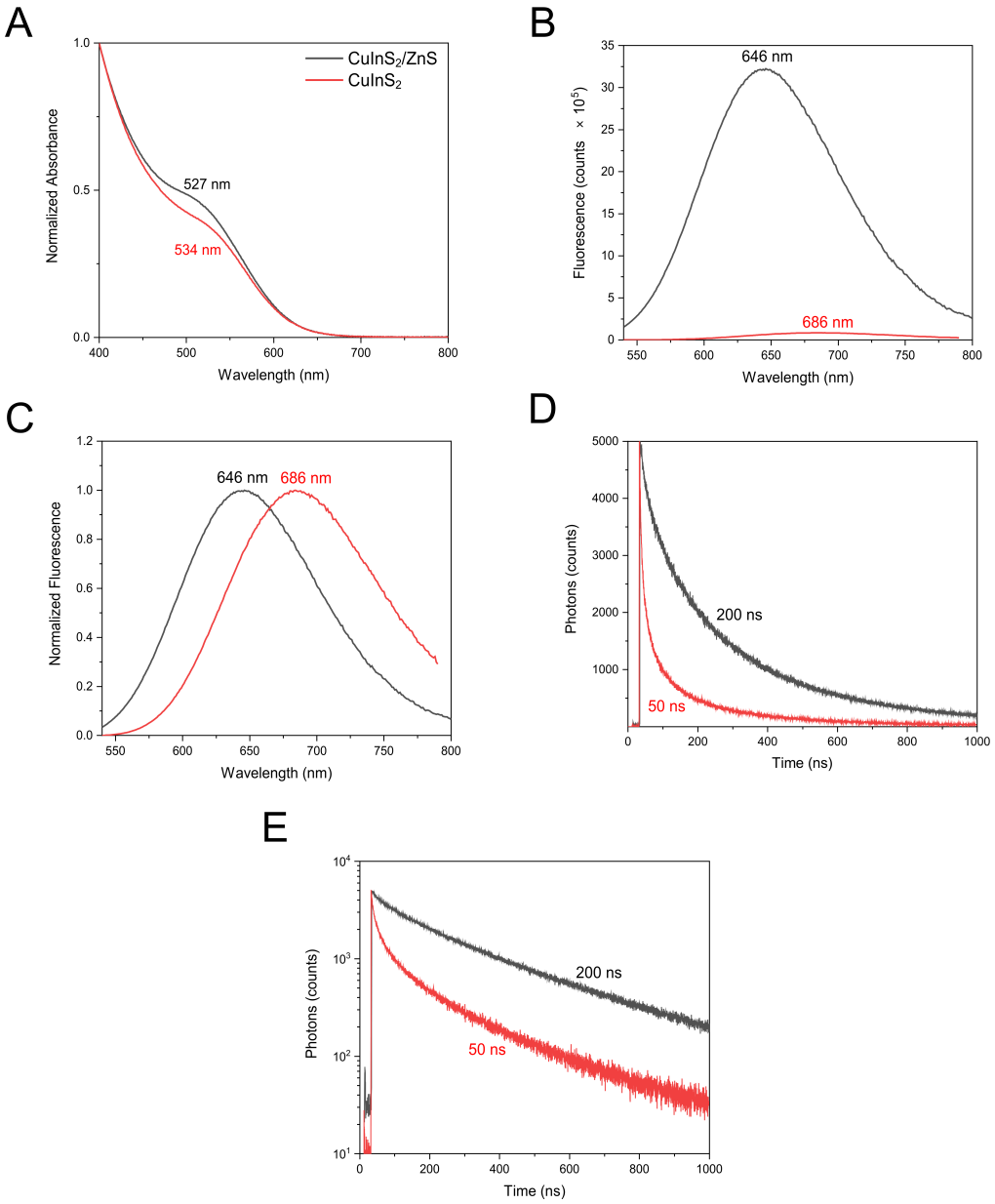

Figure 3.4: Spectra showing alteration of optical properties with shell growth for $CuInS_2$ and $CuInS_2$/ZnS QDs. (A) Normalised (400 nm) absorption spectra of nonanethiol-capped $CuInS_2$/ZnS QDs (black) and $CuInS_2$ QD cores (red) in chloroform before and after a one-hour ZnS shell growth. (B) Steady-state fluorescence emission spectra (λ_{ex} = 500 nm) of $CuInS_2$/ZnS QDs (black) and $CuInS_2$ QD cores (red) in chloroform after concentration correction. A one-hour ZnS shell growth results in a 50 nm blue-shift and a ~38 fold increase in fluorescence when compared to shell-less $CuInS_2$ QD cores. (C) Normalised steady-state fluorescence emission spectra (λ_{ex} = 500 nm) of nonanethiol-capped $CuInS_2$/ZnS QDs (black) and $CuInS_2$ QD cores (red) in chloroform. (D) Linear and (E) semi-logarithmic time-resolved fluorescence decay curves for nonanethiol-capped $CuInS_2$/ZnS QDs (λ_{ex} = 473 nm, λ_{em} = 650 nm) and $CuInS_2$ QD cores (λ_{ex} = 473 nm, λ_{em} = 690 nm) in chloroform. Deconvolution fits of this data with an IRF to extract the fluorescence lifetime are shown in Table 3.2. The mean lifetime from these fits is displayed beside the appropriate decay curve here.

vious assumption that the size distribution of an uninterrupted $CuInS_2$ core synthesis would be narrower than measured in Figure 3.1 C as the synthesis was not disturbed by aliquot extraction.

Time-resolved fluorescence measurements in Figure 3.4 D, E compare the $CuInS_2$/ZnS QDs to the $CuInS_2$ cores when fitting to a tri-exponential decay function. The fast τ_1 decay channel, originating from surface trap states, is suppressed due to the passivation of surface trap states. The length of the τ_1 also increases to ∼19 ns for the $CuInS_2$/ZnS QDs from ∼7.0 ns for the $CuInS_2$ cores at the same core seeding time, with the τ_2 and τ_3 components increasing from ∼45 ns to ∼110 ns and ∼230 ns to ∼330 ns respectively. The largest change appears to be with the τ_3 component, with the long lifetime contribution increasing from ∼16% of the overall lifetime in the $CuInS_2$ cores to ∼48% of the overall lifetimes in the $CuInS_2$/ZnS QDs. These factors contribute to a significantly longer average lifetime <t> of 200 ns when compared to the <t> of 52 ns for the $CuInS_2$ cores, confirming that the excited states of $CuInS_2$/ZnS are more stable than their shell-less $CuInS_2$ counterparts, in agreement with literature [68, 197].

3.2.4 Optimising the $CuInS_2$/ZnS Cleaning Method

Once synthesised, the final stage of $CuInS_2$/ZnS QD preparation procedure was to 'clean' the QDs to remove chemical precursors and by-products from the solution using a mixture of acetone/methanol/chloroform. This solvent mixture promotes precipitation of the QDs and enables separation of the particles from the solvent by centrifugation, with chloroform initially added to the as-synthesised solution to disperse the QDs. One challenge when processing the newly-synthesised QDs was the freezing point of octadecene (ODE) being ∼18 °C, meaning the solution could freeze at typical room temperature. The mixture would subsequently freeze in the centrifuge during the cleaning process unless the temperature was set above ∼30 °C, requiring a pre-spin cycle to raise the temperature before centrifugation and a spin-cycle that maintained the elevated temperature during removal of the supernatant. A second obstacle was that a successful pellet of QDs was

not obtained in preliminary synthesis experiments after adding the acetone during the first iteration of the cleaning procedure. For initial syntheses, acetone was added to the QDs dispersed in chloroform to a 10:1 acetone:chloroform volume/volume ratio (as suggested in the literature), however, there was a lack of cloudiness. It was hypothesised that this was due to the cleaning solvent mixture being too non-polar. Introducing methanol to the cleaning mixture increased the polarity and produced a consistent pellet, as did increasing the ratio of acetone:chloroform to 15:1. A final cleaning solution of 10:5:1 acetone:methanol:chloroform was decided upon and this consistently resulted in successful QD cleaning without fail. The cleaning cycle was repeated a further two times, before finally resuspending the QDs in 20 ml of chloroform and storing at 4 °C to prolong stability.

3.3 Initial Attempts to Form Quantum Dot Nanoclusters

3.3.1 Introduction

Once a controllable procedure for $CuInS_2$/ZnS synthesis had been achieved, the stock of colloidal QDs dispersed in chloroform solution could then be used in an attempt to form lipid-stabilised QD nanoclusters. A starting point was the expectation that the incorporation of QDs inside lipid micelles should be driven by hydrophobic interaction between the hydrocarbon tail groups of the lipid molecule and the alkyl ligand attached to the QD surface, therefore the initial aim was to stabilise the $CuInS_2$/ZnS QDs with a simple and abundant 1,2-dioleoyl-sn-glycero-3-phosphocholine (DOPC) lipid that has been well characterised. Three techniques that were previously published for associating nanoparticles with lipids were initially investigated by comparing the stability of the resultant assembled materials by making measurements using fluorescence and absorbance spectroscopy techniques over an extended period of time after preparation.

3.3.2 Attempted Nanocluster Formation by Thin Film Hydration

Firstly, QD nanocluster formation was attempted by directly hydrating a dry film of lipids and QDs with an aqueous buffer (HEPES) and performing probe sonication in an attempt to disperse and stabilise a mixture of QDs and lipids. The resulting solution was cloudy and colourless with visible agglomerates of QDs present, suggesting that incorporation was unsuccessful as no lipid-stabilised QD nanoclusters were formed. The smaller of the QDs aggregates that were apparently present eventually deposited on the bottom of the cuvette over the course of an hour, although most of the larger QD aggregates were lost during the transfer of the solution for characterisation. It is likely that the QDs were aggregated upon hydration due to instability, thus were too large to be stabilised by the lipid, hence the need for small-scale clustering. It appeared from these unsuccessful attempts that hydrophobic QDs would not be taken up by the lipid in an aqueous environment without additional stability from either a cosolvent or detergent.

3.4 Attempted Nanocluster Formation by Cosolvent Removal

The second method of QD nanocluster formation to be attempted was a cosolvent removal method via rotary evaporation, where a mixed thin film of dried lipids and QDs were re-hydrated in an organic solvent chosen for miscibility with water, with the intention of removing the co-solvent through rotary evaporation. This method has previously been used to associate iron oxide nanoparticles that have hydrophobic surface chemistry with lipids [128], where a solvent inversion method was used to self-assemble nanoparticle-containing liposomes. The modified method involved hydrating the hydrophobic QDs and the desired lipid in a moderately polar solvent which can dissolve and stabilise both. The solvent must be miscible with water, in order to form a single liquid phase, but then should have a lower boiling point than water so that the co-solvent can be removed by increasing the temperature and the water remains. THF had

been identified as a solvent that is miscible with water, with procedures also available for nanoparticle association with lipids. Butanone, methyl acetate and chloroform are somewhat miscible with water and it was thought to be possible that the method could work with partially miscible solvents, so were also trialled.

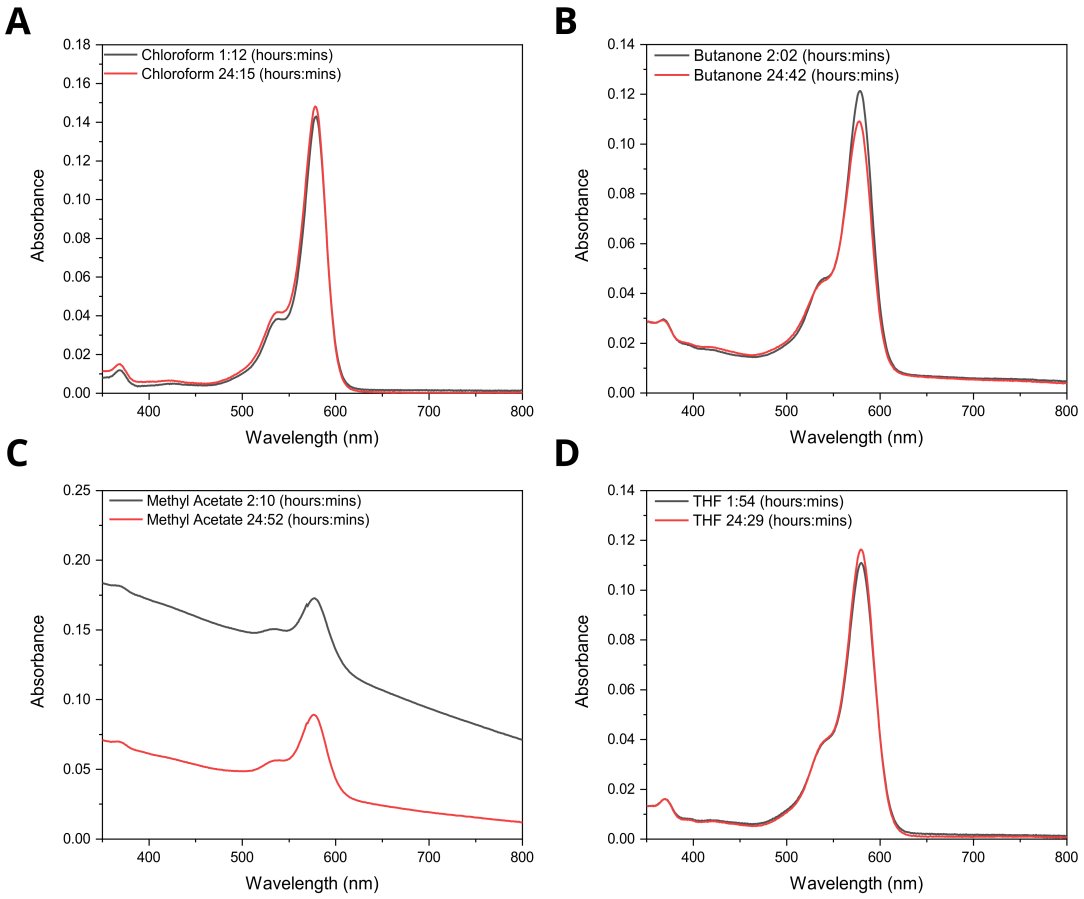

Figure 3.5: Stability of lipid-tagged dye in various solvents. Comparison of 99% DOPC, 1% Texas Red DHPE absorbance after 0 hours and 24 hours for samples suspended in (A) chloroform, (B) butanone, (C) methyl acetate, and (D) tetrahydrofuran.

To assess the stability of the QDs and lipids in the four potential solvents, four aliquots of $CuInS_2/ZnS$ QDs and four aliquots of fluorescently-labelled DOPC/Texas Red lipid were dried down separately and re-hydrated with each of the four solvents. The experiment was designed so that the absorbance of QDs and the fluorescent lipids would be 0.1 if 100% of the material was stabilised. Chloroform acted as the control solvent as

both the fluorescent lipids and $CuInS_2$/ZnS QDs are known to be stable when dispersed in this solvent. A series of absorbance and fluorescence emission spectra were taken at regular time points for each of the samples over a period of 24 hours, where a significant decrease in absorbance and fluorescence intensity would represent a drop in stability as the samples agglomerate. Both the lipids and QDs need to be stable for a number of hours to allow for lipid encapsulation during the lengthy solvent removal stage using the rotary evaporator. A decrease in the fluorescence intensity or a peak shift in the steady-state fluorescence emission spectra would be indicative of lipid instability, as an aggregation of Texas Red dye, tagged to the lipid heads, blue-shifts and quenches the fluorescence [198]. Absorbance measurements for the DOPC in three of the four solvents showed good stability, with comparable peak absorbance and position observed after a period of 24 hours for the samples in chloroform, butanone and THF (Figure 3.5), although butanone and THF show a 15% drop in absorbance compared to chloroform. The main absorption peak position of the Texas Red dye remained consistent in the chloroform, butanone and THF solvents, although a small reduction in the secondary peak was initially observed for the THF and butanone samples, again suggesting a small amount of degradation of the dye in these solvents. Significant light scattering (cloudiness) was observed initially for the lipid sample in methyl acetate, accompanied by a drop in fluorescence after 24 hours, suggesting that the lipid is unstable in the solvent and that it should not be used as a cosolvent during rotary evaporation.

Dispersing dried QDs into methyl acetate also proved to be difficult, leading to a low initial absorbance (Figure 3.6, blue data points). A clear red solution was observed for the QDs in chloroform, butanone and THF, suggesting that they were initially stable in these solvents (Figure 3.6, black/red/green data points). However, there were visible QD aggregates in methyl acetate which suggested a lack of $CuInS_2$/ZnS stability in methyl acetate with the hydrophobic ligand; the solvent was too polar. The same conclusion can be made for THF, with a sharp decrease seen in the absorbance after the first measurement due to the QDs agglomerating into large clusters and falling out of the

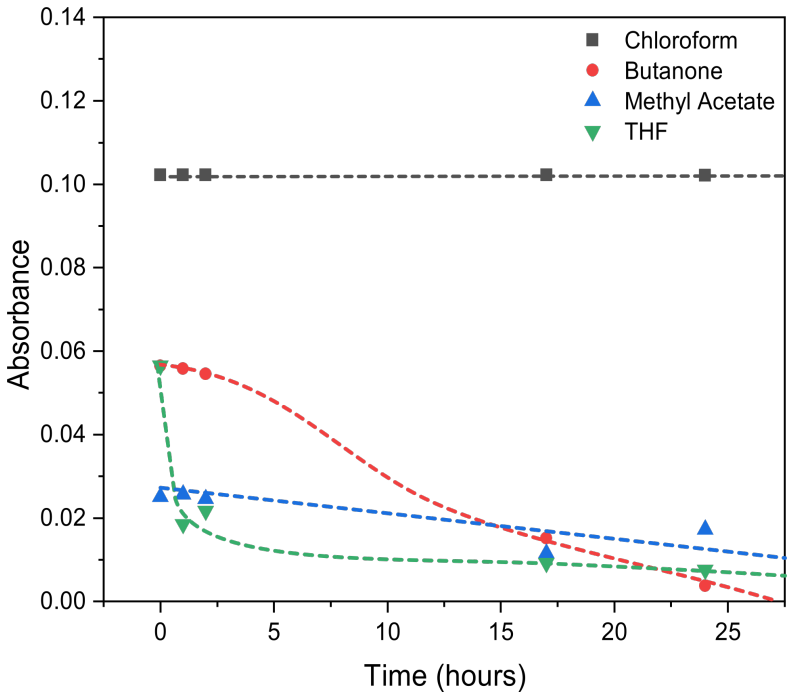

Figure 3.6: Stability measurements of $CuInS_2/ZnS$ QDs in various solvents. Absorbance of $CuInS_2/ZnS$ QDs at a wavelength of 400 nm against time when suspended in THF (black), methyl acetate (red), butanone (green) and chloroform (blue) solvents.

solution. The QDs were relatively stable in butanone over a period of three hours, and although the QDs were unstable over a 24-hour period, the rotary evaporation method could still be trialled. The fluorescence and absorbance of the $CuInS_2/ZnS$ QDs in chloroform remained consistent throughout the experiment, as expected. In summary, the only water-miscible organic solvent that stabilised both the lipids and the QDs was butanone therefore the rotary evaporation protocol was trialled with this solvent only.

3.4.1 Initial Rotary Evaporation with Butanone

After initial stability measurements, the rotary evaporation method was tested with butanone as the solvent. After adding 1 ml of butanone-QD-lipid solution dropwise to 20 ml of 50mM HEPES, visible aggregates of $CuInS_2/ZnS$ occurred in the solution. This was thought to be due to the imperfect miscibility of butanone and water. Due to the presence of large, visible QD aggregates floating in an otherwise colourless solution, the experiment was considered a failure as the DOPC lipids would be unable to encapsulate

the QDs and spectroscopy data was not taken.

It was hoped that the hydrophobic tails of the phospholipid would stay within the apolar butanone droplets, with the hydrophilic heads attracted to the polar buffer, however, it seems likely that immiscibility caused the hydrophobic QDs and/or lipids to form large aggregates in the stable butanone environment or at the liquid-liquid interfaces. Aggregation may be reduced if the solvent were perfectly miscible with water, but the surface chemistry of the QDs would need to be altered. In future work, the polarity of the surface chemistry could be increased by introducing mixed ligands during synthesis or via a ligand exchange, with nonanol similar in structure to nonanethiol with the addition of an OH bond at the cap of the ligand. Introducing a percentage of the nonanol ligand to the surface of the $CuInS_2$/ZnS QD would decrease the hydrophobicity of the QD, likely increasing stability in polar solvents such as THF and methyl acetate.

3.4.2 Surface Chemistry Alteration of the $CuInS_2$/ZnS Quantum Dots

To pursue the stabilisation of QD clusters by association with lipids using the rotary evaporation method, the surface chemistry must be optimised to allow the QDs to dissolve in THF during the initial re-hydration phase. The $CuInS_2$/ZnS QD syntheses used a nonanethiol surface chemistry, however, stability measurements showed a drop in stability over a three-hour period, thus the surface chemistry was altered to increase stability.

The synthesis procedure was altered to allow an octanethiol surface chemistry to be trialled for rotary evaporation, where the shorter stabilising ligands were hoped to slightly increase QD polarity for suspension in THF. The synthesis procedure remained the same, with minor adjustments made to the core growth time to accommodate for the observed increase in the rate of growth as the ligand length decreased, as discussed in Section 3.1. A post-synthesis ligand exchange was performed to trial a mixed-ligand (80% octanethiol, 20% mercaptononanol) surface chemistry (Figure 3.7 A-B), designed

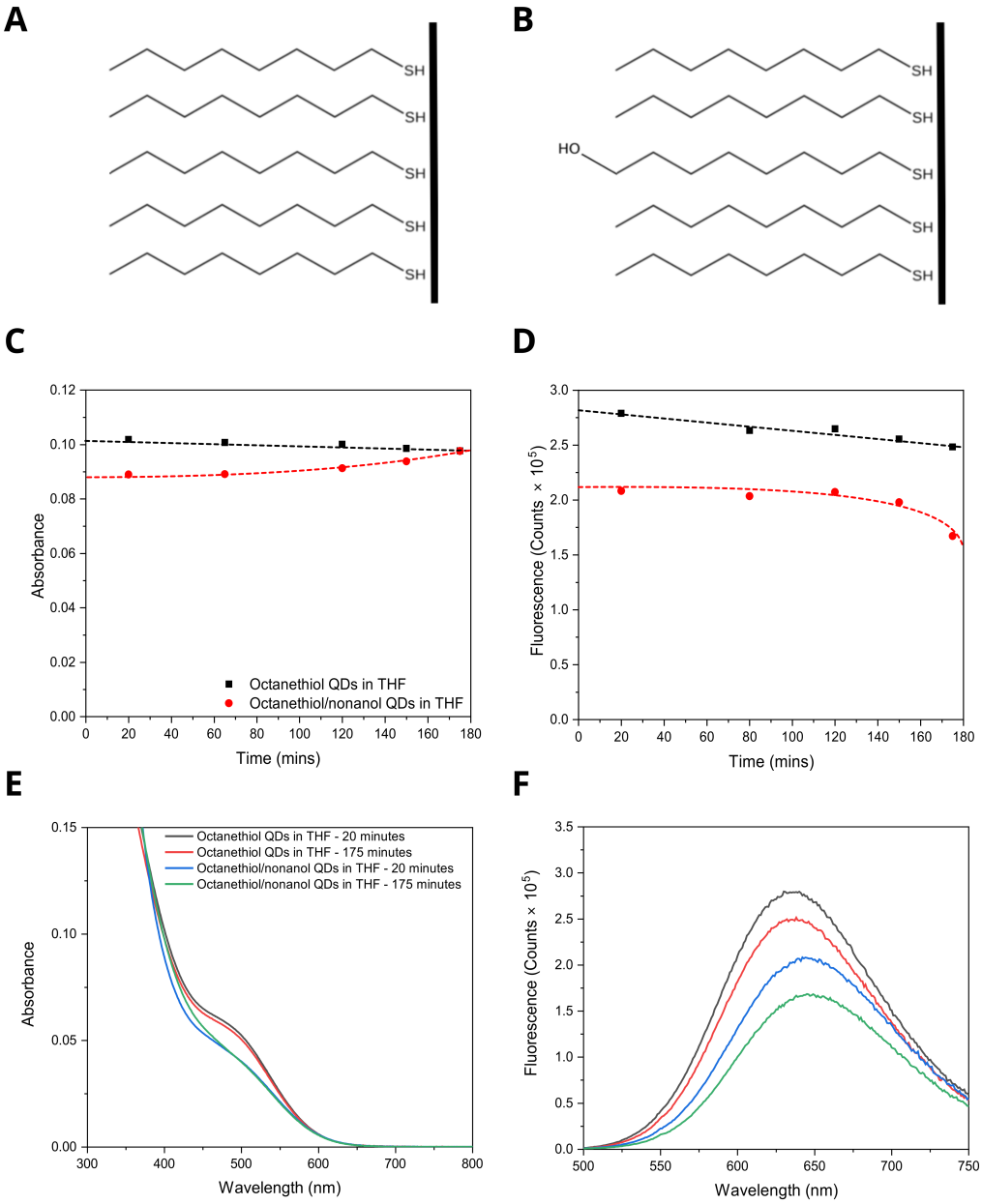

Figure 3.7: Stability and spectra of $CuInS_2$ QDs with differing surface chemistries. (A) Schematic showing the surface chemistry of the octanethiol-coated $CuInS_2$/ZnS quantum dots. (B) Schematic showing the surface chemistry of the mixed-ligand $CuInS_2$/ZnS quantum dots, consisting of 80% octanethiol and 20% mercaptononanol. (C) Plot of absorbance at 400 nm and (D) plot of steady-state fluorescence (λ_{ex} = 540 nm) at fluorescence emission peak for octanethiol-coated and 80% octanethiol/20% mercaptononanol-coated $CuInS_2$/ZnS QD-DOPC nanocomposites in THF to show sample stability. (E) Absorption spectra and (F) steady-state fluorescence emission spectra (λ_{ex} = 540 nm) of octanethiol-coated and 80% octanethiol/20% mercaptononanol-coated $CuInS_2$/ZnS QDs in THF solvent taken 20 minutes (black/blue) and 175 minutes (red/green) after solvent addition.

to further increase surface polarity and therefore stability in the water-miscible THF. The stability of octanethiol-coated $CuInS_2$/ZnS QDs was compared to QDs with an 80% octanethiol:20% mercaptononanol surface chemistry via absorbance (Figure 3.7 C) and steady-state fluorescence (Figure 3.7 D) measurements, with both surface chemistries relatively stable over a three-hour period.

3.4.3 Stability Measurements of $CuInS_2$/ZnS QDs in THF

After characterisation of the $CuInS_2$/ZnS QDs, the stability of the QDs was measured in THF over a three-hour period using absorbance and steady-state fluorescence spectroscopy, where the quartz cuvettes were sealed to reduce solvent evaporation. Absorbance measurements show a significant difference in absorbance between the octanethiol and mixed-ligand QDs when first re-hydrated in THF (Figure 3.7 E), with the octanethiol QDs showing a greater absorbance and higher stability. The fluorescence spectroscopy measurements show an even greater disparity between the initial fluorescence count for the octanethiol and mixed-ligand QDs (Figure 3.7 F), although this is due to a higher relative fluorescence based on the larger octanethiol QD size and fluorescence emission peak. The absorbance of the mixed-ligand QDs increases with time and eventually surpasses the absorbance of the octanethiol QDs, suggesting particle aggregation and increased scattering. Fluorescence spectroscopy measurements support aggregation, as they show a gradual decrease in the fluorescence and a small red-shift in both types of QDs.

The fluorescence of the octanethiol-coated QDs drops 12% over the three-hour period, compared to a 19% decrease for the mixed-ligand QDs from a lower initial value. This suggests that the octanethiol QDs are sufficiently stable for rotary evaporation experiments on a shorter timescale, and mixed-ligand QDs may be stable enough for rotary evaporation on a two-hour timescale, allowing the progression of lipid bilayer incorporation experiments. It is likely that the short-chain octanethiol ligand benefited from a sufficient increase in polarity to achieve stability in THF, whereas the combination of

the short-chain and 20% mercaptononanol in the mixed-ligand QDs resulted in a QD surface chemistry that was slightly too polar. This eventually resulted in sample aggregation and scattering over a three-hour period, leading to a sharp drop in fluorescence as particles precipitated out of the solution.

3.4.4 Attempting to Self-Assemble QD Nanoclusters Using Rotary Evaporation with THF

Once the stability of the $CuInS_2$/ZnS QDs had been achieved in THF, rotary evaporation could be trialled in an attempt to achieve lipid-stabilised QD nanocluster formation in an aqueous environment. During rotary evaporation, the THF cosolvent would be evaporated from a miscible mixture of THF and aqueous buffer by setting the temperature to 60 °C, and lowering the boiling point of THF to 40 °C by reducing the pressure of the flask containing the buffer-cosolvent mixture. As previously described, once the THF is fully evaporated, the hydrophobic QDs would associate with the hydrophobic lipid tails while the hydrophilic lipid heads should stabilise the structures within the aqueous environment. The first step would be to investigate whether significant aggregation of the $CuInS_2$/ZnS QDs occurs when the chosen buffer is added to the QDs in THF to form a co-solvent mixture. Both octanethiol-coated and 80% octanethiol/ 20% nonanol-coated $CuInS_2$/ZnS QDs were separately dried to a film then re-suspended to an absorbance of 0.1 in THF. 5 ml of 50 mM HEPES, 100 mM NaCl at pH 7.5 was added dropwise to 500 μL of the $CuInS_2$/ZnS QDs in THF under stirring to form a stable co-solvent mixture, where the solvent could then be removed during rotary evaporation.

As shown in Figure 3.8, the octanethiol-coated $CuInS_2$/ZnS QDs and the 80% octanethiol/ 20% mercaptononanol-coated QDs were still moderately stable in the water/THF solvent mixture although cloudiness was evident. The sample cloudiness observed for both QD surface chemistries may suggest either a phase separation between the THF and water [199, 200] or small-scale aggregation of the QDs. The timing of this experiment coincided with the closure of all laboratories in March 2020, so samples were

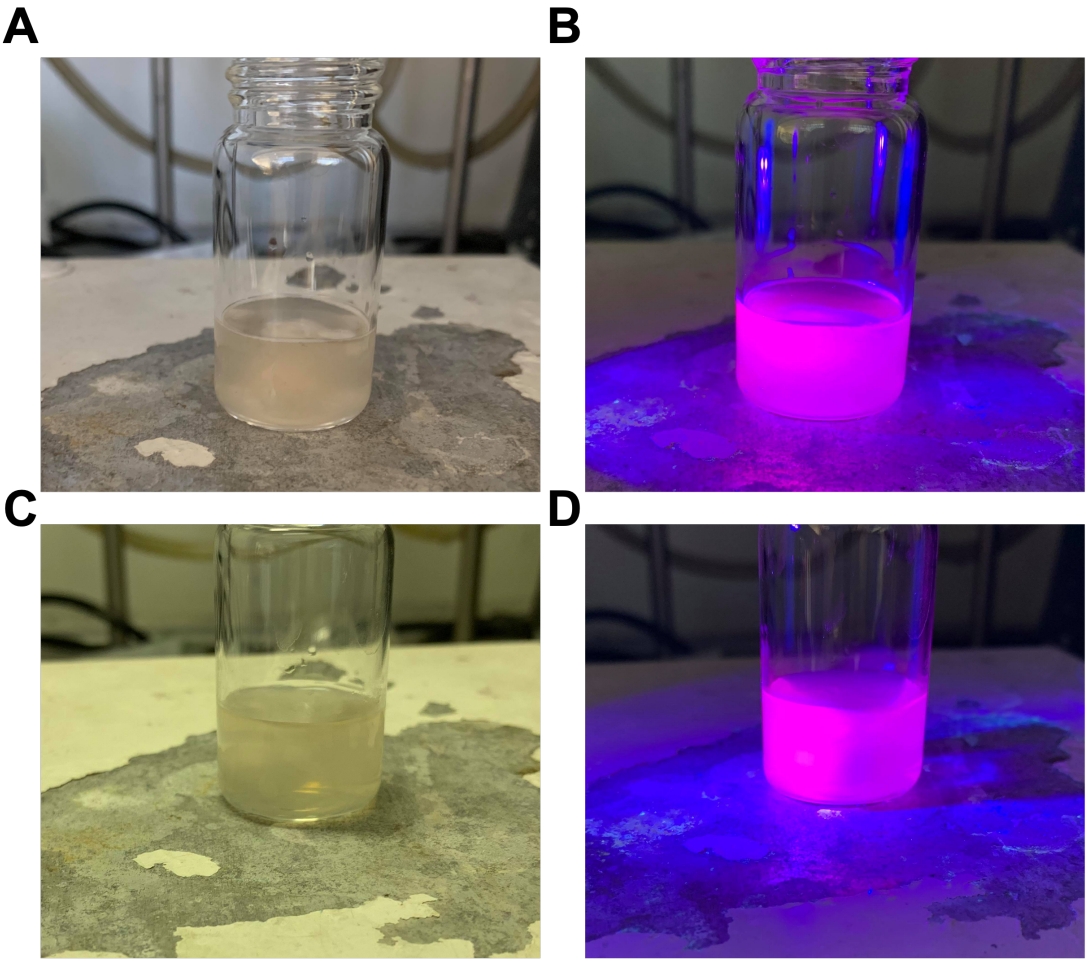

Figure 3.8: Photographs of $CuInS_2$ QDs in co-solvent mixture. Images taken (A) under natural light and (B) under UV light (λ_{ex} = 360 nm) immediately after dropwise addition of 50 mM HEPES, 100 mM NaCl at pH 7.5 to octanethiol-coated QDs in THF. Images taken (C) under natural light and (D) under UV light (λ_{ex} = 360 nm) immediately after dropwise addition of 50 mM HEPES, 100 mM NaCl at pH 7.5 to 80% octanethiol/ 20% nonanol-coated QDs in THF.

unable to be characterised using absorbance and steady-state fluorescence spectroscopy.

At the stage when experiments resumed following the lab closure, success with forming QD nanoclusters within an aqueous environment was achieved with an alternative method developed in parallel with the attempts at rotary evaporation association. Additionally, the overarching goals of the project required developments to be made with respect to QD and light-harvesting protein association, explored in Chapter 4, thus re-

search on the association of lipids and QDs by rotary evaporation via a cosolvent was halted. Although the investigated samples would need to be characterised using absorbance and steady-state spectroscopy to confirm, the images from Figure 3.8 suggest that a reasonable dispersion of the QDs was achieved throughout the co-solvent mixture and that rotary evaporation could be investigated in future studies as a promising method of associating lipids and QDs.

3.5 QD Nanocluster Formation by Detergent Encapsulation and Biobead Removal

The third potential method of forming lipid-stabilised QD nanoclusters to be investigated in parallel was a method involving detergent encapsulation and removal, where micelle-forming detergent molecules were added to a dry film of mixed lipids and QDs in an attempt to form a microheterogeneous solution with the $CuInS_2$/ZnS QDs encapsulated by the lipid and surfactant. The procedure was designed to remove the detergent gradually, in stages using macroporous polystyrene 'Biobead adsorbent', a commercially available material that is established to selectively remove detergent molecules in preference to other larger molecules. After this detergent removal, the resulting assembly should be lipid-stabilised QDs. Initial experiments using $CuInS_2$/ZnS QDs and lipids were completed using a simple zwitterionic DOPC phospholipid, although charged lipids such as DOPS and DOPG were introduced in incremental stages to optimise the formation procedure, summarised later in Chapter 3.6.1.

3.5.1 Quantum Dot and Lipid Stability in Various Detergents

To determine suitable detergents for the hydration of dried lipid/QD thin films, stability measurements must first be taken. The detergent must stabilise and disperse the lipids and QDs, allowing for lipid-stabilisation of the QDs when the excess detergent is removed using adsorbent Biobeads, therefore multiple detergents were investigated with a range of CMCs. The detergent would need to stabilise both lipids and QDs independently,

otherwise, one component would be likely to aggregate, leading to significant scattering and eventual precipitation of the lipid or QDs.

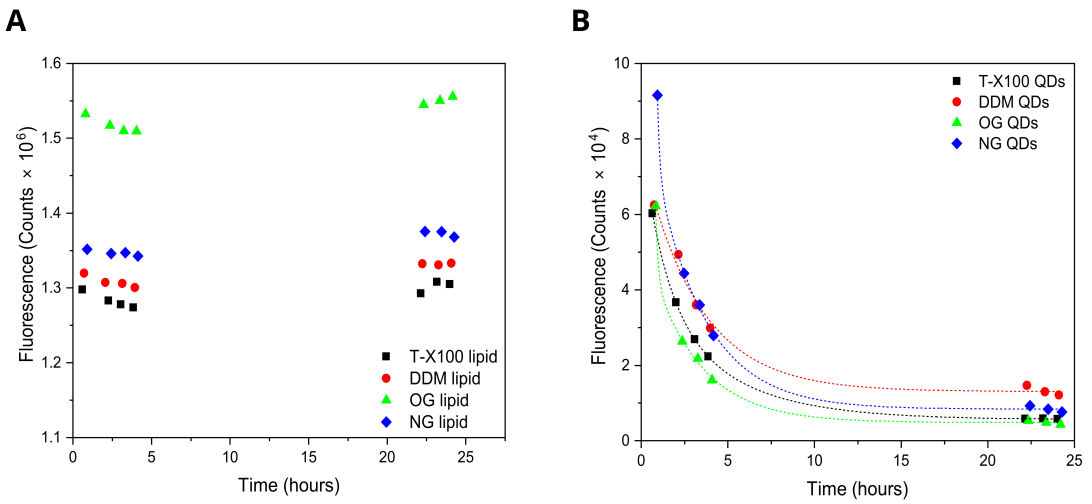

Figure 3.9: Stability of lipid-tagged dye and $CuInS_2$ QDs in various detergents. A plot of steady-state fluorescence emission peak (λ_{ex} = 500 nm) against time for (A) 99% DOPC, 1% Texas Red DHPE and (B) nonanethiol-capped $CuInS_2$/ZnS QDs. Detergents are Triton X-100 (black), α dodecyl maltoside (red), octyl glucoside (green) and nonyl glucoside (blue). Detergent concentration was 0.5% w/v.

Stability measurements were taken for both the $CuInS_2$/ZnS QDs and Texas Red-tagged DOPC lipids immediately following the addition of non-ionic 0.5% w/v detergent to the dry thin film. Initially, four different detergents were investigated side-by-side, with α-DDM, Triton X-100, OG and NG compared. The α-DDM detergent was chosen as it had previously been used to successfully incorporate plant LHCII into liposomes without denaturing the protein, simplifying any potential succeeding stages of protein association with QD nanoclusters. The Triton X-100, OG and NG detergents were chosen as they are also non-ionic detergents with similar properties to the α-DDM detergent while having different CMCs, which may positively or negatively affect the size of the lipid-stabilised QD clusters (the actual size of the initial QD-lipid clusters were unknown at this stage without imaging).

The DOPC lipid was stable in all four of the non-ionic detergents at 0.5% w/v as expected

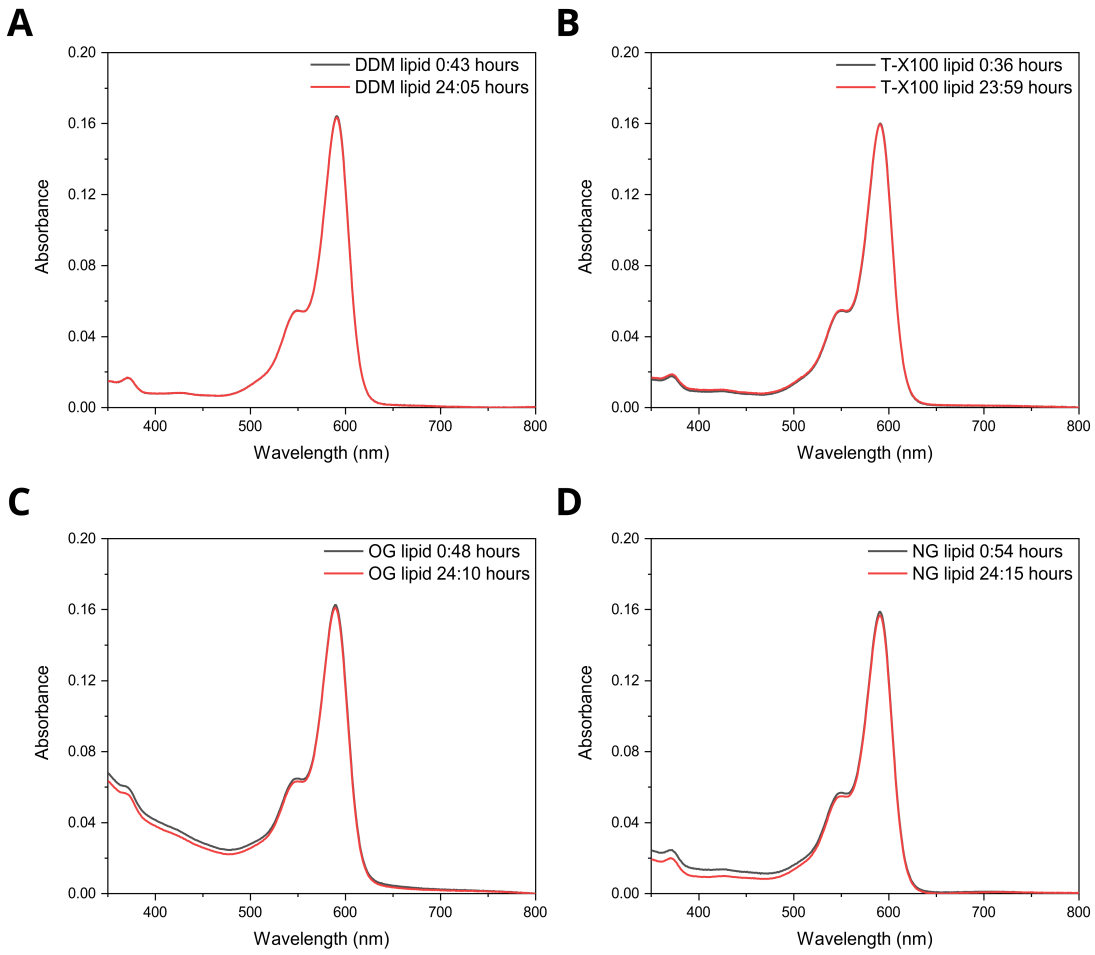

Figure 3.10: Stability of 99% DOPC, 1% Texas Red DHPE after 24 hours in various detergents. Absorbance measurements of 99% DOPC, 1% Texas Red DHPE immediately after adding detergent (black) and 24 hours after adding detergent (red) for (A) α dodecyl maltoside, (B) Triton X-100, (C) octyl glucoside and (D) nonyl glucoside.

(Figure 3.9 A), with the peak absorbance of the Texas Red decreasing by <5% for OG, the largest decrease in absorbance (Figure 3.10 C). The percentage decrease in absorbance was much smaller in α-DDM and Triton X-100, although these two detergents show a lower fluorescence than OG and NG. In contrast, the QD stability measurements showed a sharp decrease in fluorescence as they appeared to precipitate out of the solution, eventually reaching a minimum after 24 hours (Figure 3.9 B). This suggests that the QDs were either not stabilised by the lipid and therefore sedimented or the associated QD-lipid clusters were not efficiently dissolved/encapsulated by the surfactant.

3.5.2 Stability of $CuInS_2$/ZnS QDs in Sodium Cholate Detergent

After testing DDM, OG, NG and TX-100 with limited success, it was considered that another detergent with a much lower aggregation number (the number of molecules present in a micelle once the CMC has been reached) may be more effective at encapsulating the lipids and QDs, as this should lead to the formation of spherical mixed lipid-detergent micelles as opposed to elliptical micelles. This is due to an increase in the curvature of the detergent, as discussed in Section 1.4.1, which may reduce the size of the encapsulated QD clusters. The non-ionic detergents were replaced with the ionic detergent sodium cholate, where previous publications had achieved successful association of dodecanethiol-coated CdSe QDs with lipids [126]. A comparison of the CMC and aggregation number for sodium cholate and the previously-investigated detergents is shown in Table 3.3. Electrostatic interaction between the charged carboxylate group of the anionic sodium cholate detergent (Figure 3.11 A) may make it more energetically favourable for the QD to associate with the lipids, and removal of detergent monomers from the buffer using polystyrene Biobeads should remain similar to the removal of Triton X-100 [201]. Similar to the previous detergents, the next step was to investigate the stability of lipids and QDs in sodium cholate to achieve successful re-hydration of the thin film and prevent aggregation and precipitation of either component.

Properties of Detergents		
Detergent	Critical Micelle Concentration (mM)	Aggregation Number
α-DDM	0.152	90
Triton X-100	0.9	100 - 150
Octyl glucoside	~20	27 - 100
Nonyl glucoside	6.5	133
Sodium cholate	9 - 15 (20 - 25 °C)	2 - 3

Table 3.3: Critical micelle concentration and aggregation number of the detergents trialled during QD and lipid re-hydration.

Figure 3.11 B shows that the stability of the sodium cholate/lipid-stabilised QDs is similar to that of identical concentrations of QDs and lipids in the soluble chloroform over a period of five hours. A significant red-shift in fluorescence emission spectra could be attributed to electronic rearrangement of the charge carriers due to a change in the surrounding environment, but the observed 40 nm red-shift was likely due to successful clustering of the QDs and could be attributed to downhill energy transfer via FRET from the smaller, high-energy QDs to larger, lower-energy QDs. The possible photophysical interpretations are discussed in detail in Chapter 5.

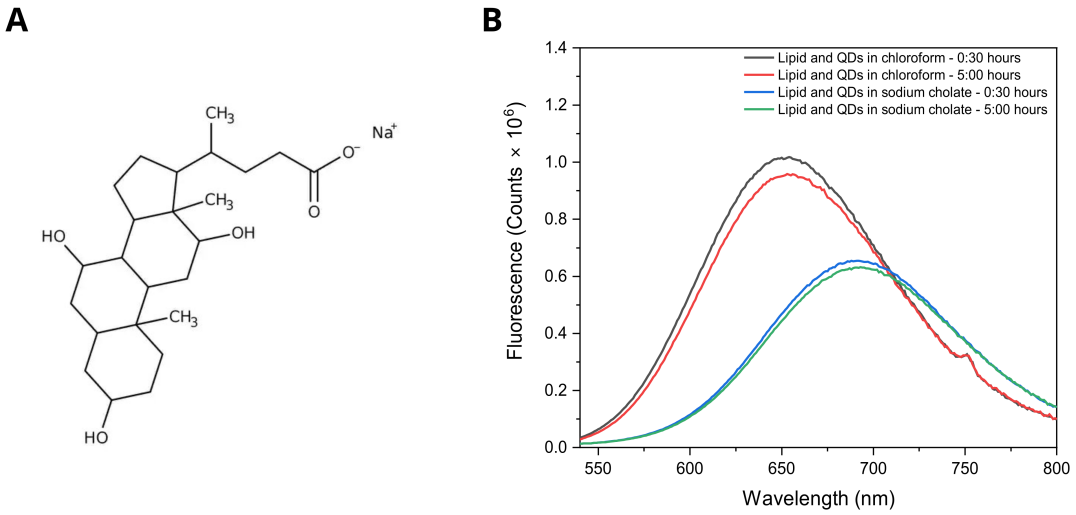

Figure 3.11: Stability of QDs with lipid in chloroform and sodium cholate detergent. (A) Sodium cholate detergent structure. (B) Steady-state fluorescence emission spectra (λ_{ex} = 500 nm) of $CuInS_2$/ZnS QDs in chloroform after 30 minutes (black) and 5 hours (red) compared to $CuInS_2$/ZnS QDs in 4% w/v sodium cholate detergent after 30 minutes (blue) and 5 hours (green) showing QDs are in a stable state. QDs are colloidal in chloroform and stabilised by a combination of the lipid and detergent in the buffer.

3.5.3 Sodium Cholate Detergent Removal Using Biobeads

As the QD-lipid assemblies were found to be stable in the sodium cholate detergent, the detergent could then be removed in the hope that the QD-lipid clusters would organise into a final stable form. The Biobead detergent removal method outlined in Methods section 2.2.6 was followed. Briefly, the lipid-nanoparticle nanocomposites were re-suspended

with sodium cholate detergent to encapsulate the structures, which was then removed using the Biobead adsorbent after short agitation periods that promote self-assembly. Six samples were prepared in parallel at a lipid:QD ratio of 1500:1 and characterised at each stage of the self-assembly procedure to investigate the importance of the lipid and detergent in stabilising the $CuInS_2$/ZnS QDs (Figure 3.12).

As seen in Figure 3.12 A, a direct overlap between the absorbance of the $CuInS_2$/ZnS QDs in chloroform and the $CuInS_2$/ZnS QDs with lipid mixture in chloroform was observed, suggesting the presence of the lipid did not disrupt the colloidal dispersion of the QDs in solvent (Figure 3.12 A, *black* vs. *red* line). When no lipid was present in the control sample (only QDs dried down and hydrated with detergent), the QDs were found to precipitate from the buffer following detergent removal with Biobeads, as expected, thus emphasising the importance of the lipid in the self-assembly procedure (Figure 3.12 A, *green* line). Significant scattering was observed for the control sample where detergent was not used for re-hydration of the QD/lipid thin film compared to samples where detergent was used (Figure 3.12 A, *blue* line), with an increase in turbidity of the sample likely due to agglomeration or larger structures being formed without the control of the sodium cholate detergent. An expected amount of scattering was observed, in line with the formation of liposomes and other lipid structures completed within the group, for both of the 1500:1 lipid:QD samples prepared according to the developed method; one characterised before the removal of the detergent with macroporous Biobeads and the second characterised after complete detergent removal (Figure 3.12 A, *gold* and *lilac* lines). The first-excitation peak is more prominent in the sample characterised prior to before the detergent was removed, with a slightly greater absorbance, suggesting a greater concentration of QDs present in the sample prior to detergent removal. This drop in concentration may be due to the adsorption of lipids by the Biobeads, with further investigation into the effect of the lipid:QD molar ratio explored briefly in Chapter 3.6.1 and in-depth during Chapter 5.3. Loss of lipid would result in a lower concentration of stabilised QDs, thus promoting QD precipitation during the detergent removal stages of

the experiment and decreasing the QD concentration in the remaining sample.

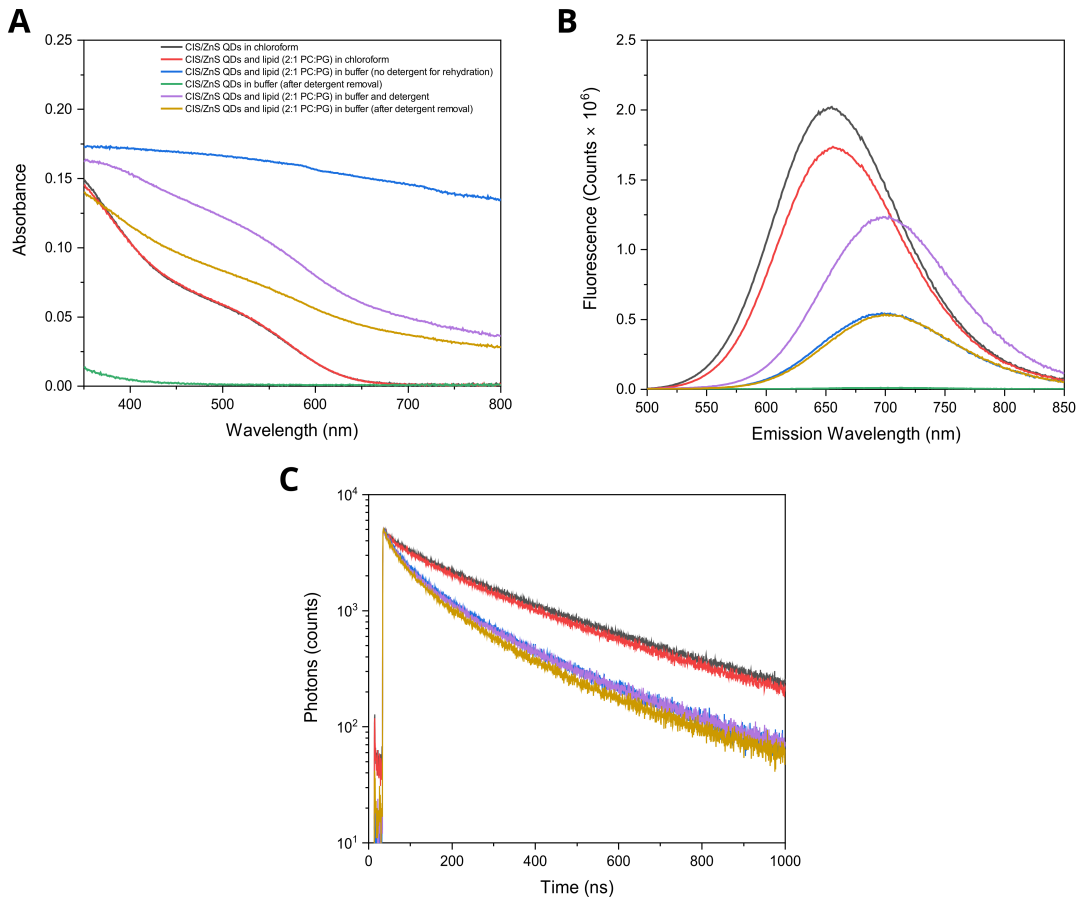

Figure 3.12: Spectra of $CuInS_2$ QDs at each stage of the nanocluster self-assembly procedure. (A) Absorbance, (B) steady-state fluorescence and (C) time-correlated single photon counting characterisation of associated QDs and lipids at each stage of the developed self-assembly procedure (with negative control measurements included).

As with the absorbance measurements, there is some overlap between the steady-state fluorescence (Figure 3.12 B) of the colloidal $CuInS_2$/ZnS QDs in chloroform (*black* line) and the $CuInS_2$/ZnS QDs with lipid in chloroform (*red* line), although the presence of the lipid contributes to a 13% drop in fluorescence intensity. A minimal signal was observed for the control sample of QDs containing no lipid (*green* line), agreeing with the data taken from absorbance measurements. Again, a large, 45 nm red-shift occurs during re-hydration of the lipid and QD thin film (*lilac* line), with this red-shift consistent in

the control sample prepared without the use of the sodium cholate detergent (*blue* line), and also in the sample prepared according to the developed method after detergent has been removed using the Biobead adsorbent (*gold* line). Again, the significant red-shift supports the theory of FRET between clustered QDs, with energy being transferred from QDs with high energy to QDs with lower energy within the Förster radius. The fluorescence emission intensity decreased by 50% when the detergent was removed using the Biobeads, thus confirming a loss of QDs during the detergent removal procedure as speculated from the absorbance data and the consistent red-shift observed in the steady-state fluorescence data. The fluorescence intensity is almost identical to that of the control sample where detergent was not used for thin-film re-hydration, suggesting firstly that the majority of the detergent was removed using the adsorbent Biobeads and secondly that the detergent may play a similar role to the lipid in stabilising the QDs, therefore that the drop in fluorescence intensity observed when removing the detergent may be negated by using a higher concentration of lipid during self-assembly. Time-correlated single photon counting measurements (Figure 3.12 C) show the presence of the lipid in chloroform leads to a slight increase in the steepness of the decay curve for the colloidal $CuInS_2$/ZnS QDs (*red* vs. *black* lines), in agreement with the steady-state fluorescence characterisation. A more rapid decay was observed for all samples where the lipid and QDs were associated within the buffer (*blue*, *lilac* and *gold* lines) compared to samples of the colloidal QDs in chloroform (*red* and *black* lines), again consistent with FRET and non-radiative energy dissipation.

From absorbance, steady-state fluorescence and lifetime measurements, it can be concluded that the $CuInS_2$/ZnS QDs are colloidal when dispersed in chloroform, but cluster together when associated with lipid after re-hydration with buffer and detergent. The detergent is a vital component in reducing turbidity and controlling the size of the resulting nanocomposite structures, and the molar ratio of lipid to QDs appears to determine the uptake of QDs, with unassociated QDs precipitating out of the buffer. A full investigation into the structure, photophysics and energy transfer pathways of the resulting

lipid/QD nanocomposites will be explored in Chapter 5, including a detailed discussion on the importance of the lipid concentration to the nanocluster formation as well as an investigation into lipid and QD co-localisation.

3.6 Optimisation of the QD Nanocluster Formation Procedure

3.6.1 Introduction

To further understand the self-assembly of the lipid/QD nanocomposite structures, optimisations were performed in an attempt to increase QD uptake and further control the formation procedure. With respect to the lipid, the effective head-group area, effective tail-group area and lipid length contribute to the geometric shape, with a charged lipid head group resulting in a larger effective head-group area due to repulsive interactions and therefore larger effective curvature (Figure 3.13 A). The effective curvature of the lipid contributes to the structure of the lipid-QD assembly, as a truncated effective shape is beneficial in reducing the formation of nodes (Figure 3.13 B) in comparison to a cylindrical effective shape [202]. This may be effective in decreasing the size of the self-assembled nanoclusters as a smaller closed lipid monolayer should form around the clustered QDs (Figure 3.13 C), therefore reducing the red-shift observed within the QD nanoclusters as less energy would be dissipated. The formation of a closed lipid monolayer may be due to the clusters of QDs acting similarly to a single large nanoparticle, with a combined effective size above the 'critical size' at which is more energetically favourable for spherical nanoparticles to form liposomes as opposed to micelle structures [202]. As the size of the QDs cannot be reduced significantly without significantly altering the optical properties [191, 203–205], the choice of lipid was varied to increase control of the nanocluster organisation and to increase the steady-state fluorescence with respect to QD uptake.

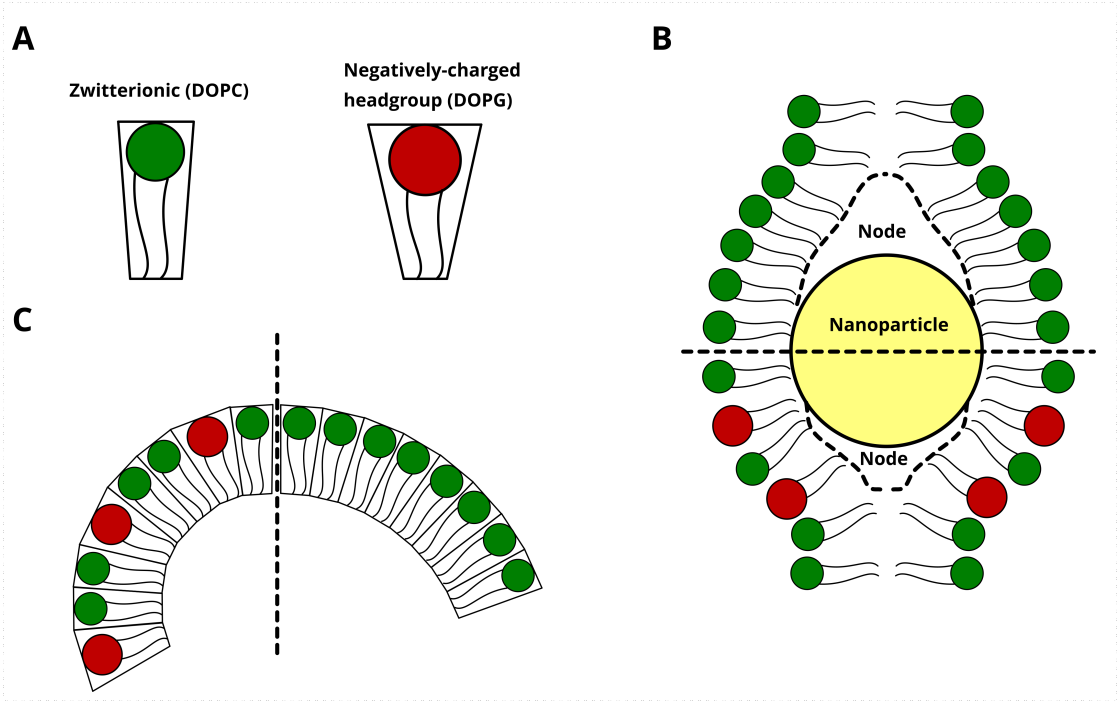

Figure 3.13: Cartoon showing the geometric shape and lipid curvature of DOPC and DOPG. (A) Comparison of the cylindrical geometric shape of zwitterionic DOPC (green) and the truncated shape of DOPG (red). (B) Comparison of the effective curvature from a 2:1 DOPC:DOPC closed lipid monolayer (left) with the effective curvature from a DOPC closed lipid monolayer (right). Not to scale.

3.6.2 Effect of the Lipid Choice on Nanocluster Formation

Initial investigations into altering the properties of the QD cluster involved introducing charged DOPG and DOPS lipids to the system in order to optimise the lipid curvature. Integration of negatively-charged lipids with the zwitterionic DOPC would increase the effective lipid curvature, due to a larger effective head-group area as previously mentioned, in turn increasing the critical QD radius for micelle formation if using spherical QDs [202]. As the self-assembly procedure uses tetrahedral $CuInS_2$/ZnS QDs, it is unlikely that decreasing the size of the QDs below the critical radius will promote the formation of a lipid bilayer as opposed to a closed lipid monolayer due to the QD shape, as nodes (energetically unfavourable areas of free space surrounding the nanoparticle) are more likely to form than when compared to spherical QDs of identical size. The introduction of a charged lipid also allows investigation into improving the stability of

the clusters, as electrostatic interactions should reduce liposome interactions and cluster-cluster aggregation.

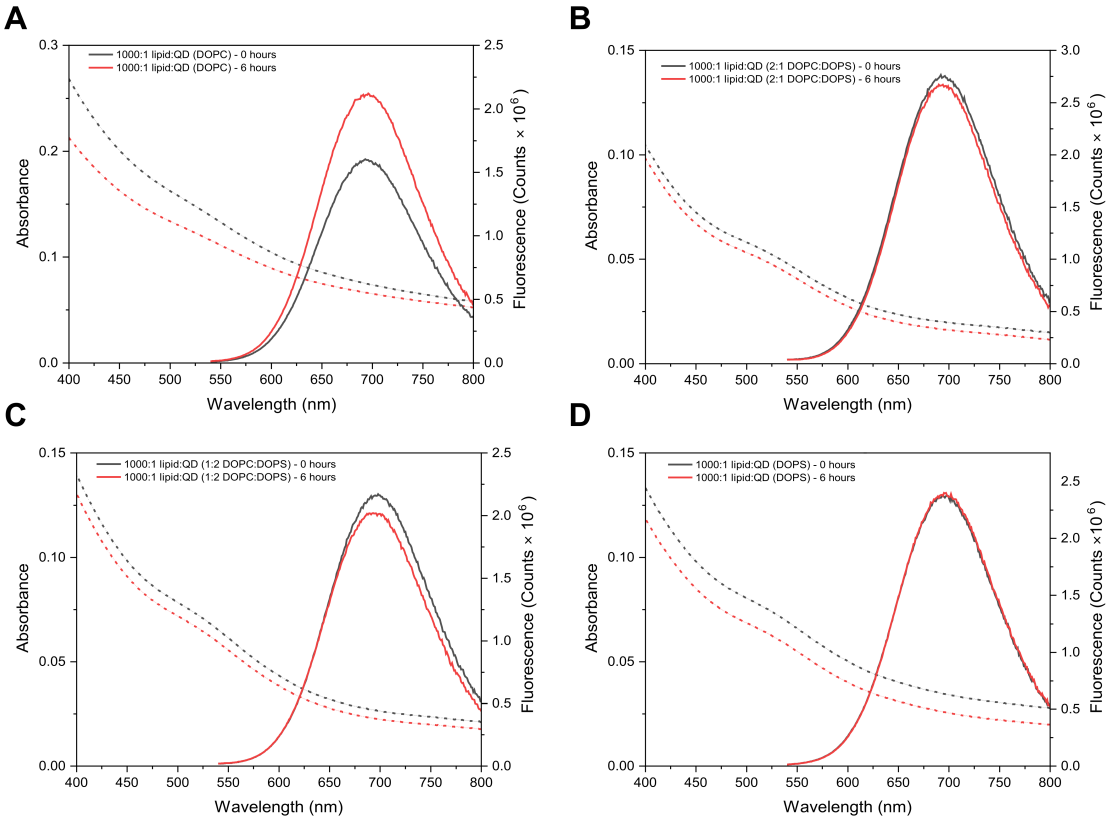

Figure 3.14: Effect of lipid ratio alteration on $CuInS_2/ZnS$ QD nanocluster spectra. Steady-state fluorescence emission spectra of nonanethiol-coated $CuInS_2/ZnS$ QD-lipid nanocomposites (1000:1 lipid:QD) in 50 mM HEPES buffer immediately after the final detergent-removal cycle (black) and 6 hours after the final detergent-removal cycle (red) for (a) DOPC lipid, (B) 1:2 DOPS:DOPC lipid, (C) 2:1 DOPS:DOPC lipid and (D) DOPS lipid.

Figure 3.14 shows an improvement in the structure stability over a period of six hours when negatively-charged DOPS was integrated with DOPC, where the steady-state fluorescence was divided by the concentration to give a relative fluorescence of the sample. The fluorescence was consistent after a six-hour period for the 100% DOPS sample in Figure 3.14 D, whereas an anomalous 25% increase in the relative fluorescence was observed for the 100% DOPC sample shown in Figure 3.14 A due to an increase in turbidity, where much of the DOPC/QD nanocomposites had agglomerated and therefore

inflated the absorbance measurements. The scattering likely occurred due to a lack of electrostatic repulsion acting between individual nanocomposites in comparison to the samples containing the negatively-charged lipid, thus leading to sample agglomeration. The mixed-lipid samples (1:2 DOPS:DOPC and 2:1 DOPS:DOPC) show decreases in relative fluorescence between those of the pure DOPC and DOPS samples as expected, although the 1:2 DOPS:DOPS sample shows greater stability after a six-hour period, as well as an optimal relative fluorescence in comparison to the other samples. This suggests that a 1:2 ratio of negatively charged to zwitterionic lipids provides the optimal curvature for the size of QDs used in the experiment with respect to QD uptake, with the presence of the red-shift still suggesting the radius of the clustered QDs is above the critical radius required for micelle formation. Another interpretation is that there is relatively little difference in the QD photophysics for different lipid types - so the lipid charge may not be very important for affecting the QD-QD interactions.

In summary, the final optimised protocol involved drying down dispersed $CuInS_2$/ZnS QDs (colloidal emission peak between 640 - 650 nm) with DOPC/DOPG lipids (1:2 ratio of DOPG:DOPC) into a thin film. The lipid:QD molar ratio was 1500:1, with 4% sodium cholate used to rehydrate the sample to form QD nanoclusters. The detailed version of the final protocol is provided in Methods section 3.2.3.

3.7 Conclusion

The goal of the research in this chapter was to optimise the $CuInS_2$/ZnS QD synthesis protocol and then to develop a method of self-assembling lipid-stabilised QD nanoclusters using hydrophobic $CuInS_2$/ZnS QDs. The $CuInS_2$/ZnS QDs synthesis was optimised to obtain bright QDs with a broad fluorescence emission to allow QD-QD energy transfer, with the production of a high concentration of nanoparticles to sustain many experiments using the same batch for consistency. The QD seeding time was optimised to obtain red QDs with an octanethiol surface chemistry, and the initially linear relationship between

the QD fluorescence emission peak and first excitonic absorption peak was investigated for QD sizes significantly below the limit of quantum confinement. This relationship can be used to synthesise $CuInS_2$ QD cores with a desired fluorescence emission peak by modifying the seeding time, with the QD emission intensity increasing ∼40-fold following passivation of surface trap states with the growth of a ZnS shell. Finally, the cleaning method for $CuInS_2$/ZnS QDs was adapted for the shorter-chain ligand-coated QDs with a slight increase in polarity compared to dodecanethiol-coated $CuInS_2$/ZnS QDs, with the addition of methanol to the cleaning solution allowing for a consistent QD pellet following centrifugation.

Once the QD synthesis had been optimised, QD nanocluster formation was trialled using a variety of techniques including the direct re-hydration of a dried lipid/QD thin film, the hydration of a dried thin film in a cosolvent solution and the use of detergent to stabilise QDs and lipids when hydrating a lipid/QD thin film in aqueous buffer. The use of a cosolvent scaffold to form stable clusters of lipid and QDs prior to solvent removal via rotary evaporation appeared to be a promising method for achieving QD nanoclusters, although time restrictions did not allow the further pursuit of this method beyond preliminary control measurements. After trialling multiple detergents, QD nanoclusters were successfully self-assembled through the use of sodium cholate to stabilise small clusters of lipid-encapsulated QDs in aqueous HEPES buffer. QD nanoclusters displayed a ∼40 nm red-shift compared to colloidal QDs dispersed in chloroform, indicative of QD aggregation and clustering. The red-shift occurred immediately following the rehydration of the thin film with detergent and remained when the detergent was removed from the buffer using polystyrene Biobeads.

Optimisation of the self-assembly procedure was achieved by modification of the lipid choice, with the introduction of a negatively-charged DOPG lipid increasing QD uptake due to a change in the effective lipid shape from cylindrical to truncated. A 2:1 ratio of zwitterionic DOPC to DOPG achieved the greatest QD uptake, with the electrostatic

repulsion of the negatively-charged DOPC head group contributing to an increase in stability as the lipid-encapsulated QD nanoclusters remained dispersed in the aqueous buffer. The direction of research following the formation of QD nanoclusters was to seek a greater understanding of the system, with the nanocluster structure and energy transfer mechanisms between the QDs within the cluster investigated in Chapter 5 via electron microscopy and various spectroscopy techniques.

Chapter 4

Results: Enhancing the Spectral Range of Light-Harvesting Complex II using Quantum Dots

4.1 Motivation

The photosynthetic apparatus of plants is the result of over three billion years of evolution to optimise the efficiency of capturing and converting solar energy into electrochemical energy [129]. The visible light spectral region (400 to 700 nm) accounts for a significant proportion (∼43%) of the total solar irradiance, with the remainder covered by low-energy infrared (IR) radiation (∼52%) and high-energy ultraviolet (UV) radiation (∼5%) [130]. Light-Harvesting Complex II (LHCII), the most abundant membrane protein on earth, contributes to the first stage of photosynthesis in plants by absorbing photons from the 400 - 700 nm region of sunlight and transferring excitation energy to the core complex [135–137], as described in Chapter 1.5.1. LHCII features a high density of pigments and a concentration of chlorophylls which cannot be achieved in organic solvents without significant concentration quenching [129], making it a desirable protein to investigate for use within artificial light-harvesting devices.

Despite the many benefits of LHCII, one disadvantage of use as a light-harvesting component is the incomplete coverage of absorption across the visible light spectrum; in the green spectral region (500 - 600 nm), LHCII has a low absorption when compared to the blue and red spectral domains [135, 136]. As discussed in Section 1.6, this 'green gap' can be filled by introducing an artificial antenna that has strong light absorption in this range to provide an excitation energy source from this region and transfer the energy to the light-harvesting protein [120, 129, 206], supplementing the poor absorption in the green spectral domain. One example of an artificial light antennae is a quantum dot, which has excellent optical properties as well as being able to transfer energy to light-harvesting proteins as a donor and receive energy as an acceptor [167, 168]. A significant limitation of previous investigations is that they required genetic modification of light-harvesting proteins to attach the QD through polyhistidine-tag adaptation in order to achieve specific binding [167, 169]. Other studies have attempted to circumvent this issue through the use of lipids as a stable environment for energy transfer between organic dye molecules and the proteins [120, 207], but a gap still remains with respect to achieving energy transfer between QDs and light-harvesting proteins without genetic modification.

The aim of the research in this chapter was to increase the absorption cross-section and spectral range of photosynthetic proteins, specifically LHCII, by designing a modular system where efficient FRET is achieved from core/shell QD energy donors without the need for genetic modification of the protein. The QDs would need to lie within the Förster radius of the LHCII, therefore hydrophobic QDs could be co-localised within a lipid-stabilised environment (Figure 4.1 A). Alternatively, covalently-bonded QD/LHCII structures could be readily incorporated into a lipid bilayer by the adoption of known proteoliposome self-assembly procedures if the QDs were hydrophilic, as the LHCII is native to the lipid bilayer (Figure 4.1 B).

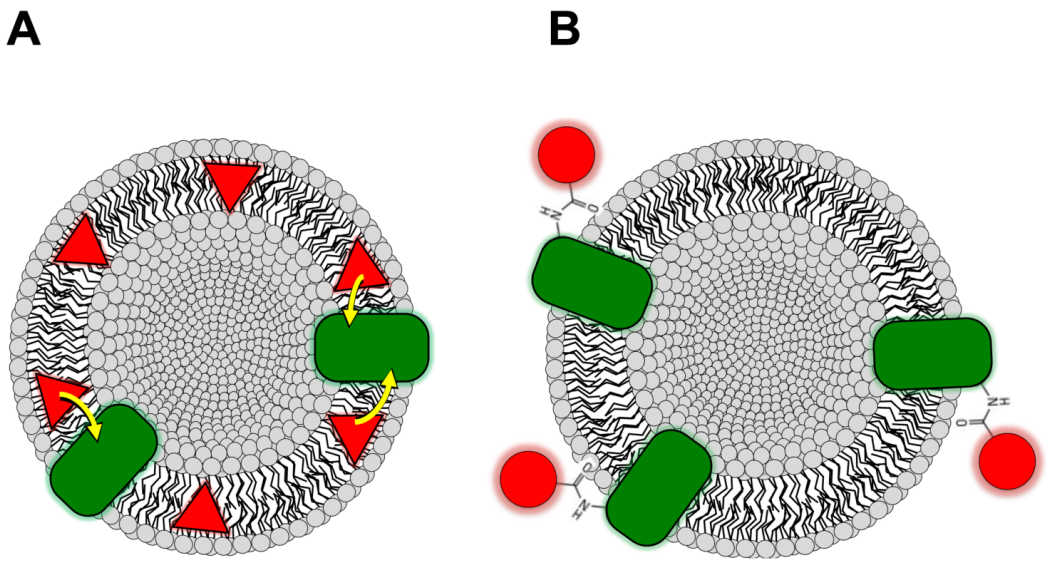

Figure 4.1: Cartoon showing potential lipid-stabilised structures where energy transfer could be achieved. (A) shows the incorporation of hydrophobic $CuInS_2$/ZnS QDs (*red* triangles) into the lipid bilayer of a liposome with LHCII (green) and (B) shows the incorporation of covalently-attached hydrophilic QDs (*red* circles)/LHCII (green) into a lipid bilayer. FRET from the QDs to the LHCII is represented by the yellow arrows.

4.2 Introduction of LHCII to QD Nanoclusters and Investigation of Energy Transfer

Initially, LHCII was introduced into the QD-lipid nanocomposites (described in Chapter 3) to investigate the potential for energy transfer due to FRET between the nanoparticles and the light-harvesting protein. The QD-lipid nanocluster preparation procedure was modified to introduce a defined quantity of LHCII at the stage where the lipid molecules and QDs are mixed and in a co-suspension with surfactants (see Methods Chapter 2.2.6). The resulting LHCII-QD-lipid samples were observed to be somewhat cloudy and led to a typical scattering curve (apparent high absorbance at lower wavelength), as demonstrated in Figure 4.2 A (*blue* line). This suggests that the resulting structures formed were quite large which is not desirable, however, the yield of LHCII incorporation was calculated to be very high after correcting for the optical effects of scattering and when

isolated from the QD-nanocluster control (*black* line). Sodium cholate (SC) appears to denature the LHCII protein, as seen in absorbance measurements (Figure 4.2 A, *blue* vs. *red* lines) with the disappearance of the 650 nm Chl *b* Q_y peak and a shift in the Chl *a* Q_y, therefore this method of incorporation was expected to be unsuitable for nanocomposites containing LHCII. Control measurements where the alternative detergent of α-DDM was used to re-hydrate the samples in place of SC yielded more promising results with respect to LHCII preservation, however, the α-DDM detergent was again unsuccessful at re-hydrating the $CuInS_2$/ZnS QDs, therefore, α-DDM cannot be used in this procedure (data not shown).

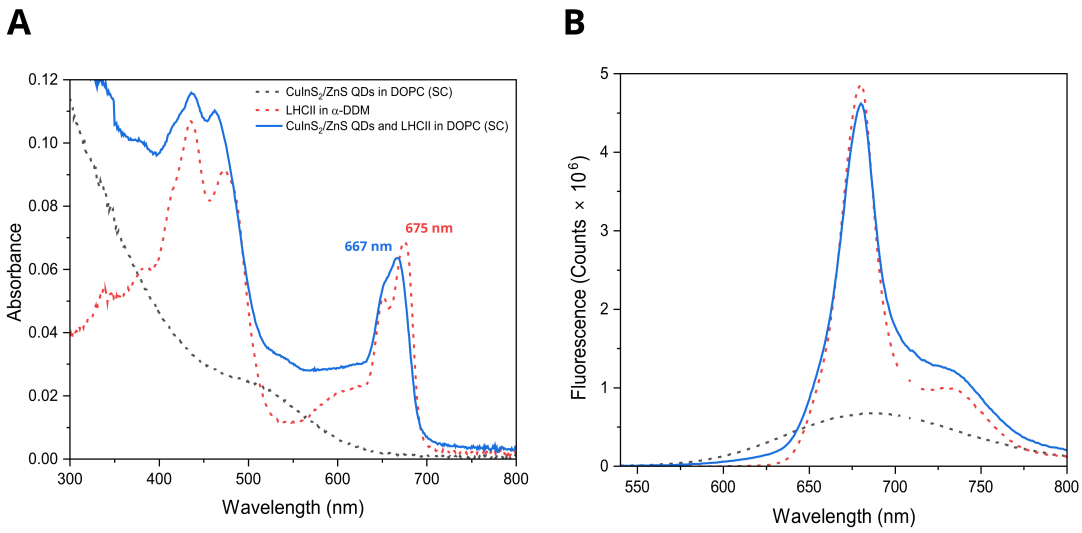

Figure 4.2: Resulting spectra from attempts to incorporate LHCII with QD nanoclusters. (A) Absorbance spectra and (B) steady-state fluorescence emission spectra of nonanethiol-coated $CuInS_2$/ZnS QD-nanoclusters in 50 mM HEPES pH 7.5 (black) self-assembled through the removal of sodium cholate detergent, LHCII proteoliposomes in 50 mM HEPES pH 7.5 (red) self-assembled through the removal of sodium cholate detergent, and QD-nanocluster-LHCII nanocomposites in 50 mM HEPES pH 7.5 (blue) self-assembled through the removal of sodium cholate detergent. Scattering was removed from the absorbance data and fluorescence data was concentration-corrected at 400 nm for the QDs and at 674 nm for the LHCII by dividing the fluorescence by the determined concentration from absorbance measurements.

Despite the imperfect state of the LHCII protein that was suggested from the absorbance spectra reported above, it is useful to assess fluorescence measurements to understand

the deficiencies of the system. Energy transfer is quantified by a quenching of the donor steady-state fluorescence, accompanied by an increase in the acceptor fluorescence [208, 209], which can be observed by deconvolution of combined sample spectra to identify individual peaks. FRET is distance-dependent, with the donor and acceptor needing to be within close proximity to each other as the efficiency of the process is dependent on the inverse-sixth distance between the two. No evidence of donor quenching and acceptor enhancement was observed for the QD-nanocluster-LHCII sample, as seen in Figure 4.2 B where the combined fluorescence of the QD-nanocluster-LHCII sample is lower than the LHCII proteoliposome fluorescence when correcting for the sample concentration (*blue* vs. *red* lines). This suggests the sample contains a combination of LHCII proteoliposomes and QD-nanoclusters that are not co-localised (i.e., could be in completely different assemblies or at least a significant separation distance from each other) and therefore are not within the Förster radius that would facilitate energy transfer. No further attempts were made to associate LHCII with the QD-nanoclusters because these negative results suggested that the resulting structures would be sub-optimal for energy transfer regardless of association due to the lack of a bilayer to accommodate LHCII stability.

4.3 Covalent Attachment of LHCII to QDs without Genetic Modification of Protein

After unsuccessful attempts at associating LHCII with self-assembled QD-nanoclusters, a decision was made to pursue the alternate method of achieving energy transfer by covalently attaching QDs to LHCII proteins. Two-step zero-length crosslinking was identified as an optimal method for attaching QDs to the protein, where N-hydroxysulfosuccinimide (sulfo-NHS) and 1-ethyl-3-(3-dimethylaminopropyl)carbodiimide hydrochloride (EDC) should allow direct binding of hydrophilic QDs that have a carboxyl surface chemistry to light-harvesting proteins through the formation of an amide bond (Figure 4.3) [178, 179]. Hydrophilic CdTe/CdS QDs can be synthesised with a carboxylate thioglycolic acid

(TGA) surface chemistry, with the optimally-short chain allowing the QD core to sit comfortably within the critical radius for efficient energy transfer to the LHCII protein. It is possible to react carboxylates to sulfo-NHS in the presence of EDC or other carbodiimides, which results in the formation of a semi-stable Sulfo-NHS ester. This ester can then be reacted with primary amines, such as those located within LHCII, to form amide crosslinks [178, 185].

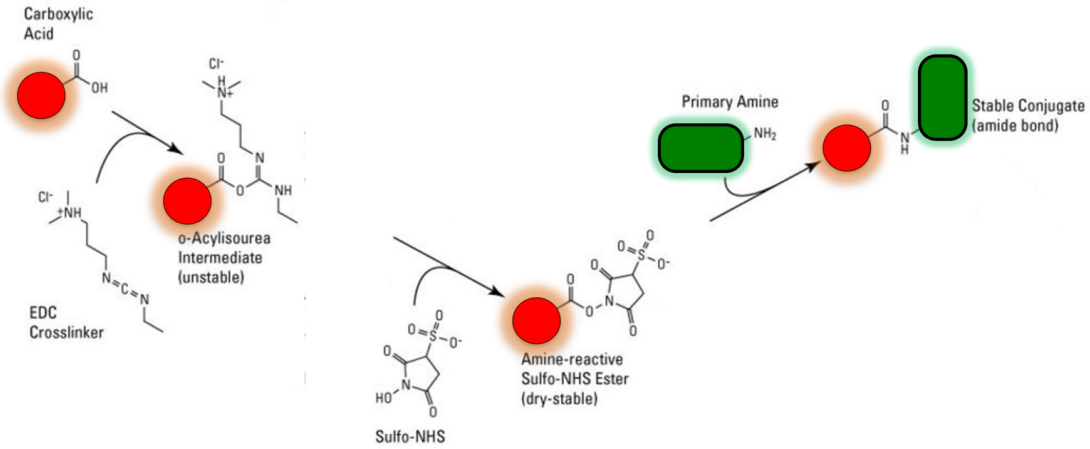

Figure 4.3: Simplified schematic of EDC/Sulfo-NHS crosslinker chemistry. Multi-stage reaction to obtain zero-length chain crosslinked CdTe/CdS QDs and LHCII protein. EDC crosslinker is added to TGA-capped QDs at pH 6.0 to form an o-acylisourea intermediate that is unstable in an aqueous buffer. Sulfo-NHS is then added to form amine-reactive sulfo-NHS esters on the QDs before the pH is raised to 7.5 and the LHCII is introduced. A stable conjugate of QDs and proteins is formed before the reaction is quenched at pH 8.6. Schematic adapted from Sulfo-NHS user guide [185].

Carbodiimides, such as EDC, can promote o-acylisourea formation for the reaction of carboxylates to amine-reactive sulfo-NHS esters, allowing amino-acid side chains in proteins to bind to carboxyl groups. The activation reaction with EDC and sulfo-NHS is most efficient in a two-stage synthesis between pH 4.5-7.2; however, sulfo-NHS esters have a short half-life of one hour at pH 8.0, therefore careful monitoring of the pH is needed to prevent premature hydrolysation of the sulfo-NHS-activated [210–212]. A good option is to perform the first reaction in a buffer at pH 6.0 in 2-(N-morpholino)ethanesulfonic acid (MES) (or an alternative non-amine, non-carboxylate buffer), then the pH should

be raised to 7.2-7.5 with phosphate buffer (or alternative non-amine buffer) immediately before the second-stage reaction to the amine-containing molecule. The pH is altered to optimise the carboxylate and amine reaction efficiencies at each stage and reduce incubation times [178].

4.3.1 Designing a QD Synthesis to Fill the Green Gap

To fill the green gap of LHCII, the CdTe/CdS QDs intended for use must absorb the majority of light in the 520-610 nm region and have a fluorescence emission peak in the 625-675 nm region (to overlap with the LHCII absorbance band in this range). QD particle size is known to increase with longer synthesis times; typically, CdTe/CdS QDs were synthesised at a lower temperature than $CuInS_2$/ZnS QDs (100°C vs 200 C) therefore it took much longer to produce the desired larger QDs that have the appropriate 'redder' peak. Smaller (<2 nm) green CdTe/CdS QDs can be obtained after a reflux time of 10 minutes, but larger red QDs can take between 24 and 48 hours to synthesise depending on the desired optical properties. Due to the slower reaction, a calibration curve was not required to determine the best stopping point for the synthesis and aliquots could be extracted and characterised to obtain a quantitative value for the fluorescence excitation and emission peaks during the synthesis procedure.

TGA-stabilised CdTe/CdS core/shell QDs were synthesised according to the method outlined in Chapter 2.3. and the growth was continued until the desired fluorescence peak was obtained. The absorbance and fluorescence emission of the synthesised CdTe/CdS QDs is shown in Figure 4.4, along with the absorbance and fluorescence emission of LHCII and the spectral overlap between the energy donor and acceptor. The CdTe/CdS QDs have a fluorescence emission peak of 626 nm and a first excitonic absorption peak of 556 nm, calculated by finding the local maximum of the second derivative of the absorbance data after applying Savitzky-Golay smoothing. The concentration of as-synthesised QD solution was determined from the QD size and absorption coefficient using the methods developed by Yu *et al.* [187]. The size and absorption coefficient esti-

mations were completed using CdTe approximations for simplicity. The CdTe diameter d was determined to be 3.3 nm using the following published empirical equation:

$$d = (9.8127 \times 10^{-7})\lambda^3 - (1.7147 \times 10^{-3})\lambda^2 + 1.0064\lambda - 194.84 \quad (4.1)$$

where λ is the wavelength of the first excitonic absorption peak. The molar absorption coefficient at the wavelength of the first excitation is determined by:

$$\varepsilon = 10043d^{2.12} \quad (4.2)$$

The absorption coefficient was calculated to be 1.26×10^5 $M^{-1}cm^{-1}$. From the Beer-Lambert law, the stock concentration of the CdTe/CdS QDs was calculated to be 31.3 μM after accounting for a 1/50 dilution when characterising the absorbance.

4.3.2 Sample Loss/Quenching Through Use of De-salting Column

Once the CdTe/CdS QDs had been synthesised, the crosslinking procedure could be optimised for the QDs and light-harvesting proteins. An optional step in the crosslinking procedure is the use of a desalting column (or other gel filtration column) to remove the inactivated crosslinker and salt from the first buffer at pH 6, allowing the addition of a new buffer to raise the pH for the second stage of the reaction. The desalting column has the potential to degrade the QDs, denature the LHCII or remove the stabilising detergent with the size-exclusion chromatography resin, therefore control measurements should be taken to test for any sample loss or any undesirable fluorescence quenching.

A small sample of CdTe/CdS QDs suspended in ultrapure water and LHCII in 0.1% α-DDM were characterised via absorbance and steady-state fluorescence measurements before and after passing the sample through a desalting column (2 ml size, 'fresh' column). Figure 4.5 shows the spectra of the QDs and LHCII before and after the use of

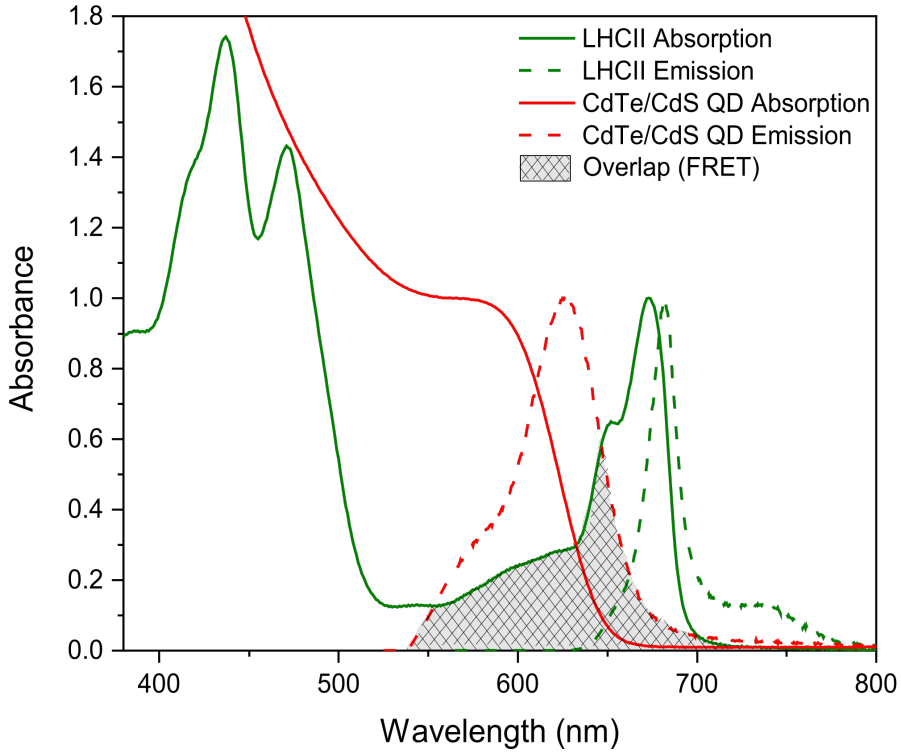

Figure 4.4: Overlap of CdTe/Cds QD and LHC II spectra. Normalised absorbance (solid line) and steady-state fluorescence (λ_{ex} = 475 nm) emission (dashed line) of monomeric LHCII (green) and CdTe/CdS QDs (red). The LHCII absorbance is normalised to the 675 nm peak and the CdTe/CdS QD absorbance is normalised to the first excitonic absorbance peak at 556 nm. Overlap between the QD (donor) fluorescence emission and LHCII (acceptor) absorbance is shown by the grey-shaded grid.

the desalting column. The absorbance of the QDs at the first excitation peak (Figure 4.5 A) had dropped by 25% after passing the sample through the desalting column, indicating a significant loss of QDs from the sample. The relative fluorescence, calculated by dividing the fluorescence emission peak of the QDs by the absorbance of the sample away from the excitation peak (Figure 4.5 B) indicated a quenching of the QDs following centrifugation, suggesting a degradation of the QDs after passing through the resin. It is possible that the resin may have stripped ligands from the surface of the QDs, leading to a decrease in stability and drop in concentration, and this would also explain the apparent quenching of the QD fluorescence emission. Similar to the CdTe/CdS QDs, the absorbance of the LHCII (Figure 4.5 C) dropped by 33%, indicating significant sample loss, although there is no evidence of protein denaturing (i.e., no change is seen to the

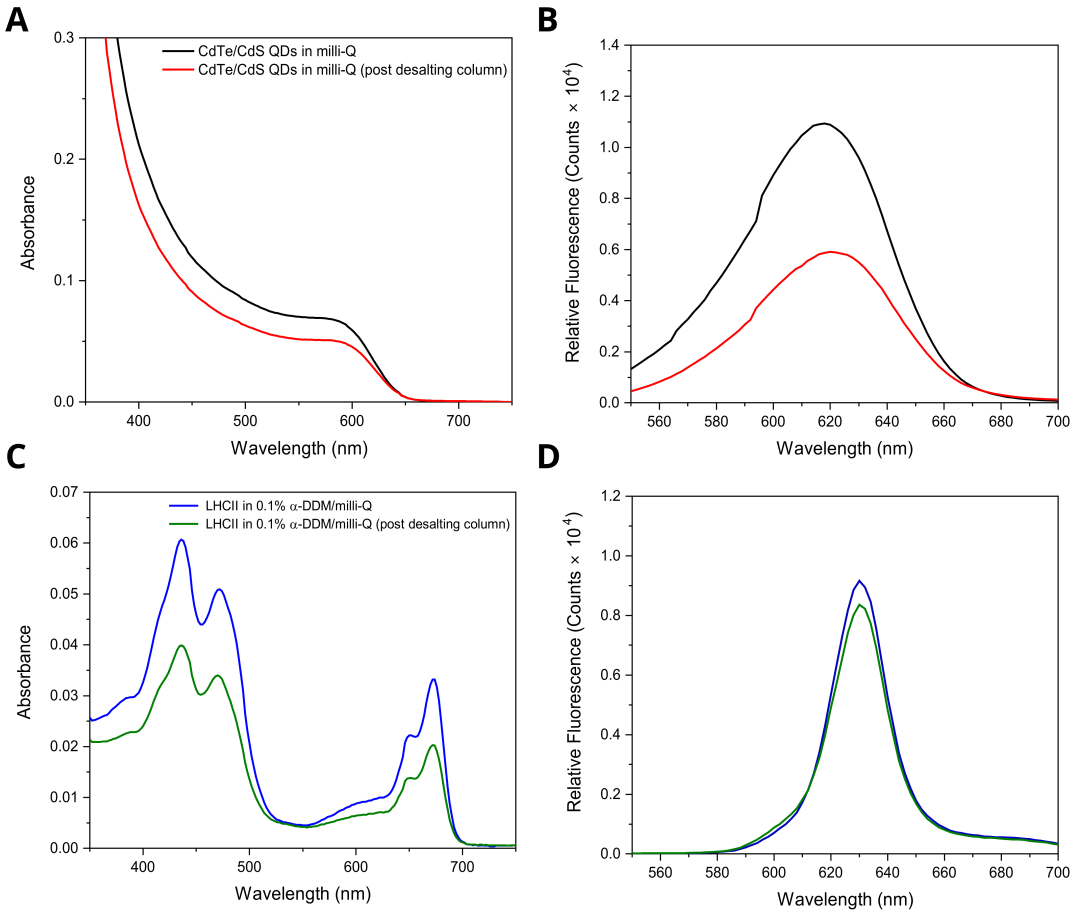

Figure 4.5: Sample loss/quenching following use of de-salting column. (A) Absorbance and (B) relative (divided by absorbance at 550 nm) steady-state fluorescence (λ_{ex} = 475 nm) of CdTe/CdS QDs in ultrapure water before (black) and after (red) passing sample through a desalting column. (C) Absorbance and (D) relative (divided by absorbance at 674 nm) steady-state fluorescence (λ_{ex} = 475 nm) of monomeric LHCII in 0.1% α-DDM and ultrapure water before (blue) and after (green) passing sample through a desalting column.

peak position and shape). A slight drop in the relative fluorescence of LHCII (Figure 4.5 D) may be indicative of quenching, but a 10% difference is not conclusive. Significant quenching of the QD fluorescence, however, is undesirable and these preliminary experiments suggest that alternative methods of raising the pH should be pursued. These options include adding a concentrated second buffer at higher pH to the original buffer or removing inactivated crosslinker removed via centrifugation following the reaction, as opposed to salt removal and addition of a fresh buffer.

4.3.3 Optimising the Buffer Concentration to Achieve CdTe/CdS QD Stability

As this crosslinking reaction depends critically on pH, it is important to consider the aqueous buffer used. As noted earlier, carboxyl-free and amine-free buffers must be used. LHCII is known to be stable in 4-(2-Hydroxyethyl)piperazine-1-ethanesulfonic acid (HEPES) buffer at pH 7.5 from previous experiments completed within the research group, therefore, this was initially chosen as the pH 7.5 buffer to be used in the second stage of the reaction. LHCII was expected to be stable in MES buffer between pH 6.0-6.5 [213–216], as are TGA-capped CdTe/CdS QDs at specific concentrations [217, 218], although the literature is sparse for the QD stability, therefore, preliminary experiments would be required to clarify QD stability in both HEPES and MES buffer solution.

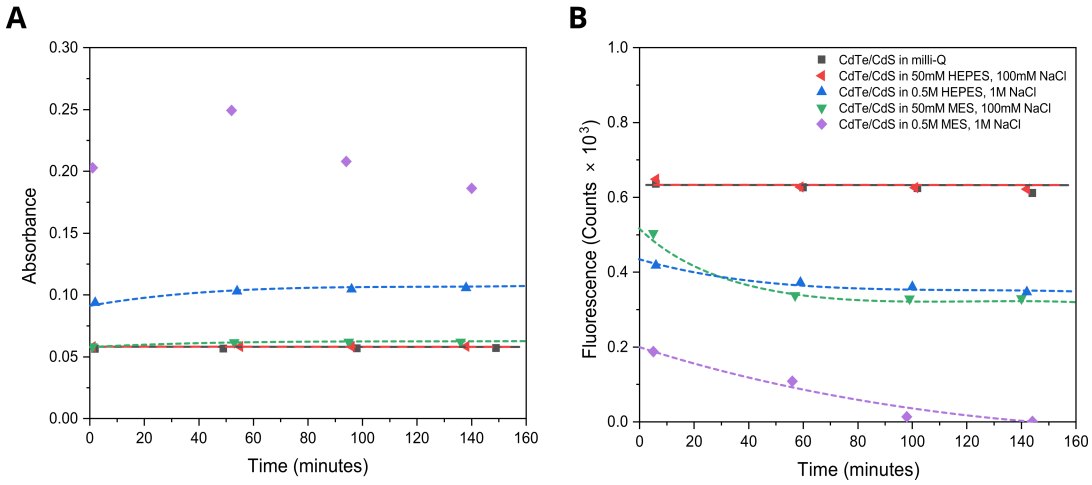

Figure 4.6: Stability of CdTe/CdS QDs in high salt and low salt buffers. (A) Absorbance at the first excitonic absorption peak and (B) steady-state fluorescence (λ_{ex} = 475 nm) at the emission peak for CdTe/CdS QDs in milli-Q (black), CdTe/CdS QDs in 50mM HEPES / 100mM NaCl at pH 7.5 (red), CdTe/CdS QDs in 0.5M HEPES / 1M NaCl at pH 7.5 (blue), CdTe/CdS QDs in 50mM MES / 100mM NaCl at pH 6.0 (green) and CdTe/CdS QDs in 0.5M MES / 1M NaCl at pH 6.0 (purple). Scattering contributes to the inflated absorbance of the QDs in the high salt buffer samples. Dashed lines represent a guide for the eye.

The TGA-capped QDs were required to be stable in the chosen MES (pH 6.0) and

HEPES (pH 7.5) buffers at a QD concentration of 0.5 μM, and two solution compositions were compared for each type of buffer. MES/HEPES concentrations of 'low salt buffer' (50 mM MES/HEPES, 100 mM NaCl) and 'high salt buffer' (500 mM MES/HEPES, 1000mM NaCl) were initially investigated in an attempt to obtain a range of concentrations at which the QDs would be stable if the procedure were to be modified. The NaCl is present to increase the ionic strength of the buffer which may help to prevent agglomeration of particles, although high ionic strengths can present other problems. Figure 4.6 A shows the stability of the CdTe/CdS QDs in low salt and high salt buffers, where the QDs in ultrapure water (*black* datapoints) represent the properties of the original sample and any deviation from this represents an undesirable change. The TGA-capped QDs are stable in both the 50 mM MES (*green* datapoints) and 50 mM HEPES (*red* datapoints) buffers, with an almost identical absorbance obtained to that of the stable QDs. In contrast, the absorbance measurements for the QDs in the higher ionic strength buffers (*blue/purple* datapoints) show significant scattering, most apparent at the MES buffer (*purple*), suggesting instability and aggregation of the QDs over time. A drop in the fluorescence emission peak intensity was observed for the QDs in 500 mM MES, supporting the theory of QD scattering and precipitation. Fluorescence quenching was also seen with the QDs in the 50 mM MES buffer over time, with the only buffer comparable to the QDs in ultrapure water being the 50 mM HEPES buffer.

A similar experiment was designed to investigate the QD stability in lower concentrations of MES buffer, both with and without the NaCl present in an attempt to determine the cause of the previous fluorescence quenching. Again, the stability of the QDs in the buffer was compared to stable QDs in ultrapure water to identify aggregation of the sample and quenching of the QD fluorescence emission intensity. From the absorbance measurements shown in Figure 4.7 A, the limit of QD stability appears to be a buffer concentration of 10 mM MES, 20 mM NaCl where an increase in scattering was observed over a period of 90 minutes. The other concentrations of MES (with and without NaCl) showed stable QDs with absorbance in agreement with the control measurements taken

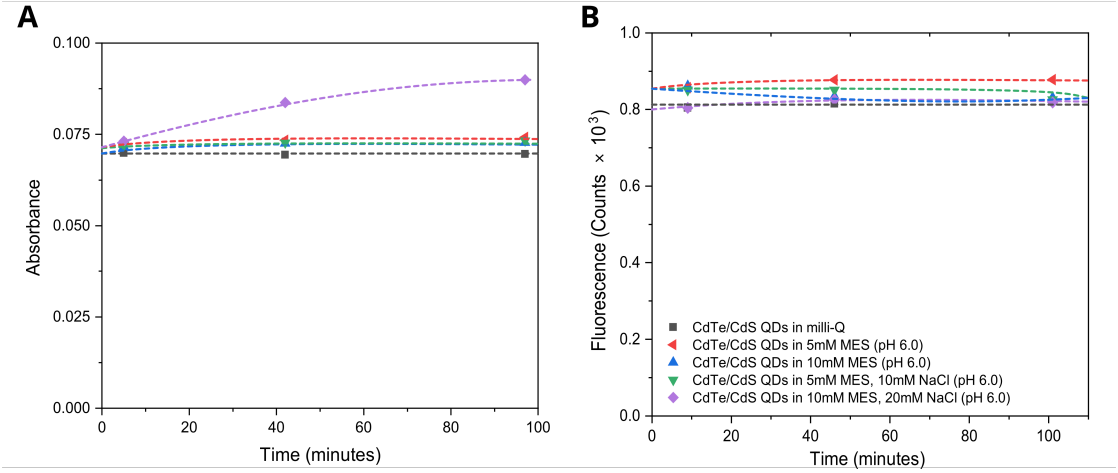

Figure 4.7: Stability of CdTe/CdS QDs at extremely low salt concentrations. (A) Absorbance at the first excitonic absorption peak and (B) steady-state fluorescence (λ_{ex} = 475 nm) at the emission peak for CdTe/CdS QDs in milli-Q (black), CdTe/CdS QDs in 5mM MES at pH 6.0 (red), CdTe/CdS QDs in 10mM MES at pH 6.0 (blue), CdTe/CdS QDs in 5mM MES / 10mM NaCl at pH 6.0 (green) and CdTe/CdS QDs in 10mM MES / 20mM NaCl at pH 6.0 (purple). Dashed lines represent a guide for the eye.

on QDs in ultrapure water. The fluorescence data (Figure 4.7 B) showed a consistent emission over a period of 90 minutes for all samples, with all samples showing a similar fluorescence emission intensity to the QD control in ultrapure water. No significant peak shifts were observed in the raw data (not shown), therefore allowing for flexibility in the buffer concentration with respect to the presence of NaCl salt. A MES buffer concentration of 5 mM was initially selected, with the potential to add 10 mM NaCl if the nanoparticles were too unstable at low ionic concentrations. Using a relatively low 5mM concentration of MES to keep the pH at 6.0 during the first stage of the reaction also allowed for the addition of a higher concentration of HEPES buffer to significantly raise the pH to 7.5 for amine activation in the second stage of the reaction without the need for a desalting column to remove the salt from the initial MES buffer.

4.3.4 Raising the pH of the Buffer by Addition of HEPES and HEPBS

As well as raising the pH to 7.5 for amine activation, the NHS esters also need to be quenched at the end of the reaction by further raising the pH. One alternative method to quench the reaction would be to hydrolyse non-reacted sulfo-NHS present on the QDs by

adding hydroxylamine, hydrolysing non-reacted NHS on the QDs to form hydroxamate, although this is known to denature PSII [219] and was believed to have a similar effect on LHCII. The NHS Esters have a half-life of 4-5 hours at pH 7.0, 1 hour at pH 8.0 and 10 minutes at pH 8.6, thus the time for a full quenching of the reaction can be calculated using $N_t = N_0(\frac{1}{2})^{-t/t_{1/2}}$, where N_0 is the initial quantity, N_t is the quantity remaining after time, t, and $t_{1/2}$ is the half-life. Re-arranging to find the time gives $t = -t_{1/2}\ ln_2(\frac{N}{N_0})$, therefore a period of 67 minutes would quench 99% of NHS esters if the final pH of the reaction was raised to 8.6. N-(2-Hydroxyethyl)piperazine-N'-(4-butanesulfonic acid) (HEPBS) buffer has a useful pH range of 7.6 - 9.0 and would be an optimal buffer to raise the pH in the final part of the reaction due to the similarity in structure and properties to HEPES buffer. To achieve an accurate change to the pH and calculate the exact concentration/volume to add in order to raise the pH to 7.5, a pH calibration curve was created which could then be scaled down to the reaction volume (20:1).

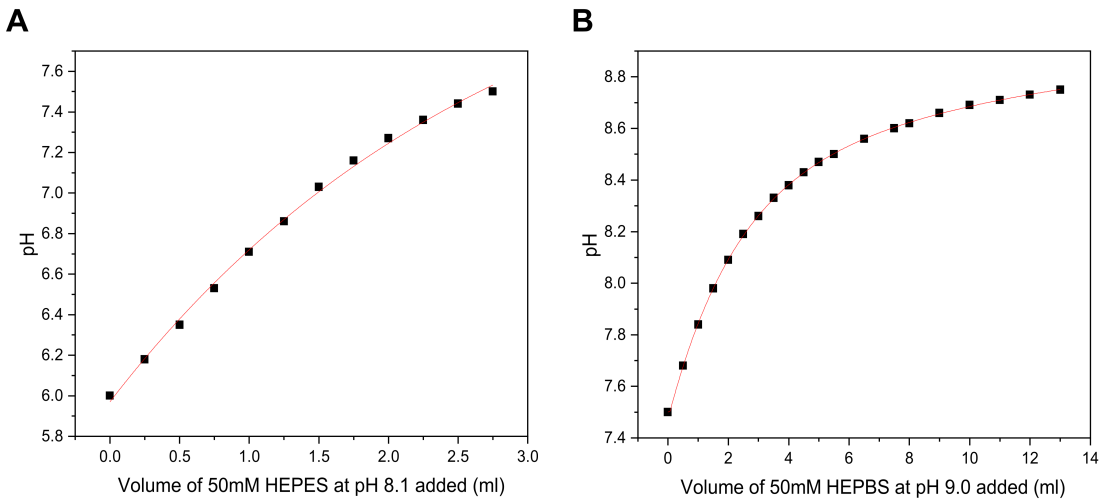

Figure 4.8: pH calibration curves used for crosslinking reaction. Calibration curves were obtained by (A) adding 50 mM HEPES at pH 8.1 to 5 mM MES at pH 6.0, and (B) 50 mM HEPBS to 2.5 mM MES / 3.44 mM HEPES at pH 7.5. HEPES buffer was added to 20 ml of 5 mM MES (pH 6.0) in 1 ml increments under stirring. The red lines represent the fit of the calibration curves.

The initial calibration curve (Figure 4.8 A) was obtained by adding 50 mM HEPES buffer at pH 8.1 to 5 mM MES buffer (starting pH 6.0) in 250 μL increments to reduce the final

concentration of buffer. This experiment was completed as a preliminary experiment to the addition of HEPBS (pH 9.0) at a concentration of 50 mM, hence why the curve cuts off as soon as pH 7.5 is achieved. A volume of 2.75 mL HEPES was needed to raise the pH to 7.5, with a final concentration of 2.5 mM MES, 3.44 mM HEPES after dilution of the final volume to 40 mL to replicate the change in volume to 2 mL upon addition of the LHCII at the reaction volume planned for (20:1). The final pH calibration curve (Figure 4.8 B) shows that a pH of 8.6 is reached upon addition of 7.5 mL HEPBS (pH 9.0) at a concentration of 50 mM, giving a final concentration of 2.1 mM MES, 2.89 mM HEPES and 7.89 mM HEPBS with no requirement for a final dilution. Scaled-down, 137.5 μL of 50 mM HEPES (pH 8.1) should be added to 1 mL of 5 mM MES (pH 6.0) to raise the pH to 7.5 for amine activation. The LHCII was then added to the reaction, with the final volume diluted to 2 mL. To quench the reaction, 350 μL of 50mM HEPBS (pH 9.0) should be added to raise the pH to 8.6 to fully quench the reaction after a period of 67 minutes.

4.3.5 Stability of CdTe/CdS QDs at Desired pH and Buffer Concentration

Once a method of quenching the reaction had been selected, control measurements were taken to determine the stability of CdTe/CdS QDs and LHCII in the final quenched buffer (2.1 mM MES, 2.89 mM HEPES and 7.89 mM HEPBS). If the stability of both the QDs and LHCII was consistent with the starting and coupling buffers, then the addition of HEPBS would be deemed a suitable method of quenching the reaction without the risk of denaturing the LHCII through the use of hydroxylamine. The QDs and LHCII need to be stable in the quenching buffer for at least 67 minutes to achieve 99% quenching of the NHS esters, therefore the stability of the LHCII in 0.1% α-DDM was measured over a period of 120 minutes in the starting buffer (50 mM HEPES at pH 6.0), the coupling buffer (2.5mM MES / 3.44mM HEPES at pH 7.5) and the quenching buffer (2.1 mM MES / 2.89 mM HEPES / 7.89 mM HEPBS at pH 8.6).

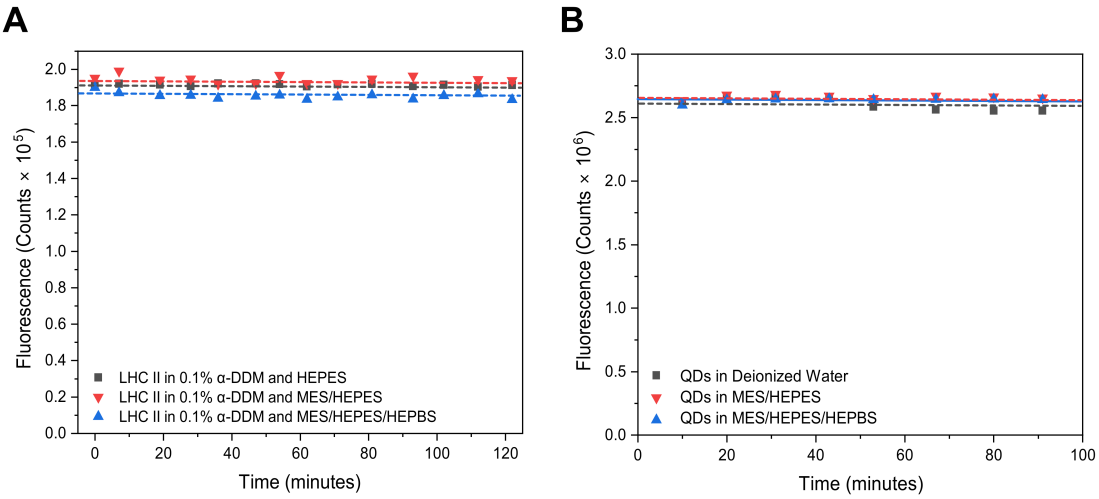

Figure 4.9: Stability of LHCII and CdTe/CdS QDs in various pH buffers. Steady-state fluorescence ($\lambda_{ex} = 475$ nm) showing emission peak intensity over time for (A) LHCII in 0.1% α-DDM and (B) TGA-capped CdTe/CdS QDs in various buffers chosen for crosslinking. For the LHCII, stability measurements were taken in 50 mM HEPES at pH 7.5 (black), 3.44mM HEPES / 2.5mM MES at pH 7.5 (red) and 2.1 mM MES / 2.89 mM HEPES / 7.89 mM HEPBS at pH 8.6 (blue). For the CdTe/CdS QDs, stability measurements were taken in ultrapure water (black), 3.44mM HEPES / 2.5mM MES at pH 7.5 (red) and 2.1 mM MES / 2.89 mM HEPES / 7.89 mM HEPBS at pH 8.6 (blue). Dashed lines represent a guide for the eye.

The fluorescence emission peak intensity was consistent over the course of 120 minutes for the LHCII in each buffer (Figure 4.9 A), with no quenching of the fluorescence and no shift in emission peak observed, therefore it can be concluded that the addition of HEPBS does not damage or denature the LHCII and that the LHCII would remain stable throughout the course of the crosslinking experiment. The stability of the CdTe/CdS QDs was also measured in the coupling buffer and quenching buffer, with control measurements taken using CdTe/CdS QDs in ultrapure water over a period of 90 minutes (Figure 4.9 B). Again, the emission peak of the QDs showed no significant drop in fluorescence in the coupling and quenching buffers, which were consistent with the QD stability in ultrapure water. A slight fluctuation in the fluorescence emission was observed for the CdTe/CdS QDs in ultrapure water, although this did not deviate from the equipment error for the steady-state fluorescence, supporting the hydrolyzation of NHS esters using HEPBS without QD degradation.

4.4 Optimising the Crosslinking Procedure to Achieve Energy Transfer

4.4.1 Introduction of the Crosslinker

To achieve energy transfer between the CdTe/CdS QDs and LHCII, a zero-length chain crosslinker should be used to link the carboxyl QD surface chemistry to the amines of LHCII. The number of carboxylic TGA ligands on the surface of the spherical CdTe/CdS QDs can be calculated from the theoretical diameter of the QD, estimated using the first excitonic absorption peak [187]. A diameter of 3.30 nm was predicted, based on a first excitation peak of 556 nm, as referenced in Section 4.3.1. The number of sulfur binding sites on the surface was estimated to be 117 assuming two sulfur sites at the face per unit cell, with a unit cell area of 0.585 nm^2. A 1 µM concentration of QDs suggests a total ligand concentration of ∼117 µM, therefore a crosslinker concentration of ∼1 mM would be sufficient to provide a ×10 molar excess in comparison to available binding sites, as suggested in the crosslinking user guide [185]. The QD fluorescence intensity can be tracked at each stage of the reaction and may be expected to change as the crosslinking reaction may cause QD-QD agglomeration. This would be acceptable so long as any agglomeration was reversible.

Figure 4.10 shows the fluorescence of the CdTe/CdS QDs at each stage of the experimental procedure in the absence of the second amide-containing protein. The initial drop in the fluorescence of the CdTe/CdS QDs upon the addition of the EDC crosslinker at pH 6.0. is accompanied by a significant red-shift in the fluorescence emission peak and an increase in absorbance (data not shown). An increase in absorbance of the QDs due to agglomeration, as well as a quenching of the fluorescence, is indicative of successful interaction between the carboxyl group of the TGA ligand and the crosslinker to form an o-acylisourea intermediate, which is unstable in aqueous environments. A sharp rise in the fluorescence is observed when the pH is raised to 7.5 with the addition of HEPES,

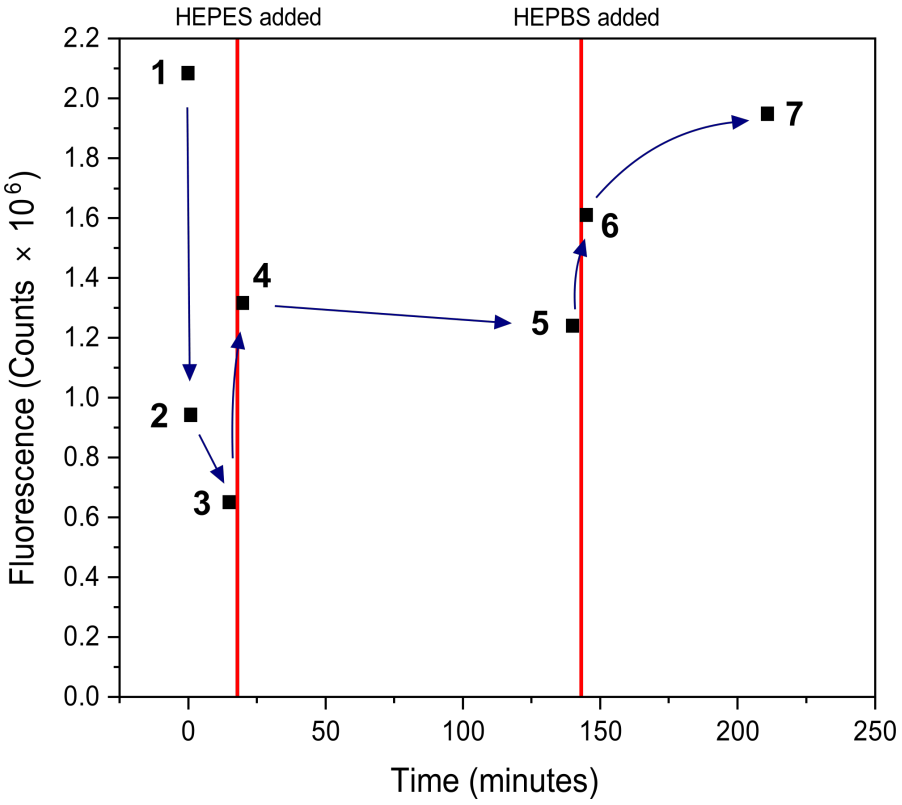

Figure 4.10: Fluorescence of CdTe/CdS QDs at each stage of the crosslinking experimental procedure. Steady-state fluorescence (λ_{ex} = 550 nm) showing the fluorescence emission peak of TGA-capped CdTe/CdS QDs, in the absence of the second protein, throughout the crosslinking experiment. Point (1) represents the CdTe/CdS QDs in 5 mM MES (pH 6.0) at T = 0 minutes, (2) represents the CdTe/CdS QDs in 5 mM MES (pH 6.0) after addition of the crosslinker at T = 1 minute, (3) represents the CdTe/CdS QDs and crosslinker in 5 mM MES (pH 6.0) at T = 15 minutes, (4) represents the CdTe/CdS QDs and crosslinker in 2.5 mM MES / 3.44 mM HEPES (pH 7.5) immediately after the pH was raised at T = 20 minutes, (5) represents the CdTe/CdS QDs and crosslinker in 2.5 mM MES / 3.44 mM HEPES (pH 7.5) at T = 140 minutes, (6) represents the CdTe/CdS QDs and crosslinker in 2.1 mM MES / 2.89 mM HEPES / 7.89 mM HEPBS (pH 8.6) immediately after quenching the reaction at T = 145 minutes, and (7) represents the CdTe/CdS QDs and crosslinker in 2.1 mM MES / 2.89 mM HEPES / 7.89 mM HEPBS (pH 8.6) after 99% quenching at T = 211 minutes.

suggesting the initial formation of the sulfo-NHS esters as activation with sulfo-NHS increases the solubility of the modified molecule due to the charged sulfonate group. A slight quenching was observed over a period of two hours as the moderately-stable sulfo-NHS esters cause slight QD aggregation in the absence of the amide-containing protein before the addition of the HEPBS buffer leads to the initial hydrolysis of the sulfo-NHS esters. A stable conjugate would be formed upon the addition of a protein containing

free-amide binding sites, thus achieving a zero-length chain crosslink between the QDs and LHCII, with an isourea byproduct formed as the reaction quenches. If an amide-containing protein is not introduced, hydrolysis will occur, reverting the carboxyl surface chemistry, or an amine-reactive sulfo-NHS ester will form which is relatively stable in the aqueous environment. These sulfo-NHS esters will begin to be quenched upon raising the pH to 8.6, where the original carboxyl groups will be regenerated. This reaction should be 99% quenched after 67 minutes, which results in a recovery of the QD fluorescence that is similar to the pre-reaction fluorescence, with a small drop which may be due to incomplete hydrolysis. Recovery of the fluorescence confirms that the QDs are not being degraded by the crosslinker, and also confirms a quenching of the reaction through the addition of the HEPBS to raise the pH of the buffer. Uncertainty still remains regarding the concentration of EDC/sulfo-NHS crosslinker to be used, and whether QD instability is detrimental to the formation of a stable QD-protein conjugate, which will be explored with and without the LHCII protein in the following section.

4.4.2 Achieving Optimal Binding of the Quantum Dots to the Light-Harvesting Protein

To achieve efficacious binding of the QDs to LHCII for efficient energy transfer, the optimal concentration of EDC/sulfo-NHS crosslinker to be used during the reaction should be determined. The molar ratio of the crosslinker was initially ten times the number of available sulfur ligands on the surface of each QD, although an increase in crosslinker concentration may result in a more-consistent binding to the QDs and an initial decrease in QD fluorescence emission upon the addition of the crosslinker. Conversely, the relatively high concentration of crosslinker may impede the binding of EDC and sulfo-NHS to the carboxyls or may prevent efficient binding due to aggregation of the QDs as a result of excessive o-acylisourea intermediate formation. The reaction volume will also affect the interaction of the crosslinker with the QDs and LHCII, with a smaller volume promoting greater contact and an increase in the percentage of QDs crosslinked to the protein.

To investigate the effect of the crosslinker concentration on the binding to TGA-capped CdTe/CdS QDs, an experiment was devised where the QD concentration was varied (0.5 µM, 1 µM and 2 µM) with three set molar concentrations of EDC/sulfo-NHS crosslinker (1.0/2.5, 2/5, 4/10 of EDC/sulfo-NHS in mM) chosen for each QD concentration. This allows the effect of increasing the crosslinker concentration to be explored whilst also allowing the effective volume to be altered by fixing the molar ratio of QDs to the crosslinker and increasing the concentration of the sample. A quenching of the relative fluorescence emission intensity of the CdTe/CdS QDs (Figure 4.11 A) was accompanied by an increase in scattering (data not shown) as the crosslinker concentration was increased at each of the three QD concentrations, suggesting that quenching of the fluorescence is due to QD aggregation. No QD fluorescence emission quenching was observed for the three samples where the concentration of the QDs and crosslinker was relatively low (0.5 µM QDs / 1 mM EDC / 2.5 mM sulfo-NHS, 0.5 µM QDs / 2 mM EDC / 5 mM sulfo-NHS, and 1 µM QDs / 1 mM EDC / 2.5 mM sulfo-NHS), suggesting a lack of contact or interaction and failure to form o-acylisourea intermediates. It could be speculated that the lack of quenching may indicate the partial formation of o-acylisourea on a fraction of the QD carboxyl binding sites as evidenced by the 1-2 nm red-shift in the fluorescence emission peak from the QDs in ultrapure water, enough to crosslink the QDs to LHCII while maintaining QD stability in the aqueous environment, although further investigation would be required after the introduction of LHCII. Significant QD quenching and a further red-shift in the fluorescence emission peak were observed as the concentration of crosslinker was increased, initially suggesting that a greater concentration of crosslinker contributes to a more efficient crosslinking reaction. However, fixing the molar ratio of the QD-crosslinker and decreasing the overall volume of the solution (Figure 4.11 B) shows how increasing the concentration of the QDs and crosslinker together leads to the largest red-shift and drop in the fluorescence emission peak. Increasing the concentration of reactants by decreasing the volume of the reaction may lead to greater efficiency of bioconjugation without altering the quantity of product through

promoting interaction.

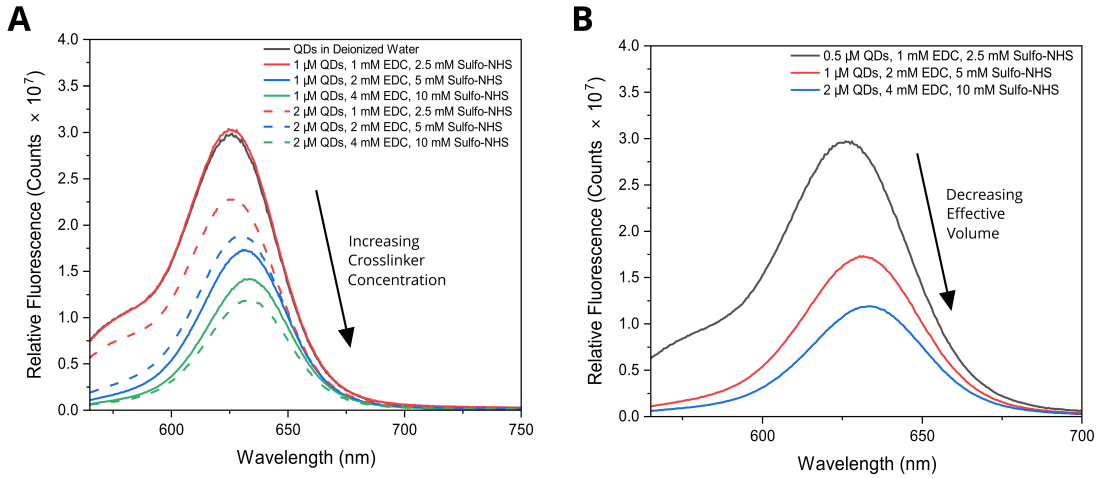

Figure 4.11: Effect of altering the crosslinker and CdTe/CdS QD concentrations on the QD fluorescence. Steady-state fluorescence (λ_{ex} = 550 nm) showing the fluorescence emission of TGA-capped CdTe/CdS QDs as (A) the crosslinker molar concentration is increased relative to the QD molar concentration and (B) the effective reaction volume is decreased by increasing the molar concentration of the QDs and EDC/sulfo-NHS crosslinker.

A significant decrease of the average fluorescence lifetime <t>, again indicative of fluorescence quenching, was observed as the molar ratio of crosslinker to QD was increased (Table 4.1), with an average lifetime of 13.6 ns and 14.9 ns when the concentration of crosslinker was highest and the concentration of QDs was 0.5 µM and 1 µM respectively. Surprisingly, little to no quenching was observed for the highest concentration of QDs regardless of the crosslinker concentration, which may prove promising should higher concentrations of QD and crosslinker need to be investigated and shows that the QDs are not degraded by the crosslinker when the molar concentration of the QDs is equal or greater than that of the crosslinker.

To finally investigate the bioconjugation efficiency, LHCII was introduced to the reaction with the volume of buffer varied in an attempt to quantify successful bioconjugation. The reaction volume was reduced to 50% (1 ml) and 25% (0.5 ml) from the original 2 ml volume at the stage of LHCII addition, with a proportional reduction of the volume

Lifetime Components and Contributions							
Sample	τ_1 (ns)	A_1 (%)	τ_2 (ns)	A_2 (%)	τ_3 (ns)	A_3 (%)	<t> (ns)
0.5 µM QDs in ultrapure water	9.3 ± 0.1	19.6 ± 0.1	27.5 ± 0.1	77.1 ± 0.2	89.8 ± 0.2	3.2 ± 0.1	26.0 ± 0.3
0.5 µM QDs / 1 mM EDC / 2.5 mM sulfo-NHS	10.8 ± 0.1	23.3 ± 0.1	28.3 ± 0.1	73.5 ± 0.2	96.0 ± 0.2	3.2 ± 0.1	26.4 ± 0.3
0.5 µM QDs / 2 mM EDC / 5 mM sulfo-NHS	9.3 ± 0.1	19.5 ± 0.1	27.7 ± 0.1	76.0 ± 0.2	84.7 ± 0.1	4.5 ± 0.1	26.7 ± 0.3
0.5 µM QDs / 4 mM EDC / 10 mM sulfo-NHS	5.5 ± 0.1	51.1 ± 0.1	18.9 ± 0.1	45.9 ± 0.1	70.9 ± 0.2	3.0 ± 0.1	13.6 ± 0.2
1 µM QDs / 1 mM EDC / 2.5 mM sulfo-NHS	9.1 ± 0.1	14.1 ± 0.1	28.9 ± 0.1	81.3 ± 0.3	86.8 ± 0.2	4.6 ± 0.1	28.8 ± 0.4
1 µM QDs / 2 mM EDC / 5 mM sulfo-NHS	6.7 ± 0.1	39.6 ± 0.1	23.6 ± 0.1	56.8 ± 0.1	84.4 ± 0.2	3.6 ± 0.1	19.1 ± 0.2
1 µM QDs / 4 mM EDC / 10 mM sulfo-NHS	5.6 ± 0.1	45.9 ± 0.1	19.4 ± 0.1	50.7 ± 0.1	71.5 ± 0.1	3.5 ± 0.1	14.9 ± 0.2
2 µM QDs / 1 mM EDC / 2.5 mM sulfo-NHS	4.1 ± 0.1	7.0 ± 0.1	31.1 ± 0.1	88.9 ± 0.2	94.9 ± 0.3	4.1 ± 0.1	31.8 ± 0.5
2 µM QDs / 2 mM EDC / 5 mM sulfo-NHS	6.7 ± 0.1	22.5 ± 0.1	27.3 ± 0.1	72.5 ± 0.2	86.7 ± 0.2	5.0 ± 0.1	25.6 ± 0.3
2 µM QDs / 4 mM EDC / 10 mM sulfo-NHS	6.3 ± 0.1	43.4 ± 0.1	20.8 ± 1	53.2 ± 0.1	75.1 ± 0.2	3.5 ± 0.1	26.0 ± 0.3

Table 4.1: Deconstruction of the tri-exponential decay of CdTe/CdS quantum dots interacting with various concentrations of EDC/sulfo-NHS crosslinker from time-resolved fluorescence lifetime measurements.

for the initial conjugation of the TGA-capped QDs and EDC/sulfo-NHS crosslinker in MES buffer at pH 6.0. The initial equilibration and LHCII bioconjugation times were kept constant, and samples were diluted to an equal volume for characterisation after the 67-minute quenching period in HEPBS buffer at pH 8.6. Significant scattering was observed from absorbance measurements as the reaction volume was reduced (data not shown), and a correction would need to be applied to quantify energy transfer via flu-

orescence de-convolution. To de-convolute the relative fluorescence of the samples and investigate energy transfer from the CdTe/CdS QDs to the LHCII, the concentration of the quantum dots and LHCII must be calculated from the absorbance in each sample. Once the concentration was calculated, the fluorescence can be divided by the concentration and normalised to give the relative fluorescence of each sample. The scattering was removed from the absorbance measurements using the C/λ^4 relationship, as scattering is inversely proportional to the fourth power of wavelength in the normal dispersion regime [220]. De-convoluted absorbance measurements for each reaction volume are shown in Figure 4.12. Once the absorption was de-convoluted, the Beer-Lambert law ($A = \epsilon Cl$) could be used to calculate the concentration of QDs and the dye. The raw fluorescence obtained from steady-state fluorescence spectroscopy was divided by the calculated concentrations to give the relative fluorescence, then normalised with respect to the control measurements to give the de-convoluted relative fluorescence, shown alongside respective de-convoluted absorbance measurements in Figure 4.12.

For a reaction volume of 2 ml (Figure 4.12 A/B), both the relative QD fluorescence and relative LHCII fluorescence are quenched in relation to the control measurements. There is no evidence of significant crosslinking between the QDs and LHCII, and no energy transfer could be determined. The quenching of the QDs could be due to aggregation, as a small red-shift is observed in the peak of the CdTe/CdS QDs, similar to the shift shown in Figure 4.11. The quenching of the LHCII may be due to denaturing of the protein in the presence of the crosslinker, with a similar denaturing observed in the presence of detergents and through the application of heat [221, 222]. For a reaction volume of 1 ml (Figure 4.12 C/D), a 27% quenching of the relative QD donor fluorescence was observed, with a 79% enhancement of the relative LHCII acceptor fluorescence. This enhancement of the energy acceptor suggests that successful crosslinking has been achieved and that the QDs and LHCII lie within the Förster radius, although the successful percentage of crosslinked conjugates cannot be quantitatively confirmed. Also, Figure 4.11 B suggests an increase in fluorescence quenching as the reaction volume is reduced, al-

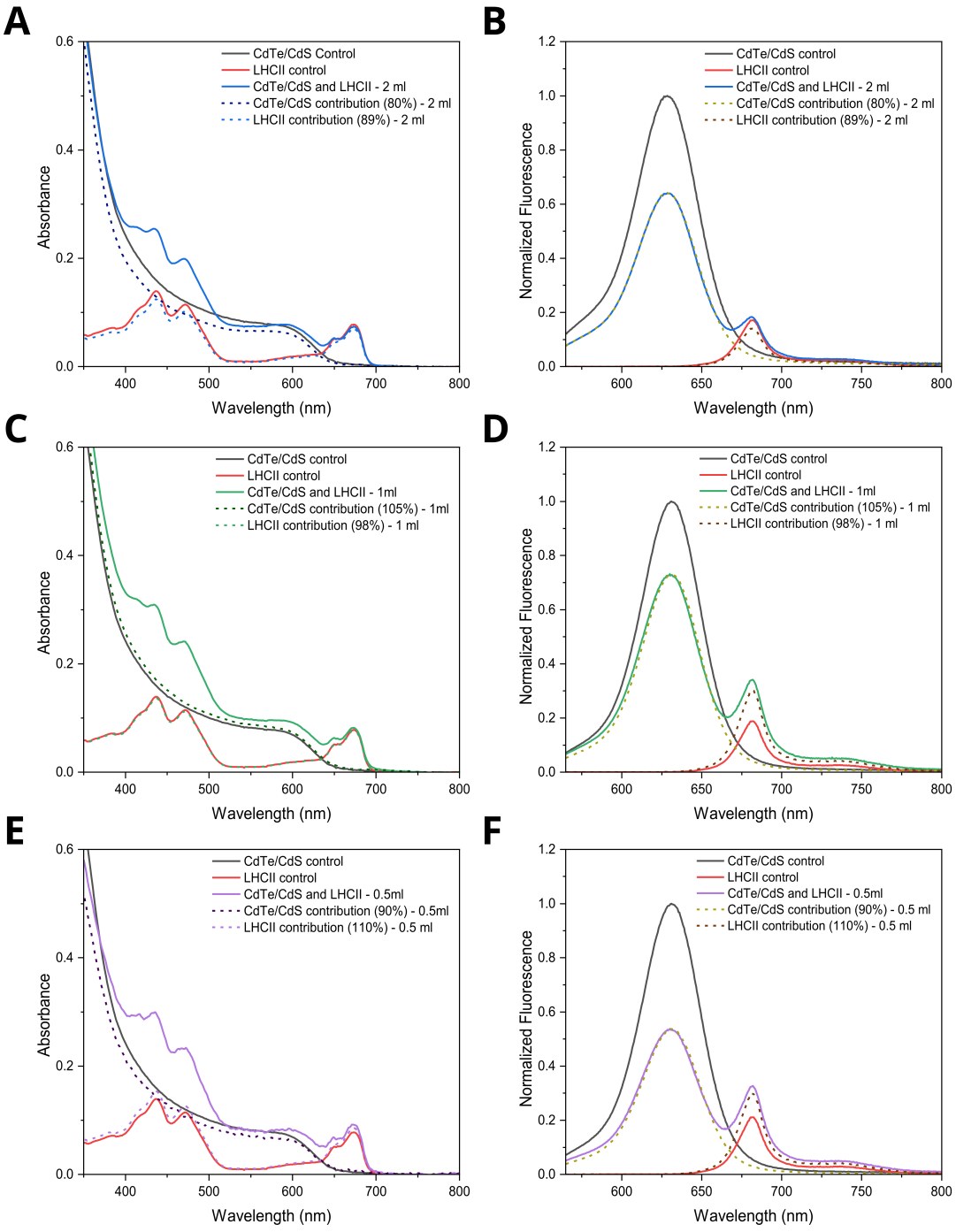

Figure 4.12: Investigation of FRET between CdTe/CdS QDs and LHCII. Deconvoluted (A) absorbance and (B) relative fluorescence for crosslinked CdTe/CdS QDs and LHCII with a reaction volume of 2 ml. Deconvoluted (C) absorbance and (D) relative fluorescence for crosslinked CdTe/CdS QDs and LHCII with a reaction volume of 1 ml. Deconvoluted (E) absorbance and (F) relative fluorescence for crosslinked CdTe/CdS QDs and LHCII with a reaction volume of 0.5 ml. Small-particle scattering was manually corrected in the absorption measurements.

though less CdTe/CdS QD quenching was observed at the lower reaction volume. For the 0.5 ml reaction volume 4.12 E/F), the CdTe/CdS QDs showed a 47% quenching of the fluorescence, with a 57% enhancement of the relative LHCII acceptor fluorescence. Significant scattering was observed during absorption measurements which made deconvolution difficult, leading to slightly noisier data, although QD and LHCII contributions could still be extracted. As expected, the smallest reaction volume contributed to the most QD fluorescence quenching, and an enhancement of the energy acceptor fluorescence again suggests successful crosslinking, although a smaller increase in the energy acceptor was observed. This suggests that the quenching of the QD fluorescence due to the crosslinker has negative connotations on the energy transfer capabilities of the QDs, and that attempting to optimise crosslinking by decreasing the reaction volume, increasing interactions, may serve as a hindrance to optimal energy transfer.

To summarise, it is unclear how successful the crosslinking is for each reaction volume, as although it appears that crosslinking and energy transfer have been achieved, there appears to be little consistency with respect to the quenching of the donor fluorescence and enhancement of the acceptor fluorescence. With a simple donor-acceptor FRET pair, a quenching of the donor fluorescence intensity (or reduction in lifetime) indicates that FRET has occurred, however, the situation is complicated here because the donors could be agglomerating and self-quenching. Quantification of the crosslinking reaction efficiency would be the next logical step, which could be done by replacing the QDs/proteins with large pre-functionalised particles that can be isolated easily from the reaction solution. If, as expected, the crosslinking is more successful as the reaction volume is increased, then an optimisation of the reaction volume must be achieved to optimise energy transfer without quenching the donor fluorescence due to an abundance of crosslinker attached to each QD, preventing optimal acceptor energy enhancement.

4.5 Future Work: Quantifying the Crosslinking of CdTe/CdS QDs and LHCII Using Polymer Microspheres

As energy transfer from the potentially-bioconjugated CdTe/CdS QDs to LHCII is inconclusive, the binding of the carboxyl to amine surface chemistries would need to be quantified. Polymer microspheres are non-fluorescent, monosized 500 nm spherical polymer particles with functionalised surface chemistry, including aminated and carboxylated functional groups [223–225]. The large size of the polymer microspheres means they would precipitate easily during low-speed centrifugation and can be crosslinked to the fluorescent QDs and LHCII independently with the correct surface chemistry. Fluorescent particles conjugated to the polymer microspheres would precipitate, then could be re-suspended in a separate aqueous buffer after supernatant removal, with steady-state fluorescence microscopy quantifying successful crosslinking.

To determine the number of microspheres needed for quantification, the number of charge groups per microsphere C_{m} should be calculated using the following equation:

$$C_{\mathrm{m}} = \frac{\pi \cdot d^2 \cdot 10^8}{P} \tag{4.3}$$

where d is the mean diameter of the microspheres (µm) and P is the packing area (or surface charge density) of the microspheres. The product information from one of the suppliers (Bangs Laboratories) gives the packing area of the carboxyl-functionalised microspheres as 9.4 $\mathrm{Å}^2$/functional group with a mean diameter of 0.51 µm. The mean diameter of the amine-functionalised microspheres was 0.53 µm although no information was given on the packing area, so this was estimated to be 9.5 $\mathrm{Å}^2$/functional group based on a similar product class. The C_{m} for the carboxyl-functionalised microspheres was calculated to be $8.69{\cdot}10^6$ and for the amine-functionalised microspheres was $9.28{\cdot}10^6$. From the product data sheet, the number of microspheres per gram was estimated to be $\sim 1.8 \cdot 10^{13}$ based on a diameter of $\sim$ 0.5 µm and a density of $\sim$ 1.05 - 1.1 g ml^{-1}, where

both the amine and carboxyl-functionalised microspheres were prepared at a 10% w/v mass concentration. With $\sim 9 \cdot 10^6$ functional groups per microsphere and $\sim 1.8 \cdot 10^{13}$ microspheres per gram, the number of functional groups per gram of microspheres (10 ml at 10% w/v) is $\sim 6 \cdot 10^{19}$. This allows the mass of polymer microspheres to be calculated as required, where the total number of functional groups in 0.5 µM CdTe/CdS (the standard concentration) or 0.5µM LHCII should be equal to the available functional groups on the microspheres per control experiment.

Due to advances made within other branches of the project, a detailed investigation into the feasibility of QD-LHCII conjugation using polymer microspheres was not pursued beyond the planning of experiments. Future work would consist of quantification of the crosslinking using the amine-functionalised microspheres attached to the carboxylic acid-functionalised QDs using an identical procedure to that outlined in Chapter 2.4., and vice versa with carboxyl-functionalised microspheres and LHCII. Control measurements would be taken with an equal quantity of non-functionalised polymer microspheres, where no fluorescent particles are expected to bind. Low-speed centrifugation should allow precipitation of fluorescent particles attached to functionalised microspheres without compromising the covalent bond, with no fluorescent particles expected upon microsphere re-hydration in the control samples. If the crosslinking of the fluorescent particles to the polymer microspheres is successful, then further optimisation of the crosslinking procedure would be made, primarily focusing on further volume reduction initially, before investigating reaction time and pH as premature quenching may hinder the reaction.

To further the quantification of the crosslinking reaction using polymer microspheres, techniques such as Transmission Electron Microscopy (TEM) and fluorescence microscopy could be employed. The binding between LHCII and the QDs could be observed directly using TEM to reveal high-resolution structures of the bioconjugates, where staining may allow the proteins to be imaged. TEM could also be used to investigate agglomeration of the bioconjugates, which may quantify the observed quenching of QD fluorescence

during spectroscopy. Co-localisation of the LHCII and QDs could also be quantified using epifluorescence microscopy, where multiple fluorescent components can be imaged within the same sample through the use of filters, as described in Chapter 2.8.1. Fluorescence lifetime imaging microscopy (FLIM), as described in Chapter 2.8.2., could also be used to quantify energy transfer between the QDs and LHCII, where single-particle measurements would allow the statistical analysis of any increase in LHCII enhancement and QD quenching through alterations in the sample lifetime. A decrease in the QD lifetime and an enhancement of the LHCII lifetime in comparison to isolated control measurements would suggest FRET between the QDs and LHCII, although aggregation must be prevented to be confident that the QD lifetime reduction is a result of energy transfer and not non-radiative dissipation.

4.6 Conclusion

The goal of the research in this chapter was to achieve FRET between a QD energy donor and an LHCII energy acceptor within a stable environment. Energy transfer could not be achieved using the lipid-stabilised $CuInS_2$/ZnS QD nanoclusters developed in Chapter 3, therefore hydrophilic TGA-stabilised CdTe/CdS QDs were chosen as an energy donor with the potential to use NHS/EDC crosslinking to covalently bind the QDs to the LHCII without genetic modification of the protein. CdTe/CdS QDs were synthesised with a fluorescence emission peak of 626 nm and a first excitonic absorption peak at 556 nm, sufficiently filling the green gap of LHCII while providing enough overlap of the fluorescence with the absorbance of LHCII to achieve FRET.

The crosslinking procedure was modified to circumvent the use of desalting columns after they were found to reduce the quantity of sample after use and also quenched the fluorescence of the QDs. Activation of the reaction in different stages relied on carefully adjusting the pH using low amounts of 50 mM concentration buffers, in comparison to the 5 mM starting buffer. The QDs and detergent-stabilised LHCII were found to be

stable in buffer concentrations below 20 mM, thus care was taken to not exceed this limit. Hydroxylamine, a standard quenching agent used in bioconjugation, is known to denature LHCII, therefore, a high-pH HEPBS buffer was used as an alternative to quench active NHS esters and end the crosslinking reaction.

Optimisation of the carbodiimide crosslinking procedure suggested that increasing the concentration of the QDs and EDC/sulfo-NHS crosslinker or decreasing the volume of the reaction, led to more efficient binding of the crosslinker to the QDs at pH 6.0. When LHCII was introduced, it was unclear whether bioconjugation and FRET between the CdTe/CdS QDs and LHCII had occurred, although a small increase in the energy acceptor fluorescence emission was accompanied by quenching of the donor fluorescence emission at the lowest reaction volume. Future work would involve quantifying the conjugation of the QDs and LHCII using functionalised polymer microspheres, where QDs should covalently bind to amine-functionalised microspheres and the LHCII should covalently bind to carboxyl-functionalised microspheres. Finally, a combination of electron microscopy and fluorescence microscopy could confirm successful crosslinking and co-localisation of the QDs and LHCII, with energy transfer quantifiable through the utilisation of FLIM.

Chapter 5

Results: Investigating the Structure and Photophysics of Quantum Dot Nanoclusters

5.1 Motivation

In Chapter 3, a method of self-assembling lipid-stabilised QD nanoclusters using hydrophobic $CuInS_2$/ZnS QDs was developed and then optimised to achieve sufficient stability and favourable optical performance. The structure and photophysics of $CuInS_2$/ZnS QDs within such assemblies have not yet been characterised and little is known about the excitation dynamics and energy transfer mechanisms of small lipid-stabilised QD nanoclusters, thus, the next step following the successful self-assembly of nanoclusters was to seek a greater understanding of the system. The research in this chapter focuses on understanding and comparing the mechanisms of fluorescence decay and energy transfer of $CuInS_2$/ZnS QDs within nanocomposites to those of colloidal $CuInS_2$/ZnS QDs, with emphasis on the relationship to size, structure and ensemble photophysics. The potential of QD nanocomposites as light-harvesting materials will be explored, serving as a stepping stone towards investigating the functionality of QD-containing bio-hybrid

light-harvesting nanocomposite materials.

Based on the self-assembly procedure and the observed red-shift in the fluorescence emission peak of the QDs that was observed in Chapter 3 when forming nanoclusters, the structure was speculated to consist of many tightly packed QDs encapsulated by a lipid monolayer, but the size of the clusters was unknown. As noted, the observed fluorescence red-shift could be explained by energy transfer between QDs, however, this could be within relatively small clusters (∼50 nm) or much larger clusters (∼1000 nm). These potential structures, along with the speculated structure at each stage of the self-assembly procedure, can be seen in Figure 5.1, with panel 6A showing a cartoon of the smaller aggregates and panel 6B showing the larger speculated clusters. TEM characterisation would be able to assess the structure of the nanoclusters. The location of the lipid within the QD nanoclusters can also be analysed, with the possibility of extending this investigation to determine the quantity of lipid required to stabilise the QDs. The preliminary investigation could be expanded further to understand the effect of altering the molar lipid:QD ratio in order to optimise the uptake of QDs. Once the structure of the QD nanoclusters and the importance of the lipid component has been determined, the ensemble photophysics can be investigated to confirm the origin of the red-shift through a combination of steady-state and time-resolved fluorescence.

Finally, $CuInS_2$/ZnS QD nanoclusters will be investigated at the single-particle level in order to understand the population distribution of the structures and their photophysics. This was performed by depositing clusters onto solid surfaces (glass) and analyzing them using fluorescence microscopy. In the past, single-particle analysis of $CuInS_2$/ZnS QDs has been difficult due to 'blinking' – random fluctuations in the QD photoluminescence resulting in long 'off' periods with short emission bursts, giving rise to large signal fluctuations and low photon counts which makes characterisation difficult [106, 107]. Blinking may also provide a potential pathway for non-radiative recombination within QD nanoclusters. There is no unified blinking theory [226], although it is accepted that

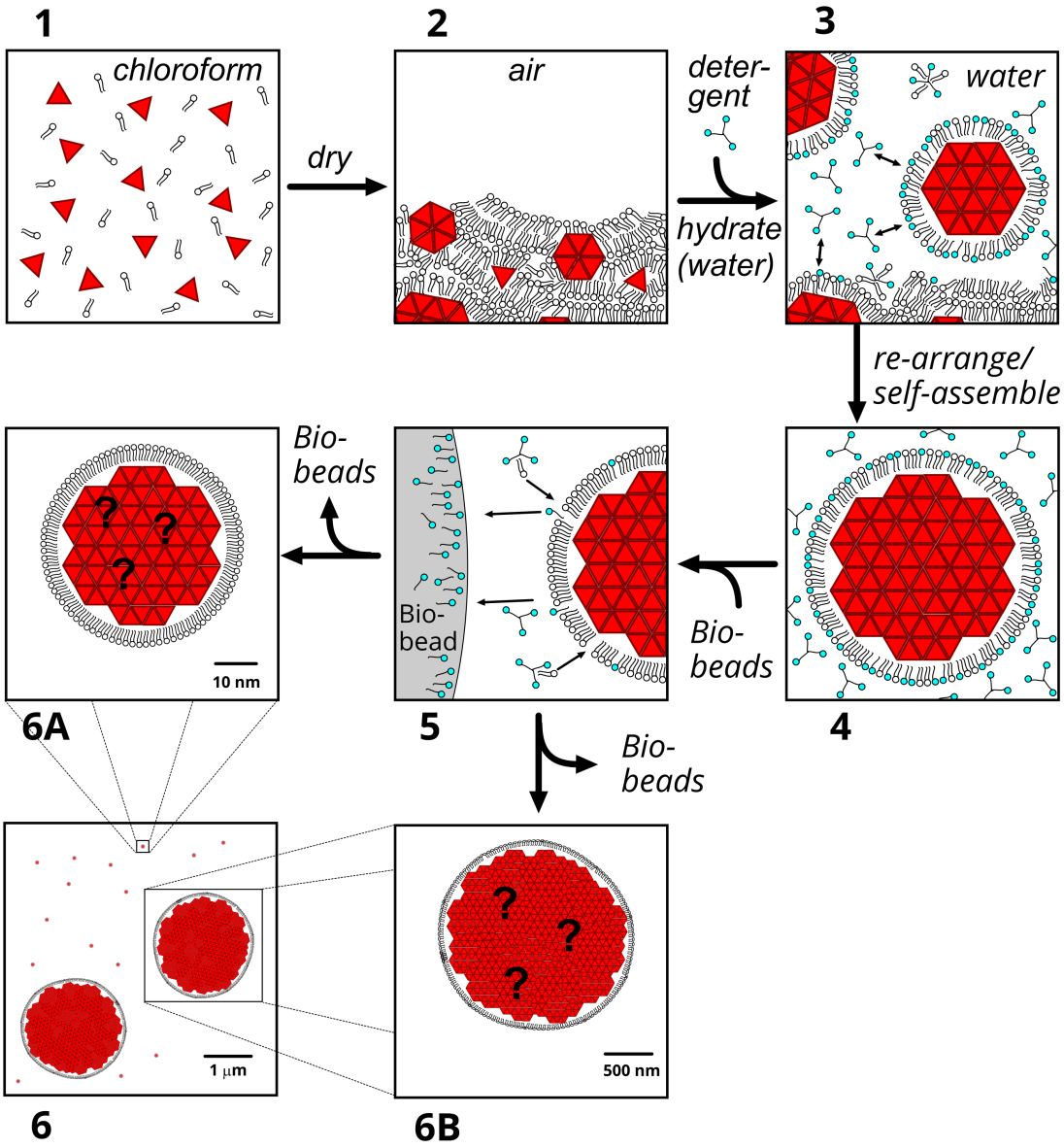

Figure 5.1: Cartoon showing the speculated self-assembly procedure of lipid-stabilised QD nanoclusters. Panel (1) shows colloidal QDs and lipids dispersed in chloroform. Panel (2) shows a dried thin film of QDs and lipids. Panel (3) shows the formation of small QD clusters upon re-hydration of the film with 4% detergent. Panel (4) shows the formation of mixed lipid/detergent micelles stabilising clusters of QDs. Panel (5) shows the removal of the detergent using adsorbent Biobeads. Panel (6A) shows the likely structure of QD nanoclusters following detergent removal, with a mixture of <50 nm QD nanoclusters, empty lipid vesicles, and large bilayer structures. Panel (6B) shows a potential structure of micron-sized QD clusters. Panel 6 shows the two potential structures side-by-side to contrast the relative difference in size.

blinking originates via two pathways; the first being non-radiative recombination via surface trap states and the second due to Auger recombination arising from induced

surface charge [227, 228]. The non-radiative recombination due to trap states results in a lower fluorescence intensity which is accompanied by a shorter QD fluorescent lifetime, although these surface trap states can be passivated through the addition of a shell, as discussed in Chapter 1.3.5. Auger recombination is a process where the excess energy from electron-hole recombination can be redistributed to a charge carrier that is excited to a higher-energy state within the same band, resulting in non-radiative recombination as opposed to photon emission. An off-state due to Auger recombination can occur if excess electrical charge builds up on the QD surface when extra electrons accumulate and change the QD surface properties. It has been proposed that these extra charges can be removed from the surface through exposure to mid-infrared light [229], which may significantly reduce the non-radiative dissipation of energy and lead to more-efficient energy transfer or radiative recombination, although was not investigated during this study.

5.2 Investigation into the Size and Structure of QD Nanoclusters

5.2.1 Optical Measurements of the Samples to Be Used for Electron Microscopy

To investigate the structure of the self-assembled QD-lipid nanoclusters and the distribution of QDs within, samples were investigated using transmission electron microscopy (TEM). $CuInS_2$/ZnS QDs were synthesised following the optimised protocol described in Chapter 3.2. $CuInS_2$/ZnS QD nanoclusters were self-assembled using the optimised protocol finalised in Chapter 3.6. Prior to TEM, the samples were characterised by absorption and fluorescence spectroscopy to confirm that the optical properties of the exact samples destined for TEM matched the other sample sets for nanoclusters. The spectra of both colloidal $CuInS_2$/ZnS QDs dispersed in chloroform (*black* line) and the $CuInS_2$/ZnS QD nanoclusters in aqueous buffer (*red* line) are displayed in Figure 5.2.

The first absorption exciton peak was determined to be 520 nm (Figure 5.2 A) for both colloidal QDs and QD nanoclusters, with the fluorescence emission maxima of 655 nm for colloidal QDs compared to 700 nm for the lipid-stabilised QD nanoclusters (Figure 5.2 B, C), resulting in a 45 nm red-shift in fluorescence as a result of QD clustering. Time-resolved fluorescence measurements are shown in Figure 5.2 D, where a more rapid decay of the QD nanoclusters (*black* line) leads to a reduction in the average lifetime to 163 ns, from a colloidal QD average lifetime of 257 ns. These results are consistent with previous samples and the expectations for QD nanoclusters (red-shifted fluorescence and reduced fluorescence lifetime suggestive of non-radiative dissipation as a result of FRET).

To set our expectations for TEM, the diameter of an individual QD was then estimated from previous studies of how size relates to absorption properties. Both colloidal $CuInS_2$/ZnS QDs and lipid-stabilised QD nanoclusters were prepared at a concentration of 6.81 µM, which was calculated from the Beer-Lambert law ($A = \varepsilon Cl$) using a molar absorption coefficient determined from a published empirical equation:

$$\varepsilon(3.1\text{eV}) = 2123d^{3.8}. \tag{5.1}$$

ε(3.1 eV) is the molar absorption coefficient at an energy of 3.1 eV, or a wavelength of 400 nm, and d is the QD size [102]. The QD core size can be determined from the fluorescence emission peak wavelength λ_{PL} as follows:

$$d = 68.952 - 0.2136\lambda_{PL} + 1.717 \times 10^{-4}\lambda_{PL}^2 \tag{5.2}$$

where a fluorescence emission peak of 655 nm gives a theoretical average QD size of 2.71 nm for the ensemble, and a molar absorption coefficient of 93 490 M^{-1} cm^{-1}. This theoretical QD size can later be compared to the average size determined from TEM analysis.

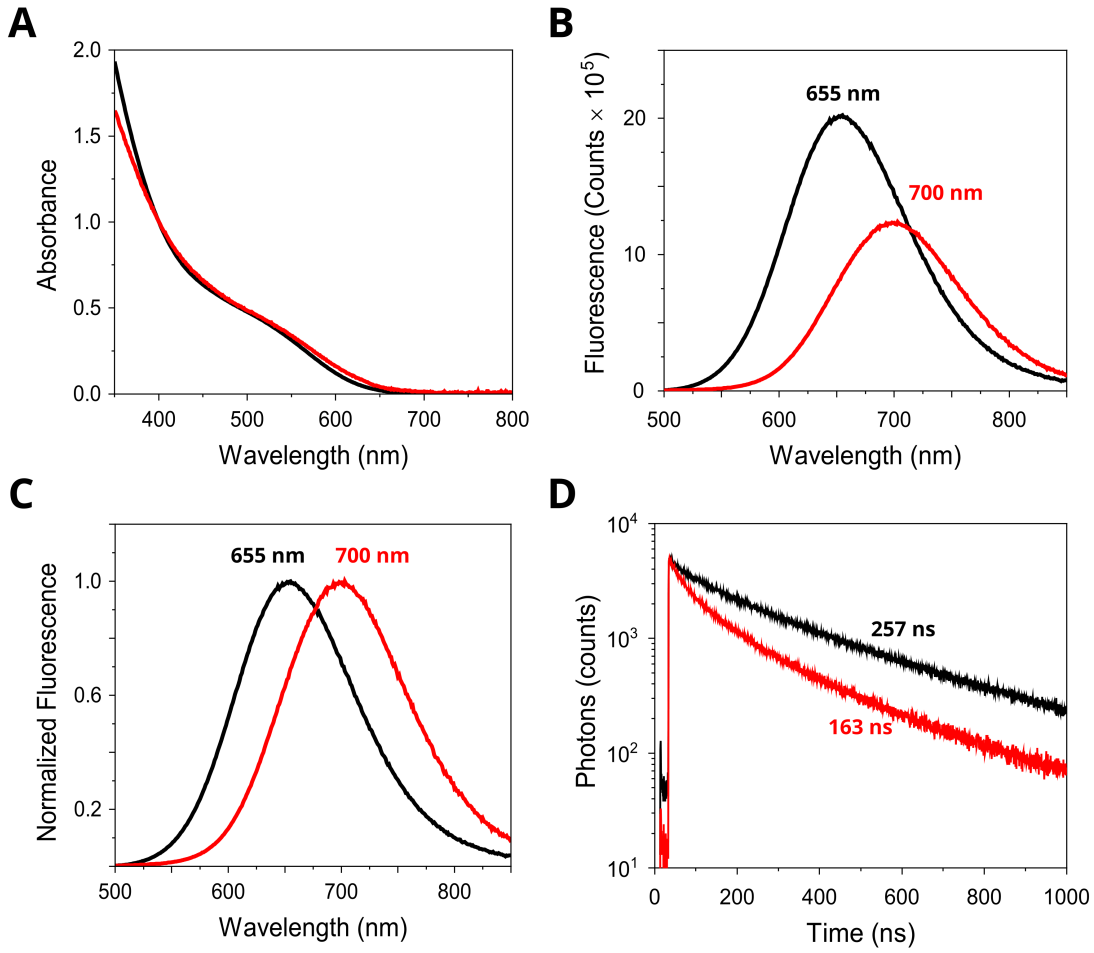

Figure 5.2: Spectra showing alteration of optical properties for colloidal $CuInS_2/ZnS$ QDs and $CuInS_2/ZnS$ QD nanoclusters. (A) Normalised (400 nm) absorption spectra of colloidal $CuInS_2/ZnS$ QDs in chloroform (black) and $CuInS_2/ZnS$ QD nanoclusters in aqueous buffer (red). (B) Steady-state fluorescence emission spectra (λ_{ex} = 475 nm) and (C) normalised steady-state fluorescence emission of colloidal $CuInS_2/ZnS$ QDs in chloroform (black) and $CuInS_2/ZnS$ QD nanoclusters in aqueous buffer (red). (D) Semi-logarithmic time-resolved fluorescence decay curves of colloidal $CuInS_2/ZnS$ QDs in chloroform (*black*, λ_{ex} = 473 nm, λ_{em} = 655 nm) and $CuInS_2/ZnS$ QD nanoclusters in aqueous buffer (*red*, λ_{ex} = 473 nm, λ_{em} = 700 nm).

5.2.2 Size Analysis of Colloidal $CuInS_2/ZnS$ Quantum Dots

To calculate the average size of the $CuInS_2/ZnS$ QDs, both semi-automated and manual analysis of STEM and TEM images was completed in ImageJ. STEM can provide higher contrast than TEM but it has lower spatial resolution. A series of example TEM images of the colloidal tetrahedral $CuInS_2/ZnS$ QDs deposited on graphene-coated grids are

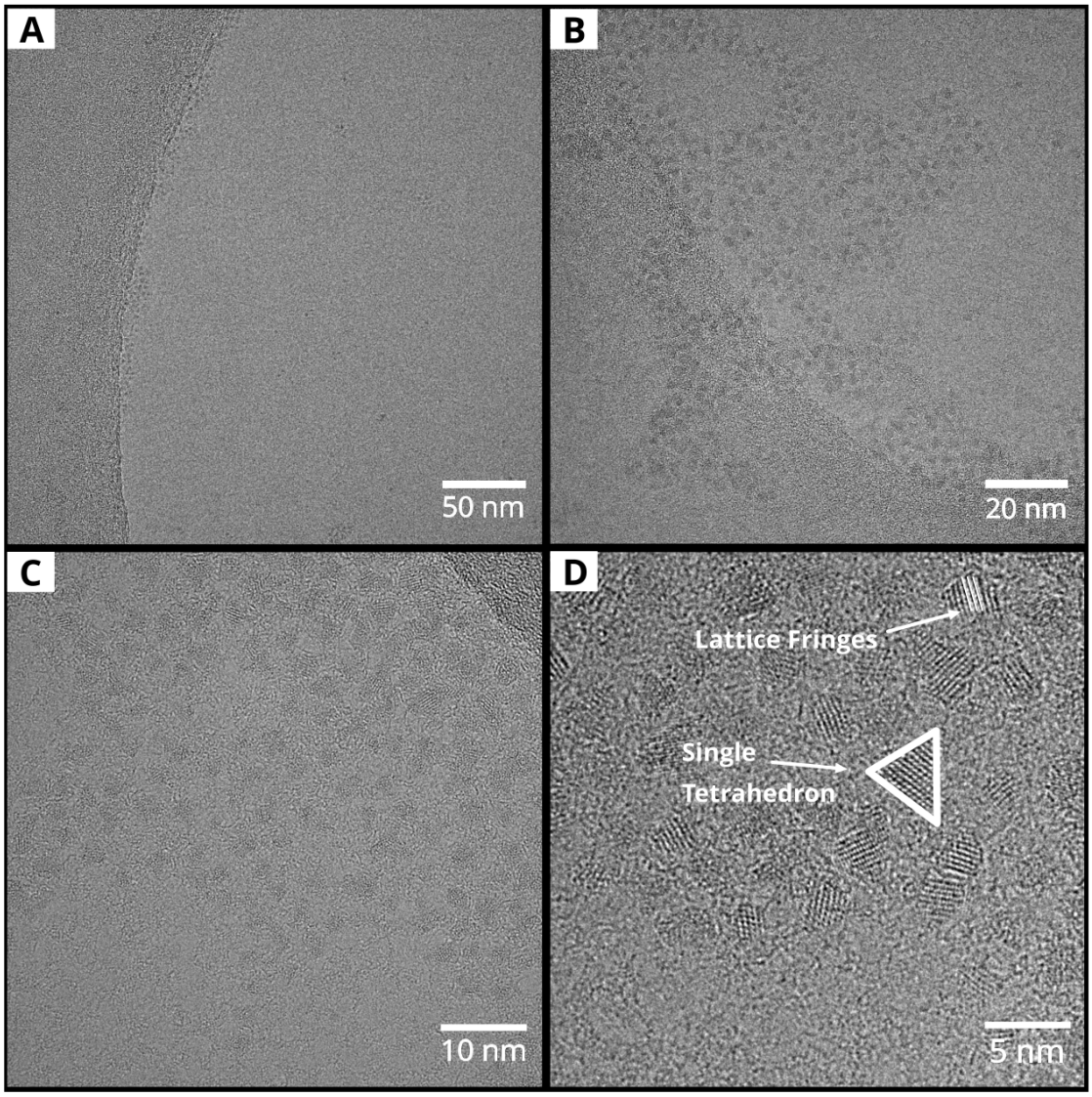

Figure 5.3: TEM images of colloidal $CuInS_2$/ZnS QDs dispersed in chloroform. Scale bars are (A) 50 nm, (B) 20 nm, (C) 10 nm, and (D) 5 nm.

shown in Figure 5.3 at increasing magnifications. The colloidal QDs appeared to associate with the edge of the TEM grid as can be seen in low-magnification TEM images (Figure 5.3 A-B), so grid boundaries were a focus in the higher-magnification images (Figure 5.3 C-D). The lattice fringes from the plane of the crystal, which correspond to the lattice spacing, are clearly visible in the high-magnification image (Figure 5.3 D) and unequivocally confirm the presence of the QDs.

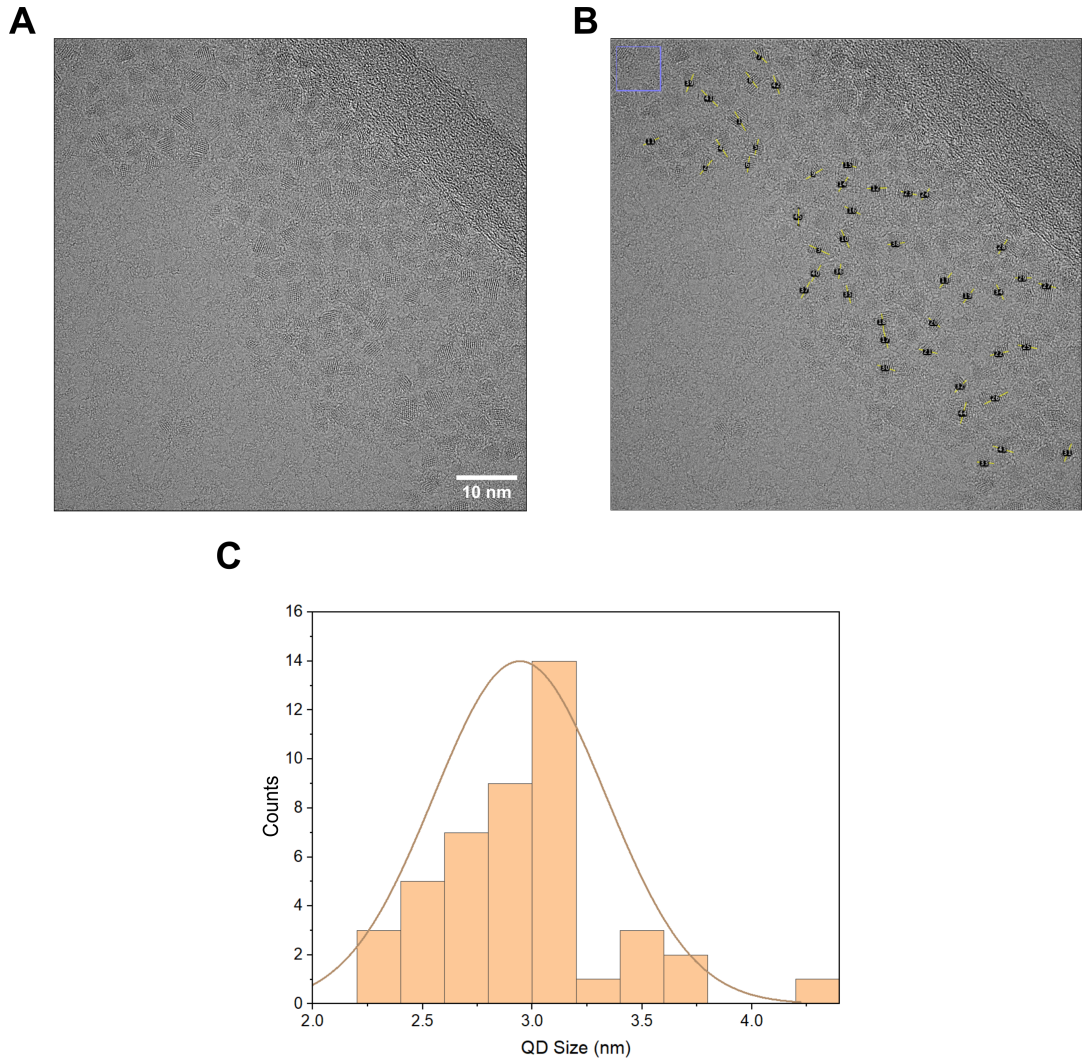

Figure 5.4: Size distribution of colloidal $CuInS_2$/ZnS QDs following manual analysis. (A) Example of original TEM image used for manual size analysis. The scale bar is 10 nm. (B) Example of manual size analysis on individual QDs. TEM image identical to (A) with scale bar removed. (C) Histogram showing the size distribution of QDs from the manual analysis. Bin widths are 0.2 nm, mean size = 2.9 ± 0.4 nm.

Manual size analysis proved difficult due to the low contrast of the TEM, as the thin QD boundaries were difficult to accurately distinguish from background noise (Figure 5.4 A). This would likely result in a particle size that was smaller than those obtained from the semi-automated analysis on high-contrast STEM but should be a good estimate of the atomically dense QD core size. The size was defined as the longest corner-to-side distance of the triangular projection, with an example analysis displayed in Figure 5.4 B.

The distribution obtained from manual size analysis is displayed in Figure 5.4 C. The average core size of the $CuInS_2$/ZnS QDs was calculated to be 2.9 ± 0.4 nm, slightly above the theoretical estimations for the ensemble average QD core size of 2.71 nm calculated using the molar absorption coefficient [102], with a size dispersion (standard deviation as a percentage of the mean) of 13%.

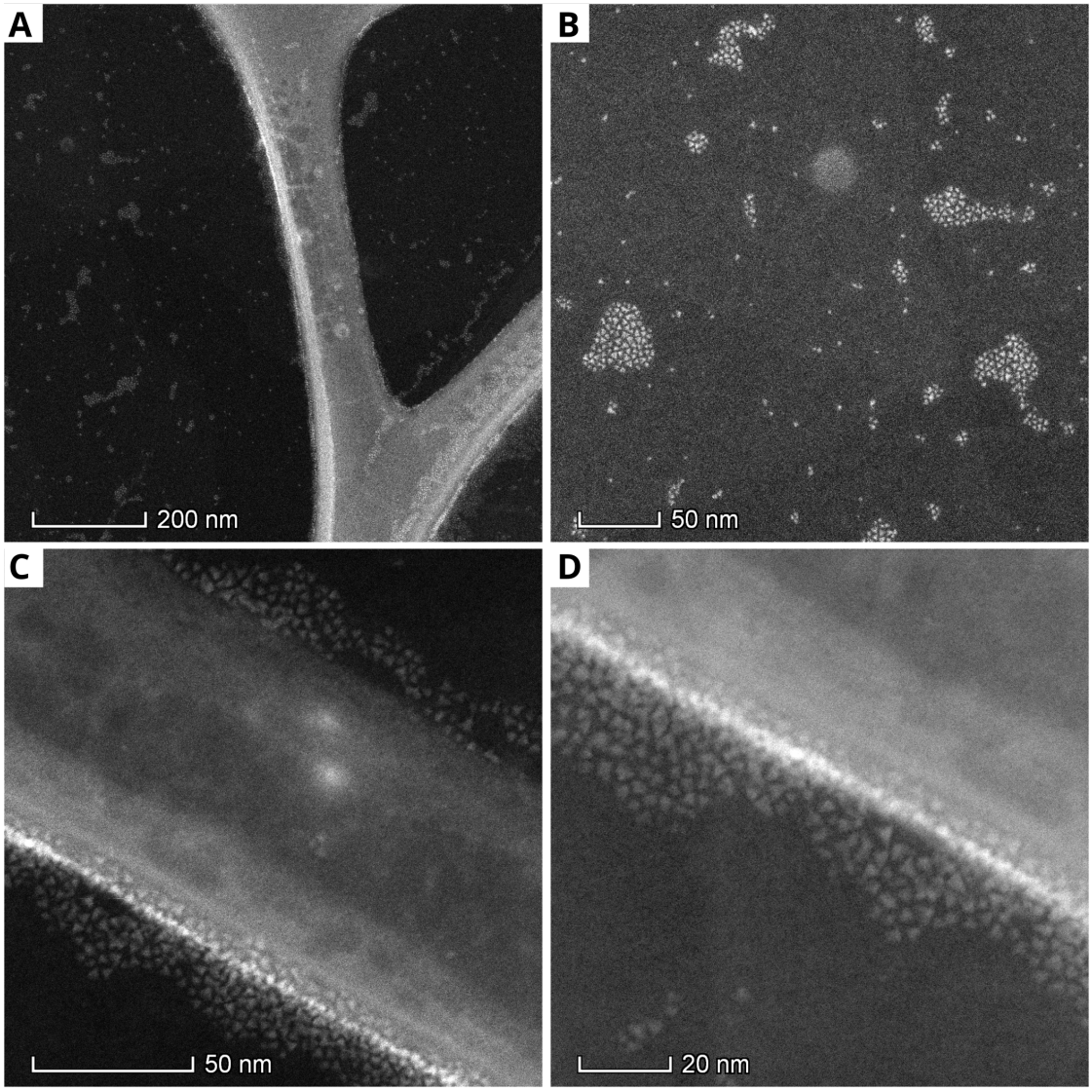

Figure 5.5: STEM images of colloidal $CuInS_2$/ZnS QDs dispersed in chloroform. Scale bars are (A) 200 nm, (B) 50 nm, (C) 50 nm, and (D) 20 nm.

To quantify that the determined size was representative of the population, the analysis

of TEM data undertaken on a smaller population of particles was compared to the semi-automated size analysis of STEM data. A series of example STEM images of the colloidal tetrahedral $CuInS_2$/ZnS QDs deposited on graphene-coated grids are shown in Figure 5.5 at increasing magnifications. The tetrahedral morphology and size distribution can be more clearly seen from these STEM images than TEM due to the high contrast between the atomically-dense QDs and the background, with visible groupings of QDs that appear to have arranged in a close-packed arrangement on the surface (Figure 5.5 A-B). QDs also associate at grid boundaries (Figure 5.5 C-D), aligning with observations made during TEM characterisation as previously noted.

Due to the high contrast between the QDs and the grid, the semi-automated analysis could be completed on the STEM images, which was compared to the manual size analysis completed on the TEM images. To calculate the 'size' of the $CuInS_2$/ZnS QDs, which refers to the longest corner-to-side distance of the triangular projection in TEM/STEM, the scale was initially calibrated using the scale bar in ImageJ (Figure 5.6 B). The threshold was then set for size analysis (Figure 5.6 C), allowing individual particles to be identifiable for automated size analysis through high contrast with the background (Figure 5.6 D).

As seen in Figure 5.7 A, the applied threshold did not separate the colloidal QDs that had dried adjacently, therefore a 'watershed' function was applied to define the boundary surrounding each individual particle. Figure 5.7 B shows the resulting particle selection, which was applied for all captured STEM images containing colloidal $CuInS_2$/ZnS QDs. A data selection parameter was applied to discount artefacts based on area, before manually removing 'extreme particles' that were not QDs but were not omitted by the software. The resulting size distribution is shown in Figure 5.7 C, with data fitting well to a Gaussian normal function. The average size was calculated to be 3.3 $\pm$ 0.6 nm, above the size obtained from the TEM images of 2.9 $\pm$ 0.4 nm, displaying a size dispersion of 18%. This is larger than the dispersion calculated from the manual analysis of TEM

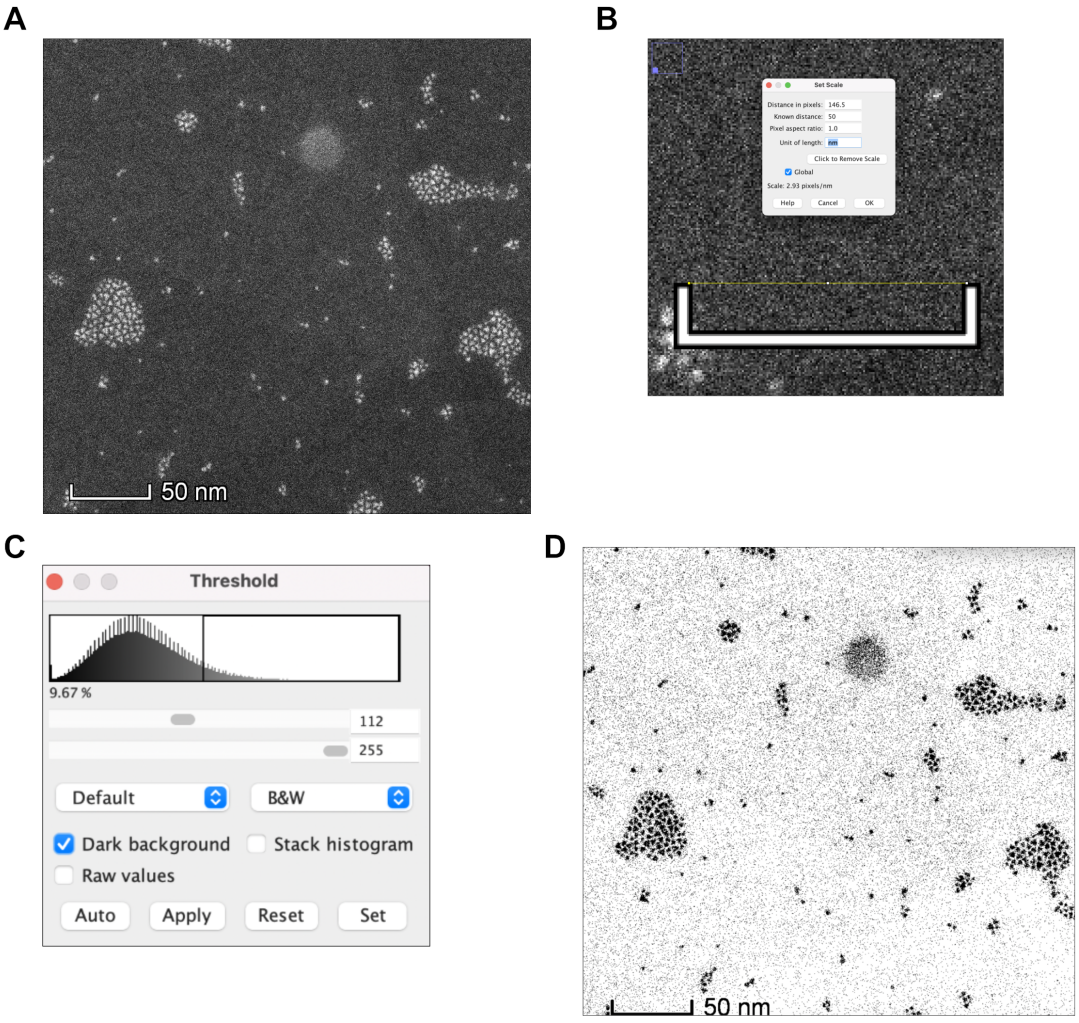

Figure 5.6: Automated analysis of colloidal $CuInS_2$/ZnS QD size. (A) Selected STEM image used for automated nanoparticle size analysis in ImageJ. Scale bar 50 nm. (B) Calibration of the scale for nanoparticle size analysis. (C) Threshold designation for nanoparticle selection. (D) The resulting contrast-enhanced image that allows nanoparticle selection after applying a threshold.

images of 13% and may be indicative of the core size being more consistent than the shell width due to variability during shell growth, or could be due to core concentration occurring due to cation exchange during shell formation as a reference in Chapter 3.2.2. The smaller distribution obtained during manual analysis may also be due to a smaller sample size, with 47 particles analysed during manual analysis compared to hundreds counted during the semi-automated analysis. The obtained size and relatively wide dispersion of the QDs is in agreement with tetrahedral $CuInS_2$/ZnS QDs synthesised using

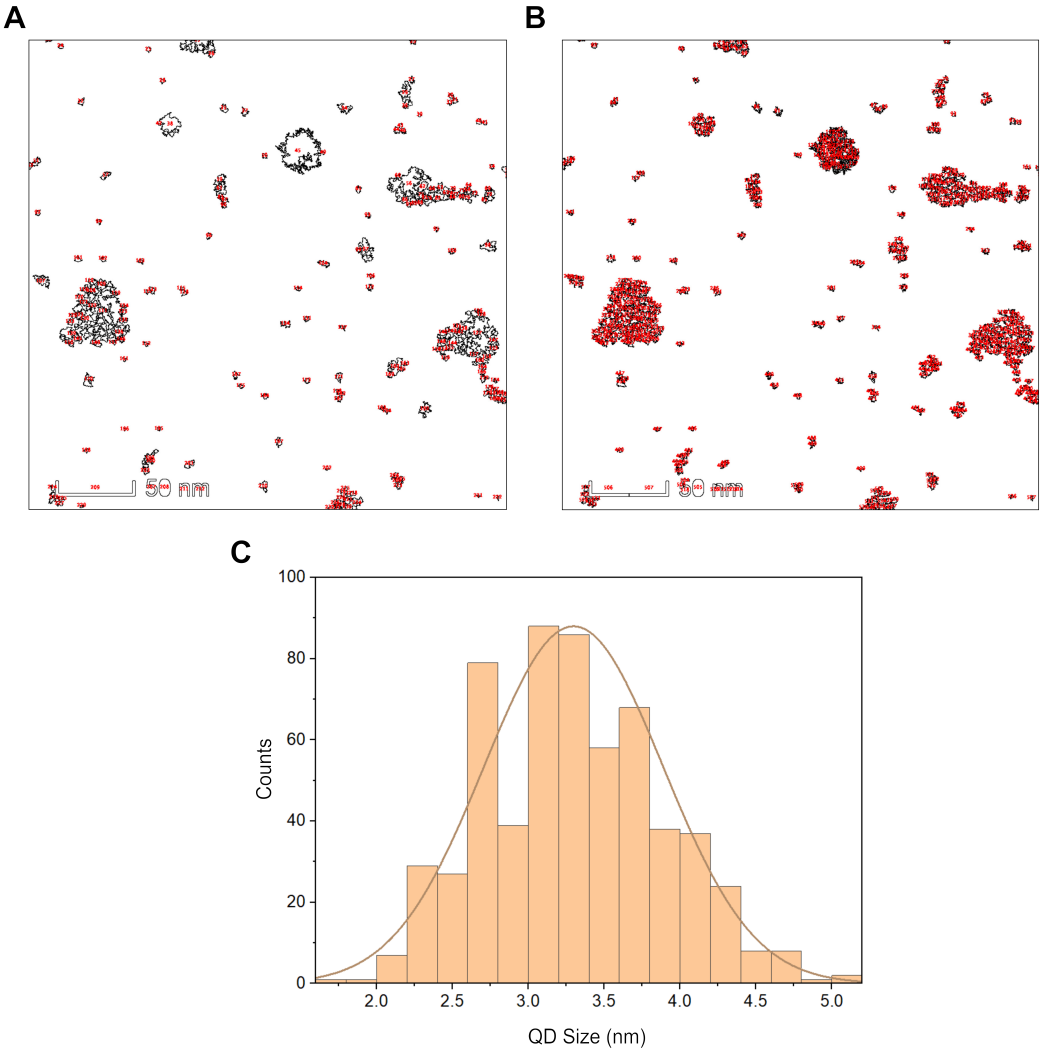

Figure 5.7: Size distribution of colloidal $CuInS_2$/ZnS QDs following semi-automated analysis. (A) Initial particle selection from original threshold parameters. (B) Final particle selection after applying a watershed function to separate boundaries of large clusters. (C) Histogram showing the size distribution of QDs from the semi-automated analysis. Bin widths are 0.2 nm, mean size = 3.3 ± 0.6 nm.

identical or similar techniques [68, 99, 191], as expected. However, the size distribution of the $CuInS_2$/ZnS QDs is larger than other investigations into the energy transfer pathways within QD nanoclusters using alternate QDs, including the early work by Crooker *et al.* where a size distribution of 7% was obtained when evaluating the strength of Förster coupling in close-packed assemblies of CdSe QDs [80]. This is expected to result in a larger energy difference between the smallest and largest QDs and could lead to a

larger reported red-shift in the fluorescence emission peak than reported or theorised in other studies [80, 88].

5.2.3 Size Analysis and Structure of $CuInS_2$/ZnS Quantum Dot Nanoclusters

Once the size distribution of the colloidal QDs had been determined, the size and structure of the lipid-stabilised QD nanoclusters could be investigated and compared. A combination of TEM/STEM images is shown in Figure 5.8 A and B showing small (<50 nm diameter) clusters that are polydisperse in size. The electron density appears to be a lot higher for the QD nanoclusters compared to colloidal QDs with darker structures displayed, suggesting a 3-D aggregate of overlapping particles as opposed to a 2-D cluster nucleated at the surface as in the colloidal TEM images. In agreement with the colloidal QD TEM data, the structure of individual QDs can clearly be seen in Figure 5.8 C, unequivocally confirming the presence of QDs.

To obtain the distribution of cluster sizes, manual size analysis was completed on particles from collected TEM images (Figure 5.9 A). The minor axis and major axis Feret diameter (a measure of size in a specific direction, defined as the distance between the two parallel planes restricting the object perpendicular to that direction) was recorded for each cluster, with example analysis shown in Figure 5.9 B. A mean minor axis Feret diameter of 33 $\pm$ 8 nm and a mean major axis Feret diameter of 43 $\pm$ 10 nm were obtained, with the data again fitting well to a Gaussian normal function. This is supportive of the steady-state fluorescence emission data previously shown in Section 5.2, with a large variation in cluster size likely to result in an equally-large variation of lowest-energy QDs per cluster. Figure 5.9 D plots the largest diameter against the smallest diameter for each QD nanocluster, showing the geometrical distribution of nanocluster shape. A perfectly spherical cluster will lie on the red line, with elliptical clusters situated furthest away from the line. QD nanoclusters were expected to be near-spherical in structure, although the high CMC of the lipid and drying effects due to cluster size may lead to the

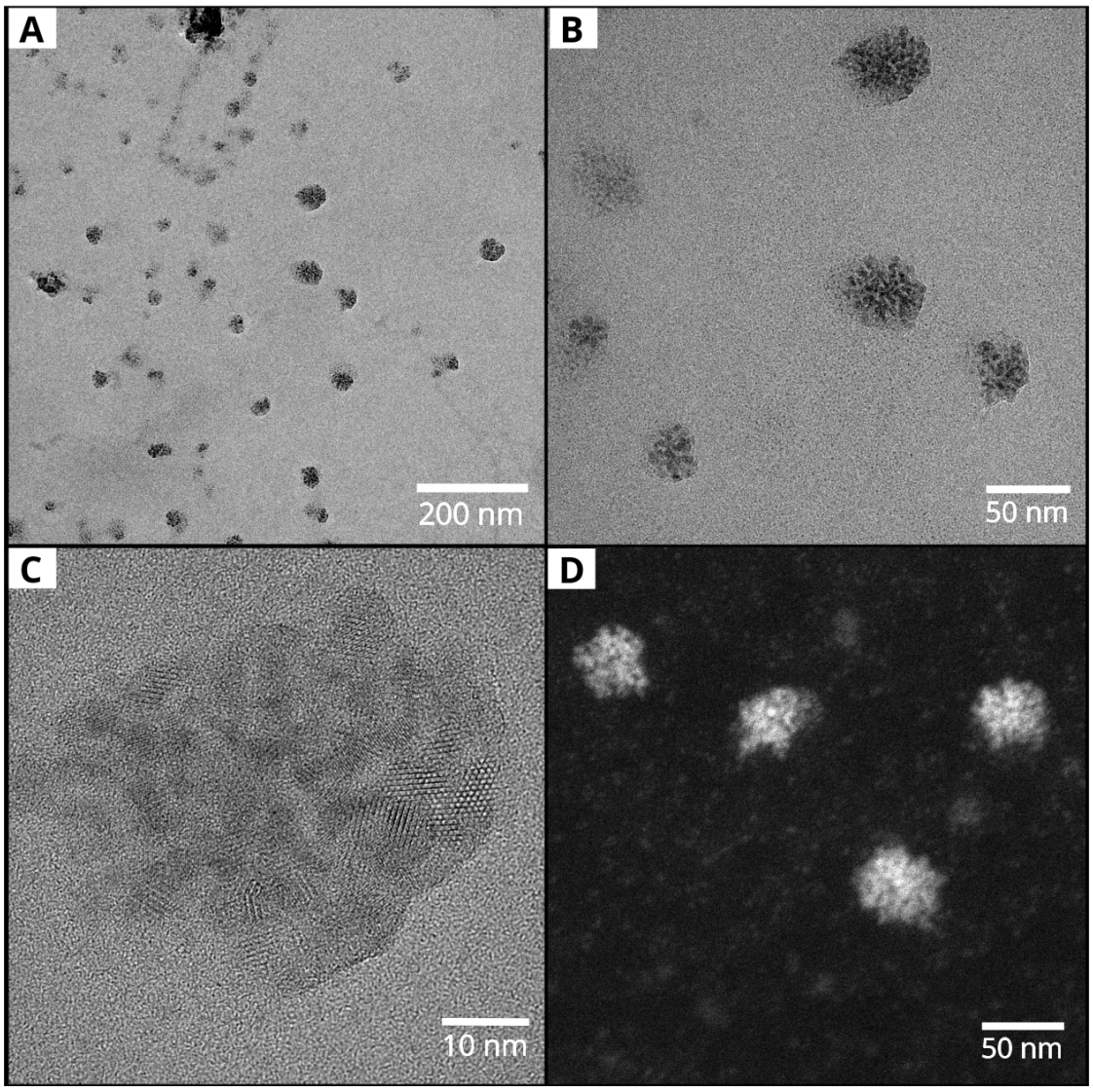

Figure 5.8: TEM/STEM images of $CuInS_2$/ZnS QD nanoclusters. Scale bars are (A) TEM - 200 nm, (B) TEM - 50 nm, (C) TEM - 10 nm, and (D) STEM - 50 nm. QD nanoclusters (QD concentration: 6.81 µM, lipid concentration: 10.2 mM) were diluted (1:100) using 50 mM HEPES, 100 mM NaCl (pH 7.5), then 2 µl of the sample was drop cast onto a TEM grid for imaging.

skew towards an elliptical structure. The structure of the QD nanoclusters determined from the TEM/STEM data and the corresponding fluorescence data correlates with reported findings of FRET within clustered QDs, with the broad fluorescence emission peak likely to result from energy being transferred downhill from QD to QD via FRET within each cluster [80, 82, 87].

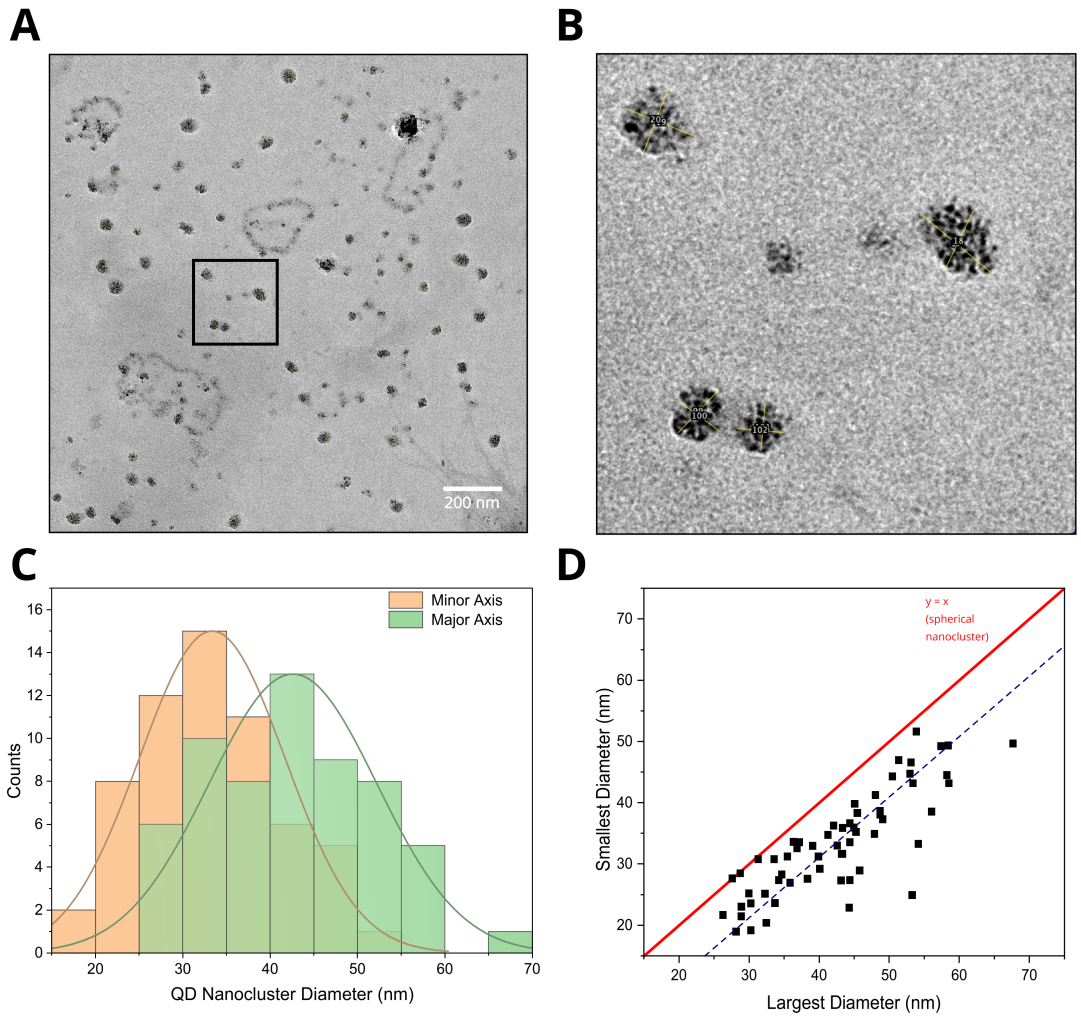

Figure 5.9: Size distribution of $CuInS_2/ZnS$ QD nanoclusters following manual analysis. (A) Example of manual size analysis using TEM image of QD nanoclusters. The scale bar is 200 nm. The highlighted area is magnified in panel (B), with examples of diameter determination shown. (C) Histogram showing the size distribution of QDs from the manual analysis. *Green* plots show the largest nanocluster diameter and *orange* plots show the smallest nanocluster diameter. Bin widths are 5 nm. (D) A plot of the smallest nanocluster diameter against the largest nanocluster diameter. The *red* line represents a perfectly spherical nanocluster where the smallest diameter is equal to the largest diameter and the *blue dashed* line represents the linear fit with a slope of 0.74 ± 0.07.

Control of the cluster size has been achieved through the use of phospholipids to stabilise hydrophobic $CuInS_2/ZnS$ QDs, allowing a stable nanocluster self-assembly in an aqueous environment without the need for solvent alteration, which provided little control over the cluster size in previous studies [87, 88]. The QD nanoclusters developed and characterised in this thesis are significantly smaller than the 100 nm diameter phospholipid-stabilised

CdSe/ZnS QDs developed by Li *et al.* [92], although is likely to contain a higher number of QDs per individual cluster due to the use of smaller, <3 nm $CuInS_2$/ZnS QDs in this research compared to the large, 16 nm mean diameter CdSe/ZnS QDs. The use of lipids also suggests that the clusters are likely to remain stable and fluorescent when deposited onto a surface as a thin film, and TEM investigation shows that the QD nanoclusters retain their size-and shape when drop-cast onto an untreated TEM grid. In summary, the structure of the QD nanoclusters is confirmed to align with the predicted structure outlined in Section 5.1, with a <50 nm QD nanocluster that is likely stabilised by co-localised lipids.

5.3 Co-localisation of the Quantum Dots and Lipids

To determine whether it is indeed the lipids that are stabilising the QDs and that the lipids and QDs are co-localised, the position of the lipid within the QD nanoclusters can be determined by incorporating fluorescently-labelled lipids through a combination of fluorescence spectroscopy and microscopy. Dye-tagged NBD-DHPE and BODIPY-DHPE lipids were chosen to map the location of lipids with respect to the QD clusters as there is little overlap between absorption and fluorescence emission spectra of the dyes and the $CuInS_2$/ZnS QDs. In both lipids, the NBD/BODIPY dye is attached to the polar head amino group of a DHPE lipid, but will still lie within the critical radius for efficient FRET to the QDs if the schematic in Figure 5.1 is correct, allowing quantification of the co-localisation via optical spectroscopy. If the clustered QDs are encapsulated by the lipid, then FRET between dye-tagged fluorescent lipids and the QDs should be observed via steady-state fluorescence spectroscopy, provided there is a spectral overlap between the absorbance of the energy acceptor and the fluorescence of the energy donor. Epifluorescence microscopy can also be used to quantify the co-localisation of the lipids and QDs, as filters allow control of excitation wavelengths as well as the wavelengths of emitted light that are collected. This allows two fluorescent components to be imaged simultaneously on the same sample, with the position of the

QDs and dye-tagged lipids identifiable through the capture of images across multiple channels.

5.3.1 Optical Spectroscopy Investigation into Energy Transfer From Lipid-Tagged Dye to $CuInS_2$/ZnS QDs

NBD-DHPE and BODIPY-DHPE lipid was introduced to separate samples at a ratio of 33:66:1 DOPG:DOPG:X-DHPE, where X represents the head-tagged NBD/BODIPY dye. The fluorescence emission peaks of NBD and BODIPY are 539 nm and 511 nm respectively, which sufficiently overlaps with the absorbance of the $CuInS_2$/ZnS QDs/ZnS shown previously in Figure 5.2 A. If the lipid and the QDs are co-localised and FRET is observed, a quenching of the dye fluorescence and an enhancement of the QD fluorescence would be expected due to downhill energy transfer. Control measurements using dye/lipid-only (no QDs) or QD/lipid-only (no dye-tagged lipid) were prepared identically (same concentrations used) to determine a reference for de-convolution, with the final concentration determinable from absorbance measurements. If the control measurements were prepared in exactly the same way and contained the same initial concentration of dye-tagged lipid/QDs, then the de-convolution can be corrected for concentration accurately and any donor/acceptor quenching/enhancement can be believed to represent FRET.

To de-convolute the relative fluorescence of the samples and investigate energy transfer from the dye to the quantum dots within the nanoclusters, the concentration of the quantum dots and lipid-tagged dye must be calculated from the raw absorbance of each sample (Figure 5.10 A). Once the concentration was calculated, the fluorescence can be divided by the concentration and normalised to give the relative fluorescence of each sample. One complication is that a small amount of light scattering affects the absorbance spectra, manifesting as an apparent increase in absorbance at lower wavelengths. The scattering was removed from the absorbance measurements using the C/λ^4 relationship, as scattering is inversely proportional to the fourth power of wavelength

in the normal dispersion regime [220]. An overlay of the scattering correction (Figure 5.10 B, *black* line) can be seen against the BODIPY-DHPE (*red* line) and NBD-DHPE (*blue* line) dye control measurements. Once the absorption was corrected for scattering, the Beer-Lambert law ($A = \epsilon Cl$) could be used to calculate the concentration of QDs and the dye, where A is the absorption of the sample component, ϵ is the molar absorption coefficient, C is the concentration and l is the path length. For $CuInS_2$/ZnS QDs with a fluorescence emission peak of 655 nm, the molar absorption coefficient is 93 490 M^{-1} cm^{-1} at 400 nm, giving an isolated QD nanocluster concentration that is in line with the control measurements. The calculated QD concentration of the QD/non-fluorescent lipid control measurement (Figure 5.10 C, *black* line) was found to be 1.16 µM, with a de-convoluted QD concentration in the QD/BODIPY-DHPE sample (Figure 5.10 C, *green* line) found to be 1.09 µM, and the de-convoluted QD concentration in the QD/NBD-DHPE sample (Figure 5.10 C, *purple* line) found to be 1.02 µM. For the NBD and BODIPY dyes, the molar absorption coefficients were 21 000 M^{-1} cm^{-1} at 400 nm and 87 000 M^{-1} cm^{-1} at 400 nm at their respective peaks [230], again leading to agreement with the control measurements. The concentration of BODIPY-DHPE in the control measurement (Figure 5.10 D, *red* line) was calculated to be 0.178 µM with the concentration of BODIPY-DHPE in the QD/BODIPY-DHPE sample (Figure 5.10 D, *green* line) determined to be 0.163 µM. For the NBD-DHPE control measurement (Figure 5.10 D, *blue* line), the NBD-DHPE concentration was calculated to be 1.06 µM and the concentration of NBD-DHPE in the QD/NBD-DHPE sample (Figure 5.10 D, *purple* line) was determined to be 1.25 µM.

The raw fluorescence obtained from steady-state fluorescence spectroscopy was divided by the calculated concentrations to give the relative fluorescence, then normalised with respect to the control measurements to give the de-convoluted relative fluorescence (Figure 5.10 E/F). If FRET occurs then the relative fluorescence of the donor must be lower when the acceptor is present and indeed this is what is observed with the BODIPY peak being less than half of its original fluorescence (*green* vs *red* plot in Fig 5.9E). The energy

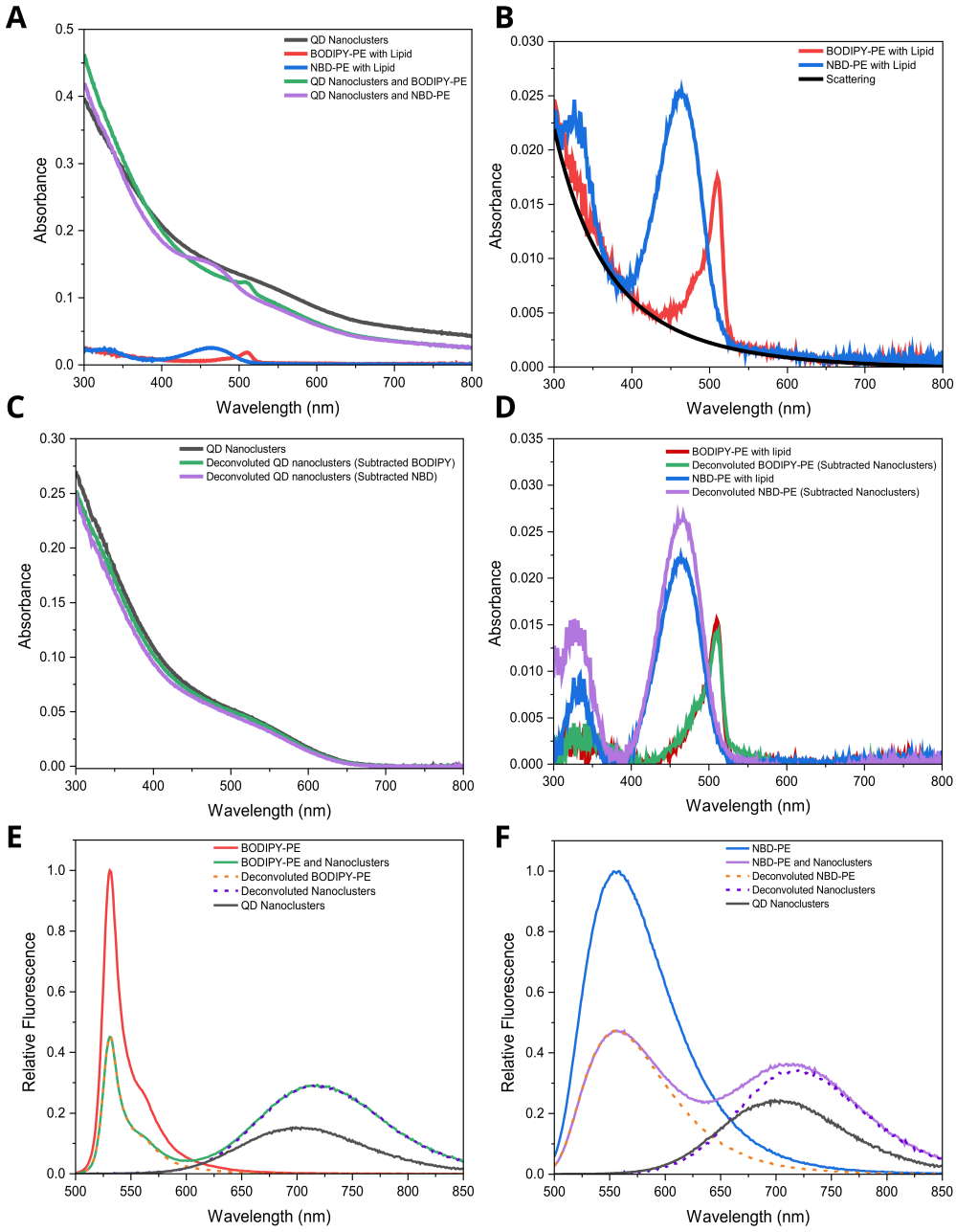

Figure 5.10: Spectra showing co-localisation of QDs and lipids within QD nanoclusters. (A) Raw absorbance of QD nanoclusters and control measurements before scattering removal. (B) Overlay of calculated scattering curve with BODIPY-DHPE and NBD-DHPE control measurements to demonstrate manual scattering removal. (C) De-convoluted absorbance of QD nanoclusters with control measurement after subtracting BODIPY-DHPE and NBD-DHPE spectra. (D) De-convoluted absorbance of BODIPY-DHPE and NBD-DHPE with control measurements after subtracting QD nanocluster spectra. (E) Relative fluorescence (fluorescence emission divided by concentration) showing fluorescence quenching of BODIPY-DHPE with an enhancement of QD emission (*green*) when compared to BODIPY-DHPE (*red*) and QD nanocluster (*black*) controls. (F) Relative fluorescence showing fluorescence quenching of NBD-DHPE with an enhancement of QD emission (*lilac*) when compared to NBD-DHPE (*blue*) and QD nanocluster (*black*) controls.

transfer efficiency (ETE) was calculated using the following equation:

$$ETE = 1 - \frac{F_{DA}}{F_{f,D}} \tag{5.3}$$

where F_{DA} is the donor fluorescence intensity in the presence of the acceptor and $F_{f,D}$ is the donor fluorescence intensity in the absence of the acceptor. An ETE of 54.7% for the BODIPY-DHPE nanoclusters was observed (Figure 5.10 E), indicative of a donor to acceptor distance of ∼4 nm. A 91.3% increase in the nanocluster fluorescence was also observed, showing clear energy transfer from the dye to the quantum dots. A 14 nm red-shift in the quantum dot fluorescence emission peak is also present, suggesting either a change in the formation or structure of the QD nanoclusters with the introduction of the lipid-tagged dye or a change in the energy transfer pathway due to the contribution of the fluorescent dye as an energy donor. A similar ETE of 52.6% was observed in the NBD-DHPE nanoclusters (Figure 5.10 F), with a 40.5% enhancement of the nanocluster fluorescence and a 16 nm red-shift in the emission peak position. The greater enhancement in acceptor fluorescence when using the BODIPY-DHPE dye likely occurs due to a greater overlap between the donor fluorescence emission and acceptor excitation compared to the NBD-DHPE dye, where the BODIPY-DHPE emission peak coincides with the spike in quantum dot absorbance.

The corresponding time-resolved fluorescence data also supports the interpretation of FRET occurring between the NBD/BODIPY-DHPE lipids and QDs, as shown in Figure 5.11. A 473 nm pulsed diode laser was used to excite all samples, as described in Methods section 2.6.3. The time-resolved data shows an exponential decay that gets less steep for the QDs in the presence of BODIPY-DHPE (Figure 5.11 A, *green* line) and steeper in the presence of NBD-DHPE (*purple* line) when compared to the QD nanocluster control (*black* line). The exponential decay becomes steeper for the BODIPY-DHPE lipid in the presence of QDs (Figure 5.11 B, *blue* line) compared to the BODIPY-DHPE controls without QDs (*dark blue* line). A similar trend is also seen for the NBD-DHPE

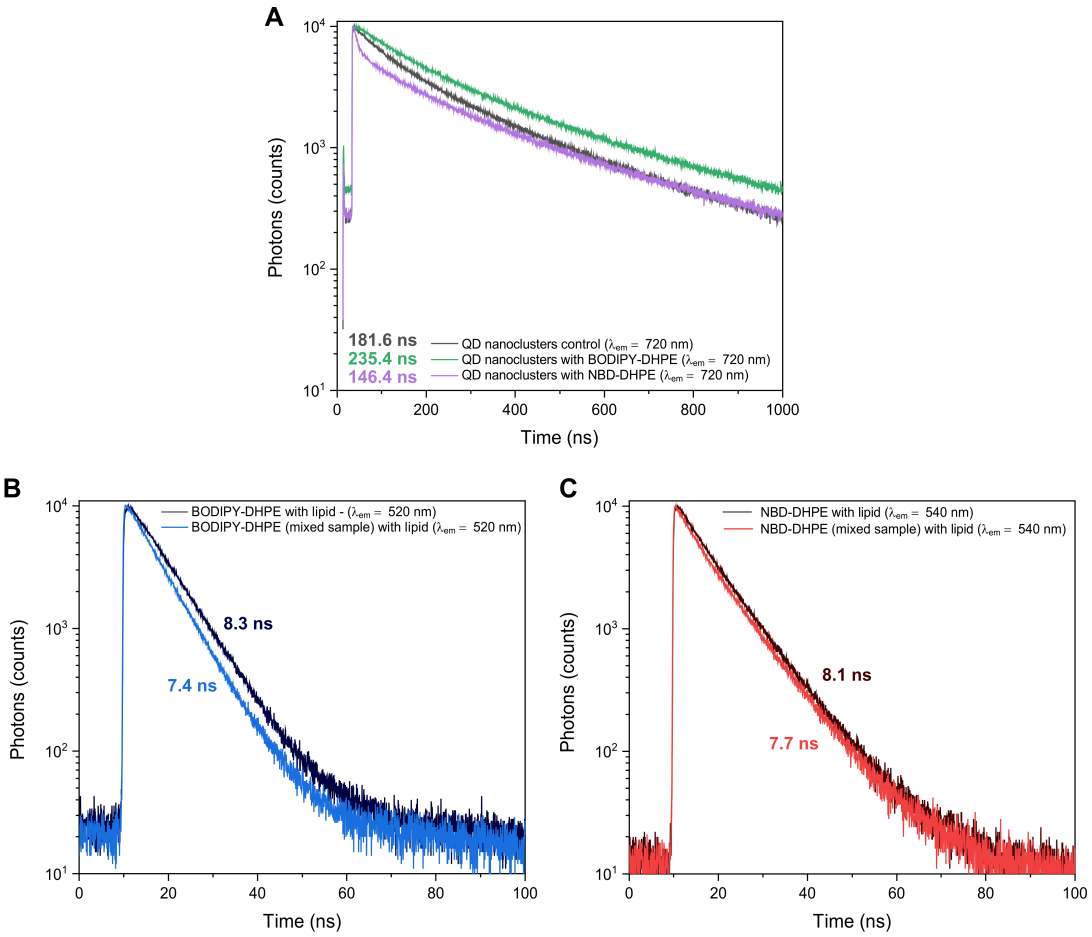

Figure 5.11: Time-resolved spectra showing the lifetime of QDs and lipids within QD nanoclusters. (A) TCSPC measurements (λ_{ex} = 473 nm) showing fluorescence lifetime of QD nanoclusters control with no dye-tagged lipid (*dark grey*) compared to QD nanocluster fluorescence lifetime with BODIPY-DHPE (*green*) and NBD-DHPE (*purple*). (B) TCSPC measurements (λ_{ex} = 473 nm) showing fluorescence lifetime of 1% BODIPY-DHPE control (*dark blue*) and 1% BODIPY-DHPE used to self-assemble QD nanoclusters (*light blue*). (C) TCSPC measurements (λ_{ex} = 473 nm) showing fluorescence lifetime of 1% NBD-DHPE control (*dark red*) and 1% NBD-DHPE used to self-assemble QD nanoclusters (*light red*).

lipid in the presence of QDs (Figure 5.11 C, *red* line), where the exponential decay is steeper than the NBD-DHPE control measurement without QDs present (*dark red* line). The amplitude-weighted average lifetime for the QD nanocluster control (Figure 5.11 A, *dark grey* line) was 181.6 ns when no fluorescent dye was present. An increase to the QD nanocluster average lifetime to 235.4 ns was observed when fluorescent BODIPY-DHPE dye was used to stabilise the QDs (Figure 5.11 A, *green* line), accompanied by a decrease in the donor BODIPY-DHPE average lifetime (Figure 5.11 B), from 8.3 ns

in the control measurements (*dark blue* line) to 7.4 ns when BODIPY-DHPE was used to stabilise the QDs (*light blue* line). Due to an overlap of fluorescence at 720 nm, a significant contribution from the NBD-DHPE lipid was observed in the time-resolved measurements of the QD nanoclusters in the mixed sample (Figure 5.11 A, *purple* line), leading to a rapid initial decay due to the short lifetime of NBD. This resulted in a much lower average lifetime for the QD nanoclusters of 146.4 ns, even though a longer lifetime was expected. The donor NBD-DHPE average lifetime (Figure 5.11 B) decreased from 8.1 ns in the NBD-DHPE control (*dark red* line) to 7.7 ns when NBD-DHPE was used to stabilise the QDs (*light red* line). The NBD-DHPE lipid fluorescence appears to be slightly less quenched (5%) than the BODIPY-DHPE lipid (11%), which is surprisingly lower than the steady-state measurements and cannot be explained. The steady-state measurements show a 52.6% donor quenching for the NBD-DHPE dye compared to a 54.7% donor quenching in the BODIPY-DHPE dye, therefore a lower quenching was observed in the NBD-DHPE, in agreement with the time-resolved data. As energy transfer between the lipid-tagged dye and the QDs has occurred, with quenching of the donor fluorescence leading to a reduction in fluorescence lifetime accompanied by an enhancement of the acceptor fluorescence, it can be concluded that the vast majority of lipid is located within the Förster radius of the QDs and therefore encapsulates the QDs to form stabilised lipid-QD nanoclusters.

5.3.2 Epifluorescence Investigation into Co-localisation of the Lipid-Tagged Dye and $CuInS_2/ZnS$ QDs

To further confirm co-localisation between the lipid and the QDs, epifluorescence microscopy was used to investigate the position of QDs and lipids when deposited on a surface. The QD nanoclusters were expected to remain stable and fluorescent if encapsulated by the lipid, thus it is important to assess the optical properties of QD nanoclusters when surface-deposited and confirm the structure with respect to the stabilising lipid. While fluorescence microscopy is diffraction-limited, it is complementary to ensemble spectroscopy and will allow individual QD nanoclusters to be identified on the planar

surface. Dye-tagged NBD-DHPE lipid was chosen to map the position of lipid on the surface as a fluorescence excitation peak at 467 nm and a fluorescence emission peak at 539 nm lie within the imaging parameters of the 'blue' excitation channel (EX 465 - 495 nm, DM 505 nm, BA 515 - 555 nm). Samples and controls were self-assembled as described in Methods section 2.2.6, with epifluorescence preparation described in Section 2.8.

When imaging multiple fluorescent samples, the optimal filter set-up for sample excitement and image capture must be determined. Control measurements were taken using a lipid-only sample (no QDs) and a separate QD nanocluster-only sample (no fluorescent lipid) to ensure minimal signal was observed in secondary filter channels (i.e., no QD signal was observed in the NBD imaging channel) using consistent collection parameters. Figure 5.12 A shows the NBD signal observed from the 'lipid-only' control in the 'blue' excitation channel using a 2-second exposure time, clearly showing the presence the fluorescent lipid. Figure 5.12 B shows the same 'lipid-only' control sample in the 'green' excitation channel (EX 540 - 580 nm, DM 595 nm, BA 600 - 660 nm) to be used for QD imaging, with negligible signal observed as expected. Figure 5.12 C shows the observed signal from the 'QD nanocluster-only' sample in the 'blue' excitation channel with a 2-second exposure time, where <1% of the signal from the corresponding image in the 'green' excitation channel (Figure 5.12 D) is observed. From the control measurements, any signal observed in the 'blue' excitation channel can assuredly be assigned to the NBD-DHPE lipid and any signal from the 'green' excitation channel can be assigned to the QDs. Channel crossover was calculated to be <1% by analysing intensity profiles across identical areas of the two channels after subtracting the 101 background count (data not shown), although a small signal can be seen in Figure 5.12 C where the signal is highly saturated in Figure 5.12 D, so care was taken to avoid signal saturation through use of ND filters in subsequent measurements.

Once it was confirmed that only the desired fluorescent component from each sample

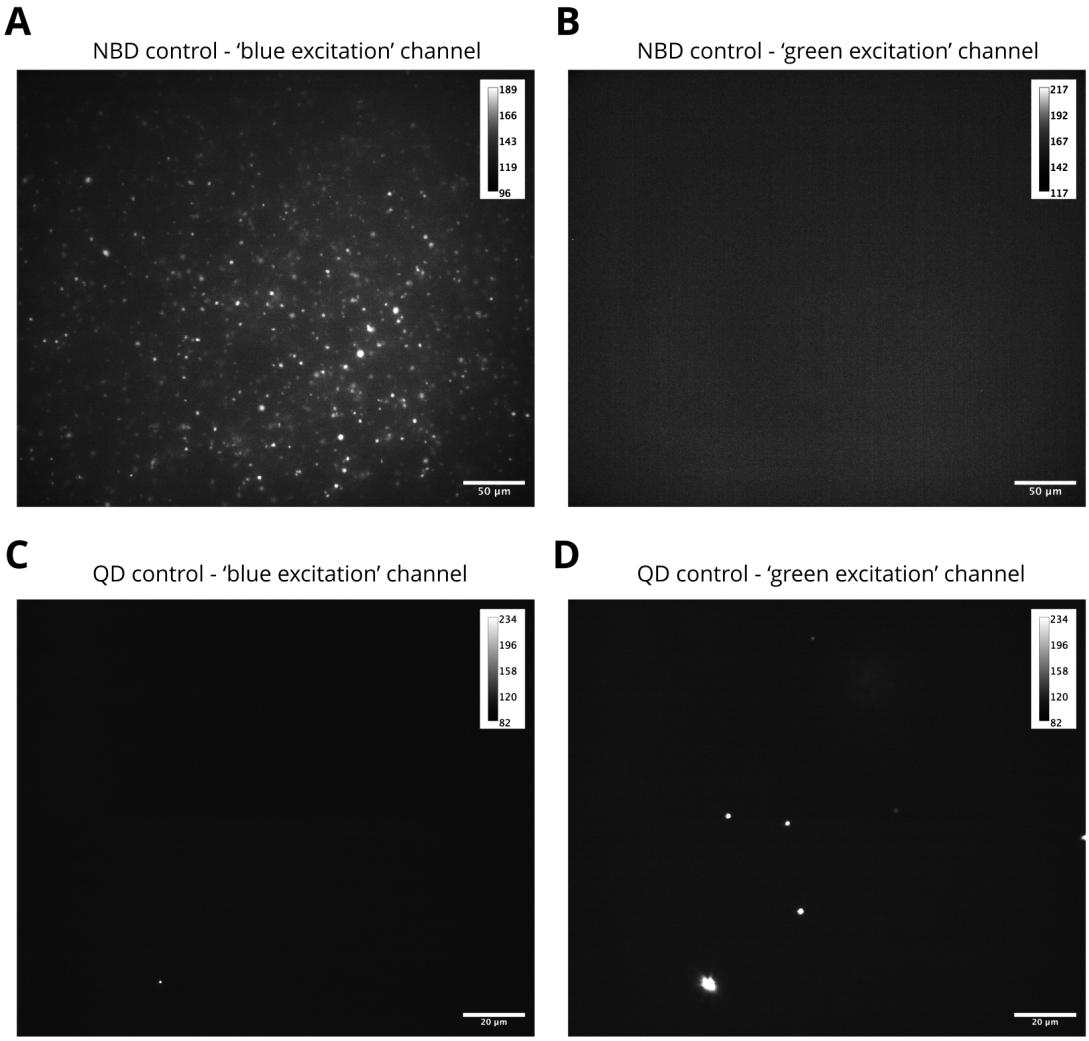

Figure 5.12: Epifluorescence microscopy control measurements of NBD-DHPE and QD nanoclusters. (A) Surface-deposited 1% NBD-DHPE, 33% DOPG, 66% DOPC assemblies (0.5 mg/ml) captured in the 'blue' excitation channel (EX 465 - 495 nm, DM 505 nm, BA 515 - 555 nm). 2-second exposure, ×40 magnification, no ND filters selected. (B) Surface-deposited 1% NBD-DHPE, 33% DOPG, 66% DOPC assemblies (0.5 mg/ml) captured in the 'green' excitation channel (EX 540 - 580 nm, DM 595 nm, BA 600 - 660 nm). 2-second exposure, ×40 magnification, no ND filters selected. (C) Surface-deposited QD nanoclusters (33% DOPG, 67% DOPC, 0.5 mg/ml) captured in the 'blue' excitation channel. 300 ms exposure, ×100 magnification, no ND filters selected. (D) Surface-deposited QD nanoclusters (33% DOPG, 67% DOPG, 0.5 mg/ml) captured in the 'green' excitation channel. 300 ms exposure, ×100 magnification, no ND filters selected.

was being imaged in the respective channels, then co-localisation of the lipid and QDs could be investigated. 1% NBD-DHPE was added to a 33% DOPG, 66% DOPC lipid mixture to form QD nanoclusters, as described in Methods section 2.2.6, with samples

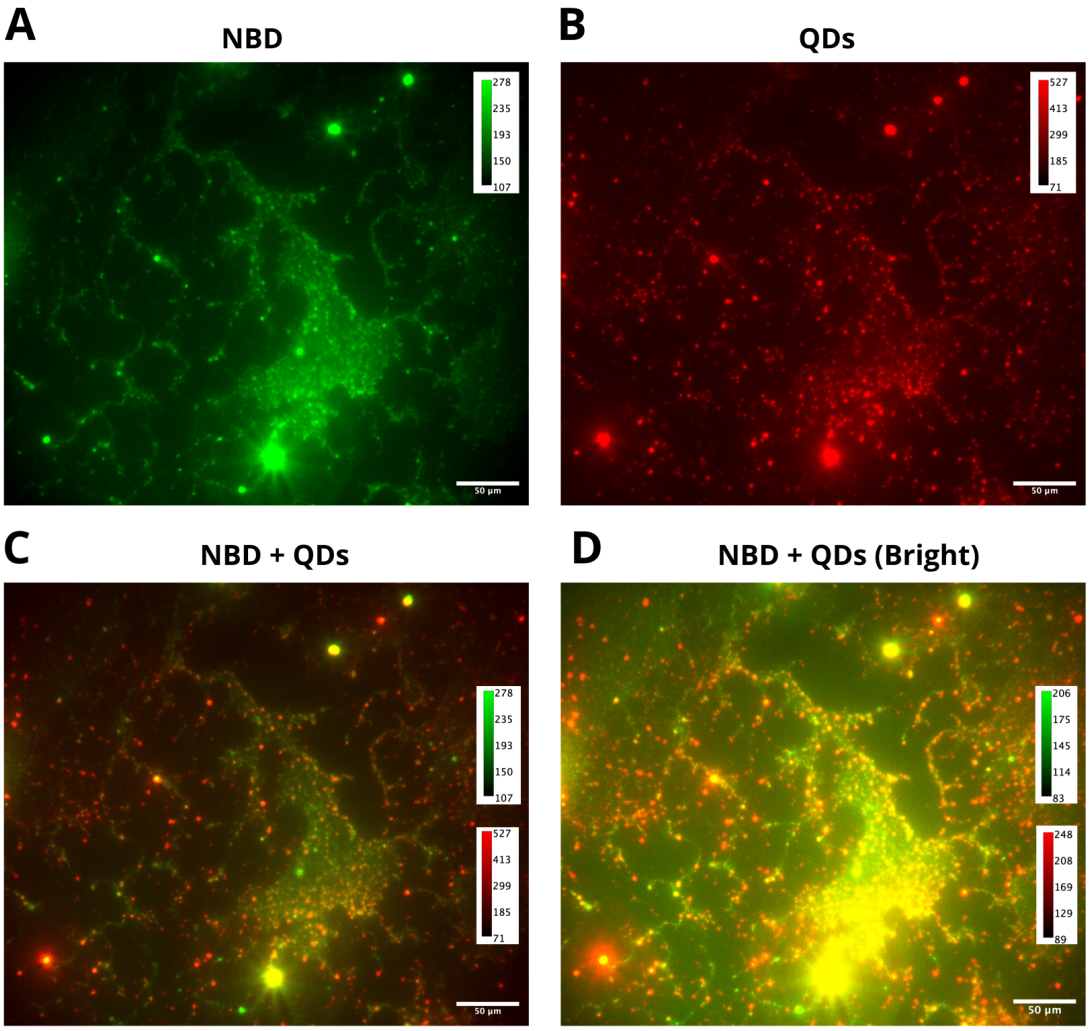

Figure 5.13: Epifluorescence microscopy showing co-localisation of QDs and lipid. (A) Surface-deposited QD nanoclusters (1% NBD-DHPE, 33% DOPG, 66% DOPC, 0.5 mg/ml) imaged in the 'blue' excitation channel (EX 465 - 495 nm, DM 505 nm, BA 515 - 555 nm). (B) Surface-deposited QD nanoclusters (1% NBD-DHPE, 33% DOPG, 66% DOPC, 0.5 mg/ml) imaged in the 'green' excitation channel (EX 540 - 580 nm, DM 595 nm, BA 600 - 660 nm). Composite images at low brightness (C) and high brightness (D) combining (A) and (B) showing co-localisation of the QDs and lipids. All images were captured with 300 ms exposure, ×40 magnification, no ND filters selected, scale bar is 50 µm.

prepared for epifluorescence microscopy as described in Section 2.8. Figure 5.13 shows the co-localisation of the fluorescent NBD-DHPE lipid and the QDs by combining identical images taken of the sample using various excitation and emission filters following surface-deposition. The NBD-DHPE fluorescence is displayed in *green* (Figure 5.13 A), with the QD fluorescence displayed in *red* (Figure 5.13 B). The composite images com-

bining both excitation channels are displayed in Figures 5.13 C and D, with areas of QD-lipid co-localisation shown in *yellow*. The bright red spots of QD fluorescence in the composite image show spatial overlap with the lipid with bright spots of yellow throughout the image, indicative of lipid and QD co-localisation. The lipid appears to be spread across the surface, although deposition appears to be non-uniform with unoccupied areas that are absent of lipids and QDs observed. The presence of *green* dots in the composite image (Figure 5.13 C) also suggest the presence of empty lipid vesicles, although the population of empty vesicles is low in comparison to QD nanoclusters.

Zooming in on bright particles further shows the spatial overlap of the QDs and the NDB-DHPE lipid (Figure 5.14), showing high concentrations of lipid surrounding large, bright clusters of QDs. The NBD-DHPE lipid is found at lower concentrations encapsulating smaller QD clusters, which appear to be diffraction-limited and fall below 300 nm in size, consistent with TEM data. The extremely bright particles may be a result of a larger cluster of QDs, or a 'clustering of clusters' following surface deposition, resulting in areas of concentrated fluorescence. A second zoomed-in epifluorescence microscopy image (Figure 5.15) again shows the spatial overlap of many smaller clusters of QDs with the NBD-DHPE lipid with many bright yellow sports observed. Again, these images provide evidence for co-localisation of the lipid and QDs through spatial overlap and suggest that an assessment of the time-resolved characteristics and single-particle dynamics using fluorescence lifetime imaging microscopy may be revealing.

5.4 Investigating the Role of the Lipid Within Nanocluster Self-Assembly

To investigate the role of lipid-QD interactions during the nanocluster formation, the lipid:QD molar ratio was modulated during nanocluster assembly. A series of samples were prepared, with the concentration of QDs fixed and the lipid-to-QD ratio varied from

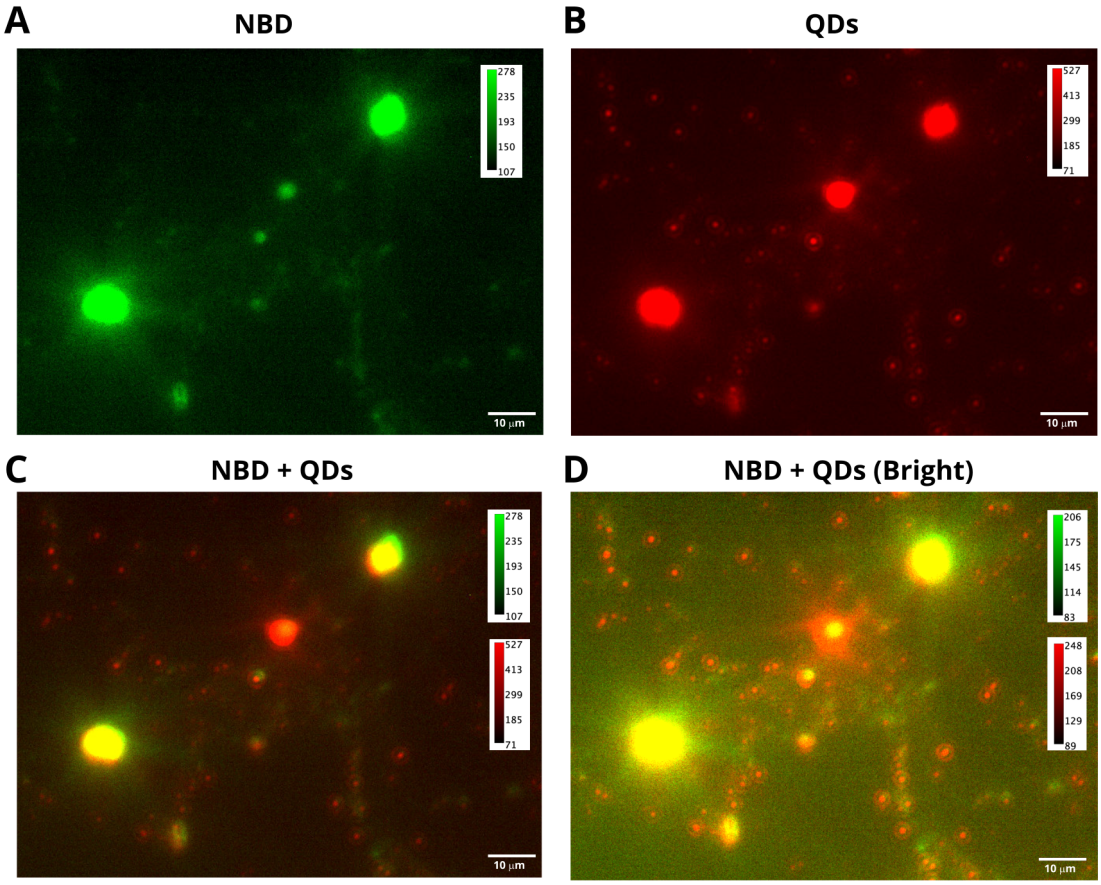

Figure 5.14: First zoomed-in epifluorescence microscopy image showing co-localisation of QDs and lipid. (A) Surface-deposited QD nanoclusters (1% NBD-DHPE, 33% DOPG, 66% DOPC, 0.5 mg/ml) imaged in the 'blue' excitation channel (EX 465 - 495 nm, DM 505 nm, BA 515 - 555 nm). (B) Surface-deposited QD nanoclusters (1% NBD-DHPE, 33% DOPG, 66% DOPC, 0.5 mg/ml) imaged in the 'green' excitation channel (EX 540 - 580 nm, DM 595 nm, BA 600 - 660 nm). Composite images at low brightness (C) and high brightness (D) combining (A) and (B) showing co-localisation of the QDs and lipids. All images were captured with 300 ms exposure, ×40 magnification, no ND filters selected, scale bar is 10 µm.

100:1 to 1750:1 (where the lipid used was a 2:1 mixture of DOPC:DOPG, as previously described). Figure 5.16 A shows the presence of QDs with increasing lipid concentration, showing the importance of the lipid in the self-assembly of QD nanoclusters. It was observed that the sample was almost colourless in the first vial and the colouration increases with lipid ratio until it is comparable to 'before' for the highest two lipid ratios. Absorption measurements (Figure 5.16 B) show a low signal at a 100:1 lipid:QD ratio (*dark green* line), indicating minimal sample present, with a lower amount of QDs

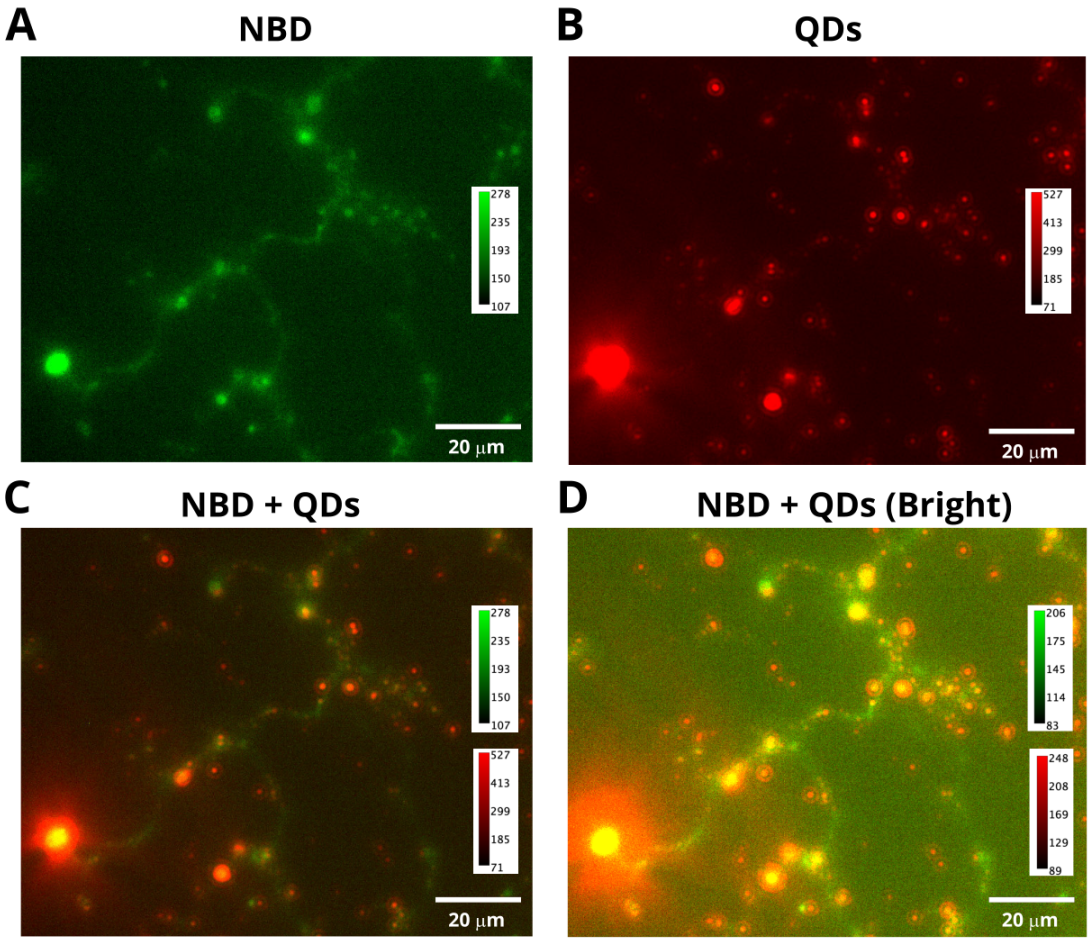

Figure 5.15: Second zoomed-in epifluorescence microscopy image showing co-localisation of QDs and lipid. (A) Surface-deposited QD nanoclusters (1% NBD-DHPE, 33% DOPG, 66% DOPC, 0.5 mg/ml) imaged in the 'blue' excitation channel (EX 465 - 495 nm, DM 505 nm, BA 515 - 555 nm). (B) Surface-deposited QD nanoclusters (1% NBD-DHPE, 33% DOPG, 66% DOPC, 0.5 mg/ml) imaged in the 'green' excitation channel (EX 540 - 580 nm, DM 595 nm, BA 600 - 660 nm). Composite images at low brightness (C) and high brightness (D) combining (A) and (B) showing co-localisation of the QDs and lipids. All images were captured with 300 ms exposure, ×40 magnification, no ND filters selected, scale bar is 20 µm.

stabilised at the lower lipid concentrations. The 250:1 and 500:1 lipid:QD signals (*green* and *lime green* lines) were larger but the first excitation peak was not as prominent, indicating that the measured absorbance contained significant scattering, evident when comparing to the control measurements of the colloidal QDs in chloroform (*black dashed* line). A large increase in absorbance was observed for the 750:1 lipid:QD concentration (*amber* line), then appears to reach a maximum QD uptake between the 1250:1 and

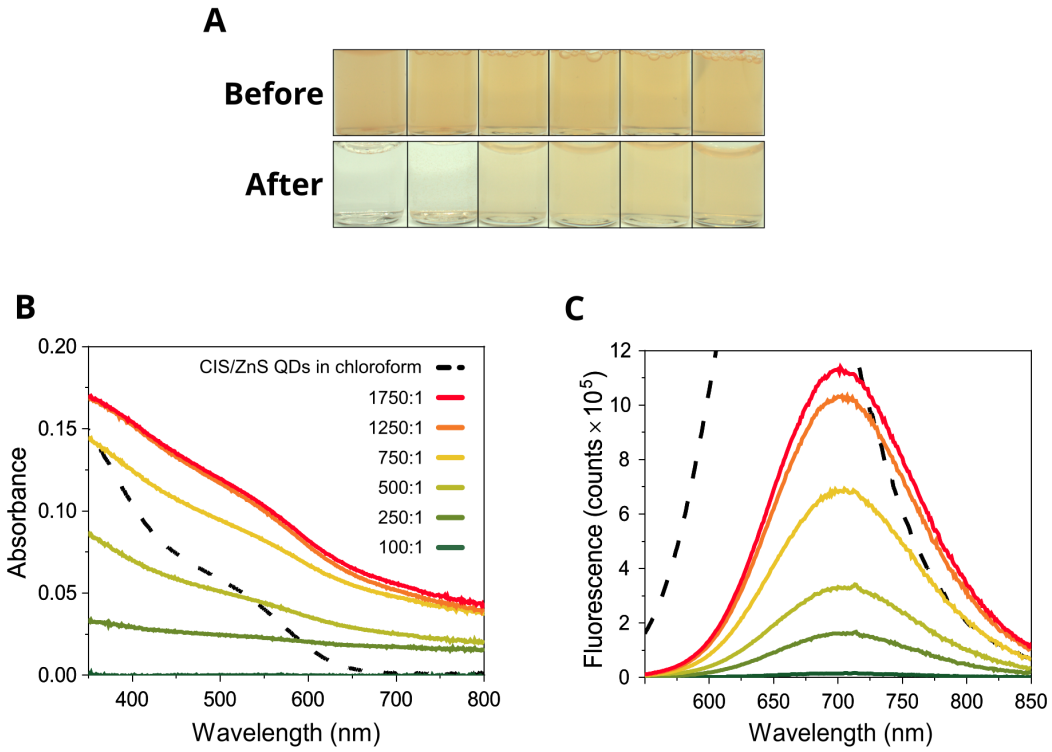

Figure 5.16: Increase in QD uptake with respect to lipid concentration. (A) Image showing the sample concentration and QD uptake before (top) and after (bottom) QD nanocluster self-assembly with an increasing molar ratio of lipid:QD. From left to right: 100:1, 250:1, 500:1, 750:1, 1250:1 and 1750:1. (B) Absorption of $CuInS_2$/ZnS QD nanoclusters in 50mM HEPES, 100mM NaCl with increasing molar ratio of lipid:QD from 100:1 (dark green) to 1750:1 (dark red) compared to colloidal $CuInS_2$/ZnS QDs in chloroform (dashed black) at a fixed QD concentration. (C) Accompanying steady-state fluorescence measurements (λ_{ex} = 475 nm) of $CuInS_2$/ZnS QD nanoclusters with increasing molar ratio of lipid:QD from 100:1 (dark green) to 1750:1 (dark red).

1750:1 lipid:QD concentrations (*orange* and *red* lines). It was surmised that the QDs that were not stabilised by the lipid had formed large, unstable aggregates that had fallen out of the solution, leading to low absorbance at low lipid concentrations. The steady-state fluorescence measurements (Figure 5.16 C) show a consistent relationship between the amount of lipid and the fluorescence intensity of the sample, with a lesser intensity increase between the 1250:1 and 1750:1 lipid:QD ratio samples consistent with absorption measurements, indicative of a maximum uptake of QDs into the lipid assembly. There was no difference in red-shift as the lipid concentration was increased, so the energy transfer pathways of the nanoclusters remained the same and it is unlikely

that the structure was significantly altered, although the clusters could be smaller or larger in size. A significant red-shift is still observed when compared to colloidal QDs in chloroform (*black dashed* line).

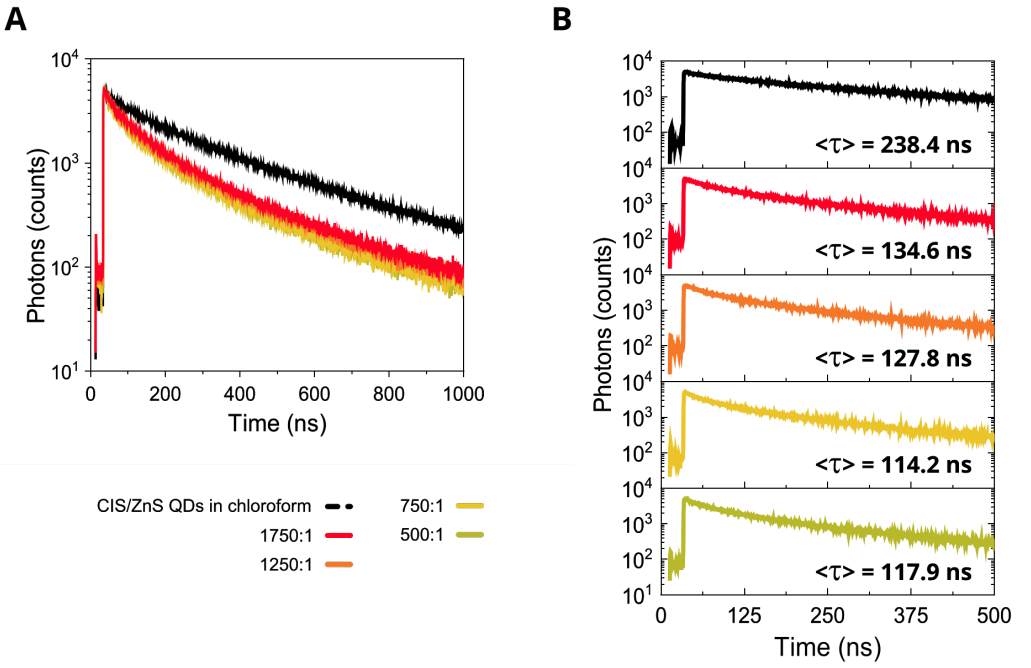

Figure 5.17: Change in QD fluorescence lifetime with respect to lipid concentration. (A) Time-Correlated Single Photon Counting (TCSPC) measurements comparing the fluorescence decay of colloidal $CuInS_2/ZnS$ QDs in chloroform (black) to $CuInS_2/ZnS$ QD nanoclusters. (B) TCSPC measurements with displayed average lifetime.

Time-correlated single photon counting decay (TCSPC) measurements (Figure 5.17) agree with the steady-state fluorescence measurements and show a reduction in the fluorescence lifetime of the QD nanocluster fluorescence compared to colloidal QD control measurement in chloroform (*black* line). An increase in fluorescence quenching that leads to a reduction in the lifetime is also observed as the amount of lipid present is reduced, where the 1750:1 sample is the least-quenched (Figure 5.17 A/B).

Plotting the fluorescence emission intensity against the lipid:QD molar ratio (Figure 5.18, *black* line) shows a linear increase in the fluorescence emission intensity until the

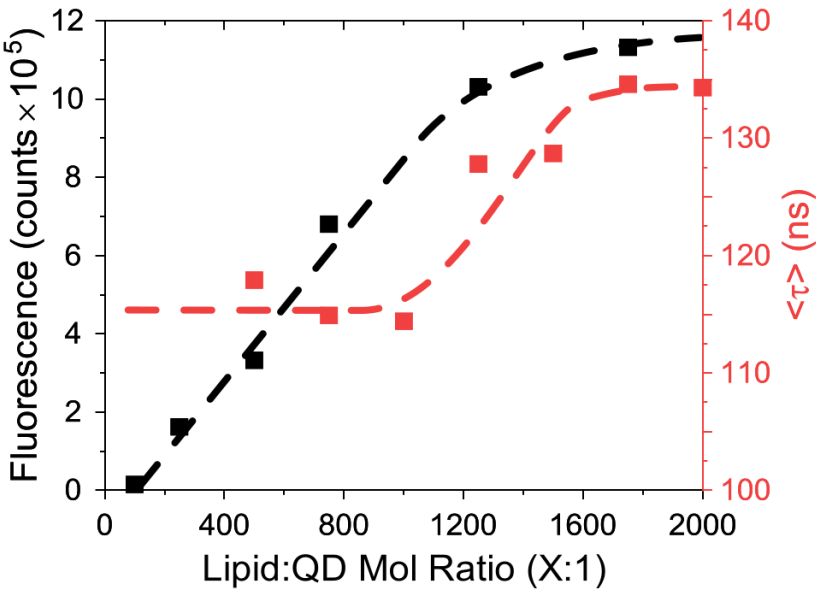

Figure 5.18: Fluorescence intensity and fluorescence lifetime against lipid:QD molar ratio. Steady-state fluorescence emission peak intensity (black) and average lifetime (red) of QD nanoclusters at varying lipid:QD molar concentrations.

QD uptake limit is reached between a lipid:QD molar ratio of 1250:1 and 1750:1. The fluorescence intensity then begins to plateau, again supporting previous absorption measurements form Figure 5.16 A. There appear to be two distinct phases based on the plot of time-resolved measurements against the lipid:QD molar ratio (Figure 5.18), with an intermediate phase between a ratio of 1000:1 and 1750:1. This may be due to a lack of stabilisation due to the low lipid concentration, with full stabilisation achieved between a lipid:QD ratio of 1500:1 and 1750:1. This may also explain the drop in absorbance due to QD uptake, with a lower percentage of clusters stabilised leading to a drop in QD concentration and therefore steady-state fluorescence emission. It seems that at 1750:1 and 2000:1 the fluorescence lifetime has plateaued. This could suggest that there is more than enough lipid to stabilize the clusters and that the maximal lifetime for clustered QDs is reached. The lifetime of the QDs may increase as the lipid concentration is increased due to the lipid controlling the cluster size. If the QD clusters decrease in size with increasing lipid, then each nanocluster will contain fewer QDs and FRET within the

individual nanoclusters will be reduced, with the likelihood of trap-state dissipation also decreasing as the number of QDs involved in downhill energy transfer will be reduced.

5.5 The Ensemble Photophysics of Quantum Dot Nanoclusters in Solution

Once the architecture of the QD-lipid nanoclusters had been determined (similar to Figure 5.1, panel 6A), the ensemble photophysics of QD nanoclusters could be investigated in an attempt to determine the pathway of energy transfer. A combination of fluorescence excitation vs. emission data and time-resolved emission spectroscopy (TRES) was used to investigate the ensemble photophysics of the QD nanoclusters, where the ensemble spectroscopy would give an insight into energy transfer pathways within the nanoclusters.

Fluorescence excitation vs. emission measurements were taken on colloidal $CuInS_2$/ZnS QDs in chloroform (Figure 5.19 A) and $CuInS_2$/ZnS QD nanoclusters in 50 mM HEPES, 100 mM NaCl (pH 7.5) to determine whether the excitation wavelength alters energy transfer pathways within the QD nanoclusters. Figure 5.19 A shows a 2-D contour plot of the fluorescence excitation vs. emission wavelengths for colloidal $CuInS_2$/ZnS QDs, with a maximum intensity at 655 nm for lower excitation wavelengths. The wavelength of the maximum intensity shifts to the red as the excitation wavelength approaches the emission peak, as shown by the *black* arrows, indicative of selective lower-energy sub-population excitement at higher wavelengths, leading to a relatively lower-energy emission. Figure 5.19 B shows a 2-D contour plot of the fluorescence excitation vs. emission wavelengths for the QD nanoclusters, where a consistent maximum intensity at 700 nm was observed with little shift in peak position. Figure 5.19 C shows the plots of fluorescence emission maxima against excitation wavelength, where the trend for $CuInS_2$/ZnS QD nanoclusters (*red*) consistently gives an emission peak of 700 nm, indicative of consistent energy transfer pathways within the QD clusters regardless of excitation energy. The emission

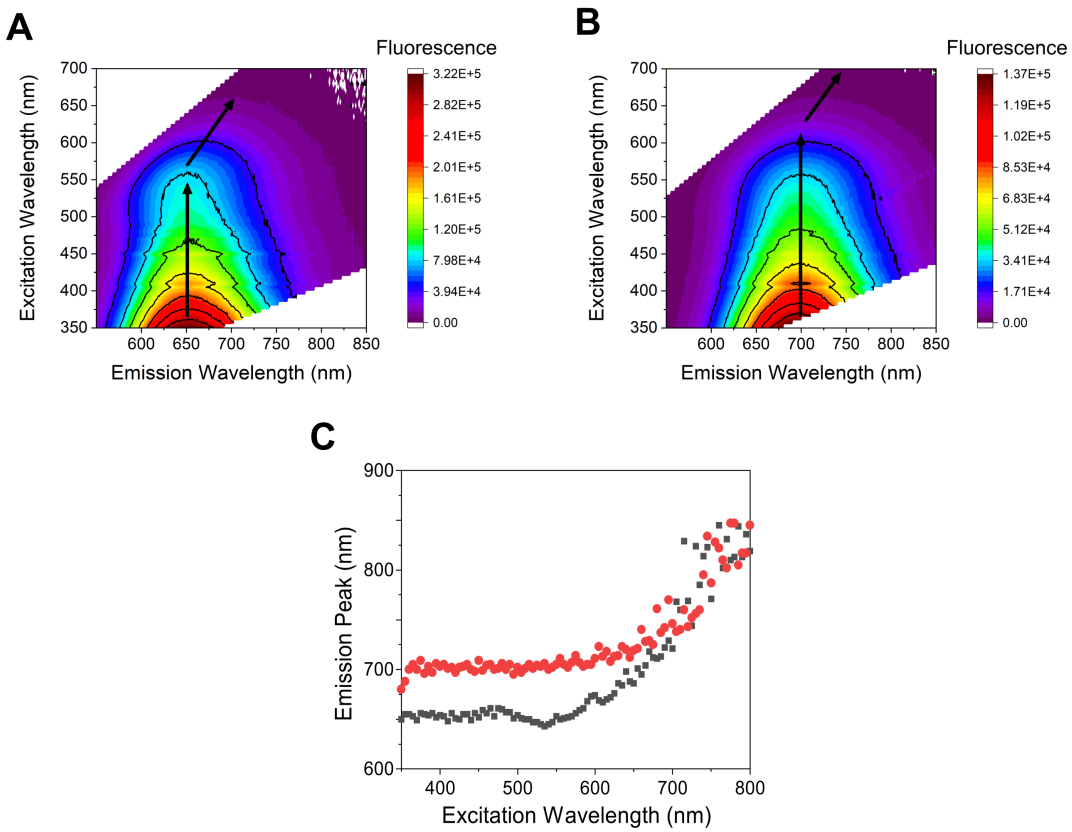

Figure 5.19: Fluorescence excitation vs. emission plots comparing colloidal $CuInS_2/ZnS$ QDs and $CuInS_2/ZnS$ QD nanoclusters. Contour plot showing fluorescence intensity as a function of fluorescence excitation wavelength and fluorescence emission wavelength for (A) colloidal $CuInS_2/ZnS$ QDs in chloroform and (B) $CuInS_2/ZnS$ QD nanoclusters in 50 nm HEPES, 100 mM NaCl (pH 7.5). (C) A plot of fluorescence emission peak against fluorescence excitation peak for colloidal $CuInS_2/ZnS$ QDs in chloroform (*black*) and $CuInS_2/ZnS$ QD nanoclusters in 50 mM HEPES, 100 mM NaCl (*red*.)

peak does not shift until the excitation wavelength approaches 700 nm, in contrast to the colloidal QDs (*black*) where a shift in the emission to lower-energy QDs is observed as the excitation wavelength approaches 600 nm. Overall, the results of these excitation vs. emission maps show that there is no excitation dependence of the QDs emission (until approaching the emission peak), whether the QDs are arranged into clusters or not, which suggests that wherever the energy enters the system that similar pathways of downhill energy transfer occur and then fluorescence occurs from the same point. The difference for the nanoclusters is that the greater degree of connectivity allows QD-to-QD transfers and leads, on average, to emission from smaller band gap QDs.

TRES measurements could provide an insight into how the excited state kinetics of the QD nanoclusters differ from those of colloidal QDs, with time-resolved measurements collected at various emission wavelengths for colloidal $CuInS_2$/ZnS QDs in chloroform and $CuInS_2$/ZnS QD nanoclusters. Figure 5.20 A shows a 3-D TRES scan taken on the colloidal QDs, with time-resolved measurements collected at 10 nm intervals and measurements halted after reaching a pre-determined collection time. A slow decay was observed along with a subtle red-shift at longer time points for dispersed QDs. Figure 5.20 B shows a 3-D TRES scan for clustered QDs, with a much steeper decay observed at all collection wavelengths. To obtain the cross-section, the TRES slices were extracted using the FLS980 software. The small red-shift can be seen much clearer in the cross-sectional data for colloidal QDs (Figure 5.20 C), with the initial peak at 0 ns occurring at ∼630 nm which tends towards a peak at ∼655 nm as the time increases. The red-shift is significantly larger for QD nanoclusters (Figure 5.20 D), with the initial peak at $T = 0$ again occurring at 635 nm, then shifting to ∼700 nm with increasing time. This is strong evidence that FRET is occurring between QDs within nanoclusters: at time zero the photon emission was similar to dispersed QDs but, after increasing timepoints as transfer of excitation has occurred, the photon emission is more likely to occur from the lower energy QDs. This is indicative of downhill FRET within the QD clusters as energy is transferred to larger QDs within each individual cluster.

The fluorescence intensity has also decreased rapidly with time in the cross-sectional data for QD nanoclusters in comparison to colloidal QDs, which may suggest a non-radiative dissipation of the energy. This may occur during FRET, as energy is likely to be lost during phonon scattering following energy transfer, but may also be the result of energy transfer to non-luminescent QDs within the cluster due to the phenomenon of 'blinking' [227–229, 231], described as random fluctuations in fluorescence. If energy is transferred via FRET to QDs in the 'off' state, where a charge has built up on the surface, then the fluorescence of these QDs may be quenched, leading to a significant

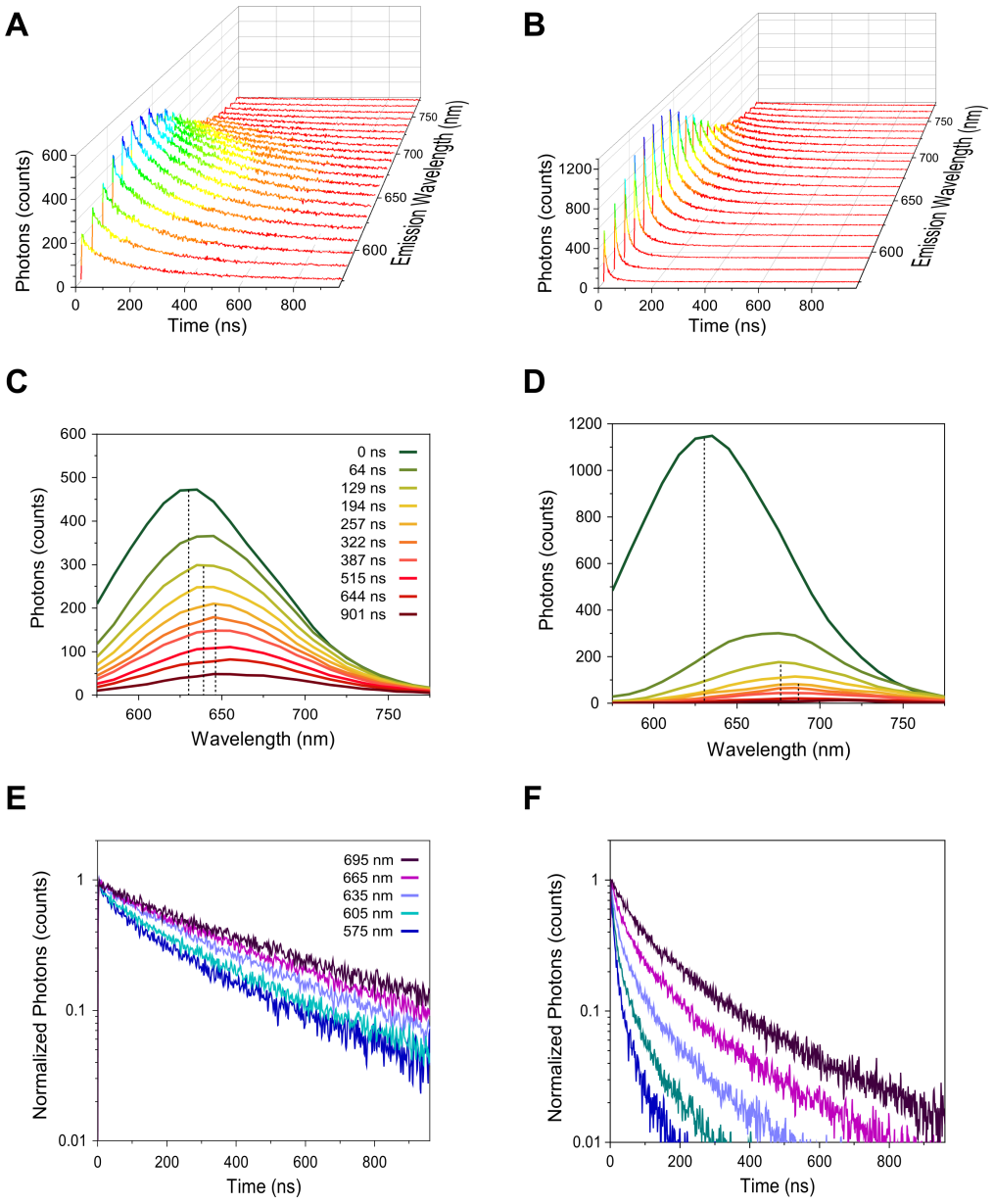

Figure 5.20: Time-resolved emission spectroscopy comparison of colloidal $CuInS_2/ZnS$ QDs and $CuInS_2/ZnS$ QD nanoclusters. Time-resolved emission spectroscopy (TRES) measurements of (A) colloidal $CuInS_2/ZnS$ QDs in chloroform and (B) $CuInS_2/ZnS$ QD nanoclusters in 50 mM HEPES, 100 mM NaCl (pH 7.5). Cross-sectional TRES slices taken at 15 decay times for (C) colloidal $CuInS_2/ZnS$ QDs in chloroform and (D) $CuInS_2/ZnS$ QD nanoclusters in 50 mM HEPES, 100 mM NaCl (pH 7.5). *Black dashed* lines represent a guide to the emission peak wavelength at 0 nm, 129 ns, and 257 ns. The TRES slices were extracted using the FLS980 fluorescence spectrometer software. Time-resolved TRES slices taken at multiple wavelengths for (E) colloidal $CuInS_2/ZnS$ QDs in chloroform and (F) $CuInS_2/ZnS$ QD nanoclusters in 50 mM HEPES, 100 mM NaCl (pH 7.5). For each cross-sectional TRES measurement, 15 slices of data were taken (starting from the maximum signal at ~35ns), with the number of bins between each slice kept consistent. Data were corrected to start at $t = 0$.

drop in fluorescence emission and a reduction in the fluorescence lifetime of the sample. Figure 5.20 E/F support this theory, as the fluorescence decay for each collection window is much shallower for the colloidal QDs (Figure 5.20 E) than for the QD nanoclusters (Figure 5.20 F), which is suggestive of significant fluorescence quenching. The time-resolved measurements show the decay in QD nanoclusters is significantly more rapid at a lower collection wavelength, as expected if FRET occurs frequently with high-energy donor QDs. The decay of the QD nanoclusters becomes shallower at a longer collection wavelength, as the energy is transferred to lower-energy QDs, and the fluorescence decay is expected to be similar to colloidal QDs at collection wavelengths above 695 nm.

The data presented in this section is in agreement with early investigations into the energy transfer pathways within layers of close-packed assemblies of QDs by Crooker *et al.*, with a faster decay observed in blue QDs due to FRET and a lifetime of larger QDs that is similar to that of colloidal QDs, evident of downhill energy transfer from 'blue' to 'red' QDs. QD-to-QD FRET within this nanocluster system is believed to occur in an identical manner to FRET between proteins and close-packed nanoparticles within similar structures, where energy is transferred to neighbouring QDs that lie within the Förster radius if they satisfy the criteria for FRET. Unlike energy transfer in proteins, FRET to non-luminescent QDs can lead to energy loss through non-radiative decay, thus prevention of blinking is important in maintaining energy transfer efficiency and avoiding dissipation of energy as energy is transferred through the nanocluster. A smaller red-shift of 35 meV was obtained by Crooker *et al.* when comparing the emission peak of colloidal QDs to clustered QDs, compared to a red-shift of 122 meV for the $CuInS_2$/ZnS QD nanocluster emission peak when compared to colloidal QDs dispersed in chloroform. This significantly larger red-shift is likely to arise from either the different structure of the assembly (QD nanoclusters vs. close-packed assemblies of QDs), or from the increased size dispersion (13% vs 7%) which would lead to a significantly larger energy difference between the smallest and largest QDs within each structure.

5.6 Investigating Surface-Deposited $CuInS_2/ZnS$ Quantum Dot Nanoclusters at the Single-Particle Level

Ensemble absorption and fluorescence spectroscopy allow the composition and photophysics of the QD nanoclusters to be assessed in bulk but do not provide information on individual particles. The fluorescence of QD clusters, resulting from FRET between high-energy to low-energy QDs, must be maintained when deposited onto a solid surface in order to have future applications in light-harvesting devices. To expand on epifluorescence microscopy measurements, fluorescence lifetime imaging microscopy (FLIM) was utilised to assess the functionality of individual QD nanoclusters and also quantify the co-localisation of lipids and QDs while deposited onto glass surfaces. FLIM allows the fluorescence intensity and lifetime of samples to be measured simultaneously. Thus, FLIM can be used to determine the lifetime of individual clusters as well as investigate whether a change in lifetime is observed in the presence of a fluorescent dye-tagged lipid. As with epifluorescence microscopy, FLIM data can only provide an indication of QD nanocluster size due to the optical diffraction limit of ∼300 nm, hence TEM was used to obtain accurate size characterisation.

Similarly to the co-localisation experiment discussed in Chapter 5.3.2, dye-tagged NBD-DHPE lipid was chosen to map the location of lipid with respect to the QD clusters and also to determine any changes in fluorescence decay due to FRET between the dye (donor) and QDs (acceptor). Figure 5.21 shows a selection of individual QD nanoclusters self-assembled with fluorescent NBD-DHPE following a ×250 dilution in which samples were deposited onto a glass substrate for imaging. Samples were imaged in a 5×5 µm area, with the signal from the QD channel shown in Figure 5.21 A/D and signal from the NBD channel shown in Figure 5.21 B/E. In the contrast-enhanced images shown in Figure 5.21 C/F, the fluorescence due to the QDs is shown in red, NBD-DHPE in green and spatial overlap in yellow for composite images. The contrast was enhanced for

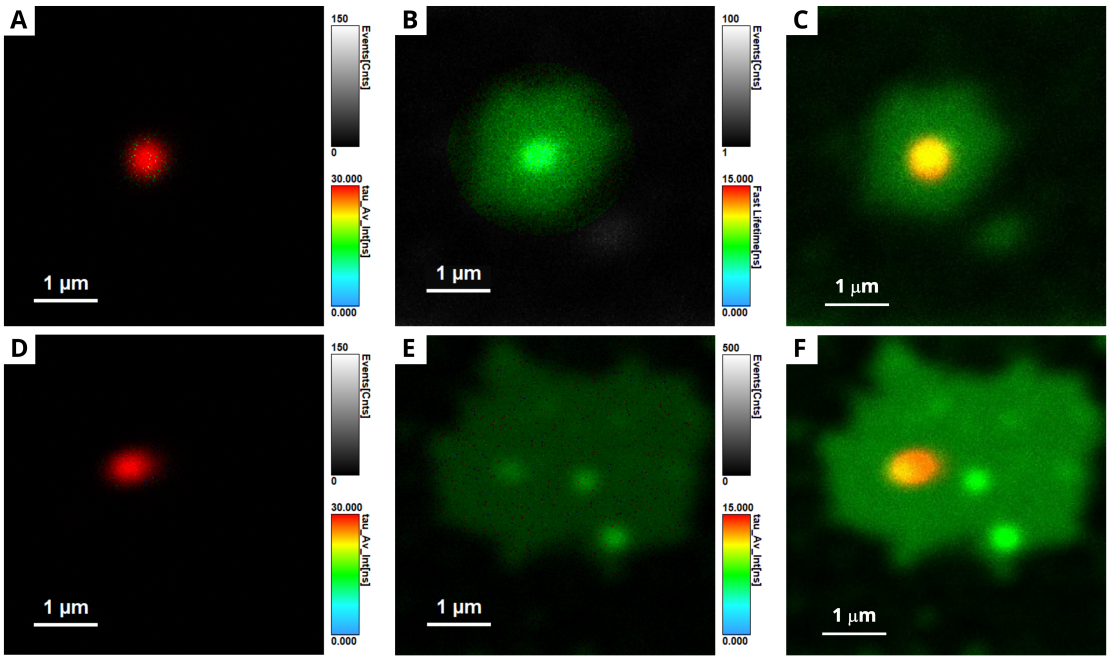

Figure 5.21: Dual-channel images from FLIM showing individual QD nanoclusters deposited on a glass substrate at a low concentration. (A/D) show the intensity and lifetime of 33:66:1 DOPG:DOPC:NBD-DHPE-coated QD nanoclusters from the QD channel. (B/E) show the intensity and lifetime of 33:66:1 DOPG:DOPC:NBD-DHPE-coated QD nanoclusters from the NBD channel. (C/F) show contrast-enhanced composite images of 33:66:1 DOPG:DOPC:NBD-DHPE-coated QD nanoclusters with the QD fluorescence shown in *red* and the NBD-DHPE fluorescence shown in *green*. Areas of strong spatial overlap are shown in *yellow*. Samples were self-assembled as described in Methods section 2.2.6 and drop-cast onto PLL-coated piranha-cleaned glass slides as described in Section 2.8.

clarity. The QDs and lipids are co-localised and support the epifluorescence measurements shown in Section 5.3.2, with the lipids encapsulating and stabilising the QDs on the surface of the glass substrate. Empty lipid vesicles and structures can also be seen in FLIM images such as Figure 5.21 H/I, as a high lipid:QD molar ratio was used to fully encapsulate the QDs, as discussed in Chapter 3.4. This suggests the excess lipid leads to the formation of large lipid structures with no co-localised QDs, which could be removed by centrifugation before surface deposition if needed.

Once the co-localisation of the lipids and QDs was confirmed, the excited-state characteristics of individual QD nanoclusters could be investigated. To assess FRET using FLIM, the average fluorescence lifetime of individual QD nanoclusters was initially de-

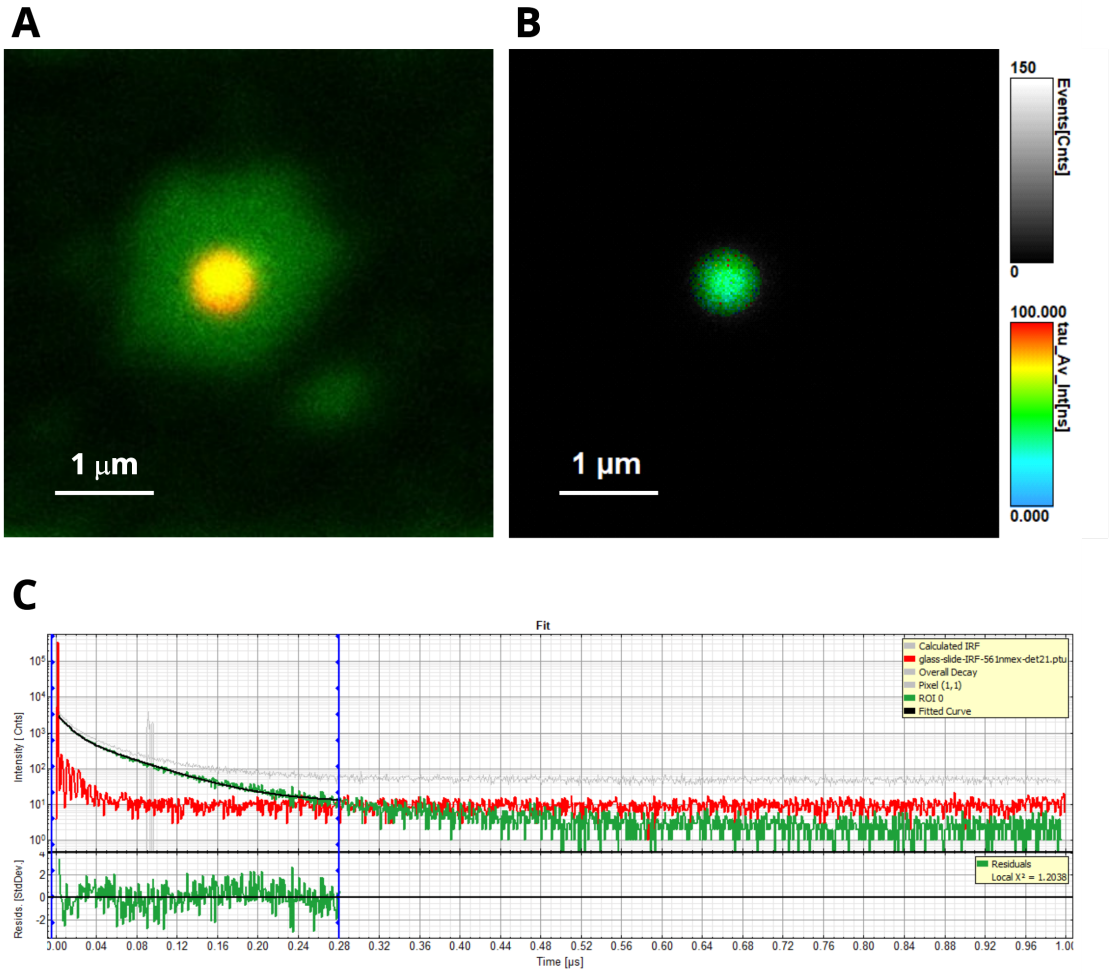

Figure 5.22: Example of lifetime determination from captured FLIM images. (A) Original composite image of a 33:66:1 DOPG:DOPC:NBD-DHPE-coated QD nanocluster with the QD fluorescence shown in *red*, the NBD-DHPE fluorescence shown in *green*, and spatial overlap between the NBD-DHPE and QDs shown in *yellow*. (B) FLIM image showing the intensity and lifetime of 33:66:1 DOPG:DOPC:NBD-DHPE-coated QD nanoclusters in a selected region of interest from the QD channel (A). (C) The resulting lifetime trace and fit taken within SymPhoTime software.

termined using both intensity-weighted and amplitude-weighted analysis. However, the amplitude-weighted mean lifetime, which reflects the quenching of the energy donor due to FRET, was chosen over the intensity-weighted average lifetime, which corresponds to the real average arrival time of the photons, to allow the FRET efficiency to be

calculated. The amplitude-weighted lifetime is calculated using the equation:

$$\tau_A = \sum_{i=1}^{p} q_i \tau_i / \sum_{i=1}^{p} q_i = \sum_{i=1}^{p} q_i \tau_i, \tag{5.4}$$

where q_i and τ_i $(i = 1, \ldots, p)$ represent the amplitude fractions and lifetimes, respectively [232, 233]. The amplitude-weighted lifetime calculations were performed with SymPhoTime software (Picoquant) by generating fluorescence decay curves from accumulated photons within a field of interest and then modelling the curve as a multi-exponential decay function. An example of this process is shown in Figure 5.22, where panel A shows the original 5×5 µm composite image. Panel B shows the NBD channel ROI, which was manually selected from the composite image to specifically identify the NBD signal that spatially overlaps with the signal obtained from the QDs, and panel C shows the lifetime histogram from the pixels in the ROI calculated in the SymPhoTime software.

For individual QD nanoclusters, the amplitude-weighted lifetime was calculated by thresholding, selecting a region of interest (ROI) and then analysing the decay cures. A threshold was applied to images to remove particles with a fluorescence that was too low to perform further analysis, with the remaining particles defined as individual ROIs to allow their amplitude-weighted lifetimes to be calculated individually. The threshold removed pixels that were below 10 counts, and then single particles were selected with care taken to omit overlapping nanoclusters. ROIs were manually drawn on the single particles using the paint ROI function in the SymPhoTime software, before fitting TCSPC data from each ROI using a bi-exponential re-convolution fit using a measured IRF. The IRF was taken on a glass slide with the same excitation lasers and objective lens, and fits with a value of χ^2 under 1.5 were excluded from statistics. The determination of the amplitude-weighted lifetime for NBD-DHPE samples was identical to that of the QD nanoclusters, although the initial thresholding was not required. Figure 5.23 shows example images of the particle selection, with the colour of the particle representing the amplitude-weighted lifetime with respect to the upper limit of the FLIM false-colour

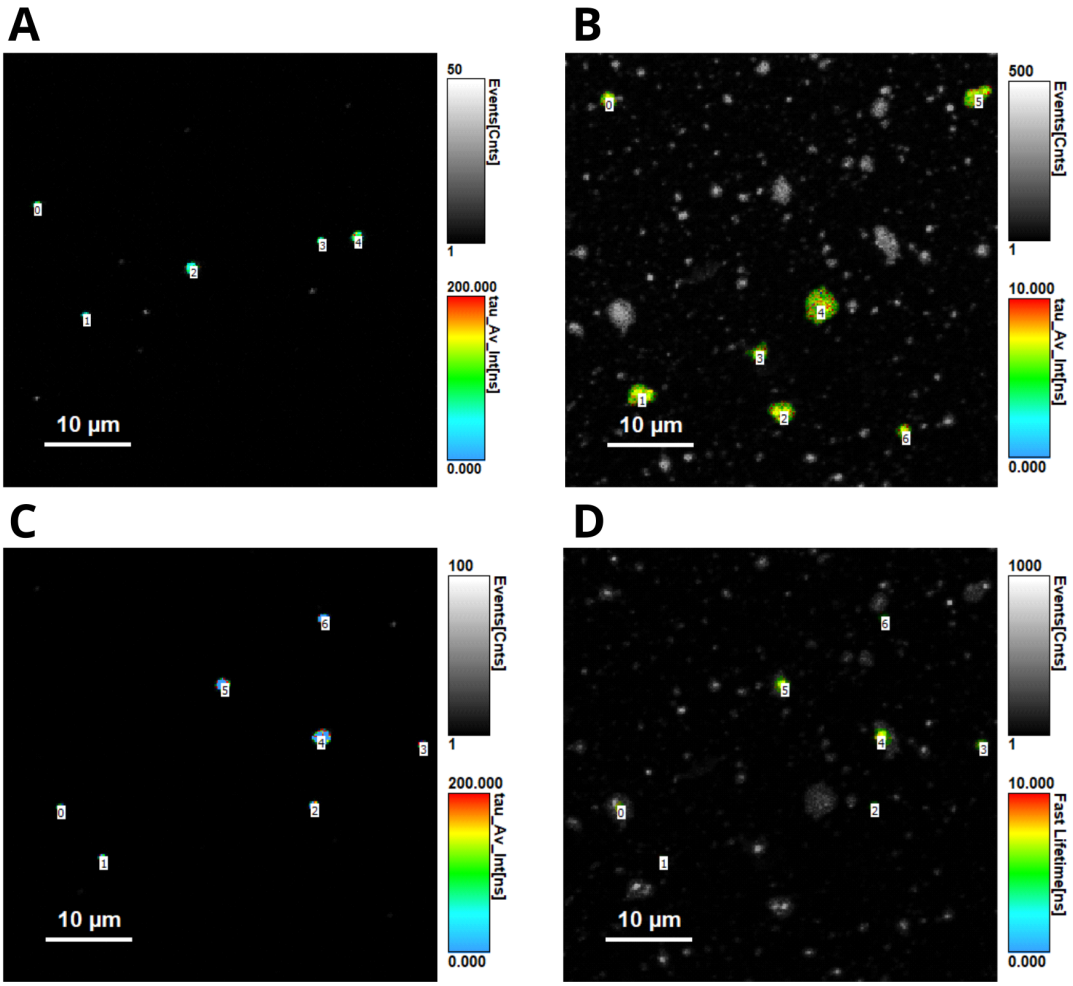

Figure 5.23: FLIM images showing both fluorescence intensity and lifetime data of selected regions of interest. (A) ROI selection to determine the lifetime of 2:1 DOPC:DOPG-encapsulated QD nanoclusters prepared at a lipid:QD molar ratio of 1500:1. (B) ROI selection to determine the lifetime of 33:66:1 DOPG:DOPC:NBD-DHPE lipid vesicles and structures. (C) ROI selection to determine the lifetime of QD nanoclusters when encapsulated by 33:66:1 DOPG:DOPC:NBD-DHPE lipid. (D) ROI selection to determine the lifetime of 33:66:1 DOPG:DOPC:NBD-DHPE lipid when encapsulating hydrophobic QDs. ROI selection is identical in (C) and (D) when determining the change in lifetime due to the presence of fluorescent lipids. All samples were deposited on a glass substrate.

scale (200 ns for A and C, 10 ns for B and D) and brightness representing fluorescence intensity. Three samples were prepared; a QD nanocluster-only sample (no NBD-DHPE present), an NBD-DHPE-only sample (no QDs present), and a mixed NBD-DHPE-QD nanocluster sample. The QD and NBD fluorescence was collected in two separate channels, with full collection parameters described in Methods section 2.8.2. Figure 5.23 A

shows the ROI selection for the QD-only sample, with five larger clusters selected with a sufficient number of counts to extract the sample lifetime. Figure 5.23 B shows the ROI selection for the NBD-DHPE-only sample which was used to determine the lifetime for control measurements. Figures 5.23 C and D show the ROI selection for the QD channel and NBD channel in the QD/NBD-lipid mixed sample, respectively. For the mixed sample, the ROI was initially chosen for the QD nanoclusters, with an identical ROI used to calculate the lifetime of the co-localised NBD in the corresponding area in order to determine if a reduction of the lifetime is observed due to energy transfer.

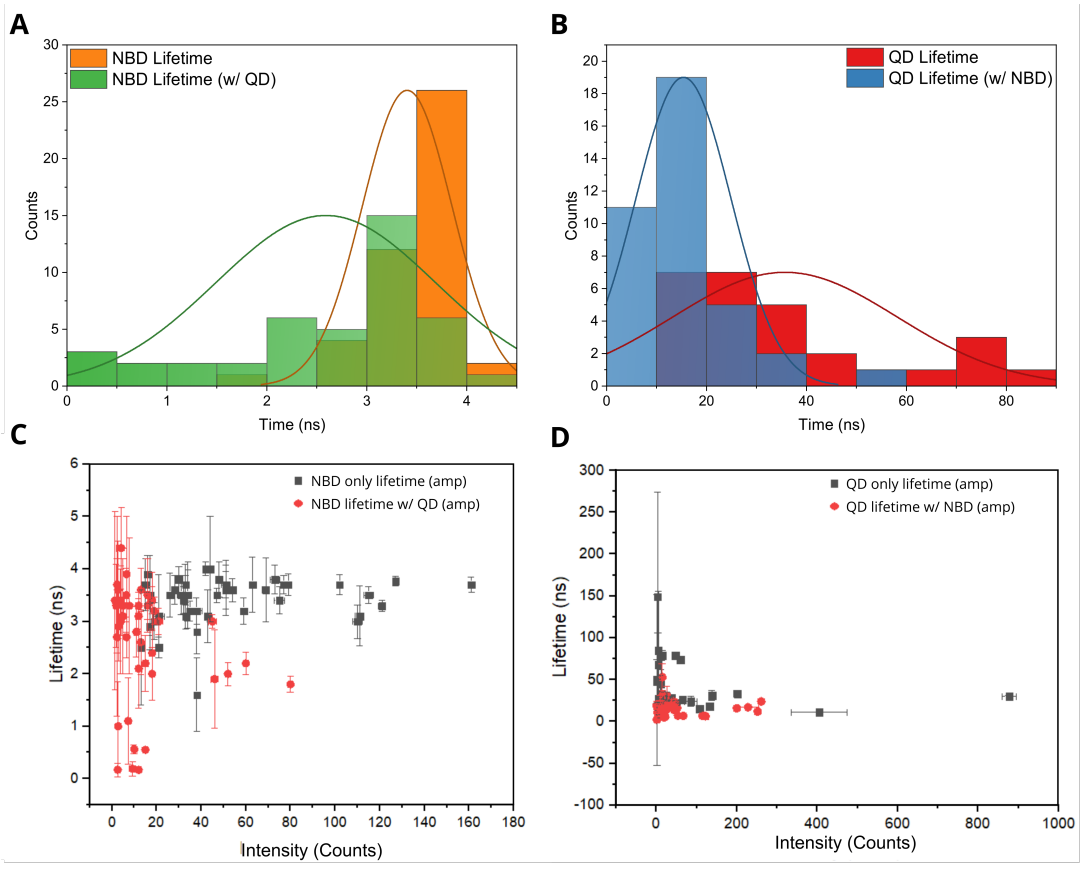

Figure 5.24: Frequency distribution of lifetimes obtained from FLIM. (A) Histogram showing lifetime distribution of NBD-DHPE control (*orange*) and NBD-DHPE lipid when co-localised with QDs (*green*). (B) Histogram showing lifetime distribution of QD nanocluster control (*red*) and QD nanoclusters when co-localised with NBD-DHPE lipid (*blue*). (C) Lifetime vs. intensity distribution for NBD-DHPE control (*black*) and NBD-DHPE lipid when co-localised with QDs (*red*). (D) Lifetime vs. intensity distribution for QD nanocluster control (*black*) and QD nanoclusters when co-localised with NBD-DHPE lipid (*red*).

The amplitude-weighted average lifetimes obtained from the ROIs were then collated into a histogram (Figure 5.24), with the NBD-DHPE lifetimes displayed in panel A and the QD lifetimes displayed in panel B. The frequency distribution of the NBD-DHPE lifetimes (Figure 5.24 A) indicates that NBD fluorescence is quenched by the $CuInS_2$/ZnS QDs, with the mean NBD fluorescence lifetime decreasing from 3.40 ± 0.45 ns (without QDs) to 2.58 ± 1.09 ns when encapsulating QD nanoclusters. This NBD fluorescence quenching that leads to a reduction in lifetime agrees with the steady-state measurements obtained in Section 5.3.1., and is unequivocal evidence of FRET from NBD to QDs, which proves that a significant amount of lipids are in close proximity to QDs for FRET to occur. The ETE can be estimated from the amplitude-weighted lifetime of the NBD using the following equation:

$$ETE = 1 - \frac{\tau_{DA}}{\tau_{f,D}} \tag{5.5}$$

where τ_{DA} and $F_{f,D}$ are the mean fluorescence lifetimes of NBD in the presence or absence of the QDs, respectively. An ETE of 24.1 ± 10.7% was obtained, which is lower than the ETE of 52.6% obtained from the steady-state measurements using NBD-DHPE in Section 5.3.1. This translates to a donor-to-acceptor distance of ∼5 nm, suggesting a significant amount of lipid/QD co-localisation, and therefore QD stability is retained when samples are deposited onto a surface. An unexpected reduction in the QD lifetime was also observed from the frequency distribution shown in Figure 5.24 B, as NBD should not be excited using the 561 nm laser used for time-resolved measurements of the QDs. The mean QD fluorescence lifetime decreased from 35.7 ± 22.5 ns (without NBD-DHPE) to 15.4 ± 9.5 ns (with NBD-DHPE present), although a large standard deviation was observed for the sample. No correlation was observed between the intensity of the signal and the lifetime of the NBD (Figure 5.24 C), although high-intensity ROIs contributed to a lower QD fluorescence lifetime for the QD-only sample and low-intensity signals generally contributed to a longer lifetime (Figure 5.24 D), suggesting a greater fluorescence quenching in brighter (potentially larger or multiple spatially-overlapping)

QD clusters. This would be explained by the larger nanoclusters containing more QDs, therefore FRET is likely to occur more frequently in transferring energy from high-energy QDs to low-energy QDs, resulting in a shorter average lifetime. This trend was not observed in the analysis of the QD fluorescence lifetime in samples containing NBD, with a random distribution observed, although no samples of a comparable high intensity were characterised. Paired (dependant) T-tests show a P value of 2.55×10^{-6} when comparing the QD lifetimes and 7.88×10^{-6} when comparing NBD-DHPE lifetimes, where a P value <0.05 suggests a significant statistical difference and is unlikely to have occurred by chance.

The retained functionality of the QD nanoclusters on a surface suggests potential applications as a photo-active light-harvesting material, with a thin film of QD nanoclusters potentially able to enhance the spectral range of solar-harvesting materials such as silicon solar cells that typically absorb well in the infrared region by transferring energy downhill from the visible spectral domain. The use of $CuInS_2$/ZnS QDs would provide a reasonable alternative to cadmium-containing devices where there is currently a drive to reduce the use of heavy metals in electronic devices, with commercial use in applications restricted by legislation worldwide. QD nanoclusters could also be a significant enhancement of colloidal QD solar cells if the self-assembly procedure is translatable to other favourable QDs [19, 234], where a large Stokes shift would typically be required for the energy absorbed by colloidal QDs to be emitted in the near-infrared (NIR) region. The lipid-based composition of the QD nanoclusters also lends well to thin-film deposition, where typical methods of controlling thin-film growth include spin-casting multi-layer deposition of QDs [235]. It may also be possible to incorporate light-harvesting proteins with QD nanoclusters on a surface at high lipid concentrations, with nanoarrays containing plant LHCII previously shown to retain their high photon absorption and fluorescence properties on surfaces [157], with such systems capable of long-range energy transfer [158]. Energy transfer efficiency has been retained in LHCII-containing bio-hybrid structures [120] when deposited onto a surface, which have the potential to

be combined with self-assembling QD nanoclusters at high concentrations to obtain a promising combination of existing light-harvesting nanomaterials. Finally, the attained brightness of the QD nanoclusters at the single-particle level may also lead to applications in bio-sensing, where the use of lipid-encapsulated nanoclusters may be beneficial in addressing some common limitations including a low emission due to the emission wavelength and limited QD brightness when detecting through biological tissue [16]. The lipid-encapsulation could reduce QD toxicity, while clustered QDs were previously demonstrated to have enhanced fluorescence emission signals [236], in agreement with the QD nanoclusters developed in this thesis which are brighter at the single-particle level than the corresponding colloidal QDs and have a longer-wavelength emission peak which would aid tissue penetration.

In summary, a reduction in the NBD-DHPE fluorescence lifetime when QD nanoclusters are formed is indicative of co-localisation of the lipid and QDs resulting in NBD-to-QD energy transfer, in agreement with the spatial overlap and fluorescence quenching observed in Section 5.3. A high-intensity signal (seemingly indicative of larger or multiple overlapping QD clusters) led to a significant lifetime reduction in the QD nanoclusters, whereas a lower signal intensity (seemingly indicative of smaller nanoclusters) resulted in a longer QD lifetime and a lower sample quenching, likely due to a reduction in FRET in clusters with fewer QDs.

5.7 Future Work: The Effect of QD Size on Nanocluster Formation

Within each quantum dot nanocluster, energy is transferred from the higher energy quantum dots to the lower energy quantum dots via FRET if the surrounding QDs lie within the Förster radius. By increasing the quantum dot size during QD nanocluster self-assembly and using QDs with a lower-energy fluorescence emission, the photophysics and structure are likely to change. Investigating the size of the QD nanocluster red-shift

when using varied sizes of QD would provide an indication of these changes and may indicate potential areas for further investigation.

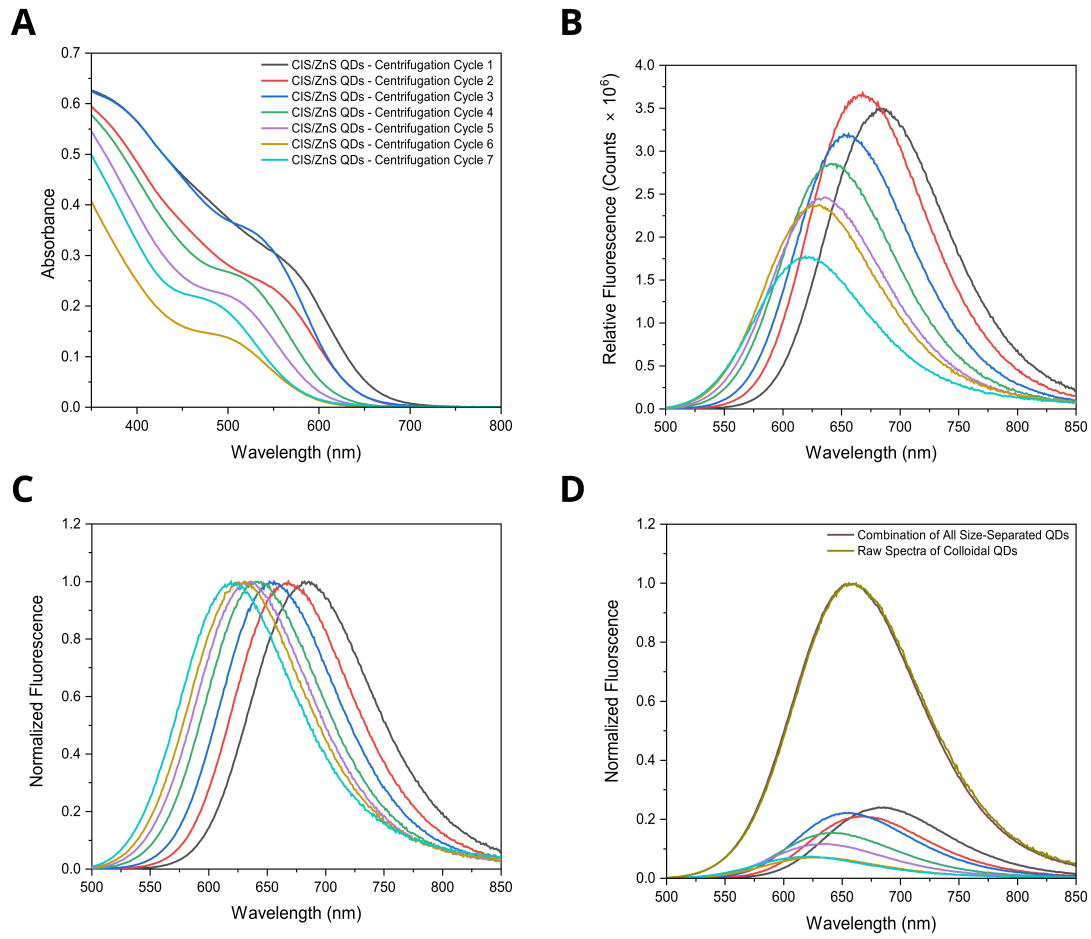

Figure 5.25: Spectra of $CuInS_2$/ZnS QDs following size separation. (A) Raw absorbance spectra of size-separated $CuInS_2$/ZnS QDs dispersed in chloroform. (B) Relative fluorescence emission (fluorescence emission divided by absorbance at 400 nm) of size-separated $CuInS_2$/ZnS QDs. (C) Normalised fluorescence emission of size-separated $CuInS_2$/ZnS QDs showing blue-shift in emission peak as QD size is reduced. (D) Normalised fluorescence emission of $CuInS_2$/ZnS QDs showing fluorescence emission overlap of combined size-separated QDs (*gold*) with QD stock solution (*maroon*).

To separate the $CuInS_2$/ZnS QDs by size, an increasing volume of ethanol was incrementally added to the dispersed QDs in chloroform to gradually increase polarity, starting at an equal ratio of chloroform to ethanol. The quantum dots were spun down in a microcentrifuge, with the pelleted quantum dots removed after each cycle before adding

a set amount of methanol and re-centrifuging. The larger quantum dots are expected to pellet first at a lower polarity, then the remaining quantum dots pellet as polarity is incrementally increased. Figure 5.25 A/B shows the resulting size separation represented by the quantum dot fluorescence emission following eight cycles of centrifugation, with the fluorescence normalised at the emission peak. A blue-shift from 680 nm to 620 nm can be seen between the first and last centrifugation cycles (Figure 5.25 C), showing full control over the quantum dot size. To confirm the stock of quantum dots was separated into distinct size populations, the fluorescence emission spectra of the eight different cycles were convoluted and compared to the raw fluorescence emission spectra of the $CuInS_2$/ZnS stock before the size separation (Figure 5.25 D). A direct overlap between the sum of the separated sample fluorescence with the stock fluorescence shows that the QDs were successfully separated into distinct sizes using ethanol with no loss of sample, and allows the nanoclusters to be self-assembled using quantum dots of different sizes.

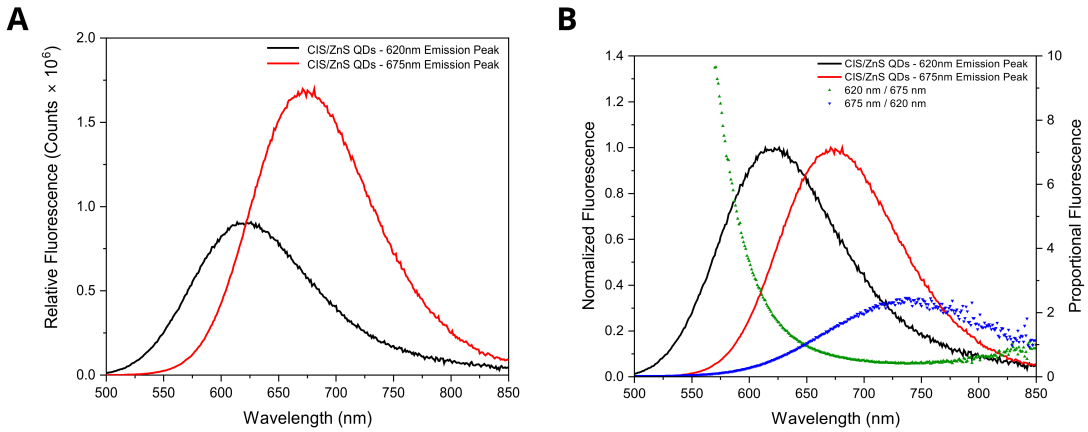

Figure 5.26: Fluorescence emission of size-separated $CuInS_2$/ZnS QDs. (A) Relative fluorescence emission spectra (fluorescence emission divided by absorbance at 400 nm) of size-separated $CuInS_2$/ZnS QDs with 620 nm and 675 nm fluorescence emission peaks. (B) A plot showing how the 620/675 nm fluorescence emission peak ratio (*green*) and 675/620 nm fluorescence emission peak ratio (*blue*) was used to determine emission collection parameters for time-resolved measurements.

To investigate the effect of QD size on the nanocluster photophysics, three distinct populations of QDs were chosen for nanocluster self-assembly. The molar concentration of

QDs used was kept consistent, with a 1500:1 lipid:QD molar ratio used. Two samples were prepared using the size-separated QDs with fluorescence emission peaks of 620 nm and 675 nm respectively (Figure 5.26 A), and a third sample was prepared by combining the 620 nm and 675 nm QD populations at a 1:1 ratio. Due to the wide size dispersion of the QD synthesis, there is significant overlap between the QDs with a 620 nm emission peak and a 675 nm emission peak, although there should be a significant difference in the mean QD size from theoretical calculations using the empirical formula [102]. The 'small' 620 nm QDs are expected to have a mean diameter of 2.52 nm, with the 'large' 675 nm QDs expected to have a mean diameter of 3.00 nm, with a significant size difference obtained between the two populations. The ratio of small to large QDs (and vice versa) at equal molar concentrations (relative to the emission peak) is shown by the *green* plots in Figure 5.26 B (*blue* plots for the ratio of large:small), along with the normalised fluorescence emission for the small (*black* line) and large (*red* line) QDs.

The absorbance of the three populations of quantum dots can be seen in Figure 5.27 A, both in chloroform (*solid* line) and after association with lipid (*dashed* line). The absorbance increases as the average QD size increases due to an increase in the molar absorption coefficient with an increasing fluorescence emission peak wavelength. A low amount of scattering is observed for the QD nanoclusters self-assembled using the small 620 nm QDs (*red dashed* line), with a larger amount of scattering observed for the mixed-population QDs (*black dashed* line) and the highest amount of scattering observed when using the largest 675 nm QDs (*blue dashed* line). This may be indicative of an increase in QD nanocluster size with increasing QD size or may be due to an increase in the quantity of large, free-lipid structures, and could be quantified through TEM analysis. A 32 nm red-shift in the emission peak was observed when nanoclusters were self-assembled using the 620 nm stock of QDs (Figure 5.27 B/C, *red solid* line), with QD nanocluster fluorescence emission peak of 652 nm (*red dashed* line). This is significantly smaller than the 46 nm red-shift when forming QD nanoclusters using the 675 nm QD stock (*blue solid* line), which has a nanocluster fluorescence emission peak of 721 nm (*blue dashed* line).

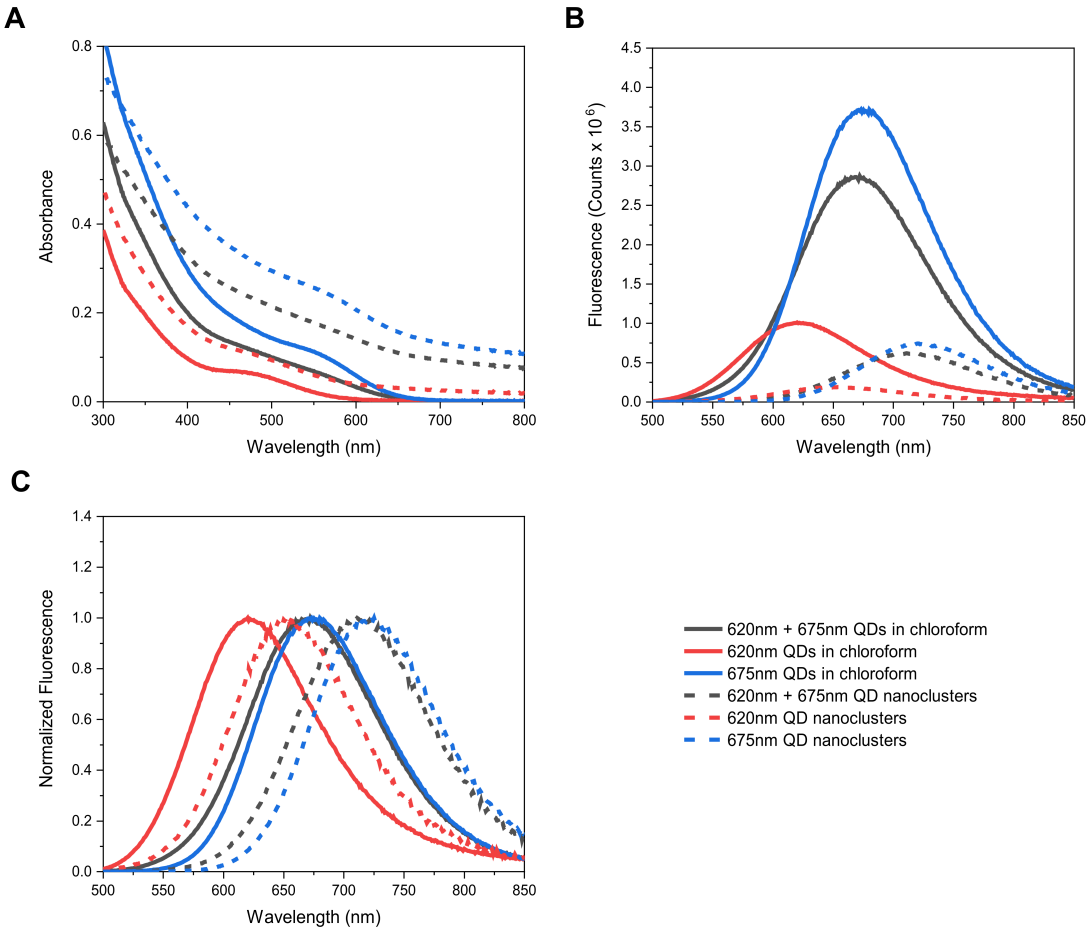

Figure 5.27: Spectra of QD nanoclusters assembled using QDs of different sizes. (A) Absorption, (B) fluorescence emission, and (C) normalised fluorescence emission of colloidal QDs in chloroform (*solid* line) QD nanoclusters (*dashed* line) assembled using $CuInS_2$/ZnS QDs with an emission peak of 620 nm (*red*), 675 nm (*blue*) and a combination of 620 nm and 675 nm QDs at a molar ratio of 1:1 (*black*).

The red-shift of 45 nm was seen in the sample where nanoclusters were formed using a combination of the 620 nm and 675 nm stocks, where the colloidal emission peak was 667 nm (*black solid* line) and the QD nanocluster emission peak was 712 nm (*black dashed* line). The mixed 620/675 nm colloidal QDs had the largest FWHM, which suggests that the size of the fluorescence emission red-shift is more dependent on the size of the QDs than the FWHM of the QDs and the energy difference between the smallest and largest QDs within the population.

One issue is the broad fluorescence emission peak of the colloidal $CuInS_2$/ZnS QDs, therefore there remains a significant overlap in QD sizes when the mean QD size is altered by ∼0.5 nm. If a fresh stock were to be used for size-separation measurements as opposed to the depleted stock, then a more-rigorous size-separation could take place allowing obtention of QDs with a significant size difference without sacrificing the QD concentration. This would allow further investigations into the effect of QD size without a significant size overlap, and could also allow the investigation of energy transfer between two distinct populations of QDs with high-energy QDs acting as the energy donors and low-energy QDs acting as the energy acceptors. Finally, TEM would be able to quantify any change in QD nanocluster size or structure from altering the QD size, and further quantification using time-resolved spectroscopy would accompany the steady-state spectroscopy and TEM measurements to provide information on how the size of the QDs and size of the structure is linked to the fluorescence decay of the QD nanoclusters.

5.8 Conclusion

The goal of the research in this chapter was to further understand the QD nanoclusters developed in Chapter 3 by investigating the structure and photophysics using a combination of characterisation techniques. TEM was used to determine the size distribution of colloidal $CuInS_2$/ZnS QDs, with an average QD diameter of 3.3 ± 0.6 nm calculated from semi-automated analysis using STEM and a QD size dispersion of 18%. Manual analysis using TEM was then completed on a smaller population of QDs to quantify the size, with undefined particle boundaries due to low particle density at the tetrahedral edge leading to a slightly smaller mean diameter of 2.9 ± 0.4 nm. The QD nanocluster size and structure were then confirmed via manual analysis of TEM images, with a minor axis mean diameter of 33 ± 8 nm and a major axis mean diameter of 43 ± 10 nm, with most nanoclusters displaying an elliptical structure. The size was in agreement with the predicted structure from self-assembly following small-scale QD aggregation.

To quantify that the lipid stabilised the QD nanoclusters, optical spectroscopy and epifluorescence microscopy experiments were conducted to quantify the co-localisation of the lipid and QDs. Fluorescent dye-tagged lipids (NBD/BODIPY-DHPE) were used to monitor the position of the lipid within the self-assembled structure, with FRET confirmed to take place between the fluorescent dye energy donor and the QD energy acceptor within the structure through steady-state and time-resolved spectroscopy measurements, supporting co-localisation. Spatial overlap between the NBD/BODIPY-DHPE lipid and the $CuInS_2$/ZnS QDs was also observed via epifluorescence microscopy, again supporting the lipid and QD co-localisation and confirming that the lipid is used to stabilise the hydrophobic QDs within the aqueous environment. Once the role of the lipid within the QD nanoclusters was confirmed, optical spectroscopy was used to investigate how the lipid:QD molar concentration affects the uptake and fluorescence quenching of the hydrophobic QDs. A linear increase in QD uptake was observed with increasing lipid concentration until the QD absorbance and fluorescence began to plateau as the limit of QD uptake was approached.

A combination of steady-state and time-resolved spectroscopy was then utilised to investigate the photophysics of the QD nanoclusters, with the origin of the red-shift corresponding to energy transfer from high-energy to low-energy QDs within individual nanoclusters. TRES measurements supported this theory, with a prominent red-shift of the emission maxima observed in cross-sectional measurements, even at very low time points (sub-1 ns), indicative of energy transfer. This initial quenching led to a reduction in the lifetime at low wavelengths, indicative of energy donor quenching, with an increase in lifetime observed at the longer wavelengths where QDs are energy acceptors. Finally, FLIM was used to investigate the QD nanocluster fluorescence at the single-particle level, with co-localisation of the lipid and QDs further quantified after a spatial overlap was observed within individual clusters. The mean QD fluorescence lifetime decreased from 35.7 ± 22.5 ns (without NBD-DHPE) to 15.4 ± 9.5 ns (with NBD-DHPE present),

although a large standard deviation was observed for the sample. No significant correlation was observed between the particle intensity and the lifetime of the NBD-DHPE lipid, although high-intensity particles appeared to contribute to a lower QD fluorescence lifetime within QD nanoclusters and low-intensity signals generally contributed to a longer lifetime, suggesting a greater fluorescence quenching in brighter (potentially larger or multiple spatially-overlapping) QD clusters.

Chapter 6

Conclusion and Future Outlook

6.1 Conclusion

The three results chapters have detailed the development and characterisation of novel light-harvesting nanomaterials using combinations of quantum dots, lipids and light-harvesting proteins.

Chapter 3 focused on the method development for controllably assembling hydrophobic $CuInS_2$/ZnS QDs into distinct 'nanocluster' structures, optimising the procedure to ensure maximum QD uptake and desired optical characteristics. The structure and photophysics of $CuInS_2$/ZnS QDs within small nanocluster assemblies have not yet been characterised and little is known about the excitation dynamics and energy transfer mechanisms of small QD nanoclusters. Firstly, the $CuInS_2$/ZnS QD synthesis protocol was optimised to obtain bright QDs with a red emission and a C-8 (octanethiol) surface chemistry, with the ligand shortened from the standard C-12 (dodecanethiol) surface chemistry to decrease the QD-QD and QD-lipid distance in an attempt to increase FRET efficiency. The initially linear relationship between the $CuInS_2$ QD fluorescence emission peak and first excitonic absorption peak was then investigated to confirm the trend and allow the established relationship to be used when targeting particular optical properties

from future QD syntheses. A ZnS shell was grown on the $CuInS_2$ QDs which passivated surface trap states and produced a ∼40-fold increase in QD emission intensity, which could suggest a reduction in the likelihood of QD blinking. The cleaning method for $CuInS_2$/ZnS QDs was then adapted for the octanethiol-coated QDs, with a slight increase in polarity observed compared to dodecanethiol-coated $CuInS_2$/ZnS QDs, where the addition of methanol to the cleaning solution allowed for a consistent QD pellet following centrifugation.

Once the QD synthesis had been optimised, controlled QD nanocluster formation was trialled using a variety of techniques. The first trialled method involved the hydration of a dried lipid/QD film using an aqueous buffer, where probe sonication was utilised to provide the energy needed to break down multilamellar vesicle (MLV) aggregates into unilamellar structures. This led to visibly large QD aggregates that precipitated out of the solution, and the method was deemed unsuitable for controlled nanocluster formation. The second trialled method where a cosolvent scaffold was used to form stable clusters of lipid and QDs prior to solvent removal via rotary evaporation appeared to be a promising method for achieving QD nanoclusters. However, time restrictions did not allow further pursuit of this method beyond preliminary control measurements. The third trialled method used detergent to stabilise QDs and lipids when hydrating a lipid/QD thin film in an aqueous buffer and proved the most fruitful. After trialling multiple detergents, QD nanoclusters were successfully self-assembled through the use of sodium cholate to allow temporary stabilisation during lipid co-assembly in an aqueous buffer, before the detergent was removed to allow the assembly of lipid-stabilised QD clusters. QD nanoclusters displayed a ∼40 nm red-shift compared to colloidal QDs dispersed in chloroform, indicative of QD clustering. The red-shift occurred immediately following the rehydration of the thin film with detergent and remained when the detergent was removed from the buffer using polystyrene Biobeads. Optimisation of the self-assembly procedure was achieved by modification of the lipid choice, with the introduction of a negatively-charged DOPG lipid increasing QD uptake possibly due

to a change in the effective lipid shape from cylindrical to truncated. A 2:1 ratio of zwitterionic DOPC to DOPG achieved the greatest QD uptake, with the electrostatic repulsion of the negatively-charged DOPG head group contributing to an increase in stability as the lipid-encapsulated QD nanoclusters remaining dispersed in the aqueous buffer. Overall, by the end of this chapter, the optimal method of QD synthesis and assembly into nanoscale clusters was established.

Chapter 4 investigated the potential opportunity for interfacing QDs with biological light-harvesting systems (proteins) in an attempt to absorb photons of energy from regions of poor absorption and then transfer the energy to the light-harvesting protein, filling the 'green gap' in the LHCII absorbance spectra [153]. This was initially attempted by incorporating LHCII into the lipid-stabilised $CuInS_2$/ZnS QD nanoclusters, but no FRET was observed and the developed system was impractical as a light-harvesting material. In an attempt to achieve FRET from QDs to LHCII within a stable environment, hydrophilic CdTe/CdS QDs were chosen as an energy donor where NHS/EDC crosslinking could be utilised to covalently bind the QDs to the LHCII as an alternative to genetic modification of the protein. CdTe/CdS QDs were synthesised with a fluorescence emission peak of 626 nm and a first excitonic absorption peak at 556 nm, sufficiently filling the green gap of LHCII while providing enough overlap of the fluorescence with the absorbance of LHCII to achieve FRET. The established crosslinking procedure was modified to include the addition of a concentrated second buffer at higher pH to the original buffer to circumvent the use of desalting columns. Desalting columns were found to reduce the sample concentration after use and also quenched the fluorescence of the QDs. Optimisation of the crosslinking procedure suggested that increasing the concentration of the QDs and EDC/sulfo-NHS crosslinker or decreasing the volume of the reaction, led to more efficient binding of the crosslinker to the QDs at pH 6.0. There was some evidence of successful crosslinking and FRET from the QDs to LHCII, as suggested by a small increase in the LHCII fluorescence intensity accompanied by quenching of the QD fluorescence. However, further work would be needed to quantify

this and optimise the system.

Chapter 5 aimed to further understand the self-assembled QD nanoclusters developed in Chapter 3 by investigating their structure, photophysics, and surface functionality using a combination of characterisation techniques. QD nanoclusters could provide a significant enhancement of colloidal QD solar cells if the self-assembly procedure is translatable to other favourable QDs [19, 234], where a large Stokes shift would typically be required for the energy absorbed by colloidal QDs to be emitted in the near-infrared (NIR) region. The attained brightness of the QD nanoclusters at the single-particle level may also lead to applications in bio-sensing, where the use of lipid-encapsulated nanoclusters may be beneficial in addressing some common limitations with current bio-sensors [16]. High-resolution electron microscopy (EM) was used to determine the size distribution of colloidal $CuInS_2$/ZnS QDs, with an average QD diameter of 3.3 $\pm$ 0.6 nm calculated from semi-automated analysis and a QD size dispersity of 18%. The QD nanocluster size and structure were quantified via manual analysis of EM images, where most nanoclusters displayed an elliptical structure with a minor axis mean diameter of 33 $\pm$ 8 nm and a major axis mean diameter of 43 $\pm$ 10 nm. The size was in agreement with the predicted structure from self-assembly following small-scale QD aggregation. To determine the importance of the lipid in stabilising the QD nanoclusters, optical spectroscopy and epifluorescence microscopy experiments were conducted to quantify the co-localisation of the lipid and QDs. Fluorescent lipids (NBD/BODIPY-DHPE) were used to monitor the position of the lipid within the self-assembled structure, with FRET confirmed to take place between the fluorescent dye energy donor and the QD energy acceptor within the structure through steady-state and time-resolved spectroscopy measurements, suggesting that lipids are within 4 nm of the nearest QDs. Spatial overlap between the NBD/BODIPY-DHPE lipid and the $CuInS_2$/ZnS QDs was also observed via epifluorescence microscopy, again supporting the lipid and QD co-localisation and confirming that the lipid does stabilise the hydrophobic QDs within the aqueous environment.

Once the role of the lipid within the QD nanoclusters was confirmed, optical spectroscopy was used to investigate how the lipid:QD molar ratio affects the uptake and fluorescence quenching of the hydrophobic QDs. A linear increase in the amount of QD stabilised was observed with increasing lipid concentration until the QD absorbance and fluorescence began to plateau as the limit of QD uptake was approached. A combination of steady-state and time-resolved spectroscopy was then utilised to investigate the photophysics of the QD nanoclusters, with the origin of the red-shift corresponding to an energy transfer from high-energy to low-energy QDs within individual nanoclusters, in agreement with other studies that have investigated energy transfer within clustered QDs [78–80]. Time-resolved measurements monitoring a range of emission wavelengths supported this theory, with a prominent red-shift of the emission maxima observed in cross-sectional measurements, even at very low time points (sub-1 ns), indicative of energy transfer. This initial quenching led to a reduction in the lifetime at short wavelengths, indicative of energy donor quenching, with an increase in lifetime observed at the longer wavelengths where QDs are energy acceptors. Finally, fluorescence lifetime imaging microscopy was used to investigate the QD nanocluster fluorescence at the single-particle level, with co-localisation of the lipid and QDs further quantified after a spatial overlap was observed within individual clusters. The mean QD fluorescence lifetime decreased from 35.7 $\pm$ 22.5 ns (without NBD-DHPE) to 15.4 $\pm$ 9.5 ns (with NBD-DHPE present), although a large standard deviation was observed for the sample. No significant correlation was observed between the particle intensity and the lifetime of the NBD-DHPE lipid, although high-intensity particles appeared to contribute to a lower QD fluorescence lifetime within QD nanoclusters and low-intensity signals generally contributed to a longer lifetime, suggesting a greater fluorescence quenching in brighter (potentially larger or multiple spatially-overlapping) QD clusters. Overall, this chapter has furthered our understanding of the structural-photophysical relationship of nanoscale clustered QDs.

6.2 Future Work

In Chapter 4, the energy transfer from potentially-bioconjugated CdTe/CdS QDs to LHCII was inconclusive, therefore the binding of the carboxyl (QD) to amine (LHCII) surface chemistries would need to be quantified. Polymer microspheres (Bangs Laboratories) are non-fluorescent, monosized 500 nm spherical polymer particles with functionalised surface chemistry, including aminated and carboxylated functional groups [223–225]. The large size of functionalised polymer microspheres means they would precipitate easily during low-speed centrifugation and can be crosslinked to the fluorescent QDs and LHCII independently with the correct surface chemistry. Fluorescent particles conjugated to the polymer microspheres would precipitate, then could be re-suspended in a separate aqueous buffer after supernatant removal, with steady-state fluorescence microscopy quantifying successful crosslinking. The binding between LHCII and the QDs could also be observed directly using TEM or cryo-EM to reveal high-resolution structures of the bioconjugates and to investigate agglomeration of the bioconjugates [144, 237, 238], which may quantify the observed quenching of QD fluorescence during spectroscopy. Co-localisation of the LHCII and QDs could be quantified using epifluorescence microscopy, where multiple fluorescent components can be imaged within the same sample through the use of filters [120]. FLIM could also be used to quantify energy transfer between the QDs and LHCII, where single-particle measurements would allow the statistical analysis of any increase in LHCII enhancement and QD quenching through alterations in the sample lifetime. A decrease in the QD lifetime and an enhancement of the LHCII fluorescence intensity in comparison to control measurements of the isolated materials (QD or LHCII) would suggest FRET between the QDs and LHCII, although aggregation must be prevented to be confident that the QD lifetime reduction is a result of energy transfer and not non-radiative dissipation.

If co-localisation and energy transfer between the QDs and LHCII was quantified, then bioconjugates could be incorporated into lipid vesicles. Covalently-bonded QD/LHCII

structures, as designed in Chapter 4, could be readily incorporated into a lipid bilayer through the adoption of known proteoliposome self-assembly procedures if the QDs were hydrophilic [119–122], as the LHCII is native to the lipid bilayer and the QDs would remain stable in the aqueous environment outside of the liposome. The efficiency of this incorporation could be investigated using optical spectroscopy, with separation of the proteoliposomes from the free bioconjugates achievable via centrifugation and re-suspension after supernatant removal. A full investigation of these hybrid QD-proteoliposomes could then be completed using a combination of TEM and FLIM to assess the structure, single-particle dynamics and energy transfer efficiency of the system. If FRET within the system is efficient, then alternative combinations of QD and light-harvesting proteins could be trialled, with many other light-harvesting proteins containing gaps in the absorption spectra that could efficiently be filled using QDs.

With respect to Chapter 5 and QD nanoclusters, tetrahedral $CuInS_2$/ZnS QDs have been successfully stabilised by lipids but QDs that are spherical in structure have not yet been investigated. It is thought that the shape of the QDs may affect the lipid encapsulation, with the formation of unfavourable nodes (energetically unfavourable areas of free space surrounding the nanoparticle) predicted to be less likely with spherical QDs compared to tetrahedral QDs due to a lower number of contact points between the lipid tails and the QD capping ligand. This may affect the structure and aggregation of the QDs when associated with the lipid, and although lipid bilayer incorporation with spherical QDs is unlikely at high-enough concentrations to achieve efficient FRET [126], the QD aggregation and therefore cluster size could be favourably reduced. Changing the type of QD would also alter the optical properties of the system, as $CuInS_2$/ZnS QDs generally have a broad emission band compared to other QDs, leading to the observed red-shift. A smaller red-shift may occur if QDs with a narrow emission band were used provided spectral overlap remains [80], as the energy difference between the smallest and the largest QDs would be significantly smaller when compared to the polydisperse $CuInS_2$/ZnS QDs. If the size distribution is narrower, it is possible that less energy would

be dissipated non-radiatively following FRET as there is likely to be less downhill energy transfer, where a reduced spectral overlap suggests a lower energy transfer efficiency would be expected. Finally, completing the investigation into how the size of the QDs alters the structure and optical properties of self-assembled QD nanoclusters through the use of TEM and time-resolved spectroscopy would help to further understand the system optimisation. If the QD size is related to a change in structure or control of the optical properties of the nanoclusters, then the red-shift and QD nanocluster fluorescence emission could be controlled to obtain NIR-emitting structures [239] that have potential use in bio-sensing [240–243], or to obtain structures that emit in the visible region for solar-harvesting enhancement [244, 245].

Bibliography

[1] Paras N Prasad. *Introduction to biophotonics*. John Wiley & Sons, 2003.

[2] Kristjan Plaetzer, Barbara Krammer, Jurgen Berlanda, Frieder Berr, and Tobias Kiesslich. Photophysics and photochemistry of photodynamic therapy: fundamental aspects. *Lasers in medical science*, 24:259–268, 2009.

[3] Joseph R Lakowicz. *Principles of fluorescence spectroscopy*. Springer, 2006.

[4] Dariusz M Niedzwiedzki and Robert E Blankenship. Singlet and triplet excited state properties of natural chlorophylls and bacteriochlorophylls. *Photosynthesis research*, 106:227–238, 2010.

[5] Th Főrster. 10th spiers memorial lecture. transfer mechanisms of electronic excitation. *Discussions of the Faraday Society*, 27:7–17, 1959.

[6] Theodor Forster. Delocalization excitation and excitation transfer. *Modern quantum chemistry*, 1965.

[7] Tihana Mirkovic, Evgeny E Ostroumov, Jessica M Anna, Rienk Van Grondelle, and Gregory D Scholes. Light absorption and energy transfer in the antenna complexes of photosynthetic organisms. *Chemical reviews*, 117(2):249–293, 2017.

[8] Paul Held. An introduction to fluorescence resonance energy transfer (fret) technology and its application in bioscience. *Bio-Tek Application Note*, 2005.

[9] Elizabeth A Jares-Erijman and Thomas M Jovin. Fret imaging. *Nature biotechnology*, 21(11):1387, 2003.

[10] Robert E Blankenship. *Molecular mechanisms of photosynthesis*. John Wiley & Sons, 2021.

[11] Luís MS Loura. Simple estimation of förster resonance energy transfer (fret) orientation factor distribution in membranes. *International journal of molecular sciences*, 13(11):15252–15270, 2012.

[12] Benjamin Schuler and William A Eaton. Protein folding studied by single-molecule fret. *Current opinion in structural biology*, 18(1):16–26, 2008.

[13] Günter Schmid. *Nanoparticles: from theory to application*. John Wiley & Sons, 2011.

[14] Kim E Sapsford, Thomas Pons, Igor L Medintz, and Hedi Mattoussi. Biosensing with luminescent semiconductor quantum dots. *Sensors*, 6(8):925–953, 2006.

[15] Peng Wu and Xiu-Ping Yan. Doped quantum dots for chemo/biosensing and bioimaging. *Chemical Society Reviews*, 42(12):5489–5521, 2013.

[16] Hyung Seok Choi, Youngsun Kim, Jae Chul Park, Mi Hwa Oh, Duk Young Jeon, and Yoon Sung Nam. Highly luminescent, off-stoichiometric cu x in y s 2/zns quantum dots for near-infrared fluorescence bio-imaging. *RSC Advances*, 5(54):43449–43455, 2015.

[17] Niko Hildebrandt, Christopher M Spillmann, W Russ Algar, Thomas Pons, Michael H Stewart, Eunkeu Oh, Kimihiro Susumu, Sebastian A Diaz, James B Delehanty, and Igor L Medintz. Energy transfer with semiconductor quantum dot bioconjugates: a versatile platform for biosensing, energy harvesting, and other developing applications. *Chemical reviews*, 117(2):536–711, 2017.

[18] Arthur J Nozik. Quantum dot solar cells. *Physica E: Low-dimensional Systems and Nanostructures*, 14(1-2):115–120, 2002.

[19] Graham H Carey, Ahmed L Abdelhady, Zhijun Ning, Susanna M Thon, Osman M Bakr, and Edward H Sargent. Colloidal quantum dot solar cells. *Chemical reviews*, 115(23):12732–12763, 2015.

[20] Prashant V Kamat. Quantum dot solar cells. the next big thing in photovoltaics. *The journal of physical chemistry letters*, 4(6):908–918, 2013.

[21] Tae-Ho Kim, Kyung-Sang Cho, Eun Kyung Lee, Sang Jin Lee, Jungseok Chae, Jung Woo Kim, Do Hwan Kim, Jang-Yeon Kwon, Gehan Amaratunga, Sang Yoon Lee, et al. Full-colour quantum dot displays fabricated by transfer printing. *Nature photonics*, 5(3):176–182, 2011.

[22] Yasuhiro Shirasaki, Geoffrey J Supran, Moungi G Bawendi, and Vladimir Bulović. Emergence of colloidal quantum-dot light-emitting technologies. *Nature photonics*, 7(1):13–23, 2013.

[23] Zhaojun Liu, Chun-Ho Lin, Byung-Ryool Hyun, Chin-Wei Sher, Zhijian Lv, Bingqing Luo, Fulong Jiang, Tom Wu, Chih-Hsiang Ho, Hao-Chung Kuo, et al. Micro-light-emitting diodes with quantum dots in display technology. *Light: Science & Applications*, 9(1):83, 2020.

[24] Charles Kittel et al. *Introduction to solid state physics*, volume 8. Wiley New York, 1976.

[25] HP Meyers and HP Myers. *Introductory solid state physics*. CRC press, 1997.

[26] Timothy Jamieson, Raheleh Bakhshi, Daniela Petrova, Rachael Pocock, Mo Imani, and Alexander M Seifalian. Biological applications of quantum dots. *Biomaterials*, 28(31):4717–4732, 2007.

[27] Małgorzata Geszke-Moritz and Michał Moritz. Quantum dots as versatile probes in medical sciences: synthesis, modification and properties. *Materials Science and Engineering: C*, 33(3):1008–1021, 2013.

[28] Louis E Brus. Electron–electron and electron-hole interactions in small semiconductor crystallites: The size dependence of the lowest excited electronic state. *The Journal of chemical physics*, 80(9):4403–4409, 1984.

[29] Louis Brus. Zero-dimensional" excitons" in semiconductor clusters. *IEEE Journal of Quantum Electronics*, 22(9):1909–1914, 1986.

[30] Moungi G Bawendi, Michael L Steigerwald, and Louis E Brus. The quantum mechanics of larger semiconductor clusters (" quantum dots"). *Annual Review of Physical Chemistry*, 41(1):477–496, 1990.

[31] WH Qi, MP Wang, and QH Liu. Shape factor of nonspherical nanoparticles. *Journal of materials science*, 40(9-10):2737–2739, 2005.

[32] Julien Vidal, Silvana Botti, Pär Olsson, Jean-Francois Guillemoles, and Lucia Reining. Strong interplay between structure and electronic properties in cuin (s, se) 2: a first-principles study. *Physical review letters*, 104(5):056401, 2010.

[33] Aron J Cohen, Paula Mori-Sánchez, and Weitao Yang. Challenges for density functional theory. *Chemical reviews*, 112(1):289–320, 2012.

[34] Marco Califano, Alberto Franceschetti, and Alex Zunger. Temperature dependence of excitonic radiative decay in cdse quantum dots: the role of surface hole traps. *Nano Letters*, 5(12):2360–2364, 2005.

[35] Marco Califano. Origins of photoluminescence decay kinetics in cdte colloidal quantum dots. *Acs Nano*, 9(3):2960–2967, 2015.

[36] Jacek Jasieniak, Marco Califano, and Scott E Watkins. Size-dependent valence and conduction band-edge energies of semiconductor nanocrystals. *ACS nano*, 5(7):5888–5902, 2011.

[37] Sergey V Gaponenko. *Introduction to nanophotonics*. Cambridge University Press, 2010.

[38] Jinjun Sun and Ewa M Goldys. Linear absorption and molar extinction coefficients in direct semiconductor quantum dots. *The Journal of Physical Chemistry C*, 112(25):9261–9266, 2008.

[39] Jasprit Singh. *Electronic and optoelectronic properties of semiconductor structures*. Cambridge University Press, 2007.

[40] DL Ferreira and JLA Alves. The effects of shape and size nonuniformity on the absorption spectrum of semiconductor quantum dots. *Nanotechnology*, 15(8):975, 2004.

[41] Wei-Yu Wu, JN Schulman, Tsung-Yuan Hsu, and Uzi Efron. Effect of size nonuniformity on the absorption spectrum of a semiconductor quantum dot system. *Applied physics letters*, 51(10):710–712, 1987.

[42] Damon A Wheeler and Jin Z Zhang. Exciton dynamics in semiconductor nanocrystals. *Advanced Materials*, 25(21):2878–2896, 2013.

[43] Andreas Othonos. Probing ultrafast carrier and phonon dynamics in semiconductors. *Journal of applied physics*, 83(4):1789–1830, 1998.

[44] U Bockelmann and G Bastard. Phonon scattering and energy relaxation in two-, one-, and zero-dimensional electron gases. *Physical Review B*, 42(14):8947, 1990.

[45] VI Klimov, DW McBranch, CA Leatherdale, and MG Bawendi. Electron and hole relaxation pathways in semiconductor quantum dots. *Physical Review B*, 60(19):13740, 1999.

[46] Al L Efros, VA Kharchenko, and M Rosen. Breaking the phonon bottleneck in nanometer quantum dots: Role of auger-like processes. *Solid State Communications*, 93(4):281–284, 1995.

[47] Anshu Pandey and Philippe Guyot-Sionnest. Slow electron cooling in colloidal quantum dots. *Science*, 322(5903):929–932, 2008.

[48] Svetlana V Kilina, Amanda J Neukirch, Bradley F Habenicht, Dmitri S Kilin, and Oleg V Prezhdo. Quantum zeno effect rationalizes the phonon bottleneck in semiconductor quantum dots. *Physical review letters*, 110(18):180404, 2013.

[49] Euan Hendry, Mattijs Koeberg, Fengfeng Wang, H Zhang, C de Mello Donegá, D Vanmaekelbergh, and Mischa Bonn. Direct observation of electron-to-hole energy transfer in cdse quantum dots. *Physical review letters*, 96(5):057408, 2006.

[50] Hamna F Haneef, Andrew M Zeidell, and Oana D Jurchescu. Charge carrier traps in organic semiconductors: a review on the underlying physics and impact on electronic devices. *Journal of Materials Chemistry C*, 8(3):759–787, 2020.

[51] Margaret A Hines and Philippe Guyot-Sionnest. Synthesis and characterization of strongly luminescing zns-capped cdse nanocrystals. *The Journal of Physical Chemistry*, 100(2):468–471, 1996.

[52] Masaru Kuno, Jong-Keuk Lee, Bashir O Dabbousi, Frederic V Mikulec, and Moungi G Bawendi. The band edge luminescence of surface modified cdse nanocrystallites: Probing the luminescing state. *The Journal of Chemical Physics*, 106(23):9869–9882, 1997.

[53] Marcus Jones, Shun S Lo, and Gregory D Scholes. Quantitative modeling of the role of surface traps in cdse/cds/zns nanocrystal photoluminescence decay dynamics. *Proceedings of the National Academy of Sciences*, 106(9):3011–3016, 2009.

[54] Baodong Mao, Chi-Hung Chuang, Junwei Wang, and Clemens Burda. Synthesis and photophysical properties of ternary i–iii–vi agins2 nanocrystals: intrinsic versus surface states. *The Journal of Physical Chemistry C*, 115(18):8945–8954, 2011.

[55] Bingkun Chen, Haizheng Zhong, Wenqing Zhang, Zhan'ao Tan, Yongfang Li, Cairan Yu, Tianyou Zhai, Yoshio Bando, Shengyi Yang, and Bingsuo Zou. Highly emissive and color-tunable cuins2-based colloidal semiconductor nanocrystals: off-stoichiometry effects and improved electroluminescence performance. *Advanced Functional Materials*, 22(10):2081–2088, 2012.

[56] A Paul Alivisatos. Semiconductor clusters, nanocrystals, and quantum dots. *science*, 271(5251):933–937, 1996.

[57] CBea Murray, David J Norris, and Moungi G Bawendi. Synthesis and characterization of nearly monodisperse cde (e= sulfur, selenium, tellurium) semiconductor nanocrystallites. *Journal of the American Chemical Society*, 115(19):8706–8715, 1993.

[58] Vitaly I Kalikmanov. Classical nucleation theory. In *Nucleation theory*, pages 17–41. Springer, 2012.

[59] Farid Abraham. *Homogeneous nucleation theory: the pretransition theory of vapor condensation*, volume 1. Elsevier, 2012.

[60] Tadao Sugimoto. *Monodispersed particles*. Elsevier, 2019.

[61] Nguyen TK Thanh, N Maclean, and S Mahiddine. Mechanisms of nucleation and growth of nanoparticles in solution. *Chemical reviews*, 114(15):7610–7630, 2014.

[62] Soon Gu Kwon and Taeghwan Hyeon. Formation mechanisms of uniform nanocrystals via hot-injection and heat-up methods. *Small*, 7(19):2685–2702, 2011.

[63] Xiaogang Peng, J Wickham, and AP Alivisatos. Kinetics of ii-vi and iii-v colloidal semiconductor nanocrystal growth:'focusing'of size distributions. *Journal of the American Chemical Society*, 120(LBNL-41792), 1998.

[64] Bashir O Dabbousi, Javier Rodriguez-Viejo, Frederic V Mikulec, Jason R Heine, Hedi Mattoussi, Raymond Ober, Klavs F Jensen, and Moungi G Bawendi. (cdse) zns core- shell quantum dots: synthesis and characterization of a size series of highly luminescent nanocrystallites. *The Journal of Physical Chemistry B*, 101(46):9463–9475, 1997.

[65] Jian Wang, Yitao Long, Yuliang Zhang, Xinhua Zhong, and Linyong Zhu. Preparation of highly luminescent cdte/cds core/shell quantum dots. *ChemPhysChem*, 10(4):680–685, 2009.

[66] Qinghui Zeng, Xianggui Kong, Yajuan Sun, Youlin Zhang, Langping Tu, Jialong Zhao, and Hong Zhang. Synthesis and optical properties of type ii cdte/cds core/shell quantum dots in aqueous solution via successive ion layer adsorption and reaction. *The Journal of Physical Chemistry C*, 112(23):8587–8593, 2008.

[67] Mark Green. The nature of quantum dot capping ligands. *Journal of Materials Chemistry*, 20(28):5797–5809, 2010.

[68] Liang Li, Anshu Pandey, Donald J Werder, Bishnu P Khanal, Jeffrey M Pietryga, and Victor I Klimov. Efficient synthesis of highly luminescent copper indium sulfide-based core/shell nanocrystals with surprisingly long-lived emission. *Journal of the American Chemical Society*, 133(5):1176–1179, 2011.

[69] Liang Li, T Jean Daou, Isabelle Texier, Tran Thi Kim Chi, Nguyen Quang Liem, and Peter Reiss. Highly luminescent cuins2/zns core/shell nanocrystals: cadmium-free quantum dots for in vivo imaging. *Chemistry of Materials*, 21(12):2422–2429, 2009.

[70] Vasudevanpillai Biju, Yoji Makita, Akinari Sonoda, Hiroshi Yokoyama, Yoshinobu Baba, and Mitsuru Ishikawa. Temperature-sensitive photoluminescence of cdse quantum dot clusters. *The Journal of Physical Chemistry B*, 109(29):13899–13905, 2005.

[71] Richard Wargnier, Alexandre V Baranov, Vladimir G Maslov, Vitali Stsiapura, Mikhail Artemyev, Michel Pluot, Alyona Sukhanova, and Igor Nabiev. Energy transfer in aqueous solutions of oppositely charged cdse/zns core/shell quantum dots and in quantum dot- nanogold assemblies. *Nano Letters*, 4(3):451–457, 2004.

[72] HE Grecco, KA Lidke, R Heintzmann, DS Lidke, C Spagnuolo, OE Martinez, EA Jares-Erijman, and TM Jovin. Ensemble and single particle photophysical properties (two-photon excitation,

anisotropy, fret, lifetime, spectral conversion) of commercial quantum dots in solution and in live cells. *Microscopy research and technique*, 65(4-5):169–179, 2004.

[73] Clare Higgins, Manuela Lunz, A Louise Bradley, Valerie A Gerard, Stephen Byrne, Yurii K Gun'ko, Vladimir Lesnyak, and Nikolai Gaponik. Energy transfer in colloidal cdte quantum dot nanoclusters. *Optics express*, 18(24):24486–24494, 2010.

[74] CB Murray, CR Kagan, and MG Bawendi. Self-organization of cdse nanocrystallites into three-dimensional quantum dot superlattices. *Science*, 270(5240):1335–1338, 1995.

[75] Cherie R Kagan, Efrat Lifshitz, Edward H Sargent, and Dmitri V Talapin. Building devices from colloidal quantum dots. *Science*, 353(6302):aac5523, 2016.

[76] Fan Xu, Xin Ma, Chelsea R Haughn, Jamie Benavides, Matthew F Doty, and Sylvain G Cloutier. Efficient exciton funneling in cascaded pbs quantum dot superstructures. *ACS nano*, 5(12):9950–9957, 2011.

[77] Gerasimos Konstantatos, Changjun Huang, Larissa Levina, Zhenghong Lu, and Edward H Sargent. Efficient infrared electroluminescent devices using solution-processed colloidal quantum dots. *Advanced Functional Materials*, 15(11):1865–1869, 2005.

[78] CR Kagan, CB Murray, M Nirmal, and MG Bawendi. Electronic energy transfer in cdse quantum dot solids. *Physical Review Letters*, 76(9):1517, 1996.

[79] CR Kagan, CB Murray, and MG Bawendi. Long-range resonance transfer of electronic excitations in close-packed cdse quantum-dot solids. *Physical Review B*, 54(12):8633, 1996.

[80] SA Crooker, JA Hollingsworth, S Tretiak, and Victor I Klimov. Spectrally resolved dynamics of energy transfer in quantum-dot assemblies: towards engineered energy flows in artificial materials. *Physical Review Letters*, 89(18):186802, 2002.

[81] T Franzl, DS Koktysh, TA Klar, AL Rogach, J Feldmann, and N Gaponik. Fast energy transfer in layer-by-layer assembled cdte nanocrystal bilayers. *Applied Physics Letters*, 84(15):2904–2906, 2004.

[82] S Gardelis, M Fakis, N Droseros, D Georgiadou, A Travlos, and AG Nassiopoulou. Energy transfer in aggregated cuins2/zns core-shell quantum dots deposited as solid films. *Journal of Physics D: Applied Physics*, 50(3):035107, 2016.

[83] Dale M Willard, Tina Mutschler, Ming Yu, Jaemyeong Jung, and Alan Van Orden. Directing energy flow through quantum dots: towards nanoscale sensing. *Analytical and bioanalytical chemistry*, 384:564–571, 2006.

[84] Kenny F Chou and Allison M Dennis. Förster resonance energy transfer between quantum dot donors and quantum dot acceptors. *Sensors*, 15(6):13288–13325, 2015.

[85] Dale M Willard and Alan Van Orden. Resonant energy-transfer sensor. *Nature materials*, 2(9):575–576, 2003.

[86] Igor L Medintz, H Tetsuo Uyeda, Ellen R Goldman, and Hedi Mattoussi. Quantum dot bioconjugates for imaging, labelling and sensing. *Nature materials*, 4(6):435–446, 2005.

[87] Jun Miyazaki, Shuichi Kinoshita, and Takashi Jin. Non-radiative exciton recombination through excitation energy transfer in quantum dot clusters. *Journal of luminescence*, 131(3):539–542, 2011.

[88] SA Tovstun and VF Razumov. Theoretical analysis of nonradiative energy transfer in nanoclusters of quasi-monodisperse colloidal quantum dots. *High Energy Chemistry*, 49:352–360, 2015.

[89] AV Nevidimov, VA Kremenets, MG Spirin, LM Nikolenko, SB Brichkin, and VF Razumov. Computer simulation of förster resonance energy transfer in nanoclusters of cadmium selenide colloidal quantum dots. *High Energy Chemistry*, 53(2):125–131, 2019.

[90] LM Nikolenko, AV Gadomskaya, MG Spirin, SA Tovstun, SB Brichkin, and VF Razumov. Förster resonance energy transfer in aggregates of cdse colloidal quantum dots with adsorbed meso-tetra (3-pyridyl) porphyrin. *High Energy Chemistry*, 54(5):316–327, 2020.

[91] SB Brichkin, SA Tovstun, MG Spirin, and VF Razumov. Förster resonance energy transfer in nanoclusters of inp@ zns colloidal quantum dots with dodecylamine ligand shells. *High Energy Chemistry*, 51:455–461, 2017.

[92] Junling Li, Yonghua Zhang, Junjie Ai, Qiang Gao, Honglan Qi, Chengxiao Zhang, and Zhiliang Cheng. Quantum dot cluster (qdc)-loaded phospholipid micelles as a fret probe for phospholipase a 2 detection. *RSC advances*, 6(19):15895–15899, 2016.

[93] Eyal Cohen, Itay Gdor, Elisabet Romero, Shira Yochelis, Rienk van Grondelle, and Yossi Paltiel. Achieving exciton delocalization in quantum dot aggregates using organic linker molecules. *The Journal of Physical Chemistry Letters*, 8(5):1014–1018, 2017.

[94] Eyal Cohen, Pavel Komm, Noa Rosenthal-Strauss, Joanna Dehnel, Efrat Lifshitz, Shira Yochelis, Raphael D Levine, Francoise Remacle, Barbara Fresch, Gilad Marcus, et al. Fast energy transfer in cdse quantum dot layered structures: Controlling coupling with covalent-bond organic linkers. *The Journal of Physical Chemistry C*, 122(10):5753–5758, 2018.

[95] Peter Reiss, Marie Carriere, Christophe Lincheneau, Louis Vaure, and Sudarsan Tamang. Synthesis of semiconductor nanocrystals, focusing on nontoxic and earth-abundant materials. *Chemical reviews*, 116(18):10731–10819, 2016.

[96] Austin M Derfus, Warren CW Chan, and Sangeeta N Bhatia. Probing the cytotoxicity of semiconductor quantum dots. *Nano letters*, 4(1):11–18, 2004.

[97] Herwig Döllefeld, Kathrin Hoppe, Joanna Kolny, Kristian Schilling, Horst Weller, and Alexander Eychmüller. Investigations on the stability of thiol stabilized semiconductor nanoparticles. *Physical Chemistry Chemical Physics*, 4(19):4747–4753, 2002.

[98] Ingvar T Kraatz, Matthew Booth, Benjamin J Whitaker, Michael GD Nix, and Kevin Critchley. Sub-bandgap emission and intraband defect-related excited-state dynamics in colloidal cuins2/zns quantum dots revealed by femtosecond pump–dump–probe spectroscopy. *The Journal of Physical Chemistry C*, 118(41):24102–24109, 2014.

[99] Andrew J Harvie, Matthew Booth, Ruth L Chantry, Nicole Hondow, Demie M Kepaptsoglou, Quentin M Ramasse, Stephen D Evans, and Kevin Critchley. Observation of compositional domains within individual copper indium sulfide quantum dots. *Nanoscale*, 8(36):16157–16161, 2016.

[100] Addis S Fuhr, Hyeong Jin Yun, Nikolay S Makarov, Hongbo Li, Hunter McDaniel, and Victor I Klimov. Light emission mechanisms in cuins2 quantum dots evaluated by spectral electrochemistry. *ACS photonics*, 4(10):2425–2435, 2017.

[101] Chenghui Xia, Weiwei Wu, Ting Yu, Xiaobin Xie, Christina Van Oversteeg, Hans C Gerritsen, and Celso de Mello Donega. Size-dependent band-gap and molar absorption coefficients of colloidal cuins2 quantum dots. *ACS nano*, 12(8):8350–8361, 2018.

[102] Matthew Booth, Andrew P Brown, Stephen D Evans, and Kevin Critchley. Determining the concentration of cuins2 quantum dots from the size-dependent molar extinction coefficient. *Chemistry of Materials*, 24(11):2064–2070, 2012.

[103] Dan Huang and Clas Persson. Stability of the bandgap in cu-poor cuinse2. *Journal of Physics: Condensed Matter*, 24(45):455503, 2012.

[104] Huidong Zang, Hongbo Li, Nikolay S Makarov, Kirill A Velizhanin, Kaifeng Wu, Young-Shin Park, and Victor I Klimov. Thick-shell cuins2/zns quantum dots with suppressed "blinking" and narrow single-particle emission line widths. *Nano letters*, 17(3):1787–1795, 2017.

[105] Masato Uehara, Kosuke Watanabe, Yasuyuki Tajiri, Hiroyuki Nakamura, and Hideaki Maeda. Synthesis of cu in s 2 fluorescent nanocrystals and enhancement of fluorescence by controlling crystal defect. *The Journal of chemical physics*, 129(13):134709, 2008.

[106] Anh T Nguyen, Feng Gao, Dustin Baucom, and Colin D Heyes. Cuins2-doped zns quantum dots obtained via non-injection cation exchange show reduced but heterogeneous blinking and provide insights into their structure–optical property relationships. *The Journal of Physical Chemistry C*, 124(19):10744–10754, 2020.

[107] Patrick J Whitham, Arianna Marchioro, Kathryn E Knowles, Troy B Kilburn, Philip J Reid, and Daniel R Gamelin. Single-particle photoluminescence spectra, blinking, and delayed luminescence of colloidal cuins2 nanocrystals. *The Journal of Physical Chemistry C*, 120(30):17136–17142, 2016.

[108] Jaehyun Park and Sang-Wook Kim. Cuins 2/zns core/shell quantum dots by cation exchange and their blue-shifted photoluminescence. *Journal of Materials Chemistry*, 21(11):3745–3750, 2011.

[109] S Jonathan Singer and Garth L Nicolson. The fluid mosaic model of the structure of cell membranes. *Science*, 175(4023):720–731, 1972.

[110] Mark S Bretscher. Asymmetrical lipid bilayer structure for biological membranes. *Nature New Biology*, 236(61):11, 1972.

[111] Dimitrios Bitounis, Raphaelle Fanciullino, Athanassios Iliadis, and Joseph Ciccolini. Optimizing druggability through liposomal formulations: new approaches to an old concept. *International Scholarly Research Notices*, 2012, 2012.

[112] Tanushree Chakraborty, Indranil Chakraborty, and Soumen Ghosh. The methods of determination of critical micellar concentrations of the amphiphilic systems in aqueous medium. *Arabian Journal of Chemistry*, 4(3):265–270, 2011.

[113] Alec D Bangham, Martyn W Hill, and NGA Miller. Preparation and use of liposomes as models of biological membranes. In *Methods in membrane biology*, pages 1–68. Springer, 1974.

[114] Miglena I Angelova and Dimiter S Dimitrov. Liposome electroformation. *Faraday discussions of the Chemical Society*, 81:303–311, 1986.

[115] Ralf P Richter, Rémi Bérat, and Alain R Brisson. Formation of solid-supported lipid bilayers: an integrated view. *Langmuir*, 22(8):3497–3505, 2006.

[116] Eugenia Nogueira, Andreia C Gomes, Ana Preto, and Artur Cavaco-Paulo. Design of liposomal formulations for cell targeting. *Colloids and surfaces B: Biointerfaces*, 136:514–526, 2015.

[117] Kant Shashi, Kumar Satinder, Prashar Bharat, et al. A complete review on: liposomes. *International Research Journal of Pharmacy*, 3(7):10–16, 2012.

[118] Michel Ollivon, Sylviane Lesieur, Cécile Grabielle-Madelmont, and Maıté Paternostre. Vesicle reconstitution from lipid–detergent mixed micelles. *Biochimica et Biophysica Acta (BBA)-Biomembranes*, 1508(1-2):34–50, 2000.

[119] Nicoletta Liguori, Xavier Periole, Siewert J Marrink, and Roberta Croce. From light-harvesting to photoprotection: structural basis of the dynamic switch of the major antenna complex of plants (lhcii). *Scientific reports*, 5(1):15661, 2015.

[120] Ashley M Hancock, Sophie A Meredith, Simon DA Connell, Lars JC Jeuken, and Peter G Adams. Proteoliposomes as energy transferring nanomaterials: enhancing the spectral range of light-harvesting proteins using lipid-linked chromophores. *bioRxiv*, page 609255, 2019.

[121] Marijonas Tutkus, Parveen Akhtar, Jevgenij Chmeliov, Fanni Gorfol, Gediminas Trinkunas, Petar H Lambrev, and Leonas Valkunas. Fluorescence microscopy of single liposomes with incorporated pigment–proteins. *Langmuir*, 34(47):14410–14418, 2018.

[122] Marijonas Tutkus, Jevgenij Chmeliov, Gediminas Trinkunas, Parveen Akhtar, Petar H Lambrev, and Leonas Valkunas. Aggregation-related quenching of lhcii fluorescence in liposomes revealed by single-molecule spectroscopy. *Journal of Photochemistry and Photobiology B: Biology*, 218:112174, 2021.

[123] Emanuela Crisafi and Anjali Pandit. Disentangling protein and lipid interactions that control a molecular switch in photosynthetic light harvesting. *Biochimica et Biophysica Acta (BBA)-Biomembranes*, 1859(1):40–47, 2017.

[124] Feng Zhou, Shuang Liu, Zhaohui Hu, Tingyun Kuang, Harald Paulsen, and Chunhong Yang. Effect of monogalactosyldiacylglycerol on the interaction between photosystem ii core complex and its antenna complexes in liposomes of thylakoid lipids. *Photosynthesis Research*, 99:185–193, 2009.

[125] Ashley M Hancock, David JK Swainsbury, Sophie A Meredith, Kenichi Morigaki, C Neil Hunter, and Peter G Adams. Enhancing the spectral range of plant and bacterial light-harvesting pigment-protein complexes with various synthetic chromophores incorporated into lipid vesicles. *Journal of Photochemistry and Photobiology B: Biology*, 237:112585, 2022.

[126] Vincenzo De Leo, Lucia Catucci, Andrea Falqui, Roberto Marotta, Marinella Striccoli, Angela Agostiano, Roberto Comparelli, and Francesco Milano. Hybrid assemblies of fluorescent nanocrystals and membrane proteins in liposomes. *Langmuir*, 30(6):1599–1608, 2014.

[127] Masayoshi Tanaka, Kevin Critchley, Tadashi Matsunaga, Stephen D Evans, and Sarah S Staniland. Fabrication of lipid tubules with embedded quantum dots by membrane tubulation protein. *Small*, 8(10):1590–1595, 2012.

[128] Oliver Bixner and Erik Reimhult. Controlled magnetosomes: Embedding of magnetic nanoparticles into membranes of monodisperse lipid vesicles. *Journal of colloid and interface science*, 466:62–71, 2016.

[129] Kristina Gundlach, Mara Werwie, Sabine Wiegand, and Harald Paulsen. Filling the "green gap" of the major light-harvesting chlorophyll a/b complex by covalent attachment of rhodamine red. *Biochimica et Biophysica Acta (BBA)-Bioenergetics*, 1787(12):1499–1504, 2009.

[130] Gary F Moore and Gary W Brudvig. Energy conversion in photosynthesis: a paradigm for solar fuel production. *Annu. Rev. Condens. Matter Phys.*, 2(1):303–327, 2011.

[131] Melih Şener, Johan Strümpfer, Jen Hsin, Danielle Chandler, Simon Scheuring, C Neil Hunter, and Klaus Schulten. Förster energy transfer theory as reflected in the structures of photosynthetic light-harvesting systems. *ChemPhysChem*, 12(3):518–531, 2011.

[132] Herbert van Amerongen and Roberta Croce. Light harvesting in photosystem ii. *Photosynthesis Research*, 116:251–263, 2013.

[133] Arthur R Grossman, Michael R Schaefer, Gisela G Chiang, and JL372933 Collier. The phycobilisome, a light-harvesting complex responsive to environmental conditions. *Microbiological reviews*, 57(3):725–749, 1993.

[134] Bertram Daum and Werner Kühlbrandt. Electron tomography of plant thylakoid membranes. *Journal of Experimental Botany*, 62(7):2393–2402, 2011.

[135] Rienk van Grondelle and Vladimir I Novoderezhkin. Energy transfer in photosynthesis: experimental insights and quantitative models. *Physical Chemistry Chemical Physics*, 8(7):793–807, 2006.

[136] Gregory D Scholes, Graham R Fleming, Alexandra Olaya-Castro, and Rienk Van Grondelle. Lessons from nature about solar light harvesting. *Nature chemistry*, 3(10):763, 2011.

[137] Bartlomiej Drop, Mariam Webber-Birungi, Sathish KN Yadav, Alicja Filipowicz-Szymanska, Fabrizia Fusetti, Egbert J Boekema, and Roberta Croce. Light-harvesting complex ii (lhcii) and its supramolecular organization in chlamydomonas reinhardtii. *Biochimica et Biophysica Acta (BBA)-Bioenergetics*, 1837(1):63–72, 2014.

[138] Werner Kühlbrandt, Da Neng Wang, and Yoshinori Fujiyoshi. Atomic model of plant light-harvesting complex by electron crystallography. *Nature*, 367(6464):614–621, 1994.

[139] Zhenfeng Liu, Hanchi Yan, Kebin Wang, Tingyun Kuang, Jiping Zhang, Lulu Gui, Xiaomin An, and Wenrui Chang. Crystal structure of spinach major light-harvesting complex at 2.72 å resolution. *Nature*, 428(6980):287–292, 2004.

[140] Jörg Standfuss, Anke C Terwisscha van Scheltinga, Matteo Lamborghini, and Werner Kühlbrandt. Mechanisms of photoprotection and nonphotochemical quenching in pea light-harvesting complex at 2.5 å resolution. *The EMBO journal*, 24(5):919–928, 2005.

[141] Tiago Barros, Antoine Royant, Jörg Standfuss, Andreas Dreuw, and Werner Kühlbrandt. Crystal structure of plant light-harvesting complex shows the active, energy-transmitting state. *The EMBO Journal*, 28(3):298–306, 2009.

[142] Stephan Hobe, Stefan Prytulla, Werner Kühlbrandt, and Harald Paulsen. Trimerization and crystallization of reconstituted light-harvesting chlorophyll a/b complex. *The EMBO Journal*, 13(15):3423–3429, 1994.

[143] Erwin JG Peterman, Stephan Hobe, Florentine Calkoen, Rienk van Grondelle, Harald Paulsen, and Herbert van Amerongen. Low-temperature spectroscopy of monomeric and trimeric forms of reconstituted light-harvesting chlorophyll ab complex. *Biochimica et Biophysica Acta (BBA)-Bioenergetics*, 1273(2):171–174, 1996.

[144] Xuepeng Wei, Xiaodong Su, Peng Cao, Xiuying Liu, Wenrui Chang, Mei Li, Xinzheng Zhang, and Zhenfeng Liu. Structure of spinach photosystem ii–lhcii supercomplex at 3.2 å resolution. *Nature*, 534(7605):69–74, 2016.

[145] Stefan Jansson. A guide to the lhc genes and their relatives in arabidopsis. *Trends in plant science*, 4(6):236–240, 1999.

[146] Joerg Standfuss and Werner Kühlbrandt. The three isoforms of the light-harvesting complex ii: spectroscopic features, trimer formation, and functional roles. *Journal of Biological Chemistry*, 279(35):36884–36891, 2004.

[147] V Barzda, V Gulbinas, R Kananavicius, V Cervinskas, H Van Amerongen, R Van Grondelle, and L Valkunas. Singlet–singlet annihilation kinetics in aggregates and trimers of lhcii. *Biophysical journal*, 80(5):2409–2421, 2001.

[148] Nathan S Lewis and Daniel G Nocera. Powering the planet: Chemical challenges in solar energy utilization. *Proceedings of the National Academy of Sciences*, 103(43):15729–15735, 2006.

[149] Patrick Criqui and Nikolaos Kouvaritakis. World energy projections to 2030. *International journal of global energy issues*, 14(1-4):116–136, 2000.

[150] James Barber et al. *Molecular to global photosynthesis*, volume 2. World Scientific, 2004.

[151] Xin-Guang Zhu, Stephen P Long, and Donald R Ort. Improving photosynthetic efficiency for greater yield. *Annual review of plant biology*, 61:235–261, 2010.

[152] David Alan Walker. Biofuels, facts, fantasy, and feasibility. *Journal of Applied Phycology*, 21(5):509–517, 2009.

[153] Robert E Blankenship, David M Tiede, James Barber, Gary W Brudvig, Graham Fleming, Maria Ghirardi, MR Gunner, Wolfgang Junge, David M Kramer, Anastasios Melis, et al. Comparing photosynthetic and photovoltaic efficiencies and recognizing the potential for improvement. *science*, 332(6031):805–809, 2011.

[154] MC Hanna and AJ Nozik. Solar conversion efficiency of photovoltaic and photoelectrolysis cells with carrier multiplication absorbers. *Journal of Applied Physics*, 100(7):074510, 2006.

[155] David A LaVan and Jennifer N Cha. Approaches for biological and biomimetic energy conversion. *Proceedings of the National Academy of Sciences*, 103(14):5251–5255, 2006.

[156] GS Beddard and G Porter. Concentration quenching in chlorophyll. *Nature*, 260(5549):366–367, 1976.

[157] Cvetelin Vasilev, Matthew P Johnson, Edward Gonzales, Lin Wang, Alexander V Ruban, Gabriel Montano, Ashley J Cadby, and C Neil Hunter. Reversible switching between nonquenched and quenched states in nanoscale linear arrays of plant light-harvesting antenna complexes. *Langmuir*, 30(28):8481–8490, 2014.

[158] Maryana Escalante, Aufried Lenferink, Yiping Zhao, Niels Tas, Jurriaan Huskens, C Neil Hunter, Vinod Subramaniam, and Cees Otto. Long-range energy propagation in nanometer arrays of light harvesting antenna complexes. *Nano letters*, 10(4):1450–1457, 2010.

[159] Peter N Ciesielski, Christopher J Faulkner, Matthew T Irwin, Justin M Gregory, Norman H Tolk, David E Cliffel, and G Kane Jennings. Enhanced photocurrent production by photosystem i multilayer assemblies. *Advanced Functional Materials*, 20(23):4048–4054, 2010.

[160] Muhammad Kamran, Juan D Delgado, Vincent Friebe, Thijs J Aartsma, and Raoul N Frese. Photosynthetic protein complexes as bio-photovoltaic building blocks retaining a high internal quantum efficiency. *Biomacromolecules*, 15(8):2833–2838, 2014.

[161] Roberta Croce and Herbert Van Amerongen. Natural strategies for photosynthetic light harvesting. *Nature chemical biology*, 10(7):492–501, 2014.

[162] Haijun Liu, Hao Zhang, Dariusz M Niedzwiedzki, Mindy Prado, Guannan He, Michael L Gross, and Robert E Blankenship. Phycobilisomes supply excitations to both photosystems in a megacomplex in cyanobacteria. *Science*, 342(6162):1104–1107, 2013.

[163] Francesco Milano, Rocco Roberto Tangorra, Omar Hassan Omar, Roberta Ragni, Alessandra Operamolla, Angela Agostiano, Gianluca M Farinola, and Massimo Trotta. Enhancing the light harvesting capability of a photosynthetic reaction center by a tailored molecular fluorophore. *Angewandte Chemie International Edition*, 51(44):11019–11023, 2012.

[164] Yusuke Yoneda, Tomoyasu Noji, Tetsuro Katayama, Naoto Mizutani, Daisuke Komori, Mamoru Nango, Hiroshi Miyasaka, Shigeru Itoh, Yutaka Nagasawa, and Takehisa Dewa. Extension of light-harvesting ability of photosynthetic light-harvesting complex 2 (lh2) through ultrafast energy transfer from covalently attached artificial chromophores. *Journal of the American Chemical Society*, 137(40):13121–13129, 2015.

[165] Dario Leister. Enhancing the light reactions of photosynthesis: Strategies, controversies and perspectives. *Molecular Plant*, 2022.

[166] Yusuke Yoneda, Akari Goto, Nobutaka Takeda, Hiromi Harada, Masaharu Kondo, Hiroshi Miyasaka, Yutaka Nagasawa, and Takehisa Dewa. Ultrafast photodynamics and quantitative evaluation of biohybrid photosynthetic antenna and reaction center complexes generating photocurrent. *The Journal of Physical Chemistry C*, 124(16):8605–8615, 2020.

[167] Mara Werwie, Xiangxing Xu, Mathias Haase, Thomas Basché, and Harald Paulsen. Bio serves nano: biological light-harvesting complex as energy donor for semiconductor quantum dots. *Langmuir*, 28(13):5810–5818, 2012.

[168] Igor Nabiev, Aliaksandra Rakovich, Alyona Sukhanova, Evgeniy Lukashev, Vadim Zagidullin, Vladimir Pachenko, Yury P Rakovich, John F Donegan, Andrei B Rubin, and Alexander O Govorov. Fluorescent quantum dots as artificial antennas for enhanced light harvesting and energy transfer to photosynthetic reaction centers. *Angewandte Chemie International Edition*, 49(40):7217–7221, 2010.

[169] Juntai Liu, Judith Mantell, and Michael R Jones. Minding the gap between plant and bacterial photosynthesis within a self-assembling biohybrid photosystem. *ACS nano*, 14(4):4536–4549, 2020.

[170] Juntai Liu, Judith Mantell, Natalie Di Bartolo, and Michael R Jones. Mechanisms of self-assembly and energy harvesting in tuneable conjugates of quantum dots and engineered photovoltaic proteins. *Small*, 15(4):1804267, 2019.

[171] Yusuke Yoneda, Masaya Kito, Daiki Mori, Akari Goto, Masaharu Kondo, Hiroshi Miyasaka, Yutaka Nagasawa, and Takehisa Dewa. Ultrafast energy transfer between self-assembled fluorophore and photosynthetic light-harvesting complex 2 (lh2) in lipid bilayer. *The Journal of Chemical Physics*, 156(9):095101, 2022.

[172] Dan-Hui Yang, Harald Paulsen, and Bertil Andersson. The n-terminal domain of the light-harvesting chlorophyll a/b-binding protein complex (lhcii) is essential for its acclimative proteolysis. *Febs Letters*, 466(2-3):385–388, 2000.

[173] Chunhong Yang, Kirstin Kosemund, Caroline Cornet, and Harald Paulsen. Exchange of pigment-binding amino acids in light-harvesting chlorophyll a/b protein. *Biochemistry*, 38(49):16205–16213, 1999.

[174] Niklas Fehr, Carsten Dietz, Yevhen Polyhach, Tona von Hagens, Gunnar Jeschke, and Harald Paulsen. Modeling of the n-terminal section and the lumenal loop of trimeric light harvesting complex ii (lhcii) by using epr. *Journal of Biological Chemistry*, 290(43):26007–26020, 2015.

[175] Aleksei Volkov, Christoph Dockter, Timo Bund, Harald Paulsen, and Gunnar Jeschke. Pulsed epr determination of water accessibility to spin-labeled amino acid residues in lhciib. *Biophysical Journal*, 96(3):1124–1141, 2009.

[176] Maryam Hashemi Shabestari, Cor JAM Wolfs, Ruud B Spruijt, Herbert van Amerongen, and Martina Huber. Exploring the structure of the 100 amino-acid residue long n-terminus of the plant antenna protein cp29. *Biophysical journal*, 106(6):1349–1358, 2014.

[177] Christian B Rosen and Matthew B Francis. Targeting the n terminus for site-selective protein modification. *Nature chemical biology*, 13(7):697–705, 2017.

[178] Zenon Grabarek and John Gergely. Zero-length crosslinking procedure with the use of active esters. *Analytical biochemistry*, 185(1):131–135, 1990.

[179] Gray R Kunkel, Margarete Mehrabian, and Harold G Martinson. Contact-site cross-linking agents. *Molecular and cellular biochemistry*, 34(1):3–13, 1981.

[180] Jin Chang and Eric R Waclawik. Controlled synthesis of cuins 2, cu 2 sns 3 and cu 2 znsns 4 nanostructures: insight into the universal phase-selectivity mechanism. *CrystEngComm*, 15(28):5612–5619, 2013.

[181] Aneeta Kharkwal, Shailesh N Sharma, Kiran Jain, and AK Singh. A solvothermal approach for the size-, shape-and phase-controlled synthesis and properties of cuins2. *Materials Chemistry and Physics*, 144(3):252–262, 2014.

[182] Nikolai Gaponik, Dmitri V Talapin, Andrey L Rogach, Kathrin Hoppe, Elena V Shevchenko, Andreas Kornowski, Alexander Eychmüller, and Horst Weller. Thiol-capping of cdte nanocrystals: an alternative to organometallic synthetic routes. *The Journal of Physical Chemistry B*, 106(29):7177–7185, 2002.

[183] Zhenyu Gu, Lei Zou, Zheng Fang, Weihong Zhu, and Xinhua Zhong. One-pot synthesis of highly luminescent cdte/cds core/shell nanocrystals in aqueous phase. *Nanotechnology*, 19(13):135604, 2008.

[184] Peter G Adams, Cvetelin Vasilev, C Neil Hunter, and Matthew P Johnson. Correlated fluorescence quenching and topographic mapping of light-harvesting complex ii within surface-assembled aggregates and lipid bilayers. *Biochimica et Biophysica Acta (BBA)-Bioenergetics*, 1859(10):1075–1085, 2018.

[185] Pierce Biotechnology and User Guide. Nhs and sulfo-nhs. *Thermo Fisher Scientific Inc.: Waltham, MA, USA*, 2011.

[186] Thermo Scientific. Zeba™ spin desalting columns instructions. 2017.

[187] W William Yu, Lianhua Qu, Wenzhuo Guo, and Xiaogang Peng. Experimental determination of the extinction coefficient of cdte, cdse, and cds nanocrystals. *Chemistry of materials*, 15(14):2854–2860, 2003.

[188] Yemliha Altıntas, Mohammad Younis Talpur, and Evren Mutlugun. The effect of ligand chain length on the optical properties of alloyed core-shell inpzns/zns quantum dots. *Journal of Alloys and Compounds*, 711:335–341, 2017.

[189] Haizheng Zhong, Yi Zhou, Mingfu Ye, Youjun He, Jianping Ye, Chang He, Chunhe Yang, and Yongfang Li. Controlled synthesis and optical properties of colloidal ternary chalcogenide cuins2 nanocrystals. *Chemistry of Materials*, 20(20):6434–6443, 2008.

[190] Luca De Trizio, Mirko Prato, Alessandro Genovese, Alberto Casu, Mauro Povia, Roberto Simonutti, Marcelo JP Alcocer, Cosimo D'Andrea, Francesco Tassone, and Liberato Manna. Strongly fluorescent quaternary cu–in–zn–s nanocrystals prepared from cu1-x ins2 nanocrystals by partial cation exchange. *Chemistry of Materials*, 24(12):2400–2406, 2012.

[191] Joanna Kolny-Olesiak and Horst Weller. Synthesis and application of colloidal cuins2 semiconductor nanocrystals. *ACS applied materials & interfaces*, 5(23):12221–12237, 2013.

[192] Haizheng Zhong, Shun S Lo, Tihana Mirkovic, Yunchao Li, Yuqin Ding, Yongfang Li, and Gregory D Scholes. Noninjection gram-scale synthesis of monodisperse pyramidal cuins2 nanocrystals and their size-dependent properties. *ACS nano*, 4(9):5253–5262, 2010.

[193] Tugce Akdas, Johannes Walter, Doris Segets, Monica Distaso, Benjamin Winter, Balaji Birajdar, Erdmann Spiecker, and Wolfgang Peukert. Investigation of the size–property relationship in cuins 2 quantum dots. *Nanoscale*, 7(43):18105–18118, 2015.

[194] Amira R AbouElhamd, Khaled A Al-Sallal, and Ahmed Hassan. Review of core/shell quantum dots technology integrated into building's glazing. *Energies*, 12(6):1058, 2019.

[195] Yi su Kim, Yonghee Lee, Youngsun Kim, Donghyuk Kim, Hyung Seok Choi, Jae Chul Park, Yoon Sung Nam, and Duk Young Jeon. Synthesis of efficient near-infrared-emitting cuins 2/zns quantum dots by inhibiting cation-exchange for bio application. *RSC Advances*, 7(18):10675–10682, 2017.

[196] D Vasudevan, Rohit Ranganathan Gaddam, Adrian Trinchi, and Ivan Cole. Core–shell quantum dots: Properties and applications. *Journal of Alloys and Compounds*, 636:395–404, 2015.

[197] Jianhui Sun, Michio Ikezawa, Xiuying Wang, Pengtao Jing, Haibo Li, Jialong Zhao, and Yasuaki Masumoto. Photocarrier recombination dynamics in ternary chalcogenide cuins 2 quantum dots. *Physical Chemistry Chemical Physics*, 17(18):11981–11989, 2015.

[198] Marlius Castillo, Sangram L Raut, Sarah Price, Ilkay Bora, Laramie P Jameson, Changling Qiu, Kevin A Schug, Zygmunt Gryczynski, and Sergei V Dzyuba. Spectroscopic differentiation between monomeric and aggregated forms of bodipy dyes: effect of 1, 1-dichloroethane. *RSC advances*, 6(73):68705–68708, 2016.

[199] J Matouš, JP Novak, J Šobr, and J Pick. Phase equilibria in the system tetrahydrofuran (1)-water (2). *Collection of Czechoslovak Chemical Communications*, 37(8):2653–2663, 1972.

[200] Micholas Dean Smith, Barmak Mostofian, Loukas Petridis, Xiaolin Cheng, and Jeremy C Smith. Molecular driving forces behind the tetrahydrofuran–water miscibility gap. *The Journal of Physical Chemistry B*, 120(4):740–747, 2016.

[201] Tsuneyoshi Horigome and Hiroshi Sugano. A rapid method for removal of detergents from protein solution. *Analytical Biochemistry*, 130(2):393–396, 1983.

[202] Soon Ki Sung, Hyuk Kyu Pak, Jong Hyeok Kwak, Sang Weon Lee, Young Ha Kim, Beong Ik Hur, Seong Jin Jin, and Gyeong Rip Kim. Specific radius change of quantum dot inside the lipid bilayer by charge effect of lipid head-group. *Open Journal of Biophysics*, 8(03):163, 2018.

[203] Stephanie L Castro, Sheila G Bailey, Ryne P Raffaelle, Kulbinder K Banger, and Aloysius F Hepp. Synthesis and characterization of colloidal cuins2 nanoparticles from a molecular single-source precursor. *The Journal of Physical Chemistry B*, 108(33):12429–12435, 2004.

[204] Wenjin Yue, Shikui Han, Ruixiang Peng, Wei Shen, Hongwei Geng, Fan Wu, Shanwen Tao, and Mingtai Wang. Cuins 2 quantum dots synthesized by a solvothermal route and their application as effective electron acceptors for hybrid solar cells. *Journal of Materials Chemistry*, 20(35):7570–7578, 2010.

[205] Matthew Booth. *Synthesis and characterisation of cuins2 quantum dots*. PhD thesis, University of Leeds, 2014.

[206] Pavlo I Gordiichuk, Dolev Rimmerman, Avishek Paul, Daniel A Gautier, Agnieszka Gruszka, Manfred Saller, Jan Willem de Vries, Gert-Jan AH Wetzelaer, Marianna Manca, Widianta Gomulya, et al. Filling the green gap of a megadalton photosystem i complex by conjugation of organic dyes. *Bioconjugate chemistry*, 27(1):36–41, 2015.

[207] Ashley M Hancock, Minjung Son, Muath Nairat, Tiejun Wei, Lars JC Jeuken, Christopher DP Duffy, Gabriela S Schlau-Cohen, and Peter G Adams. Ultrafast energy transfer between lipid-linked chromophores and plant light-harvesting complex ii. *Physical Chemistry Chemical Physics*, 23(35):19511–19524, 2021.

[208] Zongping Xia and Yuechueng Liu. Reliable and global measurement of fluorescence resonance energy transfer using fluorescence microscopes. *Biophysical journal*, 81(4):2395–2402, 2001.

[209] Taekjip Ha. Single-molecule fluorescence resonance energy transfer. *Methods*, 25(1):78–86, 2001.

[210] A Jj Lomant and Grant Fairbanks. Chemical probes of extended biological structures: synthesis and properties of the cleavable protein cross-linking reagent [35s] dithiobis (succinimidyl propionate). *Journal of molecular biology*, 104(1):243–261, 1976.

[211] James V Staros, Rick W Wright, and Deborah M Swingle. Enhancement by n-hydroxysulfosuccinimide of water-soluble carbodiimide-mediated coupling reactions. *Analytical biochemistry*, 156(1):220–222, 1986.

[212] Pedro Cuatrecasas and Indu Parikh. Adsorbents for affinity chromatography. use of n-hydroxysuccinimide esters of agarose. *Biochemistry*, 11(12):2291–2299, 1972.

[213] Dmitry Galetskiy, Iuliana Susnea, Verena Reiser, Iwona Adamska, and Michael Przybylski. Structure and dynamics of photosystem ii light-harvesting complex revealed by high-resolution fticr mass spectrometric proteome analysis. *Journal of the American Society for Mass Spectrometry*, 19(7):1004–1013, 2011.

[214] Zheng Lei, Su Mingyu, Wu Xiao, Liu Chao, Qu Chunxiang, Chen Liang, Huang Hao, Liu Xiaoqing, and Hong Fashui. Effects of nano-anatase on spectral characteristics and distribution of lhcii on the thylakoid membranes of spinach. *Biological Trace Element Research*, 120:273–283, 2007.

[215] S Vasil'ev, K-D Irrgang, T Schrötter, A Bergmann, H-J Eichler, and G Renger. Quenching of chlorophyll a fluorescence in the aggregates of lhcii: steady state fluorescence and picosecond relaxation kinetics. *Biochemistry*, 36(24):7503–7512, 1997.

[216] Said Eshaghi, Bertil Andersson, and James Barber. Isolation of a highly active psii-lhcii supercomplex from thylakoid membranes by a direct method. *FEBS letters*, 446(1):23–26, 1999.

[217] Didem Ag, Rebecca Bongartz, Leyla Eral Dogan, Muharrem Seleci, Johanna-G Walter, Dilek Odaci Demirkol, Frank Stahl, Serdar Ozcelik, Suna Timur, and Thomas Scheper. Biofunctional quantum dots as fluorescence probe for cell-specific targeting. *Colloids and Surfaces B: Biointerfaces*, 114:96–103, 2014.

[218] Rute F Domingos, Dana F Simon, Charles Hauser, and Kevin J Wilkinson. Bioaccumulation and effects of cdte/cds quantum dots on chlamydomonas reinhardtii–nanoparticles or the free ions? *Environmental science & technology*, 45(18):7664–7669, 2011.

[219] Giovanni Finazzi, Giles N Johnson, Luca Dallosto, Pierre Joliot, Francis-André Wollman, and Roberto Bassi. A zeaxanthin-independent nonphotochemical quenching mechanism localized in the photosystem ii core complex. *Proceedings of the National Academy of Sciences*, 101(33):12375–12380, 2004.

[220] Hendrik Christoffel Hulst and Hendrik C van de Hulst. *Light scattering by small particles*. Courier Corporation, 1981.

[221] Harald Paulsen, Bärbel Finkenzeller, and Nicola Kühlein. Pigments induce folding of light-harvesting chlorophyll a/b-binding protein. *European Journal of Biochemistry*, 215(3):809–816, 1993.

[222] Dirk Reinsberg, Paula J Booth, Caroline Jegerschöld, Bee J Khoo, and Harald Paulsen. Folding, assembly, and stability of the major light-harvesting complex of higher plants, lhcii, in the presence of native lipids. *Biochemistry*, 39(46):14305–14313, 2000.

[223] Lonnie J Lucas, Jin-Hee Han, and Jeong-Yeol Yoon. Using highly carboxylated microspheres to simplify immunoassays and enhance diffusional mixing in a microfluidic device. *Colloids and Surfaces B: Biointerfaces*, 49(2):106–111, 2006.

[224] Orla Deegan, Kieran Walshe, Kevin Kavanagh, and Sean Doyle. Quantitative detection of c-reactive protein using phosphocholine-labelled enzyme or microspheres. *Analytical biochemistry*, 312(2):175–181, 2003.

[225] Lin Fu, Chun-Min Kang, Peng Zhang, Xia Kang, Xin Li, Hong-Xia Wang, Hai-Xia Li, and Yu-Rong Qiu. A modified quick petia for detecting anti-ccp antibodies in human serum. *Analytical Methods*, 7(7):3134–3140, 2015.

[226] Pavel Frantsuzov, Masaru Kuno, Boldizsar Janko, and Rudolph A Marcus. Universal emission intermittency in quantum dots, nanorods and nanowires. *Nature Physics*, 4(7):519–522, 2008.

[227] Christophe Galland, Yagnaseni Ghosh, Andrea Steinbrück, Milan Sykora, Jennifer A Hollingsworth, Victor I Klimov, and Han Htoon. Two types of luminescence blinking revealed by spectroelectrochemistry of single quantum dots. *Nature*, 479(7372):203–207, 2011.

[228] Gangcheng Yuan, Daniel E Gómez, Nicholas Kirkwood, Klaus Boldt, and Paul Mulvaney. Two mechanisms determine quantum dot blinking. *ACS nano*, 12(4):3397–3405, 2018.

[229] Jiaojian Shi, Weiwei Sun, Hendrik Utzat, Ardavan Farahvash, Frank Y Gao, Zhuquan Zhang, Ulugbek Barotov, Adam P Willard, Keith A Nelson, and Moungi G Bawendi. All-optical fluorescence blinking control in quantum dots with ultrafast mid-infrared pulses. *Nature Nanotechnology*, 16(12):1355–1361, 2021.

[230] Iain Johnson. The molecular probes handbook: a guide to fluorescent probes and labeling technologies. *(No Title)*, page 1060, 2010.

[231] Alexander L Efros and David J Nesbitt. Origin and control of blinking in quantum dots. *Nature nanotechnology*, 11(8):661–671, 2016.

[232] Alain Sillen and Yves Engelborghs. The correct use of "average" fluorescence parameters. *Photochemistry and photobiology*, 67(5):475–486, 1998.

[233] Yahui Li, Sapermsap Natakorn, Yu Chen, Mohammed Safar, Margaret Cunningham, Jinshou Tian, and David Day-Uei Li. Investigations on average fluorescence lifetimes for visualizing multi-exponential decays. *Frontiers in physics*, 8:576862, 2020.

[234] Saim Emin, Surya P Singh, Liyuan Han, Norifusa Satoh, and Ashraful Islam. Colloidal quantum dot solar cells. *Solar Energy*, 85(6):1264–1282, 2011.

[235] Jacob B Hoffman, Gary Zaiats, Isaac Wappes, and Prashant V Kamat. Cspbbr3 solar cells: controlled film growth through layer-by-layer quantum dot deposition. *Chemistry of Materials*, 29(22):9767–9774, 2017.

[236] Hyeong-Gon Kang, Fuyuki Tokumasu, Matthew Clarke, Zhenping Zhou, Jianyong Tang, Tinh Nguyen, and Jeeseong Hwang. Probing dynamic fluorescence properties of single and clustered quantum dots toward quantitative biomedical imaging of cells. *Wiley Interdisciplinary Reviews: Nanomedicine and Nanobiotechnology*, 2(1):48–58, 2010.

[237] Pascal Albanese, Jon Nield, Jose Alejandro Munoz Tabares, Angelica Chiodoni, Marcello Manfredi, Fabio Gosetti, Emilio Marengo, Guido Saracco, James Barber, and Cristina Pagliano. Isolation of novel psii-lhcii megacomplexes from pea plants characterized by a combination of proteomics and electron microscopy. *Photosynthesis research*, 130:19–31, 2016.

[238] Cristina Pagliano, Jon Nield, Francesco Marsano, Tillmann Pape, Simone Barera, Guido Saracco, and James Barber. Proteomic characterization and three-dimensional electron microscopy study of psii–lhcii supercomplexes from higher plants. *Biochimica et Biophysica Acta (BBA)-Bioenergetics*, 1837(9):1454–1462, 2014.

[239] Jie Gao, Xiaoling Yao, Yingxu Chen, Zhonghong Gao, and Jingdong Zhang. Near-infrared light-induced self-powered aptasensing platform for aflatoxin b1 based on upconversion nanoparticles-doped bi2s3 nanorods. *Analytical Chemistry*, 93(2):677–682, 2020.

[240] IV Martynenko, AP Litvin, F Purcell-Milton, AV Baranov, AV Fedorov, and YK Gun'Ko. Application of semiconductor quantum dots in bioimaging and biosensing. *Journal of Materials Chemistry B*, 5(33):6701–6727, 2017.

[241] Zhengdi Wang, Tingting Hu, Ruizheng Liang, and Min Wei. Application of zero-dimensional nanomaterials in biosensing. *Frontiers in chemistry*, 8:320, 2020.

[242] Vancha Harish, Devesh Tewari, Manish Gaur, Awadh Bihari Yadav, Shiv Swaroop, Mikhael Bechelany, and Ahmed Barhoum. Review on nanoparticles and nanostructured materials: Bioimaging, biosensing, drug delivery, tissue engineering, antimicrobial, and agro-food applications. *Nanomaterials*, 12(3):457, 2022.

[243] Julie Hottechamps, Thomas Noblet, Christophe Méthivier, Souhir Boujday, and Laurent Dreesen. All-quantum dot based förster resonant energy transfer: key parameters for high-efficiency biosensing. *Nanoscale*, 2023.

[244] S Liu, Y Sun, L Chen, Q Zhang, X Li, and J Shuai. A review on plasmonic nanostructures for efficiency enhancement of organic solar cells. *Materials Today Physics*, 24:100680, 2022.

[245] Jakub Sławski, Jan Maciejewski, Rafał Szukiewicz, Katarzyna Gieczewska, and Joanna Grzyb. Quantum dots assembled with photosynthetic antennae on a carbon nanotube platform-a nanohybrid for enhancement of light energy harvesting. *Available at SSRN 4418787*, 2023.